Kohei Uosaki *Editor*

Electrochemical Science for a Sustainable Society

A Tribute to John O'M Bockris

Springer

Electrochemical Science for a Sustainable Society

Kohei Uosaki
Editor

Electrochemical Science for a Sustainable Society

A Tribute to John O'M Bockris

Springer

Editor
Kohei Uosaki
National Institute for Materials Science
Tsukuba, Ibaraki
Japan

ISBN 978-3-319-57308-3 ISBN 978-3-319-57310-6 (eBook)
DOI 10.1007/978-3-319-57310-6

Library of Congress Control Number: 2017937519

Printed on acid-free paper

This Springer imprint is published by Springer Nature
The registered company is Springer International Publishing AG
The registered company address is: Gewerbestrasse 11, 6330 Cham, Switzerland

Preface

Electrochemistry has been studied for long time and its importance is growing more and more because of its not only fundamental interest but also expected central roles in a future sustainable society. Electrochemistry mainly deals with charge transfer at solid/liquid interfaces, which is a key step in energy conversion and materials transformation as well as biological processes.

Professor John O'M Bockris contributed much not only to fundamental and applied electrochemistry such as structure of double layer, kinetics and mechanism of the electrochemistry of hydrogen and oxygen, electrocatalysis, adsorption and electrochemical oxidation of small organic molecules, fuel cells, electrocrystallization, theoretical electrochemistry, new methods, photoelectrochemistry, bioelectrochemistry, corrosion and passivity, hydrogen in metal, ionic solutions and ionic liquids, and molten silicates and glasses but also to socio-economic issues for a sustainable society such as hydrogen economy for over half a century from 1945 until his retirement in 1997. In addition to his numerous (around 750) publications of original papers, he published about 25 influential books ranging from fundamental/applied electrochemistry to socio-economic subjects including "Fundamental Aspects of Electrocrystallization (1967)," "Fuel Cells; Their Electrochemistry (1969)," "Modern Electrochemistry (1970)," "The Electrochemistry of Cleaner Environment (1972)," "The Solar Hydrogen Alternative (1975)," "Environmental Chemistry (1977)," and "Energy Options (1980)." His contribution as an Editor of the important series of "Modern Aspects of Electrochemistry" (1954–) and "Comprehensive Treatise of Electrochemistry" (10 volumes; 1980–1985) must also be mentioned. He mentored many (close to 100) Ph.D. students, who later became leaders in electrochemistry worldwide including two great electrochemists, Profs. Parsons and Conway, postdoctoral fellows, and visiting scientists.

This book honors Prof. Bockris, who passed away in July 2013. In first chapter, Prof. Bockris' article on his electrochemical life is reproduced from *J. Solid State Electrochemistry* so that not only his contribution to wide ranges of fundamental and applied electrochemistry as well as solar-hydrogen concept but also how electrochemistry has been developed in the latter half of the twentieth century can be understood. In the following chapters, leading scientists discuss current status

of the various subjects in both fundamental and applied electrochemistry and solar-hydrogen concept such as electrocatalysis, fuel cells, electrochemical theory, electrochemistry of single crystals, in situ techniques, rechargeable batteries, passivity, and solar-fuels.

I am very happy to be an Editor of this book as I am indebted to Prof. Bockris who taught me how electrochemistry is interesting and important when I was his Ph.D. student 40 years ago. I am very grateful to the authors for their contributions and Mr. Ken Howell for his help in the planning stage of this book.

Tsukuba, Japan Kohei Uosaki
February 2017

Contents

An Electrochemical Life 1
John O'M. Bockris

Electrocatalysis for the Hydrogen Economy 23
Ioannis Katsounaros and Marc T.M. Koper

Fuel Cells: An Overview with Emphasis on Polymer Electrolyte Fuel Cells 51
Masahiro Watanabe and Donald A. Tryk

On the Theory of Electrocatalysis 95
Wolfgang Schmickler

Kinetics at Single Crystal Electrodes 113
Enrique Herrero and Juan M. Feliu

Novel In Situ Techniques 147
Takuya Masuda and Kohei Uosaki

Large-Scale Batteries for Green Energy Society 175
Kiyoshi Kanamura

Sodium-Ion Secondary Batteries Using Ionic Liquids as Electrolytes 197
Rika Hagiwara

Passivity of Iron—A Review 209
R. Winston Revie

Solar Fuels 223
S.P.S. Badwal, A.P. Kulkarni, H. Ju and S. Giddey

An Electrochemical Life

John O'M. Bockris

Abstract This chapter is a reproduction of an article written by Prof. J. O'M. Bockris published in Journal of Solid State Electrocehmistry (2011) 15:1763–1775. In this article, he described his own professional life devoted to electrochemistry with stories of his colleagues. Minor editorial changes were made by the editor to meet the style of this book.

1 Part 1

It was my aunt who started it. She had some iron filings on a piece of paper and a magnet underneath. When she moved the magnet, the iron filings moved. I was only 5 years old at the time, and I could not see any way that the magnet could have touched the iron filings.

Professor John O'M. Bockris—Deceased.

J.O'M. Bockris
Gainesville, FL 32608, USA

K. Uosaki (ed.), *Electrochemical Science for a Sustainable Society*,
DOI 10.1007/978-3-319-57310-6_1

Later on, in high school, I learned something about "lines of force" which were supposed to emanate from the north pole of a magnet, pass through surrounding space, and enter the south pole. The only problem with this idea was that I still could not see them; but I did learn the word "magnetism", and I also started to collect notes based upon books that I read, and even encountered the phrase "magneto-chemistry".

Many years later, I found myself at Imperial College in London, applying for a stipend to do research. I must have been about 20. The place was dark and deserted as I walked hesitantly down the corridor, but there was a dim light glimmering under one particular door, so I knocked on it. The response was a military style "in". The owner of the voice did not waste any time. He brusquely asked the purpose of my visit before saying "sit". He then asked me several technical questions, of which I still remember three. The Third Law? Debye–Hückel Theory? Nitric oxide? The latter turned out to be an oblique query about *anesthetics*. He then asked me what kind of research I would like to do if I got a scholarship. When I told him that my greatest interest was in magneto-chemistry, his face fell. For my part, I had no idea I was talking to H.J.T. Ellingham, a world expert on the industrial applications of electrolysis, and, at night, a Lieutenant in the 2nd London Home Guard. He did not say anything. He just stood up and said "wait".

About 5 min later he returned with a tall gentleman, who turned out to be H. J. Emeléus, the leading inorganic chemist in the country. His seminal book *Modern Aspects of Inorganic Chemistry* (1938), conceived and written with his colleague J. S. Anderson, had led to a national revival of interest in that area of chemistry. Unfortunately, Emeléus spoke very quietly, and I did not catch his name. So I did not realize to whom I was speaking. He came straight to the point.

"So you want to do magneto-chemistry?"

"Yes", I said eagerly.

"Then I assume you know magnetism and electricity…?"

I nodded.

"Well, then, how about magneto-chemistry and electrochemistry…?"

I thought about it, but before I could muster a response, he continued, "If you'd like to do electrochemistry, we do have scholarships for that, but as for magneto-chemistry… the war is on and many of our people are in the army…" At that moment I knew I had become an electrochemist!

A few weeks later, I was given a room (actually an office and a lab combined) and a pep-talk from the man who was going to be my supervisor, none other than Dr. Ellingham, the man to whom I had spoken on that first day. The pep-talk lasted about 20 min, and the only outcome of significance was that he handed me a box of abstract cards on which he had written the titles of interesting papers in electrochemistry that he had read over the previous few years.

We are talking about 1943 here. War conditions were chaotic and I was unclear how to proceed. All I had were the abstract cards and a few vague hints. Ellingham added, "I'm sure you will find something that has not been done yet… if you follow up an idea, and make something of it, you should be able to write a thesis and get a

degree…" Ellingham was always brief, but 20 min hardly seemed adequate to map out the next 2 or 3 years of my life.

Anyway, I was left to my own devices, with the box of cards and a broad hint that non-aqueous solutions might be a reasonable place to start. I read, for about 3 weeks, digging out various references, reading the relevant papers. Suddenly, it hit me. *Overpotential had never been measured in non-aqueous solutions.*[1] Ah! That would be my project. If my way onwards was as open as it seemed to be, then I would set the direction myself, and here it was in work which had just been published, telling me where to go.

Well, what followed was 2 years of hard work, so I'll spare you the minor details. But after 2 years, I had accumulated lots of data, though I certainly did not understanding them all. One day, Dr. Emeléus came to see me. As usual he spoke *sotto voce.* I was eating a sandwich at the time, when he suddenly whispered, "How long will it be, Bockris, before you can write your thesis?" I probably hummed and hawed a bit before trying to answer, because he did not wait for my reply, but continued, "… because if you can finish it in time to give the lectures which Ellingham was due to give before he leaves, we would probably give you a job on the faculty…"

Of course this really made me jump, because a faculty position at Imperial College was a prime job. It implicitly held tenure, and unless you punched your supervisor in the face or did something similarly outrageous, you were there for life. The only problem was that I had to finish my thesis before the lectures were due to begin, because, by regulation, they could not have someone lecturing to students who were not fully qualified.

I wrote my thesis in 6 weeks, which included a nightmarish period of 3 days in which I did not sleep at all. But I managed to turn up at Ellingham's door one Sunday morning, very cold, at the only time he had available, 7:00 a.m. I was to present him with everything I had done. He paced up and down whilst I spoke to him, and did not seem interested in the slightest. But he told me to leave the thesis with him and he would see what could be done. "Come back next Sunday morning at 7:00 a.m."

Of course the week between the two meetings was one of extreme tensions for me, as my future career was hanging in the balance. Then, at the appointed hour, pacing up and down before a blazing fire, he told me that he did not think the thesis was good enough. The obvious question was *why?* His answer, I was not prepared for. He said that there was far too much mathematics in it. I held precisely the reverse view, that unless your thesis had some mathematics in it, then it was not up to standard. He told me to "rewrite" it, before ushering me out into the cold street at about 7:20 a.m. I was now in suspense for another week.

[1] I once set fire to a flask containing ether around 9:00 p.m. one evening. It did not seem to be the kind of thing that my supervisor would want to hear about, so I let it pass. By chance, seeing him in a queue at the hostel in which we both lived during the war, I boldly approached him hoping to get an appointment for a discussion of my work. When I got level with him in the queue and indicated that I would like to speak with him, he looked at me and said, "Is it about the theory of inflammability?" He did not give me an appointment.

To rewrite a thesis in a week is absurd, so I just rewrote the mathematical parts in plain English, indicating that they could be "supported" by mathematical equations. He was still doubtful the next week, but I explained that his departure for a job at the Royal Institute of Chemistry would leave a teaching gap in electrochemistry, and that I hoped to fill in. "If I don't get the thesis sir, I cannot carry on your tradition…" At that point he softened somewhat, and said "I'll let you go through to the oral, but the examiner may not let you through."

I did not know who the examiner was at that time, but it turned out that he was a renowned surface chemist brought down from Edinburgh. Of course, I did a good deal of touching up of the thesis before the oral. When the examiner finally started the formal examination, he went more-or-less page by page, stopping and asking little questions, which I easily batted back. But I realized that I had made a big mistake slightly past the mid-point of the thesis, and that we were about to reach it. At that moment, the Great Hand from Above entered into my life, and the examiner suddenly said, "Well that's enough for today, Bockris, well done!" And that is how I became an electrochemist.

So, in September 1945, I began my career as a young academic at the Imperial College of Science and Technology, London University. I was only 22, which was very young indeed to have a position on the faculty. There was a good explanation for my youthful appointment, though. The war was still on, and many young people who would have been my competitors were away on active service. The following year, there was of course a flood of students who wanted to work in Universities. Among the throng were Brian Conway (who later emigrated to Ottawa, Canada) and Roger Parsons, who became famous in the academic world in England, ultimately becoming President of the Faraday Division of the Chemical Society, and a Fellow of the Royal Society.

The first time finance came into things was in 1947, when I was visited by two gentlemen from the British Iron and Steel Research Association. They came right to the point within 3 or 4 min of coming into my room. They wanted to know if slags were conductive. Unfortunately, all I knew about slags at that moment was that they were supposed to be very important in steel making! However, the models used by BISRA seemed to me to be over-simplistic (i.e., they were supposed to be molecular compounds and so should be non-conducting) and after some discussion they decided to fund some research with me.

Richardson was their research director and Jim Jeffs was his companion and—it seemed to me—Jeffs was the originator of most of the queries. I answered the most important question (are slags conducting?) within the first 6 months of the contract, by which time, of course, we had learned a lot about slags. The two researchers I supervised on slags were named Liebermann and Tomlinson. After we measured the conductance of the slags at the unheard of temperature of 1,850 °C, BISRA were quite keen to extend their funding to other measurements.

What surprised those with whom we spoke about our work was the high temperature at which we worked, over 1,600 °C, which is normal in steel making but rather unusual in electrochemistry. I learned a lot about how to do this by visiting the steel makers of Britain at that time, and they willingly showed me their

technology. The man who worked on the most difficult part of these measurements was called Dennis Lowe, and he had an unfortunate accident just as he was finishing the building of an extremely complex apparatus which rose about 12 ft above the ground. Putting the finishing touches to it, he stood upon a chair, lost his balance, fell over, and the entire apparatus (which had taken more than a month to build) crashed down on top of him. This did not put him off for too long, however, as he was soon back at it and performing accurate measurements of the viscosity of liquid silicates at temperatures above 1,800 °C.[2]

When discussing those early years at Imperial College, the name of Roger Parsons inevitably turns up. Roger was an impressive student, and 60 years later I can still visualize his economy of movement. He would enter my room upon arrival every morning, and on cold days he would already be removing his overcoat with one arm as he entered. With the other arm, as it dropped down, he would be seeking to switch on his apparatus. Years later, Roger told me that he had chosen to carry out research under my direction because, whilst attending my lectures, he had noticed that I had delivered them without notes. He found this most unusual, and it had suggested to him that I must have known what I was talking about!

My own view of the young Roger Parsons was that he was an outstanding student. Indeed, his confidence and objectivity were so great that he would change his view—one theory, let us say, for another—without compunction, and without the least feeling of any great event having occurred.

When it came for Roger to get his Ph.D., and leave me, I felt that we had done a very important job for electrochemists in general, because we had actually found out how to get reproducible results. When we began, we would get certain data from certain experiments, and then go to other laboratories in England, and also some in Germany, and compare them. It was very disconcerting when we found that they were all different. But with plenty of help from Brian Conway, Roger found out how to purify solutions and electrode surfaces in such a way that the irreproducibility was overcome.

In the immediate post-war years, the University of Cambridge was the principal place in England at which first class electrochemical research was performed. The main person I knew there was John Agar. He stayed in Cambridge for his entire career, and was a leading light there for more than 30 years. T.P. ("Sam") Hoar was another person I knew in Cambridge, and his *forte* was corrosion at a very fundamental level. In fact, in the history of this rather practical subject, Agar, Hoar, and U.R. Evans are generally credited with having established, for the first time, the basic mechanisms of this very important process. Perhaps they got some theoretical ideas from the publications of Karl Wagner, but it was Evans and Hoar who proved the mechanisms experimentally.

[2]Austen Angell is also familiar with this work which took place about 1950. He tells me that because he had to use data for very high-temperature liquids he became familiar with the details of the work we did years ago, and he felt in speaking recently, i.e., 2009, that even though more than 50 years had passed since we did this work, it still remained unsurpassed because of the high temperature at which we made the measurements.

Hoar played a part in my life in the late 1940s because it was he who invited me to come with him to Brussels in Belgium where, he said, a very important meeting was to take place. I was uncertain as to what was going to happen there, until we arrived, when I was introduced to Marcel Pourbaix, a man throbbing with enthusiasm for his job which was of course the thermodynamics of corrosion. By the time that invitation came I also knew perhaps 20 or 30 electrochemists in the USA, or at least I had met them.[3]

I have already mentioned Dennis Lowe as the man who measured the viscosity of silica at high temperature. It was with him that I developed the first theory of liquid silicates, because we also measured the viscosity of various mixtures of silica and metal oxides, and we decided to propose a fairly comprehensive theory of all kinds of silicates. This needs diagrams to express it properly, but I will just say that the principle anion was $Si_3O_8^{6-}$. The paper was accepted in the prestigious *Proceedings of the Royal Society,* which meant that it was very widely read.[4]

In 1953, I was appointed Professor of Physical Chemistry at the University of Pennsylvania. In 1956 Brian Conway, who had followed me to Pennsylvania, decided that the time was ripe to accept his own Professorship, and he took a position at the University of Ottawa, where he stayed for the rest of his life. However, we had a great colleagueship which we managed to maintain for many years afterwards. With Conway I developed a good deal of my thinking on the hydrogen evolution reaction, which became the model I used for all other electrochemical reactions. Along with this, I was also interested in the oxygen reduction reaction (and its partner, the oxygen evolution reaction) because I was always interested in fuel cells.

Thinking about the evolution of oxygen puts me in mind of A.K.M. Shamshul Huq, who was a student who came over with me from London. Now, we had already established that impurities in solution were the main problem in getting reproducibility in electrochemical reactions, and so Huq and I were able to work at very low current densities or velocities of reaction. Eventually, we were able to make measurements as far down as 10^{-9} amps cm^{-2}. At the time we were doing this (1955), there was no air conditioning, except for apparatus. That is, the University would buy an air conditioner for an experimental piece of equipment,

[3]In telling amusing stories which occurred on my long pathway through life, one has to be careful not to tell too many, because of course people get bored with them. However, I feel that this three or four liner will not bore you if I tell it, as it gets something of the atmosphere of the time and also tells something about how I was regarded by my students at this early time. The two young men who comprise this story lived together to save money, and they also slept in the same bed, particularly on cold days, for they could not afford any heating. On Saturday they would stay longer in bed, and on one occasion there was a ring at the doorbell and a telegram arrived. One of the boys got out of bed to fetch it, and read it to his startled companion upon his return. It said "The early bird gathers the worms. It's already 9:30. Why aren't you here? Bockris".

[4]Proof of this statement came to me on the bullet train in Japan. I had never been on the bullet train before, and it was exciting to ride at 120 mph. However, the train does stop every now and again, and at one stop a man entered, came confidently up to me, and sat down. He explained that he had found out that I would be on the train, and wanted to congratulate me on my theory of "glasses"!.

but not for a researcher! Researchers, they thought, should sweat it out, so we tended to work after dark when it was cooler.

Meanwhile, Conway and I continued to develop our theory of proton conduction. However, there came across our bow, so to speak, a man who later on became famous in his own right, namely Manfred Eigen, a German physical chemist. After we had obtained acceptance of our paper, in the *Journal of Chemical Physics* no less, he came out and said that one of the steps we had made was wrong in not being quantized when it should have been. Fortunately, this did not affect the overall model, which was that the rate determining step was related to the rotation of water molecules with which the proton was surrounded. Of course, the rate of rotation depended upon the electric field of the proton, and later on we showed why it was that, in ice, the proton had a much greater mobility than it had in water, a counterintuitive fact.

One of the more exciting students in the 1950s was a German called Wolfgang Mehl. The excitement he brought to our group consisted of two quite separate elements. First of all he brought from Berlin, where he had been working with a German electrochemist called Heinz Gerischer, the idea of "transients", i.e., very fast measurements which could be over in a millisecond. There are various kinds of transients (do you keep the potential constant?) and with Mehl we developed several new ones. But, Wolfgang's popularity and local fame among my students was more dependent upon his stories about the war.

C. Austen Angell worked with me in the 1950s too, and later on he had a splendid career, in what you might call metastable aqueous electrochemistry. His specialty was a subject called *supercooling*. He studied this phenomenon in great detail, and the results made him well known and the recipient of many awards.

In looking back over the years, one tends to pick out individuals of an unusual character, and one person, who especially comes to mind in the late 1950s, was Erik A. Blomgren, a Swedish post-doc who was accompanied by his (unmarried) wife. He was in the habit of calling me up on the telephone when he had completed an experiment, and telling me about it by saying he had brought it "on the limit, John", meaning that he brought it to an extreme never reached before!

Aleksandar (Asa) Despić was another man who worked with me in the 1950s. He also returned in the 1960s, on which occasion he was accompanied by his colleague Dragutin M. Drazic. These fellows were both strong communists. In those days in the USA, it was considered almost dangerous to admit that one had met a communist.[5] Despić was particularly sought out by wealthy Americans, who wanted to meet an actual communist, and they were always surprised to find out that he was quite a normal and intellectual person. According to his own accounts, he actually had some success in bringing his hosts around to his way of thinking. He certainly left me with one memorable phrase from those days, "From each according to his ability, to each according to his needs."

[5]When I was invited to Russia in 1956 to give a lecture in Moscow, I felt it prudent to approach the president of the University of Pennsylvania and ask his permission to accept the invitation, so great was the negative feeling toward communism at that time.

Despić and Drazic introduced me to the very important electrochemical process by which iron dissolves and is re-deposited on solid substrates. The reasons for my interest in this go back to my earlier discussions with Hoar and Wagner, both of whom I have already mentioned. What Despić and Drazic did was to explore the detailed mechanism of the iron dissolution reaction. This was important because of its engineering implications. Why do ships and planes not last more than 30 years, or so? It is all because of corrosion, of course, and I have heard it said that 2 or 3% of the GNP of the USA is still wasted on corrosion.

Before finishing this account of derring-do among experimentalists, I would like to briefly mention *dendrites*. In case you have not heard of them, they are spike-like things which jut out from growing bodies during crystallization. All this interested a man who came to work with me from England, whose name was J.L. Barton, and he resolved to find out how they worked. We published a paper together in the *Proceedings of the Royal Society* entitled "The electrolytic growth of dendrites from ionic solutions", and that has become something of a classic. One of the more exciting mechanistic things we did was to find out why dendrites grow so fast. It turns out to be due to the spherical shape of the tip of the crystal. If the radius is less than the diffusion layer thickness then the rate of the growing crystal is dependent on R. If that is small enough, the dendrite grows so fast that it sticks out from the crystal body.

2 Part 2

1963 was a good year for me because it was the year in which I published my best paper. It was called "On the Structure of Charged Interfaces", and was co-authored with M.A.V. Devanathan and K. Müller. It was published in the *Proceedings of the Royal Society (London)*, and today is widely referred to as "The BDM Paper". Devanathan was a post-doc with me, but he had also worked in London with Roger Parsons, and he was thoroughly knowledgeable concerning the structure of the double layer. Computers were just coming into university research in 1963, and in those days there was usually only one computer in a special room, and one could only use it by appointment. I designated Müller to be the person to learn how to use it, and it was he who carried out all the calculations, of which this particular paper had many.

There was also a major innovation in this paper. It was the first time that the structure of water on the electrode was included in any model of the double layer. Obviously, a layer of water dipoles would be oriented according to the charge on the electrode surface, and the extent of orientation would vary with the applied potential. The mathematical treatment of the water, and how we accommodated the potential of the electrode, was largely developed by myself, but I must admit that I

got a bit of help from a treatise on paramagnetism in which the orientation of the magnetic moments had been worked out earlier. Devanathan was responsible for most of the ideas on specific absorption, which also allowed us to interpret the characteristic "hump" on capacitance-potential diagrams, which had long puzzled researchers. We managed to get the BDM paper into the *Proceedings of the Royal Society* and it has been the "apple of my eye" ever since.

Things were going fast and furious in my group in the mid-1960s and it grew past 25 people. Eventually, we hired a man to look after the finances, although the University also kept its eye on that, but the details were very much in our own hands. Every year we looked forwards to determining the number of coworkers we could hire.

In order to understand this story, one has to have some idea of the era to which I refer. It was the early 1950s. At that time, J.A.V. Butler was working at the Chester Beatty Research Institute, Institute of Cancer Research, which had its building remarkably close to the Imperial College building in which I worked from 1945 to 1953. Objectively speaking, Butler was a creative scientist. He was recognized in physical chemistry as a leading figure within England, and in fact was rewarded with a Fellowship of the Royal Society, a rare gift, before the end of his career.

To picture the scene in which this story takes place, one must think of an office with two tables, one of which was occupied by Butler and the other by Conway, my colleague and friend. Butler had a belief in theory rather than practice, and he would spend many hours at his desk drawing diagrams, making mini-calculations with handheld calculators, etc., before he went to the laboratory to try something in practice. One of the side effects of Butler's most intense thinking was whistling. He would do this entirely unconsciously and quite tonelessly. Now this would happen every day, and Conway knew that those times of whistling were particularly times in which Butler could not be disturbed. But the curious part is that, after a strenuous bout of whistling, Butler would often turn around in a petulant manner and demand, "stop that whistling Conway!" He never understood that he got the wrong person.

This account describes an event that occurred after Brian Conway had come to work with me at the University of Pennsylvania, where I was in my second year. When he returned to his Institute in London after a year's absence, he was coming down the stairs when he met Butler, his boss, coming in the opposite direction. Butler wore those gold rimmed, small glasses, and did not see very well, but as the two came near to each other, Butler said "Oh, err, is that you Conway?" "Have you been away? I have been looking for you."

The chairman of the committee which was going to decide the Nobel Prize was present at the banquet, and he could not understand why it was that he had to wait so long for Henry, who was nearby at the Academy's hotel. Finally, the chairman decided to send a limousine to get him to come to dinner, and eventually he did turn up, but how was he dressed? His reputation had always been that he was a great simplifier and he would give lectures on the most advanced quantum mechanics in which he simplified the whole thing down to sheep jumping over fences (or going through them). Despite this mathematical sophistication, Henry had no idea of how Swedes dressed for a formal banquet. It required not only black pants, but tails

behind the pants toward the floor. Unfortunately, Henry was dressed in an open neck shirt, yellow, and, horror of all, football shorts. The Swedes are very well-mannered people, and of course did not say anything, but that was the end of the Nobel Prize for Henry Eyring.

In 1964, Amulya K.N. Reddy joined our community. He was a post-doc, a senior man, and had been educated in the West although he came from India, indeed at the same Imperial College where I got my own Ph.D. degree. He had accepted an invitation to join my electrochemistry group on a rather tentative basis because he had no detailed knowledge of electrochemistry at all when he joined us, but he was very intelligent and later on we wrote a two-volume book together, and a famous one at that, "*Modern Electrochemistry*". In many ways, his lack of detailed electrochemical knowledge was actually a help, because I had to explain everything in detail, and when "the penny dropped" his surprise and joy came through in his good, clear writing.

When I first met Reddy, I had just returned from a trip to Norway, where in the far reaches of the north there is a small town called Trondheim, famous for a battle between the British navy and the Germans forces in 1940. The man I had gone to see in Trondheim was called Winterbotham, and he possessed an apparatus which was new to me and to others. It was called an "ellipsometer", and instead of measuring the strength of light beams as they interacted with an object, this apparatus measured the complex reflectance ratio. Although there were many mathematical disadvantages to the technique, nevertheless you could do things with it that were not possible with conventional microscopes.

Thus, when Reddy joined my group, I told him about my visit to Trondheim and the ellipsometer. He grabbed the idea of something new (in which I myself had no experience) and started to work on it, including the mathematics. Reddy proved remarkable at once, because within a few days he had not only mastered the way the ellipsometer worked, but he had also mastered the mathematics. This had not yet been computerized and one had to do every calculation by hand. Soon Reddy set about writing a computer program that would simplify the long and tedious mathematics that were needed. Today, it is possible to purchase a Fourier transform ellipsometer that performs the necessary calculations in seconds, but in Reddy's time it took more than 8 h to get a single result.

One could measure very thin films on metals down to something like 5 Å, and could also observe organic compounds at less than monolayer coverage of electrode surfaces. This set Reddy up as one of the world's leading experts in ellipsometry. Looking back and putting into a context so much that was done in the 1950s and 1960s, I would claim that Reddy's ellipsometer was the beginning of optical methods for looking at surfaces on an atomic level.

Another person who came from overseas was Alexander Damjanović. We called him Sasha. Sasha was a great man for optical microscopy and he knew a lot about new techniques, in particular Nomarski Interference Contrast microscopy. With the latter we were able to study many interesting features of crystals on surfaces, down to a level of about 500 Å. It enabled us to watch the crystals growing in solution,

whereas all the other methods (except ellipsometry) required a vacuum and therefore required removal of the sample from the growth environment.

Another technique which Damjanović introduced to us was the rotating ring-disk electrode. Rotating electrodes had been much used before Damjanović's time, particularly by Russian workers, and Damjanović had some experience of this from a lab in Moscow. By adding a ring to the rotating disk (quite electrically unconnected with it) he was able to show that he could analyze intermediate compounds which existed after the first electron transfer. This was particularly valuable to us in the study of oxygen reduction in fuel cells, and later provided the basis for a more detailed study of the oxygen reduction reaction.

I already mentioned Wolfgang Mehl, who introduced transients into our group at quite an early stage, but there was another man from Germany who was much older. That was W. Beck, and he would always emphasize to us, when he paid us a weekly visit, that he had worked with the famous German electrochemist (and Nobel prize winner) Walther Hermann Nernst. What Beck did for us was to put before us the great need for work on mechanical stress. It turns out that in metal dissolution and deposition (the all important problems of corrosion) there are unseen stresses in metals which are often the sites of the corrosion reactions which take place at a later time. Beck was keen on finding out how you could identify these areas of stress, and thus determine how the velocities of various reactions, in particular the hydrogen dissolution reaction, depended upon stress, strain, and potential.

Beck's work with us lasted for only about 6 months and he never visited us more than once per week. But one of the things I remember most from my time at the University of Pennsylvania were the results we obtained from the Beck inspired experiments.

This brings me then to speak about Shyam D. Argade, a Ph.D. student who contributed two kinds of things to our program, one of which was fundamental. I am speaking about the calculation of the absolute electrode potential. You would have to be a professional electrochemist to realize that when electrochemists speak about "potential this" and "potential that" they are not really referring to the potential as everybody thinks of it, between the metal and the solution, but to a far more complex quantity which involves also the contact between the material of the electrode and the material of the reference electrode which is measuring it. Argade took this situation to pieces, figuratively speaking, and deduced that the absolute potential of the standard hydrogen electrode was approximately 4.6 V at 25 °C. This result was close to the modern value of 4.44 V.

Among the various interesting characters who joined me at the University of Pennsylvania, the last one I would like to mention is Boris D. Cahan. I used to consult for a company called "Philco" and on one of my visits I came across Boris, who was 33, working hard, at a very much reduced salary compared with Ph.D. graduates, and yet doing the same work they did. I pointed out this discrepancy to Boris, and mentioned that he could increase his salary by 30% if only he would stop for a few years and get a Ph.D. He accepted my invitation and came to work for us in 1963. He was much more than a student. In fact, when Boris was working, you often wondered who was the supervisor and who was the student; and oftentimes he knew

more than anyone else in the group. His specialty was new equipment and new techniques, and he began working, in particular, on a technique called Mössbauer spectroscopy. We had never done anything of that kind before, and I personally knew nothing about it, but this did not deter Boris, who immediately took it up. It was a newly invented technique, with very little literature, but Boris soon mastered it. It had the drawback that it was not applicable to all metals, but it did apply to iron, which of course was super important to us in our corrosion studies.

3 Part 3

Now, let's come to the big break. By 1972, I had been at the University of Pennsylvania, for 19.5 years, when I decided it might be a good idea to continue my work elsewhere. I had been traveling a great deal at this time, in various parts of the world, and made three visits to Australia. I very much liked the atmosphere. Remember I was brought up under British rules and British atmosphere in South Africa, and it all came back to me in Australia. Although a very modern and independent country, I realized that Australia still retained a strong UK connection.

By contrast, there were things which developed at the University of Pennsylvania that I disapproved of. One was the "student revolution". The administrator's attitude was, *let the students win*. They invited them to enter the University without qualifying examinations, and although one could do this in English classes, it was not something to be done in the sciences. Another thing that hit me was the attitude of the new Head of Department, who had very extreme ideas about physical chemistry. He told me that "to do quantum mechanics with something as complex as a metal lined with water was far too difficult". His idea was to make every system simple. Go to low temperatures, use individual particles, etc. He told me outright that he did not think that electrochemistry was a good subject for the Department which he was now about to run. He never told me that I should leave, but it was quite clear that he did not want me.

I had friends in Australia, and one in particular (Harry Bloom) was a Professor in Tasmania. I mentioned to him that I would not mind spending a few years in Australia, and I suspect that it was that conversation which gave rise to a series of phone calls from an individual who kept on telling me that a new University, called Flinders, (after Captain Matthew Flinders RN, the discoverer of South Australia) was looking for someone to run the physical science section of the University. Omitting details, I joined Flinders University in 1972.

Two people at Flinders stand out in my memory. One was a man called R. Winston Revie. I never met anyone who showed more enthusiasm for his work than Winston.

He had a Ph.D. from the Massachusetts Institute of Technology. The other person who turned out to have world recognition in his field 10 years after he left me was a Japanese scientist called Kohei Uosaki. He was one of those super-energetic people who would run between locations. He was known among the other students as "the locomotive" and he worked through his Ph.D. in a short

2 years. His topic was photoelectrochemistry, i.e., the relationship between light directed at electrodes in solution, and the resulting decomposition of water.

For a brief period I think that Exxon and Co. were genuinely worried about research on photoelectrochemistry, because if it had been acceptable cost-wise, the entire petroleum industry might have been threatened. Indeed, I had a number of indications (which I shall not go into here) that I was not out of sight of the CIA and their long arm whilst down in Australia. They always knew what was going on in energy research.

Uosaki had several good ideas whilst down in Australia. One of them was to illuminate both electrodes in a photocell instead of just the one that other people had been using. Not only can one hope for a doubling of yield by doing this, but also the really fruitful thing that came to light (fully developed later, back in Texas) was that if you sprinkled a small amount of catalyst on the electrode, and was careful not to exceed a monolayer, then you could obtain a tremendous increase in the efficiency of conversion of light to hydrogen. I will say more about this later on.

I must not forget Harvey J. Flitt, who worked very hard to develop a means of detecting stress corrosion cracking. Harvey's successful development of a laser-based method for picking up tiny amounts of hydrogen in metals was important, though he did not finish his work in thesis writing till I returned to America.

In 1978, I was appointed Distinguished Professor of Chemistry at the Texas A&M University, College Station, Texas, USA. Back in America I wanted to go on a new pathway in my research and I had promised many people for years that I would go into biology and see what aspects therein might succumb to modern electrochemistry. Years ago, I published an article with Supramaniam Srinivasan in which we drew attention to the fact that the metabolism of living creatures was remarkably efficient, i.e., about half the energy we take in as food actually gets converted to energy. Looked at from a non-biological point of view, this is a very high percentage, and it is very difficult to explain unless there is some kind of "fuel cell substitute" working in the body. Shortly after arriving in Texas, I encountered a lady called Agnes Rejou-Michel, and together with M. Ahsan Habib we carried out some experiments to establish that electron transfer could occur at biosurfaces in contact with ionic solutions.

We also had some limited success in getting electrical power out of bio-fuel cells based on synthetic lipid membranes formed on metal substrates, but these ideas were not readily accepted and developed by others, at least not immediately. Were I to be able to work in the lab right now, then that is a subject that I would certainly like to develop.

A negative experience for me during the early years back in the USA was the controversy about solar energy, and the extent to which it might challenge conventional sources of energy. Eventually the politics became very distracting. Fortunately, this was partly offset by the arrival of another new colleague, Vladimir Jovancicevic. He was a tall learned-looking person who was accompanied by a most interesting wife, who made a living from paintings which were of stalinistic art. Jovancicevic was a great boon to my work as he got me back away from the sensations of the conversion of light to electricity and squarely into normal, but

advanced, research chemistry. He did two main things whilst with me. Several people had examined reduction of oxygen which comes into every fuel cell, and is the one bit of fuel cell work still open to academic research. But the systems they had chosen were always at the extremes of pH, namely acid solution and alkaline solution. No one had worked in the middle, in neutral solutions.

Jovancicevic made a good job of deducing the mechanism of oxygen reduction in neutral solution. His particular apparatus was one which we had developed earlier, the rotating disk with ring. This method allows you to find the intermediates of reactions, and if you know these and how they behave, you are well on the way to understanding the rate determining step of an electrode reaction.

Another thing that Jovancicevic did was that he showed how the ellipsometer could be used as a spectrometer, i.e., one could vary the wavelengths of the light which were falling on electrodes and subject them to ellipsometric analysis. This did not take Jovancicevic very long, maybe 6 months, and it changed ellipsometry into a really viable tool.

Before I get back to more technical matters, I would like to mention that we were not averse to a bit of sociology. Balasubramaniam Dandapani was a person who had worked in American industry for 20 years before he decided to come and give us the benefit of his knowledge. But, he did not make fast progress on any electrochemical topic I gave him, so I switched him to examining something I thought might be of more general interest. "What was the relationship" I asked, "between the amount of energy nations put into their populations and the living standard it produces?"

Of course this meant about 3 months research in the library, but eventually Dandapani turned up with a graph which was full of information. On the ordinate, or upward part, he printed the average salary per head of the population, for about 30 nations. Along the abscissa, or horizontal part, was the average energy, also per head of the population (the energy including everything to do with the military). The shape of Dandapani's curve was, understandingly enough, for low energies, perhaps 2 kW per person, and the living standard was low, i.e., people were on the starvation level. But as the amount of energy was increased, there was an exponential rise in living standard, which rose toward energies like 5 and 6 kW. Then it bent over, and became flat, and there was no more increase in the living standard by feeding more energy into the country. This seemed to me to have significance. At that time (1988), the USA was the world's largest consumer of energy at 10 kW per person. But, as I knew from my life in America, it was also an easy-going, wasteful, society in which many families had three or four cars. Therefore, it seemed to me that if one cut back the amount of energy that was used by an advanced nation, its living standard would hardly change. This idea has come into all the work that I have done more recently (indeed after retiring from the University) about the supply of energy which would be clean and inexhaustible.

A long-term colleague of mine at the University of Pennsylvania was Alan MacDiarmid, a very energetic New Zealander who came to Penn about the same time as I. Alan had previously received a Shell graduate scholarship to study silicon hydrides at Cambridge University, England under the directorship of H.J. Emeléus. After a brief appointment as a junior faculty member at Queens College of the

University of St. Andrews, Scotland, he accepted a junior position on the faculty of the Department of Chemistry at the University of Pennsylvania. Alan, together with Alan J. Heeger, and Hideki Shirakawa, won the 2000 Nobel Prize in Chemistry "for the discovery and development of conductive polymers".

MacDiarmid, Heeger and Shirakawa made their seminal findings at the end of the 1970s and conductive polymers quickly developed into a research field of great importance for chemists as well as physicists. Their discovery seemed to hold immense promise and I fell upon it from the electrochemical point of view. I reckoned that it would be easy, using electrochemistry, to make fairly slight changes in the surface of these electronically conducting polymers so that they would act as photo-electrodes, and by varying conditions appropriately, I could make a reaction go faster or slower. I still have grand fantasies of being able to patent a fuel cell electrode which can be easily and cheaply made from polymers rather than metals.

It is now 1989 at the Texas A&M, and in order to account for the atmosphere and happenings, I have to remind you that when I was at Imperial, I knew a student who was only 2 or 3 years behind me in his Ph.D. (and also in his age). His name was Martin Fleischmann and he appeared on *The MacNeil/Lehrer NewsHour* (a broadcast TV program) in March 1989, together with a colleague named Bobby Stanley Pons, to announce the discovery of something which they thought would cause a great sensation (as it did).

What they claimed was that, by chemical means, they had made a reaction occur which was *nuclear* in nature and not chemical. Of course everyone knows that nuclear reactions can cause bombs of incredible strength, a million times more powerful than ordinary bombs. So everyone expected a nuclear reaction to be much more powerful than a chemical reaction. And, so, at the time of the announcement, every scientist was up in arms at the ridiculous nature of their claim. It was also widely noted that they were chemists not physicists.

All the nuclear physicists proclaimed, as one man, that the idea could not be true. But the chief experimental result that Martin Fleischman used to back up his claim was the release of heat. He knew the amount of heat that a normal electrolysis cell should put out (it is not ambiguous), and he found that his cells were sometimes putting out more heat than that. Now I must make one thing clear. It disturbs the truth to say that he was "electrolyzing water". What he was actually electrolyzing was D_2O, deuterium oxide. He used deuterium oxide and evolved *deuterium* and *oxygen* instead of hydrogen and oxygen. It was this kind of electrolysis which he claimed was releasing additional heat. Within days the world had divided itself into two parts. 99% scoffed at the idea, saying it must be a mistake, and 1% thought that, hey, maybe it is wrong, but suppose it is right…?

Now, I would kept a loose connection with Martin over the years, seeing him at scientific conferences, etc., but it would be untrue to say he was a personal friend of mine (which some made out). When I saw the controversy shaping up after the TV appearance, I knew what I had to do; I had to see if he was right. At the time, I had 23 coworkers, a large number. I took 19 of them and asked them to work for a few months on proving or disproving the Fleischmann–Pons hypothesis. However, as a

true scientist, I chose to look at it differently from the way Fleischmann did. I did not seek to repeat his excess heat experiments, because the heat that he was measuring was not great, and errors in measuring heat are easy to make. For example, at first we did not realize how important it was to stir the solutions to be sure the temperatures were uniform, and many other things that were indeed looked at by others who tried to replicate the Fleischmann–Pons results. I went a different route. I knew that deuterium was the second isotope of hydrogen, so I decided to look for the appearance of the third isotope, called tritium. What egged me on was that tritium was radioactive, so I saw a wonderfully quick experiment.

This story goes on, so I have to cut it down. One of my students was called Nigel Packham. At the beginning, we had no special instruments in the chemistry department to give us a signal, and so we relied on the applied nuclear engineering department. It was Nigel who first came back from a visit to them, and, referring to one particular sample, said simply, "…he said this one is full of tritium". He was referring to a technician who had analyzed for tritium. It was his fourth visit and all the other cells had shown no tritium. Well, of course it seemed sensational, but we could not publish a paper on the basis of one result, so we had to wait a few weeks to see what other students got. It was not all that certain. Yes, there was tritium. No, there was no tritium. After some weeks it appeared to us that one cell in four gave tritium and it seemed worth reporting, but it was not that certain.

Now the rest of the story is not too nice, because when we said we had tritium, you could say the world imploded. The response was vastly negative. The controversy was all over the NY Times and other journals, and whatever we said in support of Fleischmann was immediately canceled by various negative persons (particularly two on the West Coast) who kept on attacking us, and who said it could not be done, we had made errors, etc. Well, to make the story super-short, the saga went on for 2 or 3 years. Of course I continued my research and got tritium a total of 18 times. But, the weak part was, I could not promise a specific day on which to come and see a positive result, because I did not know if tritium was being formed on that particular day.

Then came a new post-doc, Chun-Ching Chien, from Taiwan. I was assured by the late Norman Hackerman that he had seen Chien make tritium on a visit to Thailand. (Norman was a Texan, very tough, and he had been the chairman from 1974 to 1980 of the National Science Board, which is composed of 25 members appointed by the President and confirmed by the US Senate, representing the broad US science and engineering community.) I promptly appointed Chien and he came and worked with me for a year. Well of course I did not only want to find tritium, I wanted to find something else: because when we took Fleischmann's heat and compared it with what the production of tritium would give, the numbers did not add up. Was the heat real? There must be something else, and everyone said: helium. I knew, as a scientist, that they were talking about $D + D \rightarrow He$, an obvious alternative if one electrolyzes deuterium oxide. So I set Chien a task: "Find helium!" Well it was not so easy, for helium is an inert gas and does not react with anything chemical. But it can be detected with a super-sensitive mass spectrograph. Initially, we thought we had detected He^3 rather than the He^4 that we were looking

for, but after a couple of days we were able to find an electrode producing both He^4 and tritium. So the heat was real, and Fleischmann was right.

Some contributions of the Bockris Group, 1945–1997	
Electrode kinetics (experimental)	
Studies in hydrogen overpotential. The effect of catalytic poisons at platinized platinum and nickel, J.O'M. Bockris and B.E. Conway, Trans Faraday Soc., 45, 989 (1949)	Effect of poisons on electrode reactions, Conway, 1949
Electrode kinetics of oxygen reduction on oxide-free platinum electrodes, A. Damjanovic and V. Brusic, Electrochimica Acta, 12, 615–628 (1967)	Electrode kinetics of oxygen reduction, Damjanovic and Brusic, 1967
The Electrolytic Growth of Dendrites from Ionic Solutions, J.L. Barton and J.O'M. Bockris, Proceedings of the Royal Society of London. Series A, Mathematical and Physical Sciences, vol. 268, No. 1335 (Aug. 7, 1962). pp. 485–505	Mechanism of dendrite growth, Barton, 1962
On the calculation of potential energy profile diagrams for processes in electrolytic metal deposition, B.E. Conway and J.O'M. Bockris, Electrochimica Acta, volume 3, Issue 4, January 1961. pp. 340–366	Potential energy profiles for metal deposition, Conway, 1961
W Mehl, M.A.V. Devanathan, and J. O'.M. Bockris, Rapid Change Over Switch for use with Low Resistance Circuits, Review of Scientific Instruments, 29, 180–181 (1958)	Electrochemical measurements on short time scales, Mehl, 1958 Blomgren, 1961 (nanosecond)
E. Blomgren, D. Inman, and J. O'.M. Bockris, Arrangement for Electrochemical Potential Time Measurements in the Milli-microsecond Range, Rev. Sci. Instrum. 32, 11 (1961)	
Electrode kinetics (theoretical)	
A.J. Appleby, J.O'M Bockris, R.K. Sen, B.E. Conway, Quantum mechanical model for electronic charge transfer at interfaces. MTP Int. Rev. Sci. Phys. Chem. Ser. One. 6, 1–40 (1973)	Quantum mechanical model for electron transfer, Appleby, 1973
Electrolytic Hydrogen Evolution Kinetics and Its Relation to the Electronic and Adsorptive Properties of the Metal, B.E. Conway and J.O'M. Bockris, J. Chem. Phys. 26, 532 (1957)	Hydrogen evolution as a function of adsorptive properties of the metal, Conway, 1957
The Adsorption of Butyl, Phenyl, and Naphthyl Compounds at the Interface Mercury-Aqueous Acid Solution, E. Blomgren, J.O'M. Bockris and C. Jesch, J. Phys. Chem., 65, 2000–2010 (1961)	Adsorption of organic compounds as a function of their structure, Blomgren, 1961

(continued)

(continued)

Some contributions of the Bockris Group, 1945–1997	
On the Equivalent Circuit for the Illuminated Semiconductor Electrolyte Interface, K. Chandrasekaran, M. Weichold, F. Gutmann and J.O'M. Bockris, Electrochimica Acta, 30, 961–963 (1985)	The equivalent circuit of semiconductors, Chandrasekaran, 1985
High-temperature physical chemistry	
The activity of sulfur in liquid iron: the influence of carbon, J.A. Kitchener, J.O'M. Bockris and A. Liberman, Discuss. Faraday Soc., 4, 49–60 (1948)	The activity of sulfur in liquid iron at 1,560 °C, Liberman, 1948
Electric transport in liquid silicates, J.O'M. Bockris, J.A. Kitchener and A. E. Davies, Trans. Faraday Soc., 48, 536–548 (1952)	Ionic conductance in liquid silicates, Davies, 1952
Viscosity and the Structure of Molten Silicates, J.O'M. Bockris and D.C. Lowe, Proceedings of the Royal Society of London. Series A, Mathematical and Physical Sciences, 226, 423–435 (1954)	Viscosity of molten silicates at 1,850 °C, Lowe, 1954
The structure of liquid silicates. Part 2.—Molar volumes and expansivities, J.W. Tomlinson, M.S.R. Heynes and J.O'M. Bockris, Trans. Faraday Soc., 54, 1822–1833 (1958)	Molar volumes of liquid silicates, Tomlinson, 1958
Molten salts	
The Compressibilities, Free Volumes and Equation of State for Molten Electrolytes: Some Alkali Halides and Nitrates, J.O'M. Bockris and N.E. Richards, Proceedings of the Royal Society of London. Series A, Mathematical and Physical Sciences, 241, 44–66 (1957)	Free volumes of molten salts, Richards, 1957
Semi-empirical calculation of 3.7 RTm term in the heat of activation for viscous flow of ionic liquid, T. Emi and J.O'M. Bockris, J. Phys. Chem., 74, 159–163 (1970)	Viscous flow of ionic liquids, Emi, 1971
The lifetime of complex ions in ionic liquids: an electrode kinetic study, J.O'M. Bockris, D. Inman, A.K.N. Reddy and S. Srinivasan, Journal of Electroanalytical Chemistry, 5, 476–480 (1959)	The lifetime of complex ions in ionic liquids, Inman, 1959
Diffusion in Molten Salts at Constant Volume, M.K. Nagarajan, J.O'M. Bockris, The Journal of Physical Chemistry, 70, 1854–1861 (1966)	Diffusion in molten salts at constant volume, Nagarajan, 1966
Nuclear reactions at room temperature	
Preliminary note. Production of tritium from D_2O electrolysis at a palladium cathode, N.J.C. Packham, K.L. Wolf, J.C. Wass, R.C. Kainthla and J.O'M. Bockris, J. Electroanal. Chem., 270, 451–458 (1989)	Production of tritium from deuterium, Packham, 1989

(continued)

(continued)

Some contributions of the Bockris Group, 1945–1997	
On an electrode producing massive quantities of tritium and helium, Chun-Ching Chien, Dalibor Hodko, Zoran Minevski and John O'M. Bockris, Journal of Electroanalytical Chemistry, 338, 189–212 (1992)	Production of helium from deuterium, Chien, 1992
Spectrophotometric methods and spectra	
A.K.N. Reddy and J.O'M. Bockris, Ellipsometry in the Measurement of Surfaces and Thin Films. In: E. Passaglia, R.R. Stromberg and J. Kruger, Editors, Natl. Bur. Std. Misc. Publ. 256, U.S. Govt. Printing Office, Washington (1964). p. 229	Ellipsometry in the measurement of thin films, Reddy, 1964
The Passive Film on Iron: An Application of Auger Electron Spectroscopy, R.W. Revie, B.G. Baker, and J.O'M. Bockris, J. Electrochem. Soc., 122, 1460–1466 (1975)	Application of Auger spectroscopy to hydrous films, Revie, 1971
Passive Films on Iron: The Mechanism of Breakdown in Chloride Containing Solutions, Tong E. Pou, Oliver J. Murphy, Vaneica Young, and John O'M. Bockris, J. Electrochem. Soc., 131, 1243–1251 (1984)	SIMS analysis of depassivation, Murphy, 1986
Fourier Transform Infrared Spectroscopic Investigation of Adsorbed Intermediates in Electrochemical Reactions, J.O'M. Bockris and K. Chandrasekaran, in Electrochemical Surface Science, Chapter 24, ACS Symposium Series, vol. 378 (1988). pp. 351–368	FTIR measurements of adsorbed intermediates, Chandrasekaran, 1988
Hydrogen in metals	
Partial molar volume of H in iron. Relation of Solubility to Local Stress. Permeation as an Arbiter of Damage. W. Beck, J.O'M. Bockris, J. McBreen, and L. Nanis, Proc. Roy. Soc. London A290: 220 (1966)	Partial molar volume of hydrogen in iron, McBreen, 1966
Hydrogen Permeation in Metals as a Function of Stress, Temperature and Dissolved Hydrogen Concentration, W. Beck, J.O'M. Bockris, J. McBreen and L. Nanis, Proceedings of the Royal Society of London. Series A, Mathematical and Physical Sciences, 290, 220–235 (1966)	Hydrogen permeation in metals, Nanis, 1965
Hydrogen Evolution in Stress Corrosion Cracking, H.J. Flitt, R.W. Revie and J.O'M. Bockris, Australian J. Corrosion, 1, 4 (1976)	Hydrogen evolution in stress corrosion, Flitt, 1976
Energy conversion	
A Hydrogen Economy, J.O'M. Bockris, Science, 176, 1323 (1972)	A hydrogen economy, Bockris, 1972

(continued)

(continued)

Some contributions of the Bockris Group, 1945–1997	
Future Clean Energy Needs Hydrogen and Solar Methods now that they are Relatively Cheap. John O'M. Bockris, pp. 1–19 in Selected Articles of Hydrogen Phenomena, "As the Memory of IHEC 2007 on the Occasion of UHK 2009", Eds. Prof. Dr. T. Nejat Vezġroğlu, Prof. Dr. M. Oktay Alniak, Prof. Dr. ġenay Yalçin, Kocaeli Üniversitesi (2009)	Convert atmospheric CO_2 with hydrogen to methanol (reverse fuel cell), Bockris, 2009
Principles of ionic solutions	
Ionic solvation numbers from compressibilities and ionic vibration potentials measurements, J.O'M. Bockris and P.P.S. Saluja, J. Phys. Chem., 76, 2140–2151 (1972)	Ionic solvation numbers by acoustic interferometry, Saluja, 1972
New techniques	
Determination of Adsorption in Double Layers involving Solid Metals, E.A. Blomgren and J.O'M. Bockris, Nature, 186, 305–307 (1960)	Radiotracer measurements of absorbed molecules, Blomgren, 1960, Swinkels, 1962
Apparatus for Measuring Adsorption from Solution on Solid Metal Electrodes, M. Green, D.A.J. Swinkels, J.O'M. Bockris, Review of Scientific Instruments, 33, 18–21 (1962)	
"Ellipsometric Optics with Special Reference to Electrochemical Systems, by W.-K. Paik, in J.O'M. Bockris (ed.), MTP International Review of Science, Physical Chemistry, series 1, vol. 6, Butterworths, Univ. Park, Baltimore, pp. 239–285 (1973)	Ellipsometric optics for electrochemical systems, Paik, 1972
Corrosion mechanisms	
The electrode kinetics of the deposition and dissolution of iron, J.O'M. Bockris, D.M. Dražić and A.R. Despić, Electrochimica Acta, 4, 325–361(1961)	Rate of the deposition and dissolution of iron, Dražić and Despić, 1961
On the mechanism of the passivity of aluminum and aluminum alloys, J.O'M. Bockris and L.V. Minevski, J. Electroanal. Chem., 349, 375 (1993)	Traces of transition metals prevent corrosion, Minevski, 1993, Kang, 1997
The protectivity of aluminum and its alloys with transition metals, John O'M. Bockris and Yongku Kang, J Solid State Electrochem, 1, 17–35(1997)	
Kinetic, Solution, and Interfacial Aspects of Iron Corrosion in Heavy Brine Solutions, N.G. Smart, R.C. Bhardwaj, and J.O'M. Bockris, Corrosion, 48, 764–779 (1992)	Iron corrosion in brine solutions, Smart, 1992
Bioelectrochemistry in terms of electrodic mechanisms	
A fuel cell model in biological energy conversion, J.O'M. Bockris, F. Gutmann and M. A. Habib, Journal of Biological Physics, 13, 3–12 (1985)	A fuel cell model in biological energy conversion, Gutmann, 1985

(continued)

(continued)

Some contributions of the Bockris Group, 1945–1997	
The Effect of Electron Transfer on the Potential of Certain Electronically Conducting Membranes, J.O'M. Bockris and F. B. Diniz, J. Electrochem. Soc., 135, 1947–1954 (1988)	Membrane potential as a function of exchange current density, Diniz, 1988
Experiments on electron transfer at the membrane-solution interface, Agnes Réjou-Michel, M. Ahsan Habib and John O'M. Bockris, Journal of Biological Physics, 14, 31–42 (1986)	Electron transfer at biosurfaces in ionic solutions, Réjou-Michel, 1986
Structure of the double layer	
On the Structure of Charged Interfaces, J.O'M. Bockris, M.A.V. Devanathan and K. Müller, Proceedings of the Royal Society of London. Series A, Mathematical and Physical Sciences, 274, 55–79 (1963)	General theory of water molecules in the double layer, Devanathan and Müller, 1963
Configurational entropy of water in the double layer, J.O'M. Bockris and M.A. Habib, J. Electroanal. Chem., 65, 473–489 (1975)	Configurational entropy of water in the double layer, Habib, 1974
A Calculation of the Entropy Maximum for the Double Layer in Terms of the Water Molecule Structure, J.O'M. Bockris and M. A. Habib, J. Electrochem. Soc., 123, 24–25 (1976)	Entropy maximum for the double layer, Habib, 1975
Photoelectrochemical kinetics	
Photoelectrocatalysis and electrocatalysis on p-silicon, M. Szklarczyk and J.O'M. Bockris, J. Phys. Chem., 88, 1808–1815 (1984)	Photoelectrocatalysis on p-silicon, Szklarczyk, 1984
A model of photon-induced self-driven electrochemical cell for water splitting to hydrogen, S.U.M. Khan, R.C. Kainthla and J.O'M. Bockris, International Journal of Hydrogen Energy, 13, 225–230 (1988)	Theory of photoelectrochemical water splitting, Khan, 1988
On the photoelectrocatalytic reduction of carbon dioxide, J.O'M. Bockris and J.C. Wass, Materials Chemistry and Physics, 22, 249–280 (1989)	Photoelectrocatalytic reduction of carbon dioxide, Wass, 1989
Organic electrochemistry	
Studies of the mechanism of the anodic oxidation of ethylene in acid and alkaline media, Halina Wroblowa, Bernard J. Piersma and John O'M. Bockris, Journal of Electroanalytical Chemistry, 6, 401–416 (1959)	Anodic oxidation of ethylene, Wroblowa, 1965

Electrocatalysis for the Hydrogen Economy

Ioannis Katsounaros and Marc T.M. Koper

Abstract This chapter deals with the concept of "hydrogen economy", which was introduced by John O.M' Bockris in 1972. We summarize the fundamental principles and the progress for the reactions relevant to the hydrogen economy, namely the hydrogen and oxygen evolution for water electrolyzers, and the hydrogen oxidation and oxygen reduction for fuel cells. The activity of each reaction can be correlated to a single descriptor, i.e. the adsorption energy of a key reaction intermediate, following a volcano-type relationship. Highly active materials can be prepared with the aid of modern computational and experimental tools. Nevertheless, to develop catalysts that are substantially more active and reach the performance of ideal catalysts, the focus must be placed on materials that can break the energetic scaling relations between intermediates. The systems of choice are acidic water electrolyzers or fuel cells, using noble metals for the catalytic material, despite the great progress made in the field of alkaline systems. However, to realize the concept of hydrogen economy on a large scale, the electrode material for either reaction must combine activity, stability and abundance.

1 Introduction

In Jules Verne's 1874 novel "The mysterious island", the engineer Cyrus Smith explains to his fellow prisoners his belief that "*water will one day be employed as fuel, that hydrogen and oxygen which constitute it, used singly or together,*

I. Katsounaros
Forschungszentrum Jülich GmbH, Helmholtz-Institut Erlangen-Nürnberg (HI ERN),
91058 Erlangen, Germany
e-mail: i.katsounaros@fz-juelich.de

M.T.M. Koper (✉)
Leiden Institute of Chemistry, Leiden University, PO Box 9502,
2300RA Leiden, The Netherlands
e-mail: m.koper@lic.leidenuniv.nl

K. Uosaki (ed.), *Electrochemical Science for a Sustainable Society*,
DOI 10.1007/978-3-319-57310-6_2

will furnish an inexhaustible source of heat and light, of an intensity of which coal is not capable" [1]. One hundred years later, in a letter to *Science*, John O'M. Bockris gave a scientific outlook to these words by introducing the term "hydrogen economy": Bockris' vision for a paradigm shift in meeting the increasing global energy needs with hydrogen acting as the primary energy carrier [2]. Bockris used the term "economy" to emphasize the energetic, economic, ecological and societal aspects of his idea. In brief, this concept was originally based on converting the plentiful and inexpensive electrical energy delivered by nuclear stations to chemical energy, by splitting water and thereby producing hydrogen in onsite water electrolyzers. After transportation to distribution stations and to final locations (houses, factories, vehicles, trains, aircrafts, etc.), the produced hydrogen would be used in an onsite fuel cell to deliver electrical energy. The advantages of Bockris' concept were obvious: the rapidly increasing energy demand would be met at a lower cost without polluting the environment, while the dependence on fossil fuels would become minimal.

When Verne was writing his book, he was probably aware of two independent observations which set the scientific stage for the "hydrogen economy": In 1789, the Dutch Adriaan Paets van Troostwijk and the German-Dutch Johan Rudolph Deiman observed that gas bubbles form on two gold wires immersed in water, when they are connected to an electrostatic generator, and they realized that they had "split" water into hydrogen and oxygen [3]. Fifty years later, in 1839, the British Sir William Grove described in a letter to the *Philosophical Magazine* how he was able to produce electricity by connecting two platinum wires, immersed in an acidic solution through two glass tubes, one filled with hydrogen and one with oxygen [4]. The observation that oxygen and hydrogen can recombine by producing electricity was actually mentioned a few months before Grove's publication, by the German Christian Friedrich Schönbein [5]. In principle, Van Troostwijk and Deiman were the first ones to split water into its components, while Grove and Schönbein had prepared the first, very primitive fuel cell.

The original concept of Bockris in 1972 included the utilization of nuclear energy for supplying the necessary energy to produce H_2 via water splitting and to set the hydrogen economy in motion. In the years that followed, however, a modification of this idea became necessary: the Chernobyl accident in 1986 raised severe concerns for the use of nuclear power, and concomitantly, there was a boost in the interest for the exploitation of renewable energy sources. Therefore, the modern interpretation of the "hydrogen economy" concept involves the utilization of renewable instead of nuclear energy, as the first step to split water and generate hydrogen. It is evident, however, that the central idea of John Bockris to use hydrogen as the primary means of storing and transporting energy remained unaltered. In fact, the concept of "hydrogen economy" is nowadays at the focus of academic, technological and industrial interest and plays a key role in the research conducted in the fields of electrochemistry, (electro-)chemical engineering, materials science, computational chemistry and others.

The focus in this chapter is the core of the 'hydrogen economy' principle, namely the electrochemical reactions of hydrogen and oxygen evolution for the water electrolyzers, and the hydrogen oxidation and oxygen reduction reaction for the low-temperature hydrogen–air fuel cells. We will (i) demonstrate the fundamental principles that govern the above mentioned reactions, (ii) summarize the important progress that was made in the field over the last decades, and (iii) discuss the future prospects towards the realization of Bockris' and Verne's vision.

2 Water Electrolyzers and Fuel Cells—The Basic Principle

In water electrolysis cells (water electrolyzers) the oxygen evolution reaction (OER) occurs at the anode (positive electrode) and the hydrogen evolution reaction (HER) occurs at the cathode (negative electrode) (see Scheme 1, left). Inversely in a hydrogen–air fuel cell, the hydrogen oxidation reaction (HOR) takes place at the anode (negative electrode) and the oxygen reduction reaction (ORR) occurs at the cathode (positive electrode) (see Scheme 1, right). The overall reaction occurring in a water electrolyzer (forward reaction, left-to-right) or in a hydrogen–oxygen fuel cell (back reaction, right-to-left) is described by (1):

$$2H_2O \rightleftharpoons O_2 + 2H_2. \tag{1}$$

At standard conditions, the Gibbs free energy of the forward non-spontaneous water splitting reaction is +474.4 kJ per 1 mol of O_2 evolved. Thus, water splitting can take place only with the supply of electrical energy, i.e. by applying a potential of at least 1.229 V between the two electrodes. The Gibbs free energy of the reverse spontaneous reaction is equal but of opposite sign.

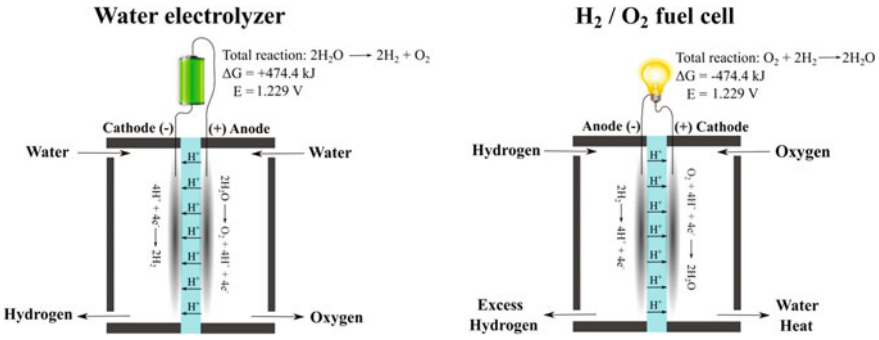

Scheme 1 Principle of operation of water electrolyzers (*left*) and hydrogen–oxygen fuel cells (*right*) under acidic conditions

2.1 Fundamentals of the ORR and the OER

The oxygen reduction and the reverse water oxidation are multi-step processes and involve the transfer of up to four electrons [6]:

$$O_2 + 4H^+ + 4e^- \rightleftarrows 2H_2O \quad E_{O_2/H_2O} = +1.229\ \text{V vs RHE} \tag{2}$$

where E is the standard equilibrium potential of the reaction with respect to the reversible hydrogen reference electrode (RHE). Such multi-electron processes proceed sequentially through the formation of several intermediates. Depending on the followed mechanism, reaction intermediates can be *OOH, *O, *OH, *HOOH or dissolved H_2O_2, where the asterisk denotes adsorbed species. The distinction between the mechanisms is based on the number of proton/electron transfer steps that precede the O–O bond cleavage (for the ORR) or formation (for the OER) [7–9]. The only possible intermediate of the overall reaction (2) that can desorb is hydrogen peroxide [10]:

$$O_2 + 2H^+ + 2e^- \rightleftarrows H_2O_2 \quad E_{O_2/H_2O_2} = +0.695\ \text{V vs RHE} \tag{3}$$

$$H_2O_2 + 2H^+ + 2e^- \rightleftarrows 2H_2O \quad E_{H_2O_2/H_2O} = +1.709\ \text{V vs RHE.} \tag{4}$$

The participation of H_2O_2 in the reaction sequence remains debateable. The standard equilibrium potentials shown in (3) and (4) are calculated for a solution with the standard activity of H_2O_2 equal to one. Thus, in thermodynamic terms it cannot be excluded that a small amount of H_2O_2 forms as an intermediate from the ORR at potentials more positive than +0.695 V_{RHE} or from the OER at potentials less positive than +1.709 V_{RHE} [10]. Indeed, the comparison between the O_2 and H_2O_2 reduction shows that the two reactions follow the same trends in different electrolytes or surfaces (low- and high-index Pt facets), indicating that the ORR is likely to proceed through an H_2O_2-mediated pathway [11–13]. Similar studies on the oxidation of H_2O_2 under conditions relevant to the OER are not known.

The ideal catalyst would carry out both reactions at the reversible potential, i.e. at +1.23 V_{RHE}. This would be achieved only if there was no uphill step during either the ORR or the OER at this potential; namely, if the difference in the free energy of the species involved in each step was zero [14]. Real catalysts, however, deviate from the ideal scenario. Density functional theory (DFT) calculations allow the calculation of the free energies of the species [14] and show that there are three endothermic steps for the ORR, i.e. OOH* formation, *O hydrogenation and *OH desorption (see the black diagram from left-to-right in Fig. 1), while the OER is associated with the strongly endothermic *O + *OH recombination (see black diagram from right-to-left). These calculations are made for Pt(111) at the reversible potential (+1.23 V_{RHE}). To render all steps exothermic for each individual reaction an overpotential is required, i.e. a potential as low as +0.78 V_{RHE} for the ORR and as high as +2.55 V_{RHE} for the OER (Fig. 1). The comparison between the solid and dashed diagrams shows the deviation of free energies for Pt(111) from the ideal

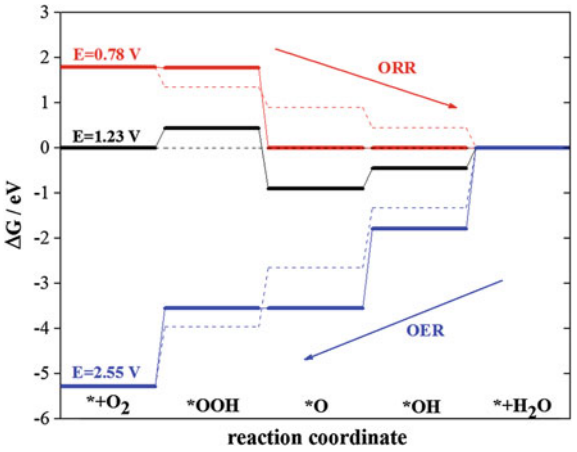

Fig. 1 Free energy diagram for the ORR (*left*-to-*right*) or the OER (*right*-to-*left*) for a bare Pt(111) surface (*solid diagram*) or an ideal catalyst (*dashed diagram*), at the reversible potential (1.23 V), and at a potential for which all steps become exothermic (+0.78 V for the ORR or +2.55 V for the OER). All free energies are expressed with respect to the free energy of liquid water. Reproduced from [14] with permission from Elsevier

catalyst. The description above includes the assumption that the ORR and the OER proceed via the same intermediates, i.e. *OOH, *O and *OH. It must be mentioned, however, that Fig. 1 shows a unified scheme for the ORR and the OER for an oxygen-free Pt(111) surface, and thus it must be assessed only qualitatively because the OER for instance takes place on an oxide-covered surface.

The deviation of real catalysts from the ideal performance is imposed by the scaling relations between the free energies of adsorption of the ORR or OER intermediates that hold for metal surfaces [15, 16]. The free energies of adsorption of *OOH, *O and *OH on (111) surfaces at a given potential, E, are related to each other through the following equations [14]:

$$\left(\Delta G^{E}_{*OOH} + 3\times E\right) = 0.53 \times \left(\Delta G^{E}_{*O} + 2\times E\right) + 3.33\,\text{eV} \tag{5}$$

$$\left(\Delta G^{E}_{*OH} + 1\times E\right) = 0.50 \times \left(\Delta G^{E}_{*O} + 2\times E\right) + 0.04\,\text{eV}. \tag{6}$$

The factors multiplied by the potential, E, represent the number of electrons required to form the respective species from water, i.e. 1 for *OH, 2 for *O and 3 for *OOH. Scaling relations also apply for metal oxides with the expressions being slightly different than for (111) metal surfaces [17]:

$$\left(\Delta G^{E}_{*OOH} + 3\times E\right) = 0.64\left(\Delta G^{E}_{*O} + 2\times E\right) + 2.40\,\text{eV} \tag{7}$$

$$\left(\Delta G^{E}_{*OH} + 1\times E\right) = 0.61\left(\Delta G^{E}_{*O} + 2\times E\right) - 0.58\,\text{eV}. \tag{8}$$

Therefore, independent of the nature of the metal or metal oxide, the difference $\Delta G_{*OOH} - \Delta G_{*OH}$ will be ca. (3.29 – 2 × E) eV for (111)-metals or (2.98 – 2 × E) eV for metal oxides, which is 0.83 or 0.52 eV higher than what is required for the

ideal catalyst for either the ORR or the OER, respectively. These differences are fixed for all metal or metal oxide surfaces, respectively, as long as (i) the reaction intermediates involved are the same and (ii) adsorbates bind in the same way, i.e. through the same atom. The thermodynamic limitations introduced by scaling relations can in principle be avoided using catalysts that bind the intermediates on different sites, as this would allow tuning the adsorption energy of one adsorbate independently of the other [15].

The scaling relations allow the derivation of standard equilibrium potentials as a function of a single free energy of adsorption, e.g. the ΔG_O:

- For ORR on (111) surfaces, assuming an $O_2 \rightarrow *OOH \rightarrow *O + *OH$ $2*OH \rightarrow H_2O$ pathway:

$$E_{O_2/*OOH} = \frac{1}{e_o} \times (\Delta G_O + 1.59) \tag{9}$$

$$E_{*OOH/*OH} = \frac{1}{e_o} \times (0.03\Delta G_O + 3.29) \tag{10}$$

$$E_{*OH/H_2O} = \frac{1}{e_o} \times (0.50\Delta G_O + 0.04). \tag{11}$$

- For the OER on metal oxides, assuming an $H_2O \rightarrow *OH \rightarrow *O \rightarrow *OOH \rightarrow O_2$ pathway:

$$E_{*OH/H_2O} = \frac{1}{e_o} \times (0.61\Delta G_O - 0.58) \tag{12}$$

$$E_{*O/*OH} = \frac{1}{e_o} \times (0.39\Delta G_O + 0.58) \tag{13}$$

$$E_{*OOH/*O} = \frac{1}{e_o} \times (-0.36\Delta G_O + 2.40) \tag{14}$$

$$E_{O_2/*OOH} = \frac{1}{e_o} \times (-0.64 + 2.52). \tag{15}$$

Thus, the ΔG_{*O} can be used as a single descriptor for the construction of thermodynamic volcano-type plots. For example, Fig. 2 shows the standard equilibrium potentials for the various steps of the ORR or the OER [15]. Note that contrary to Fig. 1 which was drawn for Pt(111) for both reactions, here the volcanoes are constructed for metal (111) and for metal oxide surfaces for the ORR and the OER, respectively. The thick curves in Fig. 2 represent the onset potential for each reaction, and the volcano develops by a change in the

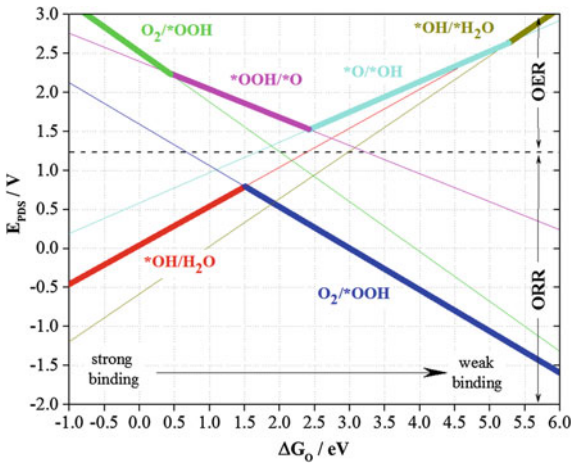

Fig. 2 Thermodynamic volcano plots for the ORR on metal (111) surfaces and for the OER for metal oxides, as derived from the solution of Eqs. (9)–(15). The *thick curves* represent the potential at which the free energy of all steps of the respective reaction is negative. The potential-determining step is denoted in the figure legends. The ORR was assumed to follow the $O_2 \rightarrow$ *OOH $\rightarrow$ *O + *OH $\rightarrow$ 2*OH $\rightarrow$ H_2O pathway, and the OER the $H_2O \rightarrow$ *OH *O $\rightarrow$ *OOH $\rightarrow$ O_2 pathway. The *dashed curve* represents the standard potential for the O_2/H_2O couple. Reproduced from [15] with permission from Elsevier

potential-determining step[1] as the metal–oxygen bond becomes weaker from left to right. For instance, on the left-hand side of the volcano (strong *O binding) the ORR is limited by *OH desorption while on the right-hand side (weak *O binding) the potential-determining step is the formation of *OOH. The optimum catalyst, i.e. at the top of the volcano, achieves a compromise between strong and weak *O binding. For the OER, there are four potential-determining steps depending on the free energy of adsorption for *O, but the most relevant ones near the top of the volcano are the O–O bond formation for strong *O binding (left-hand side) and the *OH dehydrogenation for weak *O binding (right-hand side). For both reactions, the top of the volcano is accompanied with a deviation from the reversible potential, i.e. with an overpotential, which cannot be avoided when a metal or a metal oxide surface is used for the ORR or the OER, respectively, as long as the above scaling relations are satisfied.

The volcano plot in Fig. 2, derived purely based on thermodynamics, is in principle different from an (experimental) volcano plot that has an activity term on the vertical axis and is thus based on kinetics. However, the E_{PDS} is a reliable measure of the overall reaction rate, as long as a relation between the activation

[1]The potential-determining step, E_{PDS}, is the reaction step with the most unfavourable equilibrium potential, i.e. the step that determines at which potential all reaction steps will become exothermic [18].

energy and the reaction energy (Brønsted–Evans–Polanyi principle [19]) applies. Therefore, thermodynamic volcanoes are typically in good, qualitative agreement with kinetic volcanoes.

3 Oxygen Evolution Reaction

The oxygen evolution takes place on oxide surfaces. The oxide may undergo redox transitions depending on the potential, which makes it more complicated to rationalize structure–activity relationships. Trasatti summarized the early efforts to develop activity descriptors for the OER and showed that the experimental OER activity for some rutile- or spinel-type oxides follows a volcano-type relationship, with the descriptor being the standard enthalpy of the lower-to-higher transition [20].

Rutile-type oxides of precious metals have attracted most of the interest in acidic electrolytes, because they are supposed to be more stable toward dissolution compared to oxides of non-noble metals. The activity of precious metal oxides in acid increases in the order Au < Pt < Pd < Rh < Ir < Ru [21]. The same activity trend is also observed for nanoparticulate catalysts [22]. The activities of RuO_2 and IrO_2 are lower in alkaline compared to acid; however, RuO_2 remains the most active material with the IrO_2 following [23]. These activity trends are consistent with the *O binding energy on the metal oxides; for example RuO_2 and IrO_2 bind O with nearly the optimal adsorption energy [24]. One important feature of the OER on noble metal oxide surfaces is that the mechanism of the reaction seems to be different among the oxides. Differential electrochemical mass spectrometry (DEMS) studies using isotope-labelled oxide (^{18}O) at the surface and non-labelled $H_2^{16}O$ for the electrolyte showed that the metal oxide can participate in the O_2 formation on some surfaces (e.g. gold or ruthenium oxide) [25, 26], while on others O_2 forms only from water adsorbed at the surface (e.g. platinum oxide) [27].

All noble metal oxides are unstable towards dissolution under the highly oxidizing potentials of the OER. The combination of electrochemistry with online elemental analysis of the electrolyte has shown that the dissolution of precious metals and their oxides must be distinguished between steady and transient dissolution, i.e. during potentiostatic or potentiodynamic conditions respectively [21]. Transient dissolution occurs mostly during the reduction of the metal oxide, and to a lesser extent during the reverse oxidative transition, but always during changes in the metal or metal oxide state. On the contrary, steady dissolution occurs with a constant rate at a fixed potential or current. IrO_2 and RuO_2 exhibit transient dissolution, while the steady dissolution (relevant for the OER) is very pronounced for RuO_2 only (see Fig. 3), due to the oxidation of the rutile-type RuO_2 phase to RuO_4 [28, 29]. The same trend is maintained also in alkaline solution, where the absolute dissolution rates are actually higher compared to acidic for either IrO_2 or RuO_2 [30, 31]. Therefore, despite its slightly higher overpotential for the OER, IrO_2 is the state-of-the-art catalyst for the OER because of its better stability compared to

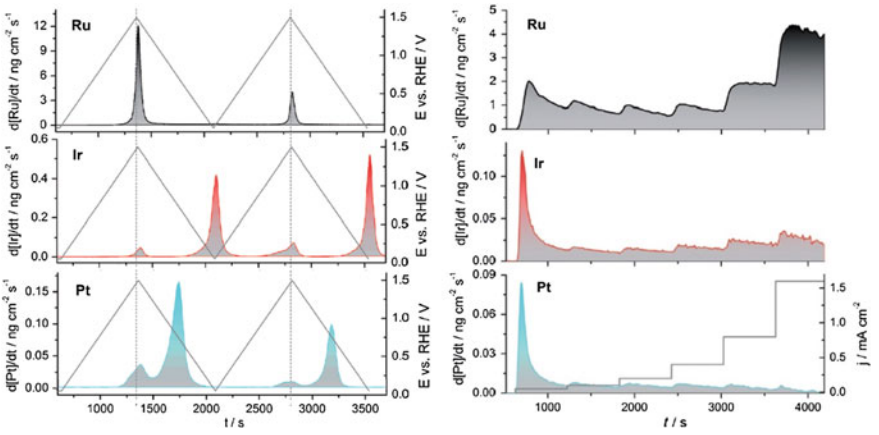

Fig. 3 Online monitoring of the dissolution rate of polycrystalline Ru, Ir and Pt during (*left*): potential ramps from 0.05 to 1.5 V_{RHE} with 2 mV s^{-1} and (*right*): galvanostatic polarization from 0.05 to 1.6 mA cm^{-2}. Electrolyte: 0.1 M H_2SO_4. Reproduced from [21] with permission from Wiley

RuO_2. One other approach to combine the higher activity of RuO_2 and the better stability of IrO_2 has been to use mixed ruthenium–iridium oxides [32, 33].

By decreasing the particle size of nanoparticulate RuO_2 or IrO_2 catalysts, not only the surface-to-volume ratio but also the area-normalized OER activity increases [34–36]. This trend has been attributed to the higher proportion of less active ordered planes at larger particles [34–36]. Therefore, in terms of mass-normalized activity the goal for RuO_2 or IrO_2 catalysts is to decrease the particle size. The stability, however, of the state-of-the-art IrO_2 catalysts decreases with decreasing the particle size [36].

Because of the amount of precious iridium needed for IrO_2 catalysts, approaches to reduce the iridium content by mixing it with another non-noble material have been explored. For instance, Nd_3IrO_7 or $Pb_2(Pb_xIr_{2-x})O_{7-y}$ were found to be about as active as IrO_2 in strongly alkaline solutions [37]. Double perovskites based on iridium and a second metal oxide, such as Ba_2NdIrO_6, can combine up to three times improved OER activity in acid and three times lower noble metal content compared to state-of-the-art IrO_2, while the stability of these materials is comparable to IrO_2 [38].

However, the main approach to replace expensive and scarce noble metals has been to develop catalysts based entirely on non-noble transition metals. In acidic solutions, IrO_2 clearly outperforms these materials which are additionally not stable (see Fig. 4). Therefore, the electrolyte for non-noble OER catalysts typically needs to be neutral or alkaline, since the dissolution of the electrode is minimal and the OER activity similar to that of IrO_2 in this medium (see Fig. 4). Neutral electrolytes, however, are expected to face issues of lower conductivity and local pH changes even for strongly buffered solutions. Different classes of such materials

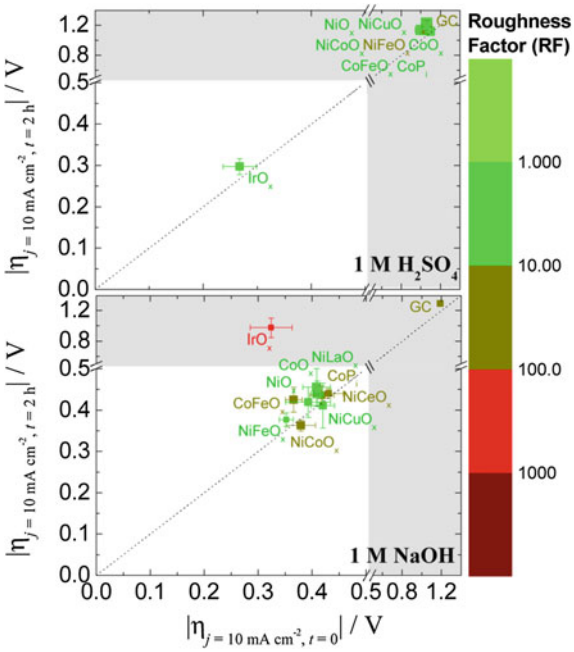

Fig. 4 Plots of catalytic activity, stability, and electrochemically active surface area for OER electrocatalysts in acidic (*top*) and alkaline (*bottom*) solutions. The x-axis and y-axis show the overpotential required to achieve 10 mA cm^{-2} per geometric area at time t = 0 and t = 2 h. The *diagonal dashed line* is the expected response for a stable catalyst. The *unshaded white region* highlights the region where the overpotential to achieve 10 mA cm^{-2} at time t = 0 and 2 h is < 0.5 V. Note the break and change in scale in both axes at overpotentials > 0.5 V. Reprinted from Ref. [40] with permission from the American Chemical Society

have been investigated; for example, rutile-type Co-, Ni- and Mn-based oxides, the activity of which increases in 0.1 M KOH in the order $MnO_x < NiO_x < CoO_x$ and they are somewhat less active compared to IrO_x [39, 40]. This activity trend is explained in terms of the oxygen binding energy of the materials [24]. Interestingly, the activity of mixed oxides such as $NiCoO_x$, $NiFeO_x$, $CoFeO_x$, etc. is higher than the activity of the individual metal oxides, almost approaching that of IrO_2 in the same solution [40]. Other interesting classes of materials are spinel- or perovskite-type electrodes. The first systematic investigations on spinels such as $NiCo_2O_4$, $NiLa_2O_4$, Co_3O_4, etc. were made by Tseung and by Trasatti in alkaline solutions [41–43]. Early studies on ABO_3 perovskites (A: a lanthanide, B: a first-row transition metal) were carried out by Bockris, who tried to identify the parameters that control the electrocatalytic activity. Bockris proposed that the rate-determining step is the desorption of OH and hypothesized that the OER activity of perovskites follows a volcano-type relationship where the activity descriptor is the adsorption energy of OH on the transition metal used in the perovskite [44, 45]. The analysis of Bockris already allowed the early prediction of

some active perovskites, such as $LaNiO_3$ or $LaCoO_3$ [45]. Using molecular orbital principles, Shao-Horn and co-workers [46] first derived a volcano-type relationship for a series of perovskite-type oxides of first-row transition metals and then predicted that $Ba_{0.5}Sr_{0.5}Co_{0.8}Fe_{0.2}O_{3-\delta}$ (BSCF) will be located at the top of this volcano. The very high activity of this material was verified experimentally, and it is by 10 times higher than the state-of-the-art IrO_2 in alkaline solution. The same group later showed that the BSCF particles in fact undergo quick amorphization during the oxygen evolution, which leads to an activity increase [47].

Another approach, finally, is the so-called "in situ formed" catalysts. Starting from a neutral, phosphate-buffered Co^{2+}-containing solution and an indium tin oxide (ITO) substrate, Kanan and Nocera showed that oxygen is evolved at positive bias, probably through the oxidation of Co^{2+} to Co^{3+}, precipitation of Co^{3+}–HPO_4^{2-} on the ITO, and consequent oxidation of Co^{3+} to Co^{4+}. The in situ grown film on the ITO is active for the OER and the formed Co^{4+} is reduced to Co^{2+}, so a new catalysis round can start [48].

4 Oxygen Reduction Reaction

Of all the monometallic catalysts, platinum exhibits the highest activity for the ORR, being located closest to the top of the volcano [49]. The trends in the ORR activity for model low- and high-index single-crystal surfaces depend on the electrolyte, which highlights the importance of the structure-sensitive adsorption of electrolyte ions on platinum. In particular, the ORR activity increases in the order (100) < (111) ≈ (110) in $HClO_4$, (111) < (100) < (110) in H_2SO_4 and (100) < (110) < (111) in KOH [50–53]. The activity of (111) increases by the introduction of (111) or (100) steps in $HClO_4$ and H_2SO_4, but has the opposite effect in KOH [13, 54]. On the other hand, the activity of (100) is not influenced by the introduction of (111) or (110) steps in $HClO_4$ and H_2SO_4, but increases in KOH [13, 54]. The sensitivity of the ORR activity on the surface atom arrangement indicates that the platinum activity can be tuned by finding the appropriate surface geometry. Indeed, high-index facets are more active than the low-index crystals in $HClO_4$, with Pt(331) and Pt(221) being the most active of all [51].

To enhance the utilization of platinum atoms in a real system, the ratio of surface to bulk atoms (surface-to-volume ratio) needs to increase using for instance finely dispersed platinum nanoparticles on a high-surface-area support. However, the decrease of the particle size does not merely increase the surface-to-volume ratio: the properties of surface atoms at nanoscale are different than in extended surfaces due to structural and electronic effects. The origin of such effects lies in the size- and shape-dependent distribution of surface atoms to various short- and long-range terraces and to different steps and defect sites [55–57]. To develop design rules for ORR catalysts from pure platinum, the impact of surface atom arrangement must be rationalized, e.g. by the introduction of activity descriptors that include structure-sensitive parameters such as the generalized coordination numbers [58, 59].

If the particles are represented as truncated octahedra, then the ratio of surface atoms on (111) and (100) terraces decreases for smaller particles [60, 61]. This is predicted to decrease the area-normalized activity toward the ORR, especially in the size range 2–10 nm (particle size effect) [60, 61]. Such a prediction has been confirmed experimentally only when uniformly defined ultrathin catalyst layers are prepared; such layers prevent any O_2 diffusion limitations within the catalyst layer [62, 63]. The mass-normalized activity is a trade-off between the better Pt utilization and the lower reaction rate by decreasing the particle size. Thus, the mass-normalized activity is maximized at ca. 3 nm [63, 64], which is the typical size for state-of-the-art carbon-supported Pt catalysts for the ORR.

The orientation of surface atoms can be also altered by the nanostructure shape. For instance, nanoparticles with dominant (100) terraces (e.g. cubic particles) are more active in H_2SO_4 but those with dominant (111) terraces (e.g. cubooctahedral or tetrahedral particles) are more active in $HClO_4$ and KOH. This is consistent with the fact that Pt(100) is more active than Pt(111) only in H_2SO_4 [65, 66]. Nanoparticles that exhibit a high proportion of high-index facets are in general much more active than particles of a similar size [67–69], which is attributed to the higher activity of high- versus low-index facets. The stability of shape-controlled nanoparticles under the ORR conditions is however an issue, especially for those enclosed by high-index facets, and eventually these particles reshape due to degradation issues that will be discussed below [70, 71].

Even though the ORR takes place at potentials below +1.0 V_{RHE}, the biggest challenge currently for Pt-based ORR catalysts is their exposure to potentials at which the catalyst or the catalyst support is unstable [72]. The cathode transiently experiences potentials as high as 1.4 V during start-up or shut-down of the fuel cell, as a result of the reverse-current decay mechanism [73]. Since the long-term performance is affected by processes during the entire operation, from start-up to regular load to shut-down, assessing the stability of ORR catalysts for a potential up to 1.5 V represents better the conditions in a fuel cell. Platinum dissolves mostly transiently, i.e. during the reduction of the metal oxide. Apart from metal dissolution, real ORR catalysts can suffer from other degradation mechanisms which are induced by the catalyst exposure to highly positive potentials [74, 75]: (i) particle migration and coalescence, (ii) dissolution of platinum from small particles and redeposition at larger particles (Ostwald ripening) and (iii) corrosion of the support which enhances particle mobility and detachment. The above mechanisms, which may take place in parallel [75], eventually result in a loss of platinum surface area. In addition, the dissolved platinum from the cathode may be reduced by hydrogen that permeates through the membrane, forming a large "Pt band" on the membrane [76].

A particularly interesting class of platinum materials that are aimed to mitigate stability issues are the "nanostructured thin-film" (NSTF) electrocatalysts innovated by 3M. They consist of non-conductive organic crystalline whiskers as the support, on which an ultrathin layer of platinum is deposited [77]. The polycrystalline thin-film catalyst morphology and the absence of a conventional conductive high-surface-area carbon support allow the NSTF catalysts to combine a

polycrystalline-like surface-normalized ORR activity, with a low amount of noble material required and an improved stability, since they are free from issues such as support corrosion, Pt particle migration and coalescence, etc. [77, 78]. However, the catalyst morphology introduces also disadvantages, such as the higher susceptibility to flooding at low temperature of operation, which decreases limiting currents and makes water management more complicated.

Returning to the volcano plot, the problem with platinum is that it binds oxygen a bit too strongly, i.e. it is located at the left side of the ORR volcano in Fig. 2 [79, 80]. In a series of patents from the United Technologies Corporation (UTC) in 1980s, it was disclosed that binary or ternary PtCr, PtV or PtCrCo alloys are more active for the ORR than pure platinum [81–85]. Since then, the strategy to weaken the Pt–O bond to move closer to the top of the volcano has been to use such Pt–M catalysts, where M is a late transition metal such as Cu, Ni, Co, Fe, etc. (see Fig. 2) [79, 86–91] or alloys with more than one alloying element [92–94]. Alloying platinum leads to a modification of the surface electronic properties, even though the atoms of the alloying metal are not present at the surface as they are not stable under the ORR conditions when in contact with the electrolyte. The enhancing effect of the alloying metal atoms to the intrinsic ORR activity has been attributed to bonding interactions between surface Pt and sub-surface M atoms (electronic or ligand effect), and to the compressed arrangement of the surface Pt atoms due to the shorter M–M interatomic distance below the surface (geometric or strain effect) [89, 91]. Even though it is hard to decouple the two effects, the consequence of both is to alter the chemisorption properties of the surface Pt atoms, and the alloying metal atoms have a stronger impact when they are located closer to the surface (see Fig. 5) [90, 91, 95, 96]. Therefore, ideally the alloying M metal must be located in the second layer.

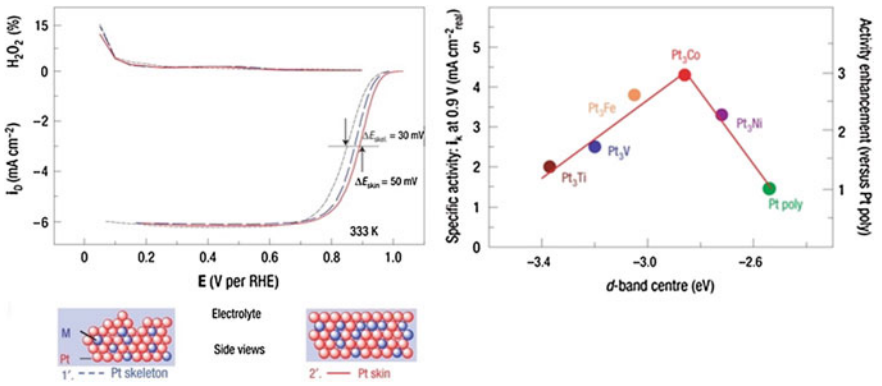

Fig. 5 *Left* Polarization curves for the ORR on polycrystalline platinum (*grey curve*), skeleton-Pt_3Fe (*blue dashed curve*) and skin-Pt_3Fe (*red curve*), in 0.1 M $HClO_4$ at 50 mV s^{-1}. *Right* Volcano-type plots of the experimentally measured ORR activity for various skin-Pt_3M surfaces at a temperature of 333 K. Reproduced from Ref. [91] with permission from the Nature Publishing Group

The activity enhancement for bimetallic Pt surfaces may depend strongly on the surface atom arrangement: for Pt_3Ni-skin[2] surfaces in $HClO_4$, the ORR activity increases by ca. 9 times for the $Pt_3Ni(111)$ versus Pt(111) and by only 2–2.5 times for $Pt_3Ni(100)$ versus Pt(100) or for $Pt_3Ni(110)$ versus Pt(110) [97]. This alters the order in which the ORR activity increases, from Pt_3Ni-skin(100) to Pt_3Ni-skin(110) to Pt_3Ni-skin(111) in $HClO_4$ (compare with Pt(100) < Pt(111) ≈ Pt(100) in the same solution) [97].

The situation is rather complex for nanoparticulate bimetallic catalysts, when the goal is to obtain the maximum possible activity enhancement. The preparation method and the post-treatment can have a significant impact on parameters such as the size or the shape of the nanostructure, porosity, alloy composition, etc., which in turn influence the ORR performance. As expected from the findings on extended bimetallic surfaces described above, the ORR activity enhancement depends strongly on the shape of the nanostructure. The ORR activity on carbon-supported octahedral Pt_3Ni particles (i.e. with a high ratio of (111) terraces) is by ca. 7 times higher than the commercial Pt/C catalyst, whereas cubic Pt_3Ni particles (i.e. with a high ratio of (100) terraces) show little enhancement [98].

To increase platinum utilization, to decrease the amount of noble metal needed, and to maximize the alloying effect, the approach that gained the largest interest is the synthesis of nanostructures with a pure Pt shell and a Pt–M core, so-called core–shell materials. The Pt shell is supposed additionally to protect the non-noble M metal atoms in the core, where M is typically a late transition metal such as Cu, Co, Ni, etc. However, as it will be described below, this is not really the case. Nanostructures with a highly ordered core are more active and stable than disordered particles [99–103] with the explanation being still under debate. For a detailed description of the methods for the preparation of core–shell structures the interested reader is referred to relevant reviews [104, 105]. In the following, we will briefly mention only the two main preparation methods:

In dealloying, the less noble metal atoms of a bimetallic alloy are rapidly and selectively dissolved. Classical dealloying involves the selective dissolution of the less noble metal, i.e. of the metal with the least positive standard reduction potential [106, 107]. The Strasser group showed that core–shell nanoparticles can be prepared by an "electrochemical dealloying" process, in which an M-rich platinum alloy precursor, e.g. $PtCu_3$, is subject to cycling within a potential region where M is unstable [89, 108, 109]. The interesting feature of dealloyed core–shell particles is that the resulting structure and its activity/stability can be controlled by parameters such as the initial alloy composition, the dealloying or post-treatment conditions, the size of the particle precursor, etc. [109].

[2] *Pt-skeleton* is the surface that remains after the dissolution of M metal atoms from Pt–M alloys exposed to oxidizing conditions. *Pt-skin* is the surface which consists of a pure topmost atomic Pt layer.

Another method of core–shell preparation is based on the spontaneous galvanic replacement of the non-noble material at the surface of the core by platinum. This can be achieved using PdM (e.g. PdCu, PdCo) cores which result in a PdCu@Pt or PdCo@Pt core–shell structure. Adzic and co-workers pioneered a more elegant method of galvanic replacement, the so-called monolayer method; a copper monolayer, formed by underpotential deposition on the surface of an M metal core, is spontaneously oxidized by platinum ions which are reductively deposited. This results in a core–shell structure with a monolayer of platinum enclosing an M core. The metal core M can be Pd, Au, Ir, or even bimetallic such as PdNi. The method was originally developed on model single-crystalline "cores" and extended to nanostructured electrodes [90, 110–112].

Except for core–shell structures, other interesting approaches for the preparation of bimetallic materials include alloys based on 3M's NSTF technology (e.g. Pt_3Ni_7-NSTF) [113] or the Pt_3Ni-skin nanoframes [114]; the latter enhance the ORR activity by 16 times compared to standard Pt/C catalysts.

The stability of bimetallic electrodes is an important issue, which limits their application in real systems. The dissolution of platinum removes Pt surface atoms from the protective shell, leading to the exposure of the otherwise protected non-noble metal atoms to the electrolyte [115]. This eventually results in the dissolution of the alloying metal atoms from the first atomic layers and the thickening of the protective Pt shell, so the enhancing effect from alloying decays with time. Even worse is the fact that the dissolved metal ions deteriorate the fuel cell performance further. For example, copper ions can be reduced and deposited at the anode of the fuel cell [116], while nickel or cobalt ions can be deposited on the membrane [113, 117].

DFT calculations predicted that alloys of platinum with rare earths (e.g. Pt_3Y and Pt_3Sc) will be not only more active, but also more stable than pure platinum or other Pt alloys [80]. The argumentation is based on the higher (more negative) enthalpy for alloy formation of such alloys compared to those with late transition metals, which is likely to render the diffusion of the alloying metal to the surface kinetically more difficult [80, 118]. The correlation between the enthalpy for alloy formation and the kinetic barrier for diffusion of the alloying element has been demonstrated in a later publication [119]. The higher activity of model Pt_5M alloys (M: a rare earth or alkaline earth element such as Sc, Y, La, etc.) for the ORR was evidenced experimentally by the Chorkendorff group and was attributed to strain [118, 120–122]. The same group also showed the enhanced activity with nanostructured electrodes [123, 124]. Long-term accelerated degradation tests on such catalysts indeed showed that the selective dissolution of the second metal is slower; however, there is still an activity loss with time and a concomitant thickening of the platinum shell, for either extended or nanostructured surfaces [120, 125].

Due to the high cost and the limited crustal abundance of platinum, extensive efforts to find alternative catalysts have been made. A good alternative to platinum would exhibit high activity for the ORR, low cost, sufficient abundance and stability under the operation conditions of a fuel cell.

Among other monometallic surfaces, mostly palladium has been considered as a potential candidate. Palladium is the metal closest to platinum in the volcano plot and its price is lower. For flame-annealed palladium single-crystal electrodes, the ORR activity increases in the order Pd(110) < Pd(111) < < Pd(100) [126]. The trend may be different for Pd(hkl) crystals annealed by other methods, e.g. inductive heating [127]. Overall, the problems with palladium are that (i) its activity must still increase to compete with platinum, (ii) it is significantly more susceptible to dissolution than Pt [21] and (iii) it is still a rather scarce metal, so a large-scale technology would increase the demand and the price for Pd substantially.

Other approaches include the use of noble metal-free catalysts, such as chalcogenides, oxides, carbides, nitrides, etc. [128]. The activity of such materials, however, remains low compared to platinum. The most promising way to replace platinum with catalysts free of noble metals is a class of materials noted generally as $Me–N_x/C_y$, where Me is a transition metal, for example, iron (Fig. 6) [129]. The first report on such materials showed that cobalt phthalocyanine can reduce O_2 in acidic solution; [130] later it was shown that also other $Me–N_4$ chelates can catalyse the reaction in either acid or alkaline [131, 132]. The activity of those catalysts was decreasing with time because of catalyst decomposition by the formed H_2O_2 but thermal treatment improves the stability of the catalyst likely by making it more active for H_2O_2 decomposition [133, 134]. It has been, however, questionable whether the metal centre is still a component of the active site or if the pyrolysis results in a new catalyst, consisting of nitrogen and carbon [135–138]. Yeager and co-workers showed later that it is not necessary to use $Me–N_4$ chelates as the precursor, but the catalyst can also be synthesized at high temperature by mixing a Me salt with a carbon–nitrogen source [139], while Dodelet and co-workers showed that the sources of carbon and nitrogen can be also different [140].

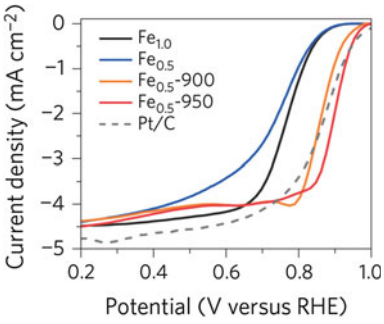

Fig. 6 ORR polarization curves for Fe–N–C catalysts and a Pt/C benchmark catalyst, recorded at room temperature in O_2-saturated pH 1 electrolyte at a rotation rate of 1,600 rpm. The current was corrected for the background current measured in N_2-saturated electrolyte. The potential was corrected for the Ohmic drop. The catalyst loadings were 818 $\mu g_{Fe\text{-}N\text{-}C}$ cm^{-2} or 16 μg_{Pt} cm^{-2}. The *subscript* shows the wt% Fe in the catalyst precursor, i.e. prior to any pyrolysis; $Fe_{0.5}$-900 and $Fe_{0.5}$-950 were obtained after pyrolysis of $Fe_{0.5}$ at 900 °C or 950 °C, respectively. Reproduced from Ref. [129] with permission from the Nature Publishing Group

The above progress indicated that (i) an important parameter for this class of materials is the density of Me–N_4 sites per unit volume, independent of whether they serve as the active sites or as the precursors for the generation of active sites after pyrolysis and (ii) the design of catalyst can be tailored by the careful choice of the transition metal, the nitrogen, and the carbon source as these can be independently added, as well as by following appropriate treatment procedures.

Following this notion, the Dodelet group synthesized a very active Fe–N/C catalyst by increasing substantially the density of active sites [141]. They used initially a mixture of a highly (micro)porous carbon support, a pore filler and ferrous acetate, which was subject to ball milling to force the pore filler and the iron precursor into the pores, and then was pyrolyzed first in Ar and then in NH_3 to generate the Fe–N_4 moieties on the carbon support. The high density of such moieties makes this catalyst active for the ORR, so the activity reaches the ca. 90% of the activity of Pt/C [141]. The Zelenay group used heteroatom polymer precursors such as polypyrrole (PPy) or polyaniline (PANI) as the template for nitrogen and carbon, aiming to a uniform distribution and high density of Me–N_4 sites. They initially showed that Co–PPy/C catalyst exhibits respectable stability and activity without any pyrolysis step [142]. Later, they synthesized pyrolyzed Fe-, Co- and FeCo-PANI/C catalysts with activity that almost matches the one of Pt/C and promising stability which was proposed to be due to a graphitized carbon phase [143].

The ORR activity and selectivity on Me–N_4 chelates (where Me: Fe, Mn, Co) is related to the binding energy of O_2, which in turn follows the redox potential for the Me(III)/Me(II) transition [144]. Catalysts with weak O_2 binding (i.e. positive redox potential) reduce O_2 to H_2O_2 and the onset potential shifts more positive in the RHE scale by making the solution more alkaline. On the other hand, catalysts with strong O_2 binding (i.e. negative redox potential) reduce O_2 to H_2O_2 and the onset potential is independent of the pH in the RHE scale.

Overall, the progress made in the last ten years in ORR catalysis with non-noble metals is impressive [128, 145]; however, the issue of stability and long-term performance remains. In fact, non-noble metal catalysts also suffer from degradation when they are exposed to potentials above 0.9 V in acidic solutions. The main origin of degradation is the oxidation of carbon, which leads to the destruction the ORR-active FeN_xC_y sites, while iron leaching from iron particles occurs already at lower potentials (<0.7 V) without though affecting the ORR activity [146].

5 Fundamentals of the HER and the HOR

The hydrogen evolution and the reverse oxidation reaction involve the transfer of two electrons:

$$2H^+ + 2e^- \rightleftarrows H_2 \quad E = 0\,V\,vs\,RHE. \tag{16}$$

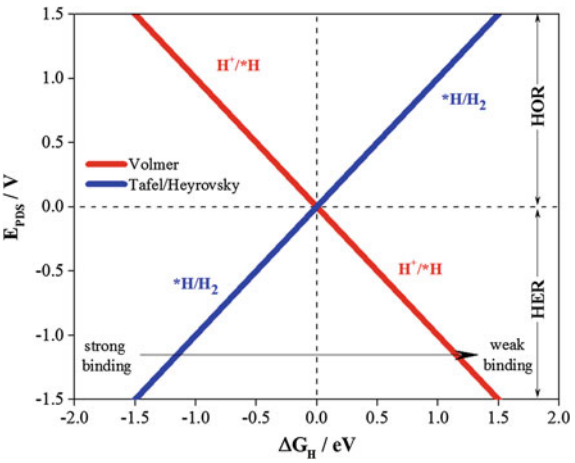

Fig. 7 Thermodynamic volcano plots for the HER and the HOR, with the energy of hydrogen adsorption as the descriptor, assuming a Volmer-Tafel/Heyrovsky pathway. Reproduced from [15] with permission from Elsevier

The generally accepted mechanism for the HER/HOR involves the following three elementary steps [147]:

$$H^+ + * + e^- \rightleftarrows H_{ads} \quad \text{Volmer step} \tag{17}$$

$$H_{ads} + H^+ + e^- \rightleftarrows H_2 \quad \text{Heyrovsky step} \tag{18}$$

or

$$2H_{ads} \rightleftarrows H_2 + 2^* \quad \text{Tafel step.} \tag{19}$$

Thus, both reactions involve the intermediate formation of H_{ads}, the binding energy of which can be used as a descriptor for the construction of volcano plots (Fig. 7), following a similar analysis as for the OER/ORR. The ideal catalyst for both reactions adsorbs hydrogen with $\Delta G_{*H} = 0$, meaning that the energy of *H is the same as that of H_2 and H^+. In that case, there are no uphill or downhill steps during any of the two electron transfer steps in the corresponding energy diagram, and thus this ideal case is associated with zero overpotential. If the binding is too strong ($\Delta G_H < 0$), then the two reactions are associated with overpotential, because the Heyrovsky/Tafel step limits the HER and the Volmer step limits the HOR. The opposite occurs for too weak *H binding ($\Delta G_H > 0$).

6 Hydrogen Evolution Reaction

Trasatti has provided the most traditional expression of a kinetic volcano for the HER [148], using the M–H bond energy as the activity descriptor. Platinum and other Pt-group metals are located near or at the top of the volcano. In the interpretation of

such an expression, however, one should take into account that the energies of *H adsorption were calculated for bare metal surfaces, which is not really representative of the conditions during the HER on all metals [149].

In fact, platinum catalyses the HER in acidic solutions with a very high rate, so that the current is entirely limited by H^+ diffusion [150, 151]. Therefore, conventional RDE measurements cannot be used to estimate the kinetics of the HER on platinum [151]. Moreover, no significant impact of the surface structure was found for the HER on low-index Pt single crystals in acid [152]. The development of platinum-free HER catalysts in acid has been explored to replace platinum in acid electrolyzers, with sulfides, carbides or phosphides being the most promising materials [153].

Contrary to acidic solutions, platinum is not as good a catalyst in alkaline (see Fig. 8) [151]. The reaction is structure sensitive on Pt, which also contrasts with acidic solutions, with the activity increasing in the order Pt(111) < Pt(100) < Pt (110) [154]. The reason for the observed structure sensitivity only in alkaline solutions and for the lower reaction rate compared to acid is still unknown [155]. The lower activity of Pt in alkaline solution implies higher cell voltage in an alkaline electrolyzer, thus other catalysts must be developed to carry out the reaction in alkaline solutions as fast as platinum does in acid. Nickel is a state-of-the-art catalyst for the HER in alkaline solution [156]; however, the catalyst deactivates and the cell voltage increases in the long term [157], which has been attributed to the formation of hydrides [158]. One approach has been to modify platinum with $Ni(OH)_2$ clusters, which was found to increase the HER activity in alkaline compared to pure Pt by a factor of 8 [155]. The promoting effect of this modification was attributed to the enhancement of water splitting by $Ni(OH)_2$, while *H recombination still occurs on platinum, in a reaction that proceeds in a bifunctional manner.

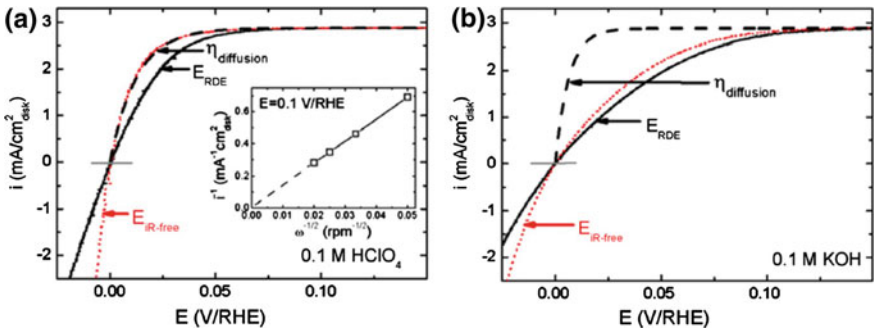

Fig. 8 HOR/HER polarization curves on polycrystalline platinum in 0.1 M $HClO_4$ (**a**) and 0.1 M KOH (**b**) at 1600 rpm. *Solid black curves* represent the voltammograms before iR-correction (E_{RDE}), *dotted-red lines* after iR-correction (iR-free) and *dashed black curves* the Nernstian diffusion overpotential. Reprinted from Ref. [151] with permission from the Electrochemical Society

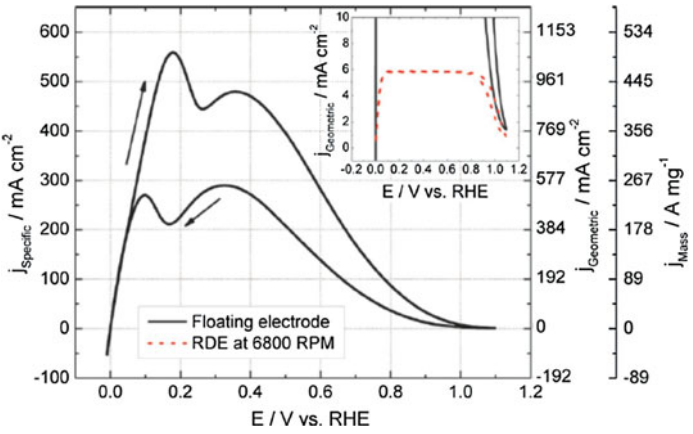

Fig. 9 HOR polarization curves using a "floating electrode" with a 2.2 μg cm^{-2} Pt/C catalyst exposed to H_2, run in 4.0 M $HClO_4$, at 10 mV s^{-1}. The *inset* shows the comparison of the floating electrode measurement with the HOR on polycrystalline platinum using an RDE (6800 rpm) in 0.5 M $HClO_4$. Reprinted from Ref. [160] with permission from the Royal Society of Chemistry

7 Hydrogen Oxidation Reaction

Platinum catalyses also the HOR with a very high rate in acid, so that the current is entirely limited by H_2 diffusion [150, 151]. The reaction is so fast that the current is fully preserved even when the surface of platinum is covered by a surface modifier such as calix[4]arene to a coverage of 98% [159]. Similar to the HER, the high reaction rate makes it impossible to correctly measure kinetics for the HOR with RDE measurements. Following the concept of the "floating electrode"[3] which allows extremely high mass transport rates of a gaseous reactant, Kucernak and co-workers managed to record HOR curves with limited hydrogen mass transport limitations [160], and the measured current densities were in the order of 0.5 A cm_{Pt}^{-2} (Fig. 9).

Similar to the HER, the HOR deviates from the ideal Nernstian behaviour in alkaline solutions on platinum [151]. Indeed, the reaction is structure sensitive only in alkaline media, with the activity increasing in the order Pt(111) ≈ Pt(100) << Pt (110) at low positive overpotential [154]. At high potentials, the inhibition from the adsorption of oxygenated species is stronger for Pt(100) and weaker for Pt(111) [154]. The lower rate of the HOR in alkaline solution implies that a higher amount of Pt (about 100 times) is required in an alkaline fuel cell to achieve the same

[3]The "floating electrode" is a three-electrode setup that consists of a porous gas diffusion working electrode floating on an aqueous electrolyte. The reference and counter electrodes are immersed into the solution. The reactant gas is supplied to the catalyst surface sites from the gas phase, on top of the floating catalyst layer. The gaseous diffusion leads to extremely fast mass transport of reactant gases to the catalyst layer.

performance as for an acidic fuel cell. Nickel-based catalysts are the only materials to date, to be successful in achieving HOR activities comparable to platinum in alkaline solutions [161].

8 Summary

In conclusion, the electrocatalysis community has developed a good understanding of the reactions involved in the hydrogen economy; the HER and OER for water electrolyzers, and the HOR and ORR for fuel cells. The activity of each reaction on different surfaces follows a volcano-type relationship where the adsorption energy of a key reaction intermediate can be used as the descriptor, for example, *H for HOR and HER and *O for ORR and OER. The highest activity is obtained for a catalyst that exhibits moderate *H or *O binding, accordingly. However, for reactions involving more than one intermediate (and typically involving more than two electron and proton transfers), such as ORR and OER, energetic scaling relations between intermediates (specifically *O, *OH and *OOH) limit the extent to which a reversible catalyst with a very small overpotential can be achieved. A minimal overpotential of ca. 0.25–0.3 V for both ORR and OER appears very difficult to overcome. Computational and experimental tools offer today the opportunity to prepare highly active materials that approach the performance of the optimal catalyst predicted by current models. However, future models and computational methods should focus on materials that can break the energetic scaling relations between intermediates, to develop catalysts with significantly enhanced properties compared to the current state-of-the-art electrocatalysts.

Despite the massive efforts that have been devoted to the development of materials that operate in alkaline environments and with lower/no noble metal content, the best systems remain to be acidic water electrolyzers or fuel cells, using Pt for the HER, the HOR and the ORR, and IrO_2 for the OER. However, such systems can be a solution only for the small scale: to realize Bockris' hydrogen economy on a large scale we need to find a combination of materials for the two electrodes that are abundant and but also stable in the long term. This is today the biggest challenge, as it will decrease the cost per device, but will also massively increase the number of devices that can be used worldwide.

References

1. Verne J (1874) The mysterious island
2. Bockris JO (1972) A hydrogen economy. Science 176:1323–1323
3. van Troostwijk AP, Deiman JR (1789) Sur une manière de décomposer l'eau en air inflammable & en air vital. Obs Phys 35:369–378
4. Grove WR (1839) On voltaic series and the combination of gases by platinum. Philos Mag 14:127–130

5. Schönbein CF (1839) On the voltaic polarization of certain solid and fluid substances. Philos Mag 14:43–45
6. Kinoshita K (1992) Oxygen electrochemistry. Electrochemical oxygen technology. Wiley, New York, pp 19–112
7. Nilekar AU, Mavrikakis M (2008) Improved oxygen reduction reactivity of platinum monolayers on transition metal surfaces. Surf Sci 602:L89–L94
8. Dau H, Limberg C, Reier T et al (2010) The mechanism of water oxidation: from electrolysis via homogeneous to biological catalysis. ChemCatChem 2:724–761
9. Katsounaros I, Cherevko S, Zeradjanin AR, Mayrhofer KJJ (2014) Oxygen electrochemistry as a cornerstone for sustainable energy conversion. Angew Chem Int Ed 53:102–121
10. Katsounaros I, Schneider WB, Meier JC et al (2012) Hydrogen peroxide electrochemistry on platinum: towards understanding the oxygen reduction reaction mechanism. Phys Chem Chem Phys 14:7384–7391
11. Katsounaros I, Schneider WB, Meier JC et al (2013) The impact of spectator species on the interaction of H_2O_2 with platinum—implications for the oxygen reduction reaction pathways. Phys Chem Chem Phys 15:8058–8068
12. Sitta E, Gómez-Marín AM, Aldaz A, Feliu JM (2013) Electrocatalysis of H_2O_2 reduction/oxidation at model platinum surfaces. Electrochem Commun 33:39–42
13. Gómez-Marín AM, Rizo R, Feliu JM (2013) Some reflections on the understanding of the oxygen reduction reaction at Pt(111). Beilstein J Nanotechnol 4:956–967
14. Rossmeisl J, Logadottir A, Nørskov JK (2005) Electrolysis of water on (oxidized) metal surfaces. Chem Phys 319:178–184
15. Koper MTM (2011) Thermodynamic theory of multi-electron transfer reactions: implications for electrocatalysis. J Electroanal Chem 660:254–260
16. Rossmeisl J, Karlberg GS, Jaramillo T, Nørskov JK (2009) Steady state oxygen reduction and cyclic voltammetry. Faraday Discuss 140:337–346
17. Rossmeisl J, Qu Z-W, Zhu H et al (2007) Electrolysis of water on oxide surfaces. J Electroanal Chem 607:83–89
18. Koper MTM (2013) Analysis of electrocatalytic reaction schemes: distinction between rate-determining and potential-determining steps. J Solid State Electrochem 17:339–344
19. Bligaard T, Nørskov JK, Dahl S et al (2004) The Brønsted–Evans–Polanyi relation and the volcano curve in heterogeneous catalysis. J Catal 224:206–217
20. Trasatti S (1980) Electrocatalysis by oxides—attempt at a unifying approach. J Electroanal Chem 111:125–131
21. Cherevko S, Zeradjanin AR, Topalov AA et al (2014) Dissolution of noble metals during oxygen evolution in acidic media. ChemCatChem 6:2219–2223
22. Reier T, Oezaslan M, Strasser P (2012) Electrocatalytic oxygen evolution reaction (OER) on Ru, Ir, and Pt catalysts: a comparative study of nanoparticles and bulk materials. ACS Catal 2:1765–1772
23. Lee Y, Suntivich J, May KJ et al (2012) Synthesis and activities of rutile IrO_2 and RuO_2 nanoparticles for oxygen evolution in acid and alkaline solutions. J Phys Chem Lett 3:399–404
24. Man IC, Su H-Y, Calle-Vallejo F et al (2011) Universality in oxygen evolution electrocatalysis on oxide surfaces. ChemCatChem 3:1159–1165
25. Wohlfahrt-Mehrens M, Heitbaum J (1987) Oxygen evolution on Ru and RuO_2 electrodes studied using isotope labelling and on-line mass spectrometry. J Electroanal Chem 237:251–260
26. Diaz-Morales O, Calle-Vallejo F, de Munck C, Koper MTM (2013) Electrochemical water splitting by gold: evidence for an oxide decomposition mechanism. Chem Sci 4:2334–2343
27. Willsau J, Wolter O, Heitbaum J (1985) Does the oxide layer take part in the oxygen evolution reaction on platinum? J Electroanal Chem 195:299–306
28. Yeo RS, Orehotsky J, Visscher W, Srinivasan S (1981) Ruthenium-based mixed oxides as electrocatalysts for oxygen evolution in acid electrolytes. J Electrochem Soc 128:1900–1904

29. Kötz R, Stucki S, Scherson D, Kolb DM (1984) In-situ identification of RuO_4 as the corrosion product during oxygen evolution on ruthenium in acid media. J Electroanal Chem 172:211–219
30. Cherevko S, Zeradjanin AR, Keeley GP, Mayrhofer KJJ (2014) A comparative study on gold and platinum dissolution in acidic and alkaline media. J Electrochem Soc 161: H822–H830
31. Cherevko S, Geiger S, Kasian O et al (2016) Oxygen and hydrogen evolution reactions on Ru, RuO_2, Ir, and IrO_2 thin film electrodes in acidic and alkaline electrolytes: a comparative study on activity and stability. Catal Today 262:170–180
32. Kötz R, Stucki S (1986) Stabilization of RuO_2 by IrO_2 for anodic oxygen evolution in acid media. Electrochim Acta 31:1311–1316
33. Angelinetta C, Trasatti S, Atanasoska LD et al (1989) Effect of preparation on the surface and electrocatalytic properties of $RuO_2 + IrO_2$ mixed oxide electrodes. Mater Chem Phys 22:231–247
34. Jirkovský J, Makarova M, Krtil P (2006) Particle size dependence of oxygen evolution reaction on nanocrystalline RuO_2 and $Ru_{0.8}Co_{0.2}O_{2x}$. Electrochem Commun 8:1417–1422
35. Jirkovský J, Hoffmannová H, Klementová M, Krtil P (2006) Particle size dependence of the electrocatalytic activity of nanocrystalline RuO_2 electrodes. J Electrochem Soc 153: E111–E118
36. Abbott DF, Lebedev D, Waltar K et al (2016) Iridium oxide for the oxygen evolution reaction: correlation between particle size, morphology, and the surface hydroxo layer from operando XAS. Chem Mater 28:6591–6604
37. ten Kortenaar MV, Vente JF, Ijdo DJW et al (1995) Oxygen evolution and reduction on iridium oxide compounds. J Power Sources 56:51–60
38. Diaz-Morales O, Raaijman S, Kortlever R et al (2016) Iridium-based double perovskites for efficient water oxidation in acid media. Nat Commun 7:art no 12363
39. Frydendal R, Paoli EA, Knudsen BP et al (2014) Benchmarking the stability of oxygen evolution reaction catalysts: the importance of monitoring mass losses. ChemElectroChem 1:2075–2081
40. McCrory CCL, Jung S, Peters JC, Jaramillo TF (2013) Benchmarking heterogeneous electrocatalysts for the oxygen evolution reaction. J Am Chem Soc 135:16977–16987
41. Tseung ACC, Jasem S (1977) Oxygen evolution on semiconducting oxides. Electrochim Acta 22:31–34
42. Jasem SM, Tseung ACC (1979) A potentiostatic pulse study of oxygen evolution on Teflon-bonded nickel-cobalt oxide electrodes. J Electrochem Soc 126:1353–1360
43. Trasatti S (1984) Electrocatalysis in the anodic evolution of oxygen and chlorine. Electrochim Acta 29:1503–1512
44. Bockris JO, Otagawa T (1983) Mechanism of oxygen evolution on perovskites. J Phys Chem 87:2960–2971
45. Bockris JO, Otagawa T (1984) The electrocatalysis of oxygen evolution on perovskites. J Electrochem Soc 131:290–302
46. Suntivich J, May KJ, Gasteiger HA et al (2011) A perovskite oxide optimized for oxygen evolution catalysis from molecular orbital principles. Science 334:1383–1385
47. May KJ, Carlton CE, Stoerzinger KA et al (2012) Influence of oxygen evolution during water oxidation on the surface of perovskite oxide catalysts. J Phys Chem Lett 3:3264–3270
48. Kanan MW, Nocera DG (2008) In situ formation of an oxygen-evolving catalyst in neutral water containing phosphate and Co^{2+}. Science 321:1072–1075
49. Nørskov JK, Rossmeisl J, Logadottir A et al (2004) Origin of the overpotential for oxygen reduction at a fuel-cell cathode. J Phys Chem B 108:17886–17892
50. Markovic NM, Gasteiger HA, Ross PN (1997) Kinetics of oxygen reduction on Pt(hkl) electrodes: implications for the crystallite size effect with supported Pt electrocatalysts. J Electrochem Soc 144:1591
51. Maciá MD, Campiña JM, Herrero E, Feliu JM (2004) On the kinetics of oxygen reduction on platinum stepped surfaces in acidic media. J Electroanal Chem 564:141–150

52. Kuzume A, Herrero E, Feliu JM (2007) Oxygen reduction on stepped platinum surfaces in acidic media. J Electroanal Chem 599:333–343
53. Rizo R, Herrero E, Feliu JM (2013) Oxygen reduction reaction on stepped platinum surfaces in alkaline media. Phys Chem Chem Phys 15:15416–15425
54. Hoshi N, Nakamura M, Hitotsuyanagi A (2013) Active sites for the oxygen reduction reaction on the high index planes of Pt. Electrochim Acta 112:899–904
55. Van Hardeveld R, Hartog F (1969) The statistics of surface atoms and surface sites on metal crystals. Surf Sci 15:189–230
56. Romanowski W (1969) Equilibrium forms of very small metallic crystals. Surf Sci 18:373–388
57. Koper MTM (2011) Structure sensitivity and nanoscale effects in electrocatalysis. Nanoscale 3:2054–2073
58. Calle-Vallejo F, Loffreda D, Koper MTM, Sautet P (2015) Introducing structural sensitivity into adsorption–energy scaling relations by means of coordination numbers. Nature Chem 7:403–410
59. Calle-Vallejo F, Tymoczko J, Colic V et al (2015) Finding optimal surface sites on heterogeneous catalysts by counting nearest neighbors. Science 350:185–189
60. Kinoshita K (1990) Particle size effects for oxygen reduction on highly dispersed platinum in acid electrolytes. J Electrochem Soc 137:845–848
61. Tritsaris GA, Greeley J, Rossmeisl J, Nørskov JK (2011) Atomic-scale modeling of particle size effects for the oxygen reduction reaction on Pt. Catal Lett 141:909–913
62. Shinozaki K, Morimoto Y, Pivovar BS, Kocha SS (2016) Re-examination of the Pt particle size effect on the oxygen reduction reaction for ultrathin uniform Pt/C catalyst layers without influence from Nafion. Electrochim Acta 213:783–790
63. Perez-Alonso FJ, McCarthy DN, Nierhoff A et al (2012) The effect of size on the oxygen electroreduction activity of mass-selected platinum nanoparticles. Angew Chem Int Ed 51:4641–4643
64. Shao M, Peles A, Shoemaker K (2011) Electrocatalysis on platinum nanoparticles: particle size effect on oxygen reduction reaction activity. Nano Lett 11:3714–3719
65. Matsuzawa K, Fukushima T, Inaba M (2010) Shape-controlled platinum nanoparticles of different sizes and their electrochemical properties. Electrocatal 1:169–177
66. Devivaraprasad R, Ramesh R, Naresh N et al (2014) Oxygen reduction reaction and peroxide generation on shape-controlled and polycrystalline platinum nanoparticles in acidic and alkaline electrolytes. Langmuir 30:8995–9006
67. Tian N, Zhou Z-Y, Sun S-G (2008) Platinum metal catalysts of high-index surfaces: from single-crystal planes to electrochemically shape-controlled nanoparticles. J Phys Chem C 112:19801–19817
68. Huang X, Zhao Z, Fan J et al (2011) Amine-assisted synthesis of concave polyhedral platinum nanocrystals having 411 high-index facets. J Am Chem Soc 133:4718–4721
69. Wang C, Ma L, Liao L et al (2013) A unique platinum-graphene hybrid structure for high activity and durability in oxygen reduction reaction. Sci Rep 3:art no 2580
70. Devivaraprasad R, Kar T, Chakraborty A et al (2016) Reconstruction and dissolution of shape-controlled Pt nanoparticles in acidic electrolytes. Phys Chem Chem Phys 18:11220–11232
71. Li D, Wang C, Strmcnik DS et al (2014) Functional links between Pt single crystal morphology and nanoparticles with different size and shape: the oxygen reduction reaction case. Energy Environ Sci 7:4061–4069
72. Borup R, Meyers J, Pivovar B et al (2007) Scientific aspects of polymer electrolyte fuel cell durability and degradation. Chem Rev 107:3904–3951
73. Reiser CA, Bregoli L, Patterson TW et al (2005) A reverse-current decay mechanism for fuel cells. Electrochem Solid-State Lett 8:A273–A276
74. Shao-Horn Y, Sheng WC, Chen S et al (2007) Instability of supported platinum nanoparticles in low-temperature fuel cells. Top Catal 46:285–305

75. Meier JC, Galeano C, Katsounaros I et al (2012) Degradation mechanisms of Pt/C fuel cell catalysts under simulated start–stop conditions. ACS Catal 2:832–843
76. Chen S, Gasteiger HA, Hayakawa K et al (2010) Platinum-alloy cathode catalyst degradation in proton exchange membrane fuel cells: nanometer-scale compositional and morphological changes. J Electrochem Soc 157:A82–A97
77. Debe MK (2013) Tutorial on the fundamental characteristics and practical properties of nanostructured thin film (NSTF) catalysts. J Electrochem Soc 160:F522–F534
78. Debe MK, Schmoeckel AK, Vernstrom GD, Atanasoski R (2006) High voltage stability of nanostructured thin film catalysts for PEM fuel cells. J Power Sources 161:1002–1011
79. Stamenkovic V, Mun BS, Mayrhofer KJJ et al (2006) Changing the activity of electrocatalysts for oxygen reduction by tuning the surface electronic structure. Angew Chem Int Ed 45:2897–2901
80. Greeley J, Stephens IEL, Bondarenko AS et al (2009) Alloys of platinum and early transition metals as oxygen reduction electrocatalysts. Nat Chem 1:552–556
81. Jalan VM, Landsman DA (1978) Noble metal-refractory metal alloys as catalysts and method for making. US Patent 4,186,110
82. Jalan VM (1978) Noble metal/vanadium alloy catalyst and method for making. US Patent 4,202,934
83. Landsman DA, Luczak FJ (1980) Noble metal-chromium alloy catalysts and electrochemical cell. US Patent 4,316,944
84. Luczak FJ, Landsman DA (1983) Ternary fuel cell catalysts containing platinum, cobalt and chromium. US Patent 4,447,506
85. Luczak FJ, Landsman DA (1985) Ordered ternary fuel cell catalysts containing platinum and cobalt and method for making the catalysts. US Patent 4,711,829
86. Mukerjee S, Srinivasan S (1993) Enhanced electrocatalysis of oxygen reduction on platinum alloys in proton exchange membrane fuel cells. J Electroanal Chem 357:201–224
87. Mukerjee S, Srinivasan S, Soriaga MP, McBreen J (1995) Role of structural and electronic properties of Pt and Pt alloys on electrocatalysis of oxygen reduction. J Electrochem Soc 142:1409–1422
88. Toda T, Igarashi H, Uchida H, Watanabe M (1999) Enhancement of the electroreduction of oxygen on Pt alloys with Fe, Ni, and Co. J Electrochem Soc 146:3750–3756
89. Strasser P, Koh S, Anniyev T et al (2010) Lattice-strain control of the activity in dealloyed core–shell fuel cell catalysts. Nat Chem 2:454–460
90. Adzic RR, Zhang J, Sasaki K et al (2007) Platinum monolayer fuel cell electrocatalysts. Top Catal 46:249–262
91. Stamenkovic VR, Mun BS, Arenz M et al (2007) Trends in electrocatalysis on extended and nanoscale Pt-bimetallic alloy surfaces. Nat Mater 6:241–247
92. Nilekar AU, Xu Y, Zhang J et al (2007) Bimetallic and ternary alloys for improved oxygen reduction catalysis. Top Catal 46:276–284
93. Srivastava R, Mani P, Hahn N, Strasser P (2007) Efficient oxygen reduction fuel cell electrocatalysis on voltammetrically dealloyed Pt–Cu–Co nanoparticles. Angew Chem Int Ed 46:8988–8991
94. Mani P, Srivastava R, Strasser P (2011) Dealloyed binary PtM3 (M = Cu Co, Ni) and ternary PtNi3M (M = Cu Co, Fe, Cr) electrocatalysts for the oxygen reduction reaction: performance in polymer electrolyte membrane fuel cells. J Power Sources 196:666–673
95. Stamenkovic VR, Mun BS, Mayrhofer KJJ et al (2006) Effect of surface composition on electronic structure, stability, and electrocatalytic properties of Pt-transition metal alloys: Pt-skin versus Pt-skeleton surfaces. J Am Chem Soc 128:8813–8819
96. Bandarenka AS, Varela AS, Karamad M et al (2012) Design of an active site towards optimal electrocatalysis: overlayers, surface alloys and near-surface alloys of Cu/Pt(111). Angew Chem Int Ed 51:11845–11848
97. Stamenkovic VR, Fowler B, Mun BS et al (2007) Improved oxygen reduction activity on $Pt_3Ni(111)$ via increased surface site availability. Science 315:493–497

98. Zhang J, Yang H, Fang J, Zou S (2010) Synthesis and oxygen reduction activity of shape-controlled Pt_3Ni nanopolyhedra. Nano Lett 10:638–644
99. Wang D, Xin HL, Hovden R et al (2012) Structurally ordered intermetallic platinum–cobalt core–shell nanoparticles with enhanced activity and stability as oxygen reduction electrocatalysts. Nat Mater 12:81–87
100. Cui C-H, Li H-H, Liu X-J et al (2012) Surface composition and lattice ordering-controlled activity and durability of CuPt electrocatalysts for oxygen reduction reaction. ACS Catal 2:916–924
101. Jung N, Chung Y-H, Chung DY et al (2013) Chemical tuning of electrochemical properties of Pt-skin surfaces for highly active oxygen reduction reactions. Phys Chem Chem Phys 15:17079–17083
102. Li Q, Wu L, Wu G et al (2015) New approach to fully ordered fct-FePt nanoparticles for much enhanced electrocatalysis in acid. Nano Lett 15:2468–2473
103. Hodnik N, Jeyabharathi C, Meier JC et al (2014) Effect of ordering of $PtCu_3$ nanoparticle structure on the activity and stability for the oxygen reduction reaction. Phys Chem Chem Phys 16:13610–13615
104. Guo S, Zhang S, Sun S (2013) Tuning nanoparticle catalysis for the oxygen reduction reaction. Angew Chem Int Ed 52:8526–8544
105. Shao M, Chang Q, Dodelet J-P, Chenitz R (2016) Recent advances in electrocatalysts for oxygen reduction reaction. Chem Rev 116:3594–3657
106. Pickering HW (1983) Characteristic features of alloy polarization curves. Corrosion Sci 23:1107–1120
107. Erlebacher J, Aziz MJ, Karma A et al (2001) Evolution of nanoporosity in dealloying. Nature 410:450–453
108. Koh S, Strasser P (2007) Electrocatalysis on bimetallic surfaces: modifying catalytic reactivity for oxygen reduction by voltammetric surface dealloying. J Am Chem Soc 129:12624–12625
109. Strasser P (2009) Dealloyed core-shell fuel cell electrocatalysts. Rev Chem Eng 25:255–295
110. Brankovic SR, Wang JX, Adžić RR (2001) Metal monolayer deposition by replacement of metal adlayers on electrode surfaces. Surf Sci 474:L173–L179
111. Zhang J, Vukmirovic MB, Xu Y et al (2005) Controlling the catalytic activity of platinum-monolayer electrocatalysts for oxygen reduction with different substrates. Angew Chem Int Ed 44:2132–2135
112. Vukmirovic MB, Zhang J, Sasaki K et al (2007) Platinum monolayer electrocatalysts for oxygen reduction. Electrochim Acta 52:2257–2263
113. Debe MK, Steinbach AJ, Vernstrom GD et al (2011) Extraordinary oxygen reduction activity of Pt_3Ni_7. J Electrochem Soc 158:B910–B918
114. Chen C, Kang Y, Huo Z et al (2014) Highly crystalline multimetallic nanoframes with three-dimensional electrocatalytic surfaces. Science 343:1339–1343
115. Schuppert AK, Savan A, Ludwig A, Mayrhofer KJJ (2014) Potential-resolved dissolution of Pt-Cu: a thin-film material library study. Electrochim Acta 144:332–340
116. Yu Z, Zhang J, Liu Z et al (2012) Comparison between dealloyed $PtCo_3$ and $PtCu_3$ cathode catalysts for proton exchange membrane fuel cells. J Phys Chem C 116:19877–19885
117. Kelly MJ, Fafilek G, Besenhard JO et al (2005) Contaminant absorption and conductivity in polymer electrolyte membranes. J Power Sources 145:249–252
118. Malacrida P, Escudero-Escribano M, Verdaguer-Casadevall A et al (2014) Enhanced activity and stability of Pt–La and Pt–Ce alloys for oxygen electroreduction: the elucidation of the active surface phase. J Mater Chem A 2:4234–4243
119. Vej-Hansen UG, Rossmeisl J, Stephens IEL, Schiøtz J (2016) Correlation between diffusion barriers and alloying energy in binary alloys. Phys Chem Chem Phys 18:3302–3307
120. Escudero-Escribano M, Malacrida P, Hansen MH et al (2016) Tuning the activity of Pt alloy electrocatalysts by means of the lanthanide contraction. Science 352:73–76

121. Pedersen AF, Ulrikkeholm ET, Escudero-Escribano M et al (2016) Probing the nanoscale structure of the catalytically active overlayer on Pt alloys with rare earths. Nano Energy 29:249–260
122. Ulrikkeholm ET, Pedersen AF, Vej-Hansen UG et al (2016) Pt_xGd alloy formation on Pt (111): preparation and structural characterization. Surf Sci 652:114–122
123. Hernandez-Fernandez P, Masini F, McCarthy DN et al (2014) Mass-selected nanoparticles of Pt_xY as model catalysts for oxygen electroreduction. Nat Chem 6:732–738
124. Velázquez-Palenzuela A, Masini F, Pedersen AF et al (2015) The enhanced activity of mass-selected Pt_xGd nanoparticles for oxygen electroreduction. J Catal 328:297–307
125. Escudero-Escribano M, Verdaguer-Casadevall A, Malacrida P et al (2012) Pt_5Gd as a highly active and stable catalyst for oxygen electroreduction. J Am Chem Soc 134:16476–16479
126. Kondo S, Nakamura M, Maki N, Hoshi N (2009) Active sites for the oxygen reduction reaction on the low and high index planes of palladium. J Phys Chem C 113:12625–12628
127. Hara M, Linke U, Wandlowski T (2007) Preparation and electrochemical characterization of palladium single crystal electrodes in 0.1 M H_2SO_4 and $HClO_4$. Electrochim Acta 52:5733–5748
128. Chen Z, Higgins D, Yu A et al (2011) A review on non-precious metal electrocatalysts for PEM fuel cells. Energy Environ Sci 4:3167–3192
129. Zitolo A, Goellner V, Armel V et al (2015) Identification of catalytic sites for oxygen reduction in iron- and nitrogen-doped graphene materials. Nat Mater 14:937–942
130. Jasinski R (1964) A new fuel cell cathode catalyst. Nature 201:1212–1213
131. Alt H, Binder H, Sandstede G (1973) Mechanism of the electrocatalytic reduction of oxygen on metal chelates. J Catal 28:8–19
132. Jahnke H, Schönborn M, Zimmermann G (1976) Organic dyestuffs as catalysts for fuel cells. In: Schäfer FP, Gerischer H, Willig F et al (eds) Physical and chemical applications of dyestuffs. Springer, Berlin, pp 133–181
133. Bagotzky VS, Tarasevich MR, Radyushkina KA et al (1978) Electrocatalysis of the oxygen reduction process on metal chelates in acid electrolyte. J Power Sources 2:233–240
134. van Veen JAR, van Baar JF, Kroese KJ (1981) Effect of heat treatment on the performance of carbon-supported transition-metal chelates in the electrochemical reduction of oxygen. J Chem Soc Faraday Trans 77:2827–2843
135. Fuhrmann A, Wiesener K, Iliev I et al (1981) A contribution to the characterization of heat-treated electrocatalytically active tetramethoxy-phenylporphyrinato-cobalt-II. J Power Sources 6:69–81
136. Gruenig G, Wiesener K, Gamburzev S et al (1983) Investigations of catalysts from the pyrolyzates of cobalt-containing and metal-free dibenzotetraazaannulenes on active carbon for oxygen electrodes in an acid medium. J Electroanal Chem 159:155–162
137. Scherson DA, Gupta SL, Fierro C et al (1983) Cobalt tetramethoxyphenyl porphyrin—emission Mossbauer spectroscopy and O_2 reduction electrochemical studies. Electrochim Acta 28:1205–1209
138. Van Der Putten A, Elzing A, Visscher W, Barendrecht E (1986) Oxygen reduction on pyrolysed carbon-supported transition metal chelates. J Electroanal Chem 205:233–244
139. Gupta S, Tryk D, Bae I et al (1989) Heat-treated polyacrylonitrile-based catalysts for oxygen electroreduction. J Appl Electrochem 19:19–27
140. Wang H, Côté R, Faubert G et al (1999) Effect of the pre-treatment of carbon black supports on the activity of Fe-based electrocatalysts for the reduction of oxygen. J Phys Chem B 103:2042–2049
141. Lefevre M, Proietti E, Jaouen F, Dodelet J-P (2009) Iron-based catalysts with improved oxygen reduction activity in polymer electrolyte fuel cells. Science 324:71–74
142. Bashyam R, Zelenay P (2006) A class of non-precious metal composite catalysts for fuel cells. Nature 443:63–66
143. Wu G, More KL, Johnston CM, Zelenay P (2011) High-performance electrocatalysts for oxygen reduction derived from polyaniline, iron, and cobalt. Science 332:443–447

144. Zagal JH, Koper MTM (2016) Reactivity descriptors for the activity of molecular MN_4 catalysts for the oxygen reduction reaction. Angew Chem Int Ed 55:14510–14521
145. Jaouen F, Proietti E, Lefèvre M et al (2011) Recent advances in non-precious metal catalysis for oxygen-reduction reaction in polymer electrolyte fuel cells. Energy Environ Sci 4:114–130
146. Choi CH, Baldizzone C, Grote J-P et al (2015) Stability of Fe-N-C catalysts in acidic medium studied by operando spectroscopy. Angew Chem Int Ed 54:12753–12757
147. Markovic N, Ross PN (2002) Surface science studies of model fuel cell electrocatalysts. Surf Sci Rep 45:117–229
148. Trasatti S (1972) Work function, electronegativity, and electrochemical behaviour of metals. J Electroanal Chem 39:163–184
149. Conway BE, Jerkiewicz G (2000) Relation of energies and coverages of underpotential and overpotential deposited H at Pt and other metals to the "volcano curve" for cathodic H_2 evolution kinetics. Electrochim Acta 45:4075–4083
150. Auinger M, Katsounaros I, Meier JC et al (2011) Near-surface ion distribution and buffer effects during electrochemical reactions. Phys Chem Chem Phys 13:16384–16394
151. Sheng W, Gasteiger HA, Shao-Horn Y (2010) Hydrogen oxidation and evolution reaction kinetics on platinum: acid vs alkaline electrolytes. J Electrochem Soc 157:B1529–B1536
152. Seto K, Iannelli A, Love B, Lipkowski J (1987) The influence of surface crystallography on the rate of hydrogen evolution at Pt electrodes. J Electroanal Chem 226:351–360
153. Vesborg PCK, Seger B, Chorkendorff I (2015) Recent development in hydrogen evolution reaction catalysts and their practical implementation. J Phys Chem Lett 6:951–957
154. Marković NM, Sarraf ST, Gasteiger HA, Ross PN (1996) Hydrogen electrochemistry on platinum low-index single-crystal surfaces in alkaline solution. J Chem Soc Faraday Trans 92:3719–3725
155. Subbaraman R, Tripkovic D, Strmcnik D et al (2011) Enhancing hydrogen evolution activity in water splitting by tailoring Li^+-$Ni(OH)_2$-Pt interfaces. Science 334:1256–1260
156. Gong M, Wang D-Y, Chen C-C et al (2016) A mini review on nickel-based electrocatalysts for alkaline hydrogen evolution reaction. Nano Res 9:28–46
157. LeRoy RL (1979) Analysis of time-variation effects in water electrolyzers. J Electrochem Soc 126:1674–1682
158. Soares DM, Teschke O, Torriani I (1992) Hydride effect on the kinetics of the hydrogen evolution reaction on nickel cathodes in alkaline media. J Electrochem Soc 139:98–105
159. Genorio B, Strmcnik D, Subbaraman R et al (2010) Selective catalysts for the hydrogen oxidation and oxygen reduction reactions by patterning of platinum with calix[4]arene molecules. Nat Mater 9:998–1003
160. Zalitis CM, Kramer D, Kucernak AR (2013) Electrocatalytic performance of fuel cell reactions at low catalyst loading and high mass transport. Phys Chem Chem Phys 15:4329–4340
161. Zhuang Z, Giles SA, Zheng J, et al (2016) Nickel supported on nitrogen-doped carbon nanotubes as hydrogen oxidation reaction catalyst in alkaline electrolyte. Nat Commun 7:art. no. 10141

Fuel Cells: An Overview with Emphasis on Polymer Electrolyte Fuel Cells

Masahiro Watanabe and Donald A. Tryk

Abstract A brief overview is presented of the general topic of fuel cells as it relates to the work of John Bockris and was inspired by him. We trace some of the historical development of the field, starting in 1839 with Sir William Grove, up to the present, with some comments on the proliferation of fuel cells in electric vehicles and residential electric power units. We also illustrate some of the development of the field with examples from our own research.

1 Introduction

The fuel cell was one of Prof. John Bockris's favorite topics, for several reasons. First, it combines the fundamental topic of electrocatalysis with the practical topic of energy production. Second, it circumvents the Carnot limitation of the conventional heat engine and thus is in principle much more efficient. Third, it forms one of the main components of the hydrogen economy, which he was one of the first to envision. Particularly, the hydrogen–oxygen fuel cell was close to his heart, because it fit into his concept of the hydrogen economy. This grand concept is still in the making and will take many years to fully realize. Many of us are still driven by the magnificent idea that water can be split using renewable energy, and the resulting hydrogen can be recombined with atmospheric oxygen to produce pure water.

Both of the present authors owe their initial interest in electrochemistry and fuel cells in great part to John Bockris's books [1–6]. His enthusiasm, passion, and grand vision comes alive in his books, and we are honored to be able to contribute to the present volume, which we hope will expose a new generation of readers to his ideas and to the ideas and results that have resulted from his work.

M. Watanabe (✉) · D.A. Tryk
Fuel Cell Nanomaterials Center, University of Yamanashi, Kofu, Yamanashi, Japan
e-mail: m-watanabe@yamanashi.ac.jp

K. Uosaki (ed.), *Electrochemical Science for a Sustainable Society*,
DOI 10.1007/978-3-319-57310-6_3

1.1 John Bockris's Vision for Fuel Cells and the Hydrogen Economy

Prof. Bockris can be credited with coining the term "hydrogen economy," around 1970 and popularizing the concept, even though the idea had been raised earlier. It gained impetus around that time due to the oil crisis and further hope that hydrogen could be produced with renewable solar energy [7]. In the first edition of their classic textbook, Modern Electrochemistry, in 1970, Bockris and Reddy briefly discussed the history of fuel cells [8], starting with the invention by Sir William Grove in 1838 [9], although Sir Humphry Davy was thought to have come up with the idea prior to this, using carbon black as a fuel. Grove had the brilliant idea of simply reversing a water electrolysis cell in order to produce electric power from hydrogen and oxygen. There was some interest in this invention, and in 1894, as Bockris and Reddy [10] relate, Friedrich Wilhelm Ostwald predicted the air pollution that would result from combustion of fossil fuels, recommending instead the use of fuel cells for vehicles. However, as they further relate, society took a wrong turn around the turn of century. It was not until around 1932 that the British engineer Francis Thomas Bacon, a descendent of Sir Francis Bacon, who described the scientific method, reinvented the hydrogen–oxygen fuel cell and developed it with his team to the point where it was used to power a forklift in 1959. Then, NASA noticed this technology and decided to use it in their space missions for auxiliary power due to the high energy density and lack of noxious emissions. Fuel cells were then used on all of the space shuttles. Bacon finally received a special award from US President Nixon for his contributions to the space program. In the second edition of their now three-volume book, Bockris and Reddy stated that "the pollution-free production of electricity within electrochemical generators is a major step forward in technology," and predicted that, "in the twenty-first century, transportation—cars, trains, and ships—will all be driven by electric motors powered by electricity derived from fuel cells" [11]. They were also enthusiastic about the prospect of the commercialization of fuel cell vehicles [10]. We will discuss these prospects in more detail later.

In their book, Bockris and Reddy discuss in detail the fact that the fuel cell is intrinsically more efficient than the internal combustion engine (ICE), because it does not suffer from the well-known Carnot limitation [12]. They go on to discuss the kinetics of fuel cell reactions and the various sources of overpotential.

Bockris and Reddy point out that usually it takes about 75 years for an invention to become commercialized, whereas, for various reasons, it has taken roughly twice this time for fuel cells. This is a very interesting point, which must be considered in more depth as we try to accelerate their widespread dissemination.

1.2 Various Types of Fuel Cells

1.2.1 Alkaline Fuel Cells

The alkaline fuel cell is the one that was developed by Bacon starting around 1932 and was developed for NASA by Pratt and Whitney Aircraft (later, the Power Division of United Technologies Corporation, UTC) for the Apollo moon landing and subsequent space shuttles. This type of cell has one great advantage, i.e., that it does not require platinum as a catalyst, partly due to the intrinsically better O_2 reduction kinetics in alkaline solution and partly due to the high temperature (ca. 200 °C) that was used. Even at lower temperatures, platinum is not required. However, there is a one great disadvantage, in that pure O_2 must be carried, due to the problem of carbonate precipitation from CO_2 in the air. For this reason, as well as the corrosiveness of concentrated alkaline solutions, anion exchange membrane fuel cells are being intensively developed (see below).

1.2.2 Phosphoric Acid Fuel Cells

Phosphoric acid fuel cells (PAFCs) were first developed in the 1960s. They operate at approximately 200 °C with platinum catalysts. They were developed to a high level by the UTC Power and Fuji Electric and have been used in many medium-scale stationary electric power plants. They are highly efficient, ca. 80%, for the conversion of chemical energy to electrical plus heat energy, because the heat generated can be used to heat residential and commercial buildings in the so-called co-generation mode, also known as the combined heat and power (CHP) mode. The high temperature also is convenient for the reforming of natural gas, or methane produced by fermenting biomass, to hydrogen. Finally, the high temperature greatly lessens the poisoning of the hydrogen oxidation reaction by carbon monoxide, due to its weakened adsorption strength.

Early work was done at UTC Power to develop platinum alloy catalysts [13–16] which are still being used today in these cells, as well as in the lower temperature polymer types. These types of alloys generated a lot of scientific interest even in the 1980s. Early work at the University of Yamanashi was devoted to this topic, as we will discuss later [17–21]. Early work was also carried out on the problem of simultaneously optimizing the utilization of platinum and achieving good gas mass transport [22].

1.2.3 Molten Carbonate Fuel Cells

Molten carbonate fuel cells (MCFCs) make use of molten salts made up of mixtures of lithium, sodium and potassium carbonates, operating in the temperature range of 700–900 °C. Due to the high temperature, these cells can make use of hydrocarbon

fuels directly, without the need of a reformer. They also do not require platinum group metals (PGMs) as catalysts. As with PAFCs, a co-generation system can achieve very high efficiencies for the conversion of chemical energy to electrical plus heat energy, ca. 85%. One disadvantage of the MCFC is that of material durability, because the electrolyte is extremely corrosive. Nevertheless, the technology is mature and has been commercialized for stationary power applications, although the lifetime problem still remains.

1.2.4 Solid Oxide Fuel Cells

At the top of the temperature spectrum is the solid oxide fuel cell (SOFC), operating in the 900–1000 °C range. It is attracting interest in the application to power generation systems, particularly as combined systems with gas and/or steam systems, for which the electric power production efficiency can be expected to exceed 70%. Intermediate temperature versions are also being intensively developed, in the 700–800 °C range, in order to avoid some of the materials problems associated with the higher range. A residential co-generation system has been developed at the 750 W level for electric power production combined with water heating, which has been named the "EneFarm," together with a polymer electrolyte fuel cell (PEFC) version, as discussed in the Applications section. Higher temperatures are required in order to achieve reasonable oxide ion conductivities for the electrolyte, for example, yttria-stabilized zirconia (YSZ). SOFCs have the same advantages as MCFCs, i.e., direct use of hydrocarbon fuels and ability to utilize non-PGM catalysts. They are also mainly used in stationary applications with high efficiencies in the co-generation mode. Interestingly, Nissan Motor Company is developing an SOFC-based electric vehicle that will run on either methanol or ethanol with an internal reformer.

One of the interesting points about SOFCs is that they can be used in tandem with solid oxide water electrolysis cells (SOWECs) in a highly efficient manner. This type of system is being developed in several laboratories, including the Clean Energy Research Center (CERC) at the University of Yamanashi, for the storage of electric power from intermittent renewable energy sources such as solar and wind energy [23].

1.2.5 Polymer Electrolyte Fuel Cells, Acid and Alkaline

Polymer electrolyte fuel cells (PEFCs) include both the acid type, the proton exchange membrane fuel cell (PEFC) and the basic type, the anion exchange membrane fuel cell (AEMFC). Some variations on this terminology can be found in the literature. The early PEFC was developed by Grubb and Niedrach at General Electric, with a polystyrenesulfonic acid (PSSA) electrolyte. This technology was used for auxiliary power on the later Gemini spacecraft. As we can well appreciate today, there were problems with membrane stability, and the fuel cells were prone

to generating copious quantities of water when a hole in the membrane allowed hydrogen and oxygen to make direct contact. This problem prompted the change to the AFC for the Apollo program and space shuttles. Later, Walther Grot of Dupont helped to develop the much more robust perfluorosulfonic acid (PFSA) Nafion, which was then used in PEFCs. However, interestingly, as discussed later, researchers around the world are carrying out intensive work to return to the hydrocarbon-based membrane, but with high stability.

Above, we pointed out the problem with the AFC that high-purity O_2 is needed to avoid carbonate precipitation. This problem was the motivation of recent intensive research to develop a membrane version of the AFC, in which air could be used directly, in a hydroxyl-conducting AEMFC. Hydrocarbon-based AEMs are rather vulnerable to hydroxide attack, however, and this is one of the major challenges of this type of fuel cell, although one of the main advantages of the AFC remains, i.e., non-PGM catalysts can be used. We note briefly here that the AEMFC is being developed by Daihatsu for use in inexpensive electric vehicles. These efforts and others will be discussed in more detail below.

1.3 Comments on Fuels

Even though Bockris in his brief memoir [24] stated that "Several people had examined reduction of oxygen which comes into every fuel cell, and is the one bit of fuel cell work still open to academic research," there are other areas that deserve academic research, including the development of new ionomers for both PEFCs and AEMFCs, as already mentioned, as well as the development of other types of fuels. We have briefly discussed the fact that hydrocarbons and alcohols can be used in fuel cells. A fuel that is being used in the Daihatsu FCV is hydrazine hydrate. Gaseous hydrazine is somewhat hazardous, but the hydrate can be used with a high degree of safety. It is also environmentally friendly, because the products of the fuel cell reactions are N_2 and H_2O.

On the topic of safety, hydrogen has a popular reputation for being hazardous, but such a reputation is not deserved. High-pressure oxygen is far more hazardous. Even our ICE-based cars carry the highly toxic, flammable fuel gasoline. Battery-based electric vehicles also have safety issues, particularly for lithium-based batteries. A full treatment of the safety issue is beyond the scope of the present review, but one must be careful to avoid preconceptions.

Methanol is considered to be quite safe, but its toxicity and flammability can be problems, particularly for enclosed environments. These problems have led researchers at the University of Yamanashi and the University of Poitiers to develop a new type of fuel, the hydrolyzed polyoxymethylenedimethylethers (POMMEs) [25]. At the operating temperature of the cell, the fuel breaks down into methanol and formaldehyde catalytically under the acidic conditions, i.e., in contact with the acidic binder in the anode or flowing through an axially packed proton exchange resin. The methanol and formaldehyde are then oxidized directly.

2 Electrocatalysis

The topic of electrocatalysis will be discussed at length in a separate chapter in this book by Koper. However, we would like to make some brief comments here that we hope will not overlap too much with his comments.

2.1 Cathode Electrocatalysis

In their book, Bockris and Reddy discuss the desire to use oxygen from air, so as "avoid the necessity of carrying a second fuel for the cathodic reaction." They go on to say that "There is a grave disadvantage in this important (and inevitable) electrode reaction. It has an i_0 [exchange current density] value in the region of 10^{-10} A cm^{-2} and hence … the reaction usually contributes considerably to the overpotential in the functioning of an air-burning electrochemical converter. Electrocatalysis of this reaction is needed more than any other in electrochemical energy converters" [10]. This statement remains true even today.

2.1.1 Platinum and Its Alloys

As we mentioned, PGM-based catalysts are nearly obligatory for acid-based fuel cells. Surprisingly, platinum alloys, even after over 40 years, are still the catalysts of choice for the acid environment, including PEFCs. Indeed, these are special materials, with unique properties. There has been a huge amount of research that has been carried out to try to understand them, and certainly a degree of understanding has been reached [18–21, 26–29]. The conventional view is that alloy elements such as cobalt tend to weaken the adsorption of intermediates such as atomic oxygen O_{ad} and hydroxyl OH_{ad}, so that the surface remains open for the adsorption of the reactant O_2. This idea is in line with theoretical calculations, using density functional theory (DFT), which show this weakening effect [30, 31]. The weakening also correlates with the central, maximum occupation energy of the d-band electronic states, often referred to as the d-band center, measured with ultraviolet photoelectron spectroscopy (UPS), and also the surface core level shift, measured with x-ray photoelectron spectroscopy (XPS) (Fig. 1) [32]. A third correlation exists with the density of states (DOS) at the Fermi level [33].

This idea certainly has its merits, being grounded in the classic Sabatier principle, i.e., that the adsorption of reactants and products must not be too strong nor too weak for maximum activity [34]. On some catalyst surfaces, this is probably valid, but the results from our laboratory have tended to suggest that it is not the case for platinum or its alloys. In fact, results from XPS combined with electrochemistry (EC-XPS) [35–40] in situ electrochemical quartz crystal microbalance (EQCM) [41], and cyclic voltammetry [40] over a wide range of cobalt

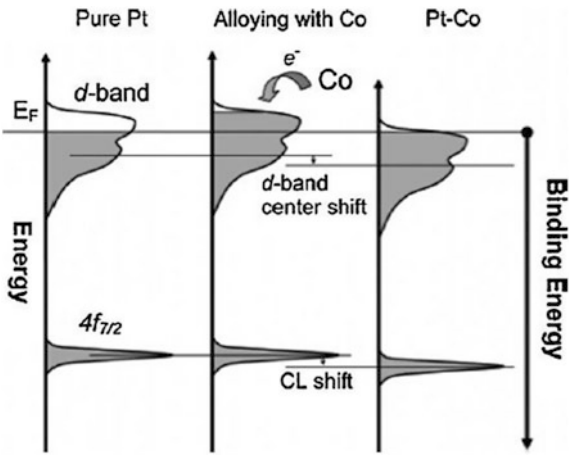

Fig. 1 Schematic explanation of the alloying effect of Co on the electronic structures of Pt. In XPS measurements, the binding energy should be referred to the Fermi energy E_F, so that filling the d-band has the effect of lowering both the d-band center and core level [32] (reprinted with permission from Ref. [32]. Copyright 2006 American Chemical Society)

concentration in Pt–Co alloys, indicate that it might actually be beneficial for intermediates such as O_{ad} or OH_{ad}, which are produced via O_2 dissociation, to be more strongly adsorbed. The O_2 reduction activity appears to be higher when there are higher levels of such adsorbed species, specifically O_{ad} in the case of EC-XPS.

It is well known that the adsorption strengths of various adsorbates tend to scale linearly on various surfaces; for example, O_{ad}, OH_{ad}, and OOH_{ad} all tend to have the same relative adsorption strengths on a given surface. Our DFT calculations also indicate that O_2 adsorption strengths scale in the same way. Thus, if OH_{ad} adsorption is weakened, O_2 adsorption is also weakened. Such a weakening of O_2 adsorption is counterproductive, because its adsorption is an obligatory first step in the reduction process.

Early work with Pt alloys at the University of Yamanashi [19–21] showed a "volcano" relationship between ORR activity and alloying metal (M = Fe, Co, Ni) concentration in Pt–M alloys (Fig. 2a) [20]. Recently, based on a novel technique for preparing well-defined Pt–Co(111) single crystal alloys [42], we have found an even more striking dependence upon the alloy element concentration (Fig. 2b) [40]. It is very intriguing that the concentration dependence is so large, i.e., a factor of ca. 25. In the cyclic voltammetry, one can see that the oxidation of the surface to form OH_{ad} is pushed to higher potentials with increasing Co concentration (Fig. 3a). According to the conventional view, one would expect that there should be a strong dependence of the electric charge for OH_{ad}, Q_{OH}, summing the current to 0.9 V versus RHE, where the ORR measurements are made. However, as shown in Fig. 3b, the Q_{OH} values are nearly constant up to 25 at.%, where the maximum in activity is found. This result casts doubt upon the idea that OH_{ad} is a blocking species.

At present, we are in the process of further elucidating the alloy effects, making use of both EC-XPS with single crystal alloy electrodes of varying composition and DFT calculations.

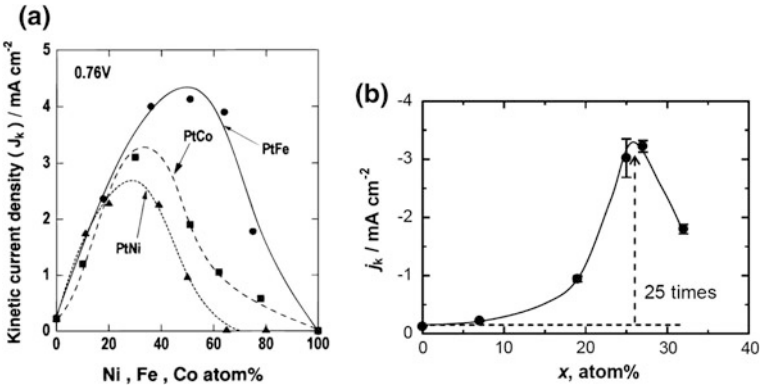

Fig. 2 **a** Kinetically controlled current densities for the ORR at 0.76 V as a function of the bulk composition of alloy electrodes [20]; (reprinted from Ref. [20] with permission from The Electrochemical Society.) **b** Kinetically controlled area-specific activities for the ORR, j_k, of the $Pt_{100-x}Co_x(111)$-RDEs at 0.9 V as a function of the Co content [40] (reprinted from Ref. [40] with permission from Elsevier)

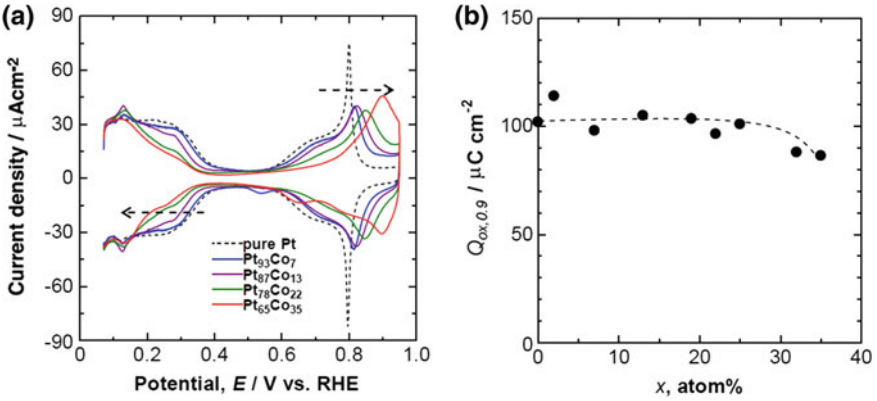

Fig. 3 **a** Cyclic voltammograms of $Pt_{100-x}Co_x(111)$ electrodes at 0.05 V s^{-1} in N_2-purged 0.1 M $HClO_4$. The CVs were recorded in a hanging meniscus configuration. **b** Surface oxidation charges up to 0.9 V, $Q_{ox,0.9}$ for $Pt_{100-x}Co_x(111)$ electrodes [40] (reprinted from Ref. [40] with permission from Elsevier)

We note here that strong efforts have been under way to convert this fundamental knowledge regarding Pt alloys to practical use by optimizing nanoparticle catalysts with stabilized characteristics, so that the alloy element is protected by two Pt skin layers. Pt and non-precious metal alloy particles of mean particle size of 3 nm level with distinctively small size distribution and uniform dispersion on carbon black supports were successfully prepared by the nanocapsule method [43]. Pt-skin formation, with precisely designed atomic layers on the particle surfaces,

was newly developed by us and applied for the alloy catalysts. In this way, the durability during accelerated potential cycling tests, simulated start/stop cycles or load change cycles in the practical PEFC cell operation is greatly improved, compared to the catalysts without such a special skin formation or pure Pt catalyst, resulting from the suppression of de-alloying with an optimum, uniform Pt-skin layer (Figs. 4, 5 and 6).

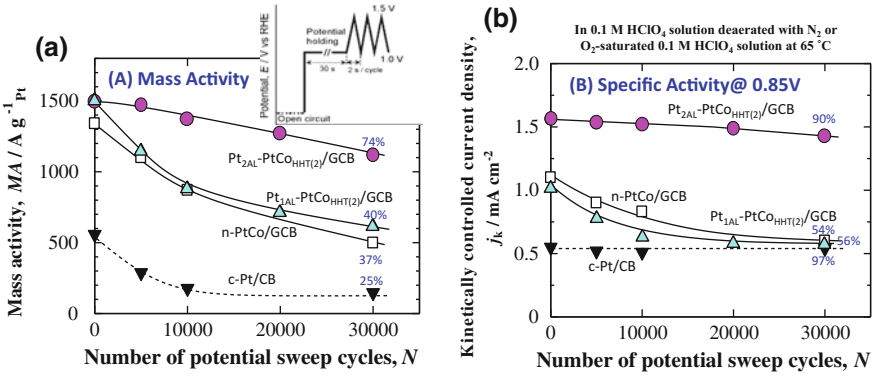

Fig. 4 **a** Mass activities and **b** kinetically controlled current density for the ORR during accelerated durability testing with potential sweep cycles of various catalysts: Pt/C, n-PtCo/GCB, Pt_{1AL}–$PtCo_{HHT(2)}$/GCB, Pt_{2AL}–$PtCo_{HHT(2)}$/GCB in 0.1 M $HClO_4$, deaerated with N_2 or in O_2-saturated solution at 65 °C [43] (reproduced from Ref. [43], with permission of The Electrochemical Society, Inc.)

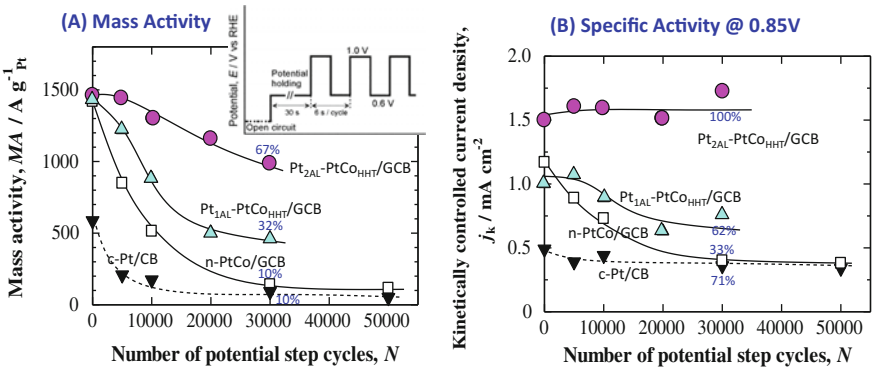

Fig. 5 **a** Mass activities and **b** kinetically controlled current density for the ORR during accelerated durability testing with potential step cycles of various catalysts: Pt/C, n-PtCo/GCB, Pt_{1AL}–$PtCo_{HHT(2)}$/GCB, Pt_{2AL}–$PtCo_{HHT(2)}$/GCB in 0.1 M $HClO_4$, deaerated with N_2 or in O_2-saturated solution at 65 °C [43] (reproduced from Ref. [43], with permission of The Electrochemical Society, Inc.)

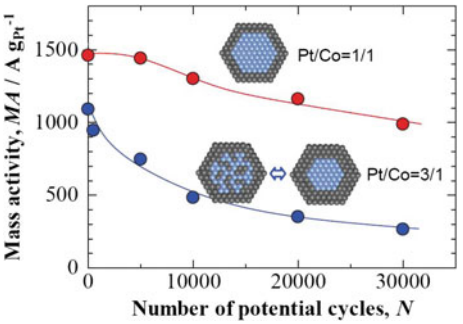

Fig. 6 Mass activities of stabilized Pt–Co nanoparticles during potential sweep cycle testing, showing the influence of the bulk Co concentration of the starting core nanoparticles [43] (reproduced from Ref. [43], with permission of The Electrochemical Society, Inc.)

2.1.2 Alternative Catalysts

Again, from Bockris's brief memoir, "I still have grand fantasies of being able to patent a fuel cell electrode which can be easily and cheaply made from polymers rather than metals" [24]. There are probably many people who would like to avoid metals, especially PGMs, in cathodes for PEFCs. For the latter, it is our opinion that PGMs, at least in small quantities, are required for O_2 reduction to water with performance that is sufficient for practical application in FCVs or CHP units. We hope that it will be possible to greatly decrease Pt loadings for PEFCs. There have been intensive efforts along these lines [44].

For alkaline membrane fuel cells (AEMFCs), it is certainly possible to have excellent catalysis of O_2 reduction to the hydroperoxyl anion HO_2^- without any metal present. Even a pure carbon material with appropriate surface functional groups such as quinones can be active [45]. However, it seems necessary to have a metal present in some form, for example as an oxide, in order to decompose the HO_2^- and thus to complete the reduction of O_2 to H_2O. Over the past several years, there has been enormous activity in the area of C–N polymers, and it has often been stated that the materials are metal-free. A comprehensive review on this topic has appeared recently, in which it is shown conclusively that even extremely small quantities of metallic impurities, so small that they escape detection via XPS, can have a large impact on the catalytic activity [46].

Going back to Bockris's idea of a cheap polymer electrode, the group of Ernest Yeager at Case Western Reserve University was the first to show that it was possible to pyrolyze a C–N polymer in the presence of a metal salt such as cobalt acetate to produce an active O_2 reduction catalyst for alkaline solution [47]. It was hypothesized that the pyrolysis would possibly produce active sites similar to those of porphyrins or phthalocyanines via a templating reaction, i.e., that metal ions could coordinate with nitrogens from the polymer to make square planar complexes. Indeed, the active sites appear to be somewhat similar to the ones that are obtained when porphyrins are pyrolyzed [46, 48]. This field has expanded greatly, with hundreds of publications [49]. This general strategy seems to be more cost-effective than synthesizing the actual macrocyclic complexes and then pyrolyzing them, particularly if the active sites are similar.

2.2 Anode Electrocatalysis

2.2.1 Platinum and Its Alloys

For the PEFC anode fed with reformate-derived hydrogen, it is necessary either to have an extremely low CO concentration (<10 ppm) or to have a highly CO-tolerant HOR catalyst. This is a topic that is still being actively researched. Let us first trace some of the background. Following early work at the University of Yamanashi on Pt with adsorbed adatoms of Ru to catalyze CO oxidation [50], it was found that adatoms of Ru, Sn, and As were able to enhance the CO tolerance of HOR catalysis [51]. Later, it was suggested by Ross that, because CO adsorbs more weakly on platinum alloys than on pure platinum, such alloys would be more tolerant to the presence of CO [52]. This idea was supported by work of Igarashi et al. with in situ infrared measurements that, for several different Pt–skin-covered Pt alloys, particularly Pt–Fe; they found that the CO tolerance is enhanced due to the increased mobility of CO on the surface due to the lowered CO-bonding strength on the skin surface sites (Fig. 7) [53]. However, Ross and coworkers subsequently concluded, based on their infrared measurements, that Pt–Sn alloys are CO-tolerant due to Sn, probably in the hydroxide form, assisting in CO oxidation at low potentials [54].

Interestingly, the University of Yamanashi group has also recently found experimentally at practical nanoparticle catalysts that the surface area-normalized HOR activity itself is improved for Pt–Fe, Pt–Co and Pt–Ni alloys (Fig. 8a), due to weakening of the bonding of H atoms to the surface, based on DFT calculations (Fig. 8b) [55, 56]. This correlation initially suggested that the rate-determining step (rds) in the HOR is the oxidation of adsorbed H atoms H_{ad}, but it was found, even more importantly, that the rds is the surface diffusion or "spillover" of H_{ad} from step edges to terraces [56]. In the left panel of Fig. 8b, the adsorption strengths for H on

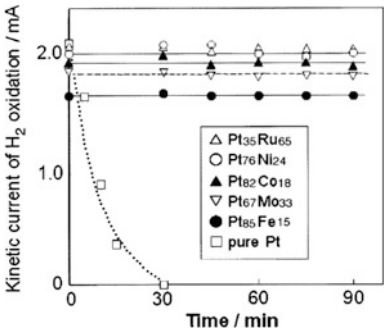

Fig. 7 Time courses of H_2 oxidation currents on the CO-tolerant alloys and pure Pt in 0.1 M $HClO_4$ saturated with 100 ppm CO (balance H_2); potential for CO adsorption, 50 mV versus RHE; rotation rate during CO adsorption, 1500 rpm; potential for the evaluation of HOR current, 20 mV versus RHE; temperature, 26 °C [53] (reproduced from Ref. [53] with permission from the PCCP Owner Societies)

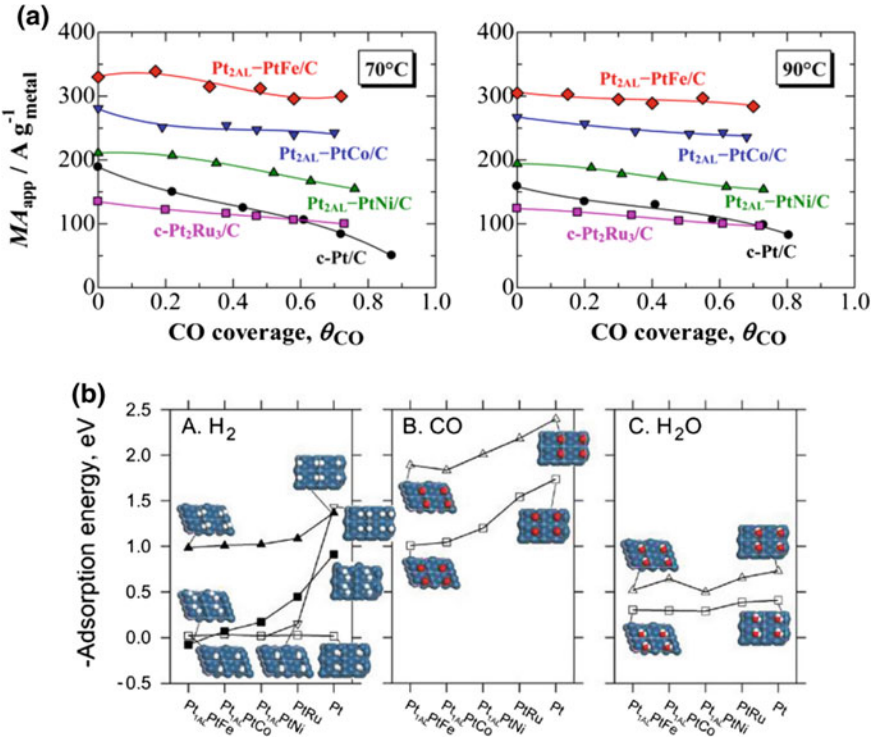

Fig. 8 **a** Dependence of MA_{app} at 20 mV versus RHE on θ_{CO} at Nafion-coated electrodes measured in H_2-saturated 0.1 M $HClO_4$ solution at 70 and 90 °C. **b** Adsorption energies for (*A*) H_2 or 2H, (*B*) CO, and (*C*) H_2O at step edges (*triangles*) and terraces (*squares*). In (*A*), the *solid symbols* denote dissociated 2H, while the *open symbols* denote undissociated H_2. In all cases except for PtRu, undissociated H_2 does not adsorb on the surface, at either step edges or terraces. On pure Pt(221), H_2 dissociates spontaneously when close to the surface, while on Pt_{1AL}–PtFe, Pt_{1AL}–PtCo and Pt_{1AL}–PtNi, it "floats" away from the surface [56] (reprinted with permission from Ref. [56]. Copyright 2017 American Chemical Society)

the (110) steps of (221) Pt alloy surfaces are shown to be nearly constant for Fe, Co and Ni, but shows a much stronger dependence on the adsorption strength at the (111) terraces.

Turning now to the HOR in alkaline solution, there has been a controversy concerning the mechanism and rationale for developing new, higher activity catalysts. There is a problem in alkaline solution, including AEMFCs, that the HOR activity of Pt is relatively low compared to that in acid solution. A full treatment would be beyond our present scope, but it might be interesting to have a brief look at the arguments. One view has been stated by Markovic and coworkers, which is that the oxidation of H_{ad} is made easier by the presence of OH_{ad} to produce water, so that a more oxophilic surface should be more active [57]. An alternate view has been stated by Gasteiger and coworkers that the key factor that determines the HOR activity in alkaline solution is the H_{ad} adsorption strength [58]. This is because the

rds is thought to be the oxidative desorption step, known as the Volmer step. Thus, even though iridium metal is more oxophilic than platinum, it does not have higher HOR activity. More recently, Wang et al. have concluded that Pt–Ru alloys have higher HOR activity in alkaline solution, because H_{ad} is more weakly adsorbed, specifically, at (110) steps [59].

2.2.2 Alternative Catalysts

Pt and its alloys are such highly active HOR catalysts in acid solution that there has not been such a strong emphasis on finding alternatives. Very low loadings can be used, so that the amounts will not contribute greatly to the cost of the fuel cell.

As stated above, the situation in alkaline media is different. If Pt is used, higher loadings are required, which will contribute significantly to the cost. Therefore, there is a strong push to discover new, low-cost HOR catalysts. One example is the CoNiMo alloy catalyst [60]. It is reported to have higher activity than Pt. The H_{ad} adsorption strength seems to be an important quantity here too: it should be minimized in order to accelerate the oxidative desorption step. Recently, a novel Pd/C-CeO_2 HOR catalyst has been reported for the AEMFC [61].

In the area of alternative fuels, hydrazine hydrate oxidation is important; a promising Ni–Zn alloy has been developed recently [62], as well as encouraging results in our laboratory with carbon-modified Ni [63], so the dream of the low-cost PGM-free fuel cell for FCVs is coming closer to reality. However, the membrane is still a limiting factor, as discussed later.

3 Catalyst Support Materials

One of the intrinsic problems with fuel cell materials in general is that they have often been developed for other applications and thus have not been optimized especially for fuel cells. This is because those materials are low in cost and readily available. However, as fuel cells become more developed and commercialized, it will be possible to develop special materials with specific properties. Both catalyst support materials and membranes fall into this category. During the past several years, however, there has been much interest in developing novel support materials, including various forms of carbons, metal oxides, carbides, and others [64].

3.1 Carbon Materials

As an example, the carbon blacks (CB) that are so commonly used as supports for Pt nanoparticles were originally developed mainly for the rubber industry for use in automobile tires. Fortuitously, these materials have been well-suited for use in both

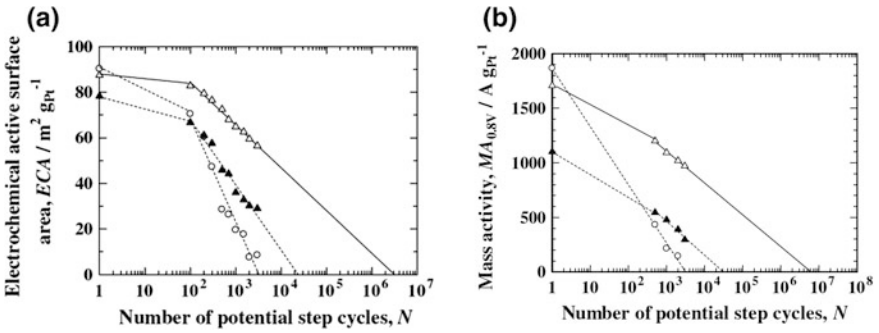

Fig. 9 **a** Plots of electrochemically active surface area (ECA) at Nafion-coated (M) n-Pt/GCB, (N) c-Pt/GCB, and (s) c-Pt/CB electrodes as a function of log [*N*] (*N* = number of potential step cycles). **b** Plots of MA at 0.80 V ($MA_{0.8V}$) on Nafion-coated (M) n-Pt/GCB, (N) c-Pt/GCB, and (s) c-Pt/CB electrodes as a function of log [*N*] [70] (reprinted from Ref. [70] with permission from Elsevier)

PAFCs and PEFCs. However, they are somewhat deficient in durability and ability to immobilize Pt particles.

To make them more durable, one popular approach is to simply graphitize them, which greatly decreases the presence of edge planes and defects. However, this has a disadvantage, because then, the Pt particles can tend to deposit in a nonuniform way. This problem was solved by modification [65] of a reverse micelle technique that was originally developed for the production monodisperse magnetic nanoparticles for the hard disk drive industry [66, 67]. The organic moieties that form the reverse micelles are retained long enough to deposit them on the CB or GCB support, which effectively keeps them well dispersed, and are then removed via heat treatment [68]. This approach greatly improves the durability of Pt/GCB catalysts under potential cycling conditions (Fig. 9) [69, 70]. This technique was originally developed for magnetic Pt alloys and is thus well suited for the preparation of the Pt–M alloys that are used in both fuel cell cathodes and anodes [71, 72].

Another possible approach is to use conductive diamond particles as supports. Undoped diamond is an insulator, but it can be doped with boron or other dopants so that its conductivity becomes sufficient to be useful in fuel cell catalyst layers (CLs) [73–76]. The cost of such materials would be quite high, if bulk doped material is first made and then crushed to powder. However, if undoped powders can be doped, it would greatly decrease the cost. If low-cost impure detonation diamond nanoparticles can be adequately cleaned [77] and then doped, these would possibly still be low enough in cost to be considered [75].

3.2 Oxides

Graphitized carbons are much more stable than their non-graphitized counterparts, but we would like to increase the stability even further. Conductive oxides such as

doped titanium dioxide [78, 79], including a mixed Ti–Ru oxide [80], and tin oxide [81–85] are prime candidates. Oxides often suffer from low conductivity, and it can be beneficial to synthesize fused agglomerates with structures similar to those of carbon blacks, which have a grape cluster-like structure (Fig. 10) [82]. Interestingly, the presence of deposited Pt has a significant effect in improving the conductivity [82, 83]. The Pt-free doped SnO_2 surface can adsorb O_2 and related species, which can drain electron density from the material's conduction band, effectively decreasing the electronic conductivity. However, the presence of Pt is thought to dissociate O_2 and H_2O_2, producing water, which has little effect on the

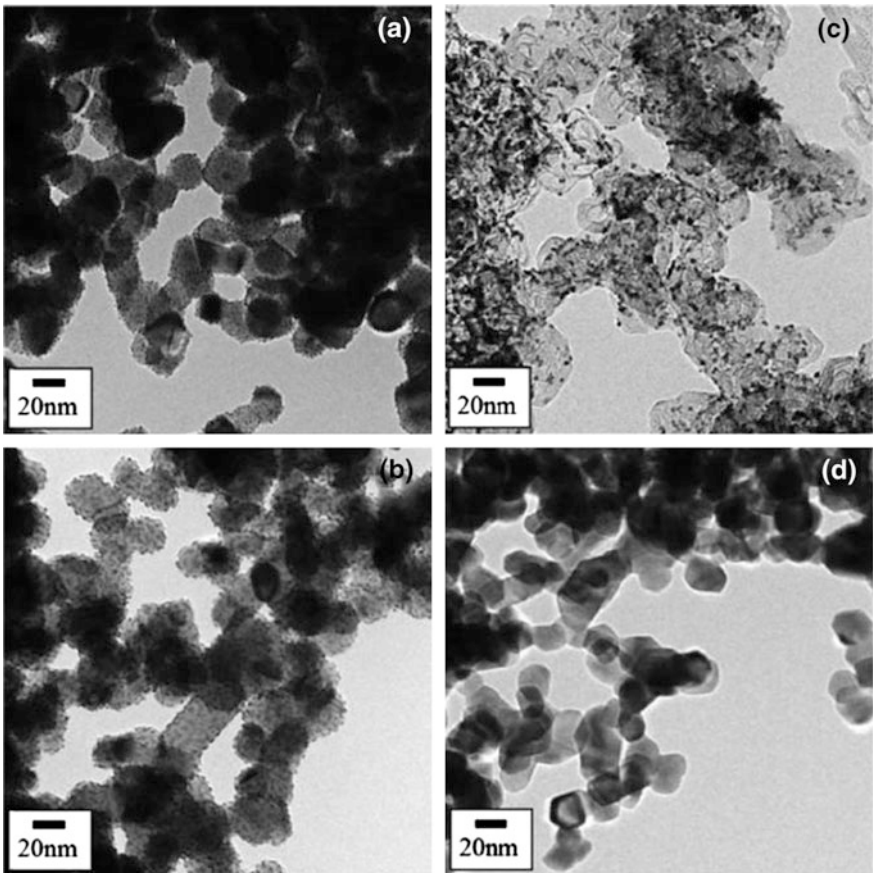

Fig. 10 TEM images of **a** 9 wt% Pt/Nb–SnO_2, **b** 17 wt% Pt/Nb–SnO_2, **c** commercial P/GCB and **d** Nb–SnO_2 support [83] (reproduced from Ref. [83], with permission of The Electrochemical Society, Inc.)

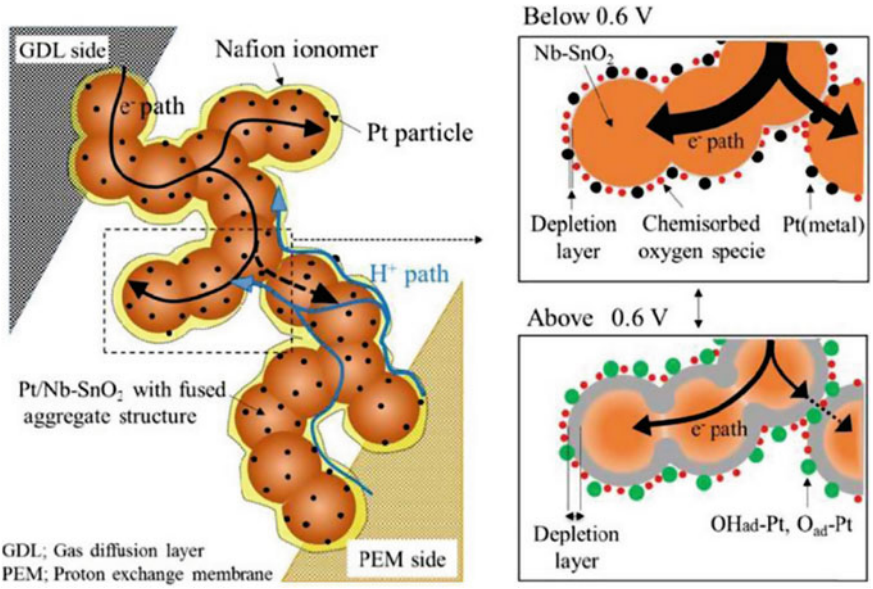

Fig. 11 Schematic model of depletion region for Pt/Nb–SnO_2 CL *below/above* 0.6 V. OH_{ad}–*Pt* OH-adsorbed Pt nanoparticle, O_{ad}–*Pt* O-adsorbed Pt nanoparticle [83] (reproduced from Ref. [83], with permission of The Electrochemical Society, Inc.)

conductivity. It was also found that higher loadings of Pt are needed to avoid conductivity losses at higher potentials (Fig. 11).

Another advantage of oxides is the strong interaction of the surface with Pt, which can impede the movement of nanoparticles and thus slow down aggregation [82, 83, 85].

3.3 Others

Metal carbides [86] and nitrides [87] are also promising candidate support materials.

4 Membranes

4.1 Proton Exchange Membranes

As already mentioned, PEMs have started from hydrocarbons, moved toward perfluorocarbons, and are now returning to hydrocarbons. We will summarize this area based on the recent chapter of Miyatake [88].

4.1.1 Perfluorinated Membranes

PFSA ionomers have perfluorocarbon main chains with side chains containing the perfluorosulfonic acid groups. PFSA resins, membranes, and solutions are supplied by DuPont, 3M, Asahi Kasei, Asahi Chemicals, and Solvay Solexis. The chemical structure is shown in Fig. 12, together with molecular models in which the sulfonic acid groups are hydrated. In work carried out at the University of Yamanashi, a new model for proton conduction was proposed based on DFT calculations, as shown in the figure [89, 90]. This model helps to explain why Nafion has good ionic conductivity even at low humidities.

There are differences in the composition and the length of the side chains. DuPont developed these PFSA membranes initially as separators for chlor-alkali cells in the manufacture of chlorine gas for the plastics industry. These membranes exhibit hydrophilic/hydrophobic phase separation. Aggregated sulfonic acid groups become hydrated and form the hydrophilic domains (5–6 nm in diameter), providing the ionic conduction channels. The fluorinated main chains form the hydrophobic domains. A short side chain version, with higher ion exchange capacity (IEC) and higher proton conductivity was developed by Dow; these were used by Ballard Power Systems in their PEFCs in the 1980s.

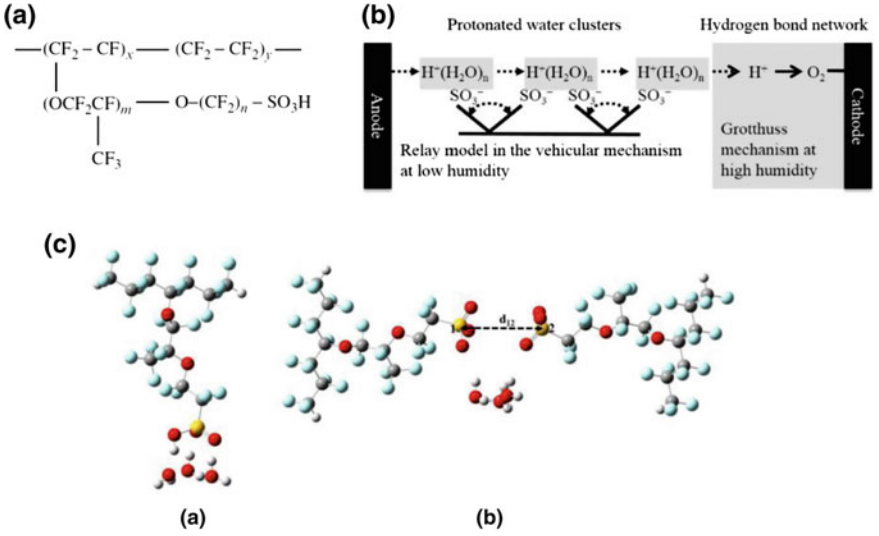

Fig. 12 **a** General chemical structure of PFSA ionomers. **b** Schematic diagram for the relay model for proton conductance in Nafion [89] (reprinted from Ref. 89 with permission from Elsevier). **C** *a* Calculated models of a single chain with hydrated water molecules; and *b* two chains in which two sulfonic acid groups are associated with the same water cluster in a Nafion membrane, where d_{12} is the distance between the sulfur atoms of two sulfonic acid groups [90] (reprinted with permission from Ref. [90]. Copyright 2016 American Chemical Society)

Proton conductivity can be increased by increasing the IEC, via the use of short side chains, or via increasing the concentration of sulfonic acid groups. The short side chain approach was used in manufacturing Dow membranes, but these are no longer available due to the synthetic difficulties involved. Several other companies are now supplying these, notably Solvay Solexis, which developed a simpler synthetic method. Their membrane is called Aquivion.

The proton conductivities of PFSA membranes with different IEC values increase monotonically with increasing humidity (Fig. 13). The proton conductivities of several PFSA membranes at 110 °C, 20% RH are plotted versus their respective IEC values in Fig. 14. So far, none have approached the target value of 0.1 S/cm, which would in principle be reached at an IEC of 2–3 meq/g. However, at such high values, the membranes are expected to have poor mechanical properties. Short side chain ionomers generally have higher glass transition temperatures and decomposition temperatures. For example, Aquivion's glass transition temperature is 160 °C, ca. 50 °C higher than those of long side chain PFSAs.

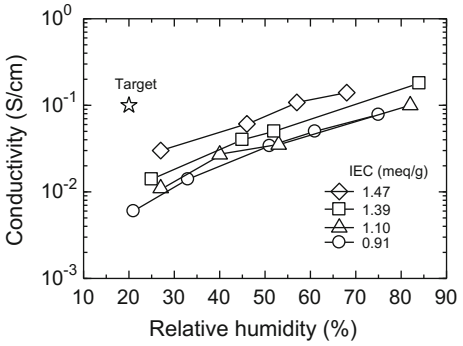

Fig. 13 Humidity dependence of the proton conductivity of perfluorosulfonic acid (PFSA) membranes at 110 °C [88] (reprinted from Ref. [88] with permission from Springer Science + Business Media)

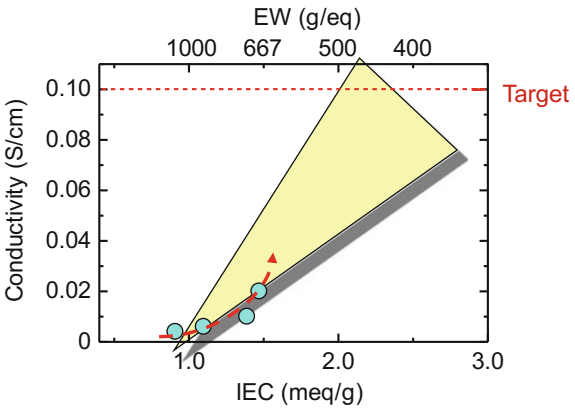

Fig. 14 Proton conductivity of perfluorosulfonic acid (PFSA) membranes at 110 °C and 20% RH versus ion exchange capacity (IEC) [88] (reprinted from Ref. [88] with permission from Springer Science + Business Media.)

Thus far, there are few viable approaches for the synthesis of sulfonated perfluorovinyl monomers, and these are quite complicated. A promising lower cost approach has been developed by Asahi Glass, which involves the perfluorination of partially fluorinated aliphatic esters containing sulfonyl fluoride groups.

There are three main degradation mechanisms for polymers: (1) degradation of end groups, (2) decomposition of sulfonic acid groups, and (3) hydrogenation of C–F to C–H by H_2 gas. The first two are thought to result from attack from oxygen radicals such as OH• or OOH•, which can be produced from hydrogen peroxide, which results from the chemical combination of H_2 and O_2 at Pt particles. Direct attack is also possible by hydrogen peroxide. Various measures have been developed to try to avoid these degradation pathways.

4.1.2 Hydrocarbon Membranes

The PFSA materials have three main disadvantages: (1) high cost, (2) environmental incompatibility, and (3) poor mechanical properties. The environmental incompatibility is based on the assumption that used membranes would have to be incinerated, and the products would include various low molecular weight fluorocarbons, which have enormous global warming effects. For example, over a 20-year period, tetrafluoromethane is over 5000 times more effective than CO_2 for global warming, and hexafluoroethane is over 8000 times more effective. Another major product would be HF, which is extremely corrosive.

Non-fluorinated hydrocarbon ionomers were first developed over 100 years ago as cation exchange resins, used, for example, in water softeners and were sulfonated polystyrenes or polyphenols. As mentioned, Grubb and Niedrach of General Electric developed the first PEFC in the 1960s, which was a brilliant idea, but these suffered from short lifetimes. For this reason, PFSAs were then used in further development in various laboratories, including Los Alamos National Laboratory (LANL), Texas A&M and Ballard. The hydrocarbon-based ionomers have experienced resurgence due to their lower cost, greater flexibility, and better environmental compatibility.

There are two main types of hydrocarbon ionomers: aromatic and aliphatic. The former have been more studied due to their chemical robustness. A low-cost route to their production is via sulfonation of commercially available engineering plastics, such as poly(phenylene)s, polyimides, poly(arylene ether)s, and poly(ether ether ketone)s. Recent efforts have yielded membranes that can successfully compete with PFSA ionomer membranes at higher humidity but still lack sufficient ionic conductivity at low humidity. Durability is also an issue.

One of the promising types of ionomer is the poly(phenylene), which has good chemical stability and good mechanical properties, because the aromatic–aromatic linkages result in a rigid, rod-like structure. Other types of hydrocarbon-based ionomers that contain heteratom-based linkages are vulnerable to chemical attack, particularly at ether groups.

The JSR Corporation has developed a highly successful type of poly (p-phenylene) with 3-sulfobenzoyl groups. These exhibit excellent hydrophilic/hydrophobic microphase separation. Surprisingly, the high IEC values, which can exceed 3 meq/g, do not lead to poor mechanical or chemical stability. One of the advantages of this ionomer, as well as several others, is the quite low gas permeability, compared with those of PFSA membranes, which typically are highly permeable to both H_2 and O_2. This is a serious problem, because it leads to the production of hydrogen peroxide and radical attack, as mentioned above. JSR membranes have been used on the Honda FCX Clarity FCV. Several other approaches to the synthesis of poly(p-phenylene) ionomers have been developed, as reviewed by Miyatake [88].

Another approach is to synthesize block copolymers, which involve the coupling of hydrophilic and hydrophobic oligomers of specific lengths in specific ratios. This approach has the effect of developing interconnected ionic domains. This approach is fairly general, being used successfully with various types of oligomers. Block copolymer membranes typically exhibit significantly higher proton conductivities compared with corresponding random copolymer membranes with similar IEC values, even at low humidity. The proton conductivity these membranes increases significantly with increasing block chain length, which are thought to facilitate the formation of ionic channels.

Promising results were obtained at the University of Yamanashi by Miyatake and coworkers with sulfonated polyimides [91]. They examined sulfonated polyimides containing aliphatic segments in both the hydrophobic main chains and in the hydrophilic side chains. A block copolymer with very long block segments (150 repeat units for both hydrophilic and hydrophobic blocks) showed a high proton conductivity of 2×10^{-2} S/cm at 80 °C and 48% RH, which compares well with those of PFSA membranes (Fig. 15).

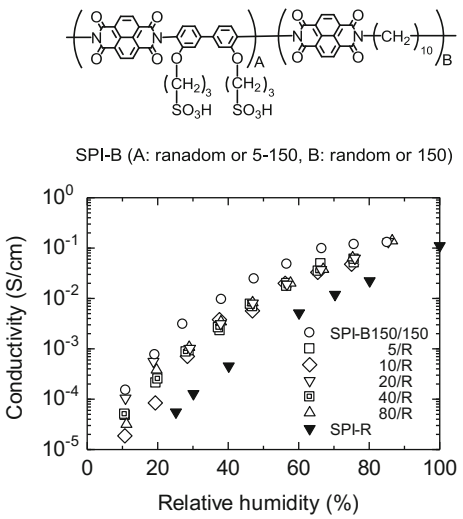

Fig. 15 Humidity dependence of the proton conductivity of sulfonated block copolyimide membranes at 80 °C [88] (reprinted from Ref. [88] with permission from Springer Science + Business Media)

Another approach to increasing ionic conductivity was initiated by Hay and coworkers at McGill University, which involves the synthesis of clusters containing large numbers of sulfonic acid groups, up to 18, which leads to good phase separation and connections between hydrophilic domains [92, 93]. A similar approach has also been utilized at the University of Yamanashi [93]. Some of these materials have exhibited excellent ionic conductivity and stability under hydrolytic conditions but less than optimal stability under oxidizing conditions.

A number of other approaches have been developed, including the use of side chains containing the sulfonic acid groups, similar to the Nafion structure, the use of superacid groups, via fluorination of the chains containing the sulfonic acid groups. Some groups have also developed organic–inorganic hybrid materials. All of these have been reviewed by Miyatake [88].

One other approach that should be mentioned briefly is that of high temperature membranes, which can operate at temperatures as high as 120 °C or even higher. At such temperatures, it is expected that the kinetics of both reactions, i.e., at the anode and cathode, would be improved, and the HOR catalyst would be able to withstand higher CO concentrations in H_2 reformed from hydrocarbons, similar to the situation with PAFCs. One such material is based on polybenzimadazole (PBI), originally developed by Savinell, Litt and coworkers at Case Western Reserve University [94, 95]. In this system, the PBI is saturated with concentrated phosphoric acid (PA), so there are certainly some similarities with the PAFC. The success of this system led to subsequent work at a number of laboratories. One problem is that the PA is usually present in liquid form and can leach out of the cell as water is produced at the cathode. Various strategies have been proposed to avoid this problem, for example, through the use of larger, less mobile acids such as polyvinylphosphonic acid [96].

4.2 Anion Exchange Membranes

AEMs are now becoming a subject of intense research, since they appear to be the main obstacle in the way of AEMFCs becoming the path toward FCVs that most car owners could afford, i.e., around 10,000 USD. There has been an active program at Daihatsu Motors, in collaboration with several other groups, including the University of New Mexico, to develop such a vehicle, with steady progress being made. The main problem is their short lifetime under fuel cell operating conditions, at present, not much more than 100 h. The strongly alkaline conditions are very harsh for organic materials in general. This area has been reviewed recently [97, 98].

Several representative approaches are shown in Fig. 16 [99–101]. At the University of Yamanashi, we have used a biphenylfluorene moiety as the hydrophilic unit (Fig. 16d) [102].

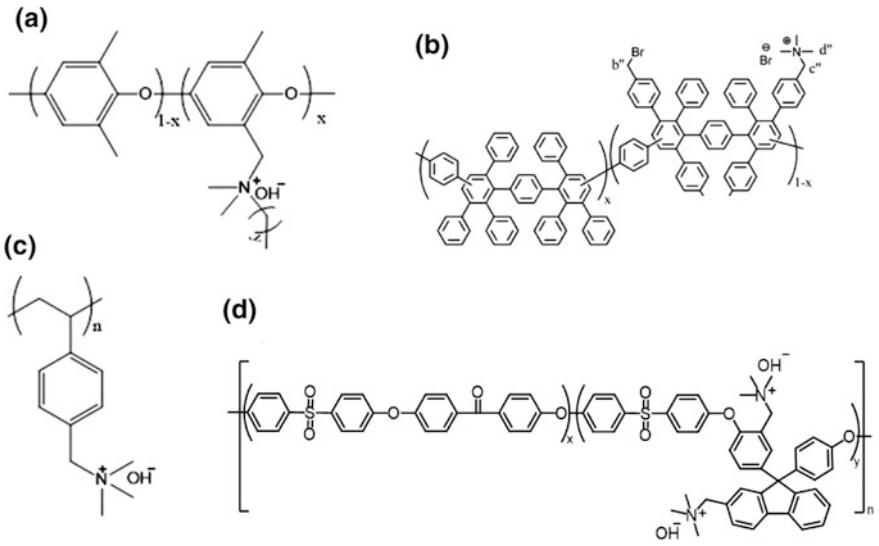

Fig. 16 Representative examples of AEMS based on (**a**) polyphenylene oxide (PPO) [101], (**b**) polyphenylene [99], and **c** polystyrene [100], **d** tetraalkyl ammonium block copolymer QPE-bl-1 [102]

5 Structures

5.1 Catalyst Layers

In their book, Bockris and Reddy describe some of the early work in their laboratory on porous electrodes, the three-phase boundary (TPB), i.e., electrons in the solid phase, gas phase reactants and products, and ions in the liquid-like ionomeric phase, and the importance of the electrolyte meniscus [8]. Much of this work had been carried out by Bockris's doctoral student Boris Cahan [103]. Since that time, much work has been carried out, both experimentally and theoretically, regarding the microstructure of the catalyst layer (CL) and ways to optimize the transport of electrons, gases and ions. Much work has also been carried out to characterize the microstructure, as discussed later.

The meniscus idea is still very useful, because it provides a near-ideal geometry for the transport of ions, gases, and electrons on the macroscopic scale as well as microscopic scale (Fig. 17). The transport of ions and electrons occurs mainly in the vertical direction in this schematic diagram, whereas the transport of gases occurs mainly in the horizontal direction. This is the reason that the gas–liquid or gas–ionomer interface must not be vertical, but must slope from thick at the bottom to thin at the top. The gas transport through the gas phase is very fast compared to that in the liquid or ionomer phase, so that it is beneficial to keep the latter thin, but unfortunately the ionic conductance in the vertical direction would be limited if the layer is too thin. Thus, it is necessary to have some thicker ionic-conducting layers

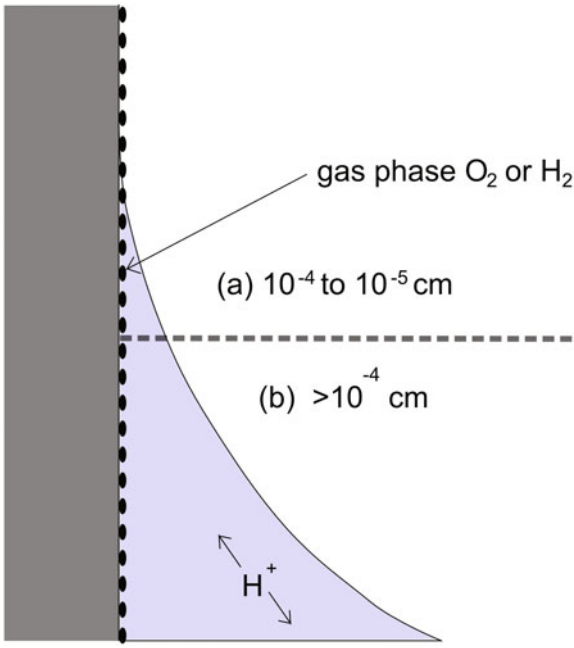

Fig. 17 Schematic diagram of an electrolyte meniscus based on work of Bockris and Cahan [103]. The liquid or polymer electrolyte phase is *light blue*, the electrode is *gray*, with *black* catalyst particles, and the gas phase is *white*. **a** Shows the narrow region from 10^{-5} to 10^{-4} cm from the tip of the meniscus, in which 90% of the current flows, while in (**b**) $>10^{-4}$ cm, only 10% flows (See color figure online)

nearer to the membrane for good ionic conductance and some thin layers for good gas mass transport further away from the membrane; this is essentially a meniscus-like geometry. Bockris and Cahan estimated that a large percentage (>90%) of the current would flow in a very narrow region close to the tip of the meniscus [103–105]. They also estimated that at least 90% of the electrode surface would be wasted in this arrangement, as shown diagrammatically in Fig. 17.

Further work was carried out on this topic after Bockris moved to Texas A&M, and colleagues Appleby and Srinivasan were also involved with the Center for Electrochemical Systems. The insight provided by the meniscus model allowed this team to significantly decrease the Pt loading in the cathode CL. This work was important in the eventual success of efforts at Ballard in Canada in developing their initial fuel cells.

Along these lines, work in the Eikerling group at Simon Fraser University [104–106], and our group at the University of Yamanashi, initially targeted toward PAFCs and later to PEFCs [22, 107–113] as well as other groups has been carried out to try to increase the utilization and effectiveness of the catalyst by optimizing the CL microstructure. Also, along these lines, there was early work carried out on the benefits of uniform dispersion of Pt nanoparticles in order to enhance mass transport [113]. This work was especially interesting, because it provided a way to increase the performance of CLs with small nanoparticles. Efforts have continued to optimize the CL structure and ionomer distribution, based on the meniscus idea, as shown in Fig. 18 [111].

There have also been numerous theoretical (modeling) studies devoted to understanding and optimizing CL microstructure [114]. It has become possible to

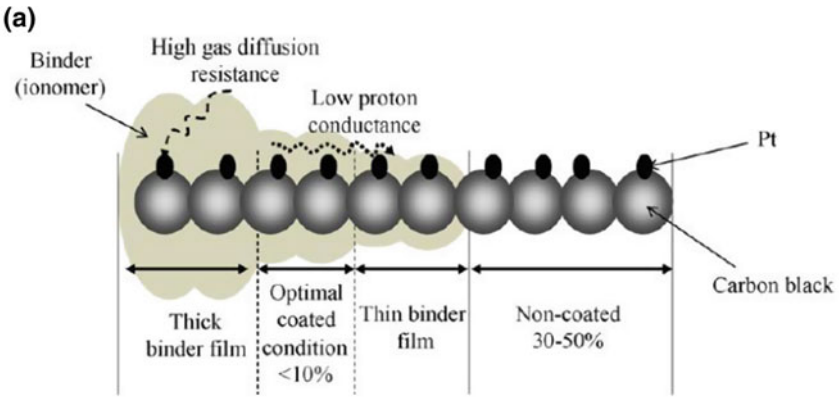

(b)

		Case 1	Case 2	Case 3	Case 4
Concepts		Ionomer; Pt particlenot in ionic contact	Proton Conductance is very low; Gas diffusion resistance is low	Proton Conductance is optimal; Gas diffusion resistance is optimal	Proton Conductance is high; Gas diffusion resistance is very high
Contribution rate	U_{Pt}	None	High	High	High
	Ef_{Pt}	None	Low	High	Low

Fig. 18 Schematic depiction of **a** the variation of Nafion film thickness with depth within the catalyst layer; **b** variations of the Nafion film thickness in the catalyst layer on carbon support particles with Pt deposited nanoparticles and Nafion films, showing the difference between the effectiveness of proton conduction versus gas diffusion through the film [111]. U_{Pt} is utilization of Pt, and Ef_{Pt} is the effectiveness of Pt (reprinted from Ref. [111] with permission from Elsevier)

model fuel cell performance to a high degree. Recent efforts have been devoted to modeling low Pt loadings, which are necessary for cost reduction [44]. One of the problems with modeling in general is that it is quite difficult to obtain detailed experimental characterization results that adequately capture the great complexity of the structure, although much progress has been made [115]. One possible way to improve this situation might be to design and fabricate microstructures in a highly controlled, rational approach [116].

Highly uniform dispersions of monodisperse Pt nanoparticles have also been found to increase the durability of CLs [117]. One reason for this is that Ostwald ripening is suppressed when the particles are all the same size, because all particles undergo equal dissolution and redeposition rates, in principle, although this situation is unstable given sufficient time.

It is highly desirable to fabricate very thin cathode CLs, as pointed out by Bockris and Reddy [10]. However, it is difficult to obtain highly uniform layers.

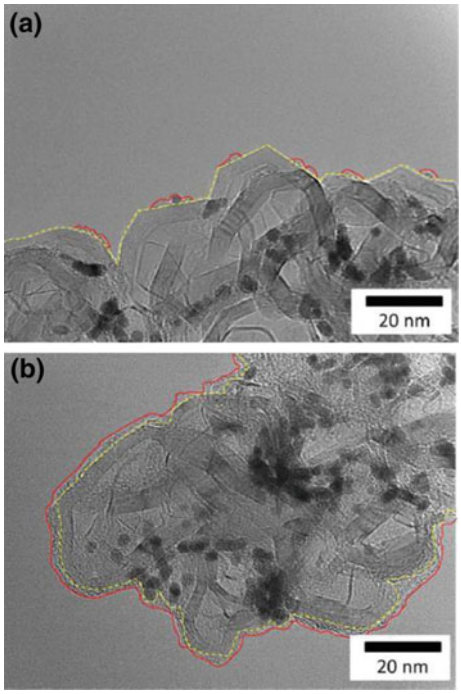

Fig. 19 Morphologies of the ionomer covered on carbon-supported Pt catalysts in the PSS electrode (**a**) and ES electrode (**b**). The *dashed line* indicates the carbon surface, and the *solid line* indicates the ionomer surface [118] (reproduced from Ref. [118], with permission of The Electrochemical Society, Inc.)

Recently in our laboratory, it was found that the electrospray technique is well suited for this task. Interestingly, with this technique, the ionomer layer becomes very uniform in thickness (Fig. 19), and the ohmic resistance and ORR performance is improved [118].

The structure of the CB support particle itself is important for effective gas and proton transport. If there are deep nanopores, for example, it is also difficult to deposit the ionomer, so that Pt particles within these pores might not be effectively utilized. If CB particles without nanopores are used, this problem is avoided (Fig. 20) [119].

6 Characterization and Visualization Methods

It is extremely important to be able to characterize the microstructure of the CLs and other fuel cell components with high resolution, with elemental chemical specificity and under meaningful conditions, perhaps even under operating or "operando" conditions. Clearly, there are tradeoffs that must be made. No single technique can meet all of these requirements simultaneously, but some are very well suited for specific tasks. Combinations of techniques can yield insights that cannot be obtained with single techniques. It is beyond our present scope to review all of this work, but we will simply present some examples from our own work.

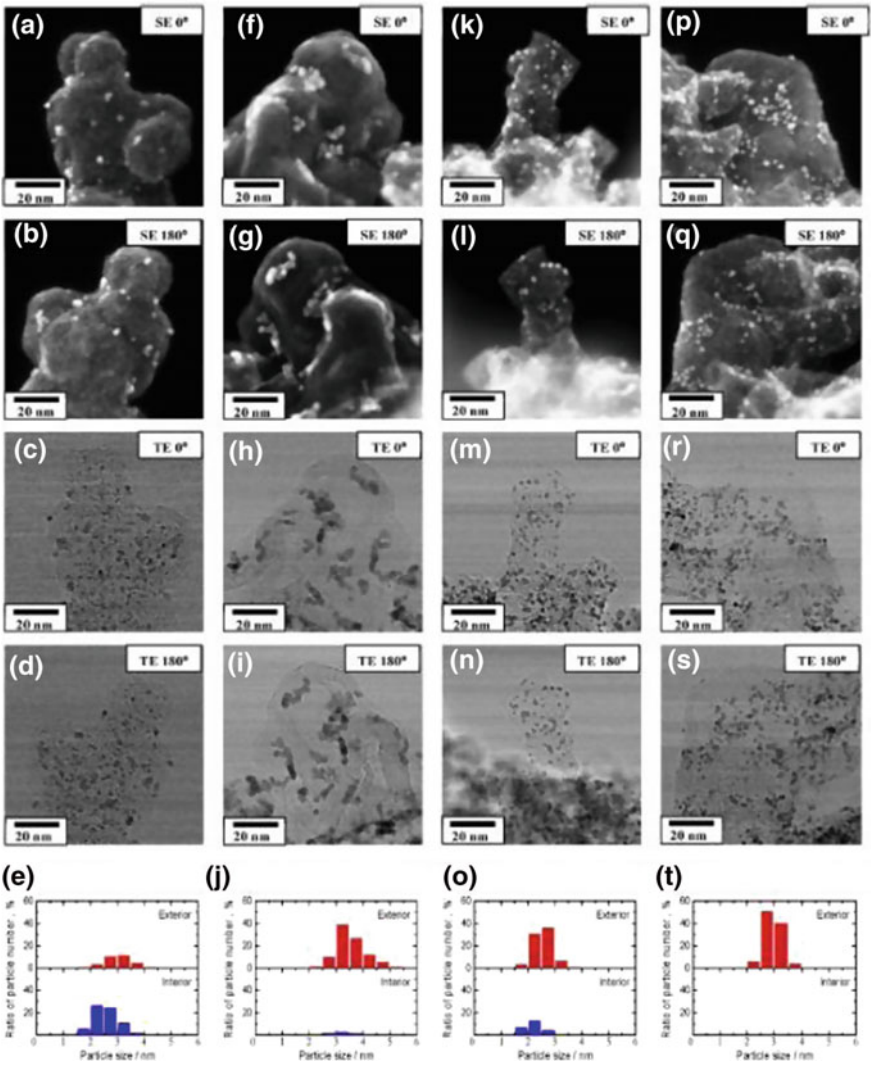

Fig. 20 STEM images and Pt distributions at both interior and exterior surfaces of the carbon-supported Pt catalysts (SE mode, SEM image; TE mode, TEM image): **a** SE mode 0° of c-Pt/CB, **b** SE mode 180° of c-Pt/CB, **c** TE mode 0° of c-Pt/CB, **d** TE mode 180° of c-Pt/CB, **e** Pt distribution of c-Pt/CB, **f** SE mode 0° of c-Pt/GCB, **g** SE mode 180° of c-Pt/GCB, **h** TE mode 0° of c-Pt/GCB, **i** TE mode 180° of c-Pt/GCB, **j** Pt distribution of c-Pt/GCB, **k** SE mode 0° of n-Pt/AB800, **l** SE mode 180° of n-Pt/AB800, **m** TE mode 0° of n-Pt/AB800, **n** TE mode 180° of n-Pt/AB800, **o** Pt distribution of n-Pt/AB800, **p** SE mode 0° of n-Pt/AB250, **q** SE mode 180° of n-Pt/AB250, **r** TE mode 0° of n-Pt/AB250, **s** TE mode 180° of n-Pt/AB250 and **t** Pt distribution of n-Pt/AB250 [119] (reprinted from Ref. [119] with permission from Elsevier)

6.1 Non operando

If one can study the structure of the CL, membrane and other fuel cell components ex situ, one can make use of the full power afforded by vacuum-based techniques, including transmission electron microscopy (TEM), scanning electron microscopy (SEM), scanning transmission electron microscopy (STEM) and X-ray energy dispersive spectroscopy (XREDS). As shown in the previous section, TEM can be very powerful in characterizing catalysts at the near-atomic level. At slightly higher scales, TEM can provide a picture of the agglomerate-pore structure and, with care, even the distribution of ionomer, as shown in Fig. 19. It is even possible to obtain three-dimensional images of catalyst layers, as in an early study carried out at the University of Yamanashi with reconstruction of microtome slices (Fig. 21) [115]. More recently, a similar technique involves focused ion beam (FIB) milling, with which it is possible to visualize the complete pore structure and ionomer distribution.

Recently, through the efforts of people like Kamino of Hitachi, it has become possible to visualize processes occurring in the presence of certain pressures of gases in the TEM [120]. In this way, one can nearly bridge the gap between ex situ and in situ. There have also been efforts to carry out normally vacuum-based spectroscopic techniques like XPS at ambient pressures [121].

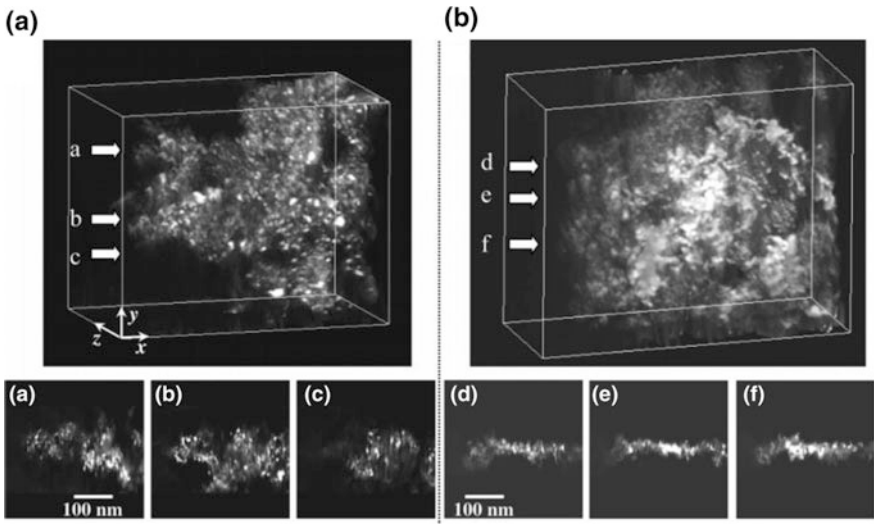

Fig. 21 3D reconstructed images of Ag+-Nafion-Pt/CB (N/C) 0.7 with (**a**) and without (**b**) autoclave treatment. Section images (slices parallel to *x*-*z* plane) perpendicular to the *y*-axis at the locations of *arrows a–f* are shown in panels **a–f**, respectively [115] (reprinted with permission from Ref. 115. Copyright 2006 American Chemical Society)

6.2 Operando

In situ techniques and operando techniques certainly are the wave of the future, although some in situ techniques have been used for a long time. This is an area that

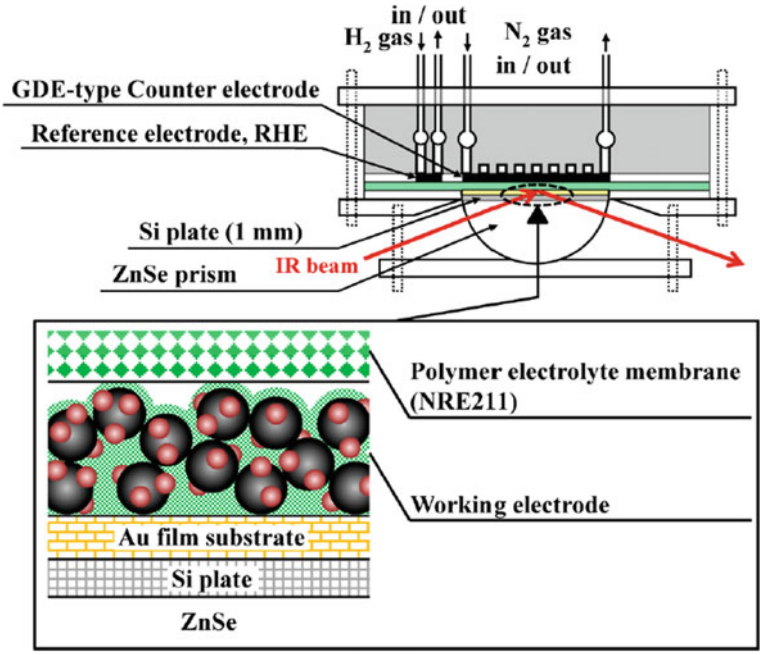

Fig. 22 Experimental setup of the MEA-type cell for the in situ ATR-FTIR measurements at the Nafion–Pt/C and Pt_3Co/C interfaces [127] (reprinted with permission from Ref. [127]. Copyright 2012 American Chemical Society)

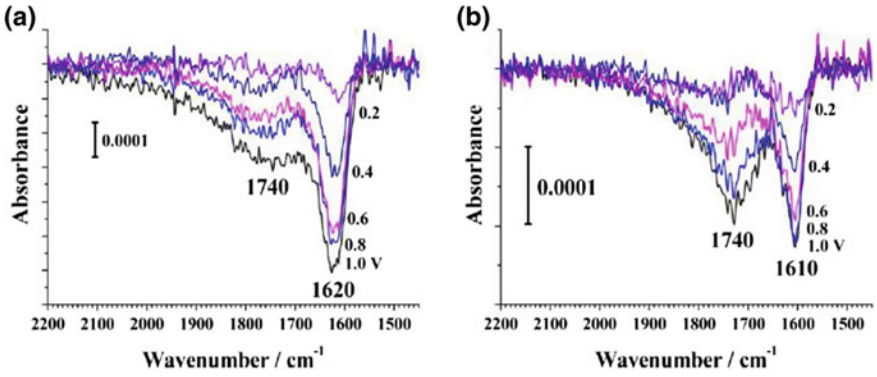

Fig. 23 Changes in ATR-SNIFTIR spectra of the δ(HOH) region obtained at the **a** Nafion–Pt/C and **b** Nafion–Pt_3Co/C interfaces in N_2 atmosphere at 100% RH [127] (reprinted with permission from Ref. [127]. Copyright 2012 American Chemical Society)

was of great interest to Bockris, as described in Modern Electrochemistry 2A [11, 122]. One example is in situ Fourier transform infrared (FTIR) spectroscopy, which was developed initially by Bewick and coworkers at Southampton [122]. This technique was used for smooth, solid electrodes in the beginning, but later, one of Bewick's former colleagues, Kunimatsu started using it for fuel cell catalysts [123], at first in liquid solution [123–125] and finally with a layer of Nafion (Figs. 22, 23) [126, 127]. Kunimatsu also used in situ FTIR to study hydration–dehydration cycles in PEMs [128].

Raman spectroscopy can also be used in situ, also going back to early days on solid electrodes. Recently, it has also been used in operating fuel cells [129]. Raman can allow us to more closely approach operando conditions, because it uses visible

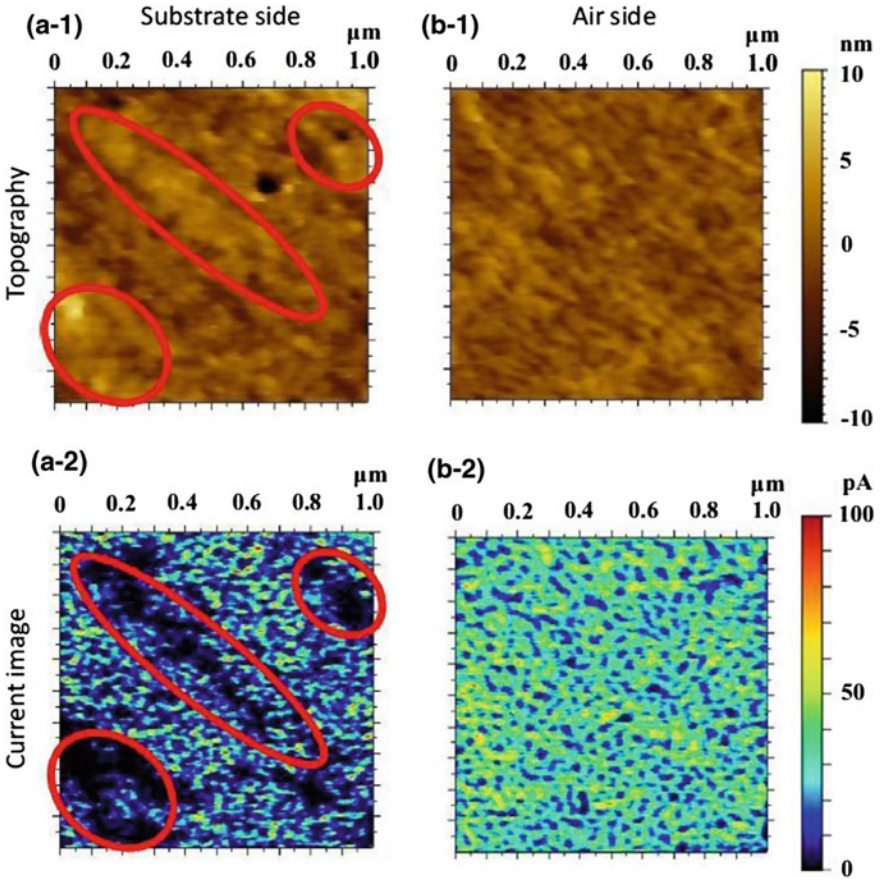

Fig. 24 Surface topographies of the substrate side (**a-1**) and the air side (**b-1**) of a pristine SPK-bl-1 membrane obtained at 50 °C and 40% RH under 5% H_2. Current images were simultaneously obtained on the substrate side (**a-2**) and the air side (**b-2**). Sample bias voltage = 0.6 V [131] (reprinted from Ref. [131] with permission from Elsevier)

light. Hara et al. examined the movement of water through Nafion in an operating mini fuel cell [129].

Another technique that can examine processes occurring on a membrane under operating conditions is current-sensing atomic force microscopy (CSAFM). This technique has been used in our laboratory to compare various types of membranes (Fig. 24) [130, 131]. One can obtain both physical topography and distribution of ion transport simultaneously, for both PEMs and AEMs [132].

On a more macroscopic scale, there have been intense efforts to examine processes in real operating fuel cells. An interesting technique that is well suited to study water transport is neutron imaging, since water has a relatively large cross section for neutron absorption. Much useful information has been obtained this way.

One would also like to image the distribution of O_2 inside the fuel cell. This is more difficult, since O_2 does not have a unique spectroscopic "tag" that can be used conveniently. However, if one employs a dye molecule whose fluorescence is quenched by O_2, it becomes possible to image O_2 indirectly. This strategy has been developed to a high degree by a consortium of researchers from the University of Yamanashi, Waseda University, Keio University, the Shimadzu Corporation, Mizuho Information & Research Institute, and Panasonic [133–135] As an example, we can see how O_2 is depleted along a gas channel during current flow in an actual fuel cell as a function of current, and what happens when the channel becomes plugged with a droplet of product water (Fig. 25). Based on this research, Shimadzu has begun to commercialize a turn-key instrument for this technique (Fig. 26).

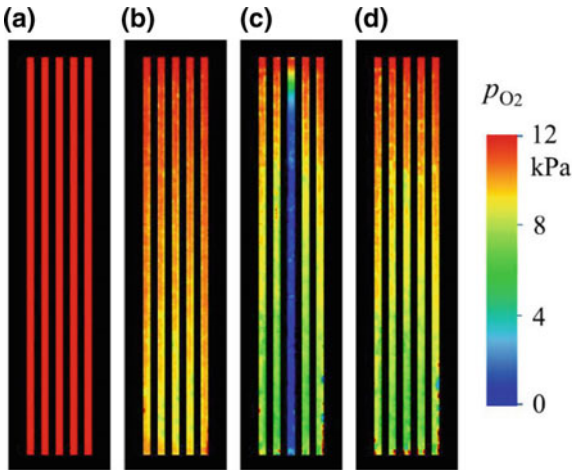

Fig. 25 pO_2 on the GDL surface visualized in an operating PEFC. **a** O_2 utilization U_{O_2}, 0%, Air flow rate, 0.332 dm^3 min^{-1}, **b** U_{O_2}, 15%, Air flow rate, 0.332 dm^3 min^{-1}, **c** U_{O_2}, 30%, Air flow rate, 0.166 dm^3 min^{-1}. Water blockage existed at the end of Channel 3. **d** U_{O_2}, 30%, Air flow rate, 0.166 dm^3 min^{-1}, no water blockage, cell temperature, 80°C; relative humidity, 90%; H_2 flow rate, 0.200 dm^3 min^{-1}; current density, 0.6 A cm^{-2} except (**a**) [134] (reprinted from Ref. [134] with permission from Elsevier)

Fig. 26 Fuel cell visualization system (courtesy of Shimadzu Corp.)

7 Recent Applications

7.1 Automobiles and Other Vehicles

The first known FCV can be traced back to Karl Kordesch, who was working for Union Carbide in the US, which later became Energizer Battery. He fitted his personal car with high pressure H_2 cylinders strapped to the roof in 1970, feeding an alkaline fuel cell, and drove around the Cleveland area in Ohio for 3 years [136, 137]. This system made use of air, from which CO_2 was removed, as well as lead–acid batteries in a hybrid configuration. The design for the fuel cell he used in his car was later adapted to power a General Motors van. Kordesch also favored the use of ammonia as a fuel [138]. Interestingly, in 1967, he also converted a motorcycle to run as a hybrid system with Ni/Cd batteries and a hydrazine fuel cell.

However, it was not until much later that the development of FCVs again became active. The idea was developed to use the PEFC with Nafion, and, almost by accident, work was started at Ballard in Vancouver, Canada, which had previously only worked on batteries [139]. With help from LANL and Texas A&M, they developed PEFCs that could be used in FCVs. As they progressed, they partnered with Daimler and other carmakers to produce FCVs and buses. They are still one of the largest producers of fuel cells in the world and have recently signed an agreement to supply fuel cells for a number of buses in Beijing [140].

An overall plan for the commercialization of FCVs of all types is shown in Fig. 27, in which it is expected that widespread commercialization will be possible starting around 2025, as the Pt loadings decrease below 10 g/100 kW, i.e., approximately the power output of a full-size sedan.

At this moment, there are three models of FCVs that are available commercially, the Honda Clarity-FC, the Hyundai Tuscon and the Toyota Mirai (Fig. 28). The Mirai is currently the only one available for sale, while the other two are only for lease. Mercedes-Benz is also poised to begin releasing an FCV in 2017 [141]. Recently, battery-powered vehicles have become more affordable, higher in performance and longer in range, so that FCVs face some stiff competition in the environmentally friendly car market. FCVs retain two advantages, one being their longer range for the same weight, and their short refueling time, which is essentially the same as that for a gasoline-powered car.

Two of the main disadvantages are the relatively high cost and the lack of hydrogen fueling stations. We have already touched upon some of the efforts to lower costs in this chapter. The hydrogen infrastructure depends upon where one lives. In southern California, one has no problem whatsoever, and if one lives in northern California, the northeastern US, most of Japan and much of Europe, there are already a fair number of stations, with more on the way soon (Fig. 29).

Fig. 27 University of Yamanashi 5-year plan (2015–2020) for research and development of fuel cells, with widespread commercialization possible starting in 2025 (NEDO)

Fig. 28 Examples of fuel cell vehicles that are either being commercialized or are close to being commercialized, from *upper left*, going clockwise: Honda Clarity, Hyundai Tuscon, Toyota Mirai and Ford military vehicle

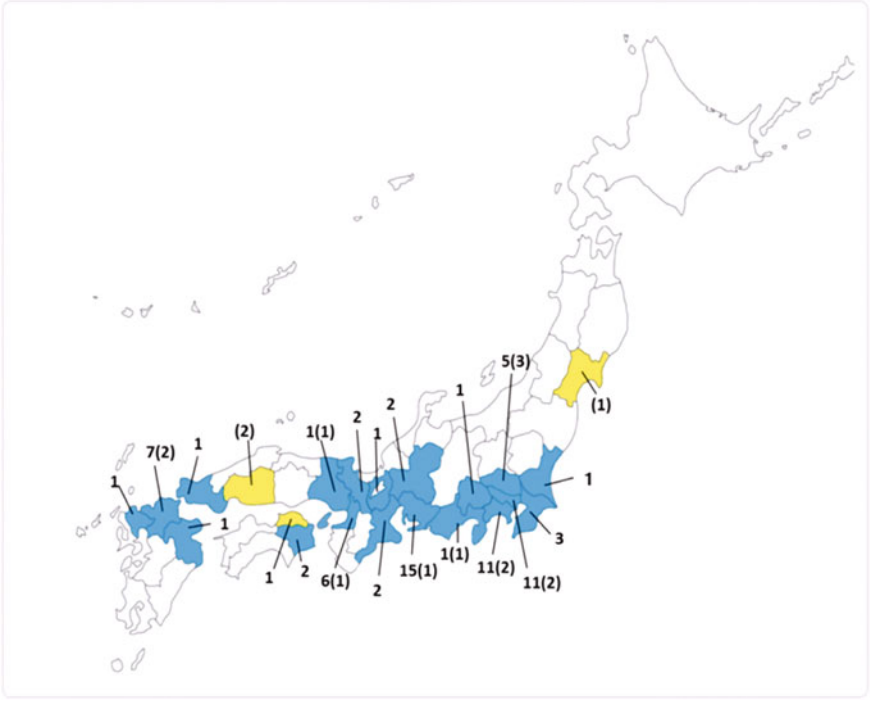

Fig. 29 Hydrogen fueling stations in Japan in operation (ca. 75) as of January 2017 (those planned are in parentheses (ca. 16)) (courtesy of the Fuel Cell Commercialization Congress of Japan)

By 2020, there are plans to have a solar farm-based hydrogen infrastructure in place in the US that is being installed through the Nikola Motor Company, named after Nikola Tesla, the Tesla Company already having taken his last name. The Nikola One is a long distance fuel cell-powered semi-truck with significantly higher power than conventional models (Fig. 30) [142]. In this category, it is the only one we have seen.

We have already mentioned buses, which have been powered by PEFCs for a number of years and continue to be viable. Toyota is planning to deploy PEFC-powered buses with Hino for the 2020 Tokyo Olympics (Fig. 30). Other FCV applications were already envisioned by Bockris but have been slow in being realized, although recently it has been announced that an FCV train will be operating in Germany (Fig. 30). This is a sensible application for more rural areas, which have not been electrified. There has been discussion of powering ferries by fuel cells, but there are so far no firm plans, as far as we know. This will certainly change in the near future. Finally, as mentioned by Bockris and Reddy, fuel cells can even be used to power airplanes. So far, the only examples we know about are small, unmanned versions, but this will also change in the near future.

Fig. 30 Examples of fuel cell vehicles that are being commercialized in the near future, from *upper left*, going clockwise: San Francisco Bay ferry, Nikola One semi-truck, Alstom-Coradia-Ilint train, and Toyota bus

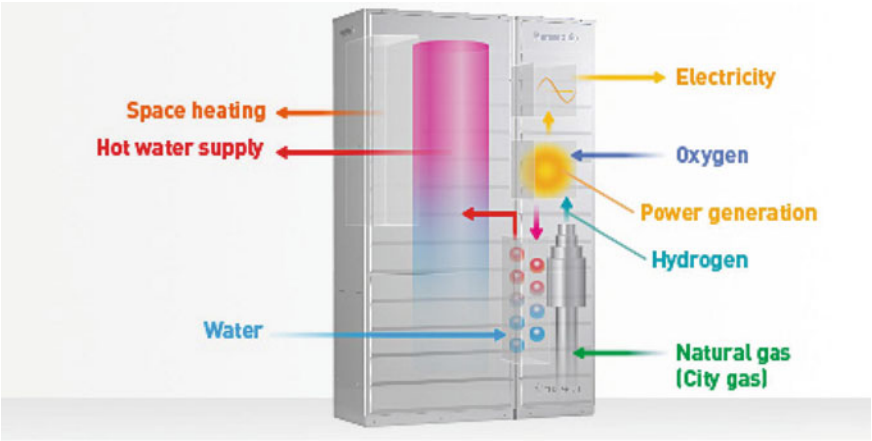

Fig. 31 Schematic diagram of the Ene-Farm residential electric power/water heater unit (courtesy of Panasonic Corp.)

7.2 Residential Fuel Cells

In the area of residential fuel cells, there has also been much activity. We would like to briefly outline the activity in Japan, which was initially planned in 1999 and eventually started in 2005 as a demonstration project that involved several government agencies, including the Ministry of Economy, Trade and Industry (METI) and the New Energy and Industrial Development Organization (NEDO), and several companies, including Toshiba, Panasonic, Tokyo Gas, Osaka Gas and JX Nippon Oil & Energy [143]. As part of this project, about 3000 units combining electric power plus hot water heating were installed in homes around Japan, and their operation was monitored for four years. Energy savings and CO_2 emissions were found to be quite significant. Then, based on the results, as well as cost reductions and improvements in the systems, commercialization was started in 2009 under the brand name "Ene-Farm". These are supplied with natural gas, which is reformed within the system (Fig. 31). Thus far, as of early 2014, there had been over 70,000 units sold. In total, for the SOFC version, 24,119 units have been sold since 2001 and, for the PEFC version, 166,494 units since 1998 in Japan alone.

8 Future Directions

There are many topics that we have neglected in this brief overview due to space-time constraints. These include direct alcohol fuel cells, biofuel cells, microbial fuel cells and many others, which will become increasingly important as they are developed. Other, related topics include clean hydrogen production and

storage, which are also extremely important for the realization of the hydrogen economy or hydrogen society. Increasing concerns about climate change and environmental pollution will motivate people to work on these problems.

Also, our increasingly information-driven society is going to demand more electric power per person, including mobile power. Thus, smaller mobile fuel cells should be developed. Initial efforts in this direction have not resulted in widespread usage, but this could well change, because there certainly has been some interesting technology that has already been developed.

Finally, we would like to once again salute John O'Mara Bockris for his vision and enthusiasm in pursuing research related to fuel cells and many other topics. These qualities, plus his fearless independence, led him into controversial areas toward the end of his career, specifically, his work on cold fusion, or low-energy nuclear reactions, as it is now termed. We would like to support such independence of scientific spirit, because it will be a much-needed quality for the next generation of scientists and engineers.

Acknowledgements The authors wish would like to express gratitude for financial support via several National projects, including those from the Ministry of Education, Culture, Sports, Science and Technology (MEXT) of Japan, and from the New Energy and Industrial Technology Development Organization (NEDO) of Japan for the projects "Nanotechnology for High Performance Fuel Cells" and "Superlative, Stable, and Scalable Performance Fuel Cells." We also would like to express great appreciation of the contributions of Professors Hiroyuki Uchida, Kenji Miyatake, Makoto Uchida, Kazutoshi Higashiyama, Tomio Omata, Shigehito Deki, Junji Inukai, Hiroshi Yano, Katsuyoshi Kakinuma, Toshiro Miyao, Takao Tsuneda, Mitsuru Wakisaka, Masanori Hara, Kiyoshi Yagi, Keiji Kunimatsu and Takeo Kamino, as well as many students and researchers.

References

1. Bockris JOM, Srinivasan S (1969) Fuel cells: their electrochemistry. McGraw-Hill, New York
2. Bockris JOM, Reddy AKN (1970) Modern electrochemistry: an introduction to an interdisciplinary area, vol 1. Springer, US, New York
3. Bockris JOM, Reddy AKN (1970) Modern electrochemistry: an introduction to an interdisciplinary area, vol 2. Springer, US, New York
4. Bockris JOM (ed) (1972) Electrochemistry of cleaner environments. Springer US, New York. doi:10.1007/978-1-4684-1950-4
5. Bockris JOM, Fredlein RA (1973) A workbook of electrochemistry. Springer US, New York. doi:10.1007/978-1-4613-4562-6
6. Bockris JOM, Nagy Z (1974) Electrochemistry for ecologists. Springer US, New York. doi:10.1007/978-1-4684-2058-6
7. Fujishima A, Honda K (1972) Electrochemical photolysis of water at a semiconductor electrode. Nature 238(5358):37–38. doi:10.1038/238037a0
8. Bockris JOM, Reddy AKN (1970) Some electrochemical systems of technological interest. Modern electrochemistry: an introduction to an interdisciplinary area, vol 2, 1st edn. Springer, US, New York, pp 1265–1432

9. Grove WR (1839) XXIV. On voltaic series and the combination of gases by platinum. Philos Mag 3 14(86–87):127–130. doi:10.1080/14786443908649684
10. Bockris JOM, Reddy AKN (2000) Modern electrochemistry 2B: electrodics in chemistry, engineering, biology, and environmental science. Springer, US, New York
11. Bockris JOM, Reddy AKN, Gamboa-Aldeco M (2000) Modern electrochemistry 2A: fundamentals of electrodics. Springer, US, New York
12. Bockris JOM, Reddy AKN (2000) Conversion and storage of electrochemical energy. Modern electrochemistry 2B: electrodics in chemistry, engineering, biology, and environmental science. Springer, US, New York, pp 1789–1901
13. Jalan VM, Landsman DA (1980) Noble metal-refractory metal alloys as catalysts and method for making. US Patent 4,186,110, 29 Jan 1980
14. Landsman DA, Luczak FJ (1982) Noble metal-chromium alloy catalysts and electrochemical cell. US Patent 4,316,944, 23 Feb 1982
15. Luczak FJ, Landsman DA (1984) Ternary fuel cell catalysts containing platinum, cobalt and chromium. USA Patent US Patent 4,447,506, 8 May 1984
16. Luczak FJ, Landsman DA (1987) Ordered ternary fuel cell catalysts containing platinum and cobalt and method for making the catalysts. USA Patent US Patent 4,677,092, 30 Jun 1987
17. Watanabe M, Uchida M, Motoo S (1987) Preparation of highly dispersed Pt + Ru alloy clusters and the activity for the electrooxidation of methanol. J Electroanal Chem Interfac Electrochem 229(1–2):395–406. doi:10.1016/0022-0728(87)85156-2
18. Watanabe M, Tsurumi K, Mizukami T, Nakamura T, Stonehart P (1994) Activity and stability of ordered and disordered Co-Pt alloys for phosphoric acid fuel cells. J Electrochem Soc 141(10):2659–2668. doi:10.1149/1.2059162
19. Toda T, Igarashi H, Watanabe M (1998) Role of electronic property of Pt and Pt alloys on electrocatalytic reduction of oxygen. J Electrochem Soc 145(12):4185–4188. doi:10.1149/1.1838934
20. Toda T, Igarashi H, Uchida H, Watanabe M (1999) Enhancement of the electroreduction of oxygen on Pt alloys with Fe, Ni, and Co. J Electrochem Soc 146(10):3750–3756. doi:10.1149/1.1392544
21. Toda T, Igarashi H, Watanabe M (1999) Enhancement of the electrocatalytic O_2 reduction on Pt-Fe alloys. J Electroanal Chem 460(1–2):258–262. doi:10.1016/S0022-0728(98)00361-1
22. Watanabe M, Makita K, Usami H, Motoo S (1986) New preparation method of a high performance gas diffusion electrode working at 100% utilization of catalyst clusters and analysis of the reaction layer. J Electroanal Chem 197(1–2):195–208. doi:10.1016/0022-0728(86)80149-8
23. Nishida R, Puengjinda P, Nishino H, Kakinuma K, Brito ME, Watanabe M, Uchida H (2014) High-performance electrodes for reversible solid oxide fuel cell/solid oxide electrolysis cell: Ni-Co dispersed ceria hydrogen electrodes. RSC Adv 4(31):16260–16266. doi:10.1039/C3RA47089J
24. Bockris JOM (2011) An electrochemical life. J Solid State Electrochem 15:1763. doi:10.1007/s10008-011-1298-7
25. Baranton S, Uchida H, Tryk DA, Dubois JL, Watanabe M (2013) Hydrolyzed polyoxymethylenedimethylethers as liquid fuels for direct oxidation fuel cells. Electrochim Acta 108:350–355. doi:10.1016/j.electacta.2013.06.138
26. Watanabe M, Stonehart P, Tsurumi K, Yamamoto N, Hara N, Nakamura T (1993) Electrocatalyst and process of preparing same. US Patent 5,189,005, 23 Feb 1993
27. Markovic NM, Schmidt TJ, Stamenkovic V, Ross PN (2001) Oxygen reduction reaction on Pt and Pt bimetallic surfaces: a selective review. Fuel Cells 1(2):105–116. doi:10.1002/1615-6854(200107)1:2<105:AID-FUCE105>3.0.CO;2-9
28. Paulus UA, Wokaun A, Scherer GG, Schmidt TJ, Stamenkovic V, Markovic NM, Ross PN (2002) Oxygen reduction on high surface area Pt-based alloy catalysts in comparison to well defined smooth bulk alloy electrodes. Electrochim Acta 47(22–23):3787–3798. doi:10.1016/S0013-4686(02)00349-3

29. Stamenkovic V, Schmidt TJ, Ross PN, Markovic NM (2002) Surface composition effects in electrocatalysis: kinetics of oxygen reduction on well-defined Pt_3Ni and Pt_3Co alloy surfaces. J Phys Chem B 106(46):11970–11979. doi:10.1021/jp021182h
30. Xu Y, Ruban AV, Mavrikakis M (2004) Adsorption and dissociation of O_2 on Pt-Co and Pt-Fe alloys. J Am Chem Soc 126:4717–4725. doi:10.1021/ja031701+
31. Kitchin JR, Norskov JK, Barteau MA, Chen JG (2004) Modification of the surface electronic and chemical properties of Pt(111) by subsurface 3d transition metals. J Chem Phys 120 (21):10240–10246. doi:10.1063/1.1737365
32. Wakisaka M, Mitsui S, Hirose Y, Kawashima K, Uchida H, Watanabe M (2006) Electronic structures of Pt-Co and Pt-Ru alloys for CO-tolerant anode catalysts in polymer electrolyte fuel cells studied by EC-XPS. J Phys Chem B 110(46):23489–23496. doi:10.1021/jp0653510
33. Nilsson A, Hasselström J, Föhlisch A, Karis O, Pettersson LGM, Nyberg M, Triguero L (2000) Probing chemical bonding in adsorbates using X-ray emission spectroscopy. J Electron Spectrosc Relat Phenom 110–111:15–39. doi:10.1016/s0368-2048(00)00155-9
34. Medford AJ, Vojvodic A, Hummelshøj JS, Voss J, Abild-Pedersen F, Studt F, Bligaard T, Nilsson A, Nørskov JK (2015) From the Sabatier principle to a predictive theory of transition-metal heterogeneous catalysis. J Catal 328:36–42. doi:10.1016/j.jcat.2014.12.033
35. Wakisaka M, Suzuki H, Mitsui S, Uchida H, Watanabe M (2008) Increased oxygen coverage at Pt-Fe alloy cathode for the enhanced oxygen reduction reaction studied by EC-XPS. J Phys Chem C 112(7):2750–2755. doi:10.1021/jp0766499
36. Watanabe M, Wakisaka M, Yano H, Uchida H (2008) Analyses of oxygen reduction reaction at Pt-based electrocatalysts. ECS Trans 16(2):199–206. doi:10.1149/1.2981855
37. Wakisaka M, Watanabe M, Uchida H (2010) Mechanism of an enhanced oxygen reduction reaction at platinum-based electrocatalysts: identification and quantification of oxygen species adsorbed on electrodes by X-ray photoelectron spectroscopy. In: Wieckowski A, Nørskov JK (eds) Fuel cell science: theory, fundamentals, and biocatalysis. Wiley, Hoboken, NJ, USA, pp 147–168. doi:10.1002/9780470630693.ch4
38. Uchida H, Yano H, Wakisaka M, Watanabe M (2011) Electrocatalysis of the oxygen reduction reaction at Pt and Pt-alloys. Electrochemistry 79(5):303–311
39. Wakisaka M, Udagawa Y, Suzuki H, Uchida H, Watanabe M (2011) Structural effects on the surface oxidation processes at Pt single-crystal electrodes studied by X-ray photoelectron spectroscopy. Energy Env Sci 4:1662–1666. doi:10.1039/C0EE00756K
40. Wakisaka M, Kobayashi S, Morishima S, Hyuga Y, Tryk DA, Watanabe M, Iiyama A, Uchida H (2016) Unprecedented dependence of the oxygen reduction activity on Co content at Pt skin/Pt-Co(111) single crystal electrodes. Electrochem Commun 67:47–50. doi:10.1016/j.elecom.2016.03.015
41. Omura J, Yano H, Tryk DA, Watanabe M, Uchida H (2014) Electrochemical quartz crystal microbalance analysis of the oxygen reduction reaction on Pt-based electrodes. Part 2: adsorption of oxygen species and ClO_4^- anions on Pt and Pt–Co alloy in $HClO_4$ solutions. Langmuir 30(1):432–439. doi:10.1021/la404188p
42. Wakisaka M, Hyuga Y, Abe K, Uchida H, Watanabe M (2011) Facile preparation and electrochemical behavior of $Pt_{100-x}Co_x(111)$ single-crystal electrodes in 0.1 M $HClO_4$. Electrochem Commun 13(4):317–320. doi:10.1016/j.elecom.2011.01.013
43. Watanabe M, Yano H, Tryk DA, Uchida H (2016) Highly durable and active PtCo alloy/graphitized carbon black cathode catalysts by controlled deposition of stabilized Pt skin layers. J Electrochem Soc 163(6):F455–F463. doi:10.1149/2.0331606jes
44. Yoon W, Weber AZ (2011) Modeling low-platinum-loading effects in fuel-cell catalyst layers. J Electrochem Soc 158(8):B1007–B1018. doi:10.1149/1.3597644
45. Hossain MS, Tryk D, Yeager E (1989) The electrochemistry of graphite and modified graphite surfaces: the reduction of O_2. Electrochim Acta 34:1733–1737. doi:10.1016/0013-4686(89)85057-1

46. Masa J, Xia W, Muhler M, Schuhmann W (2015) On the role of metals in nitrogen-doped carbon electrocatalysts for oxygen reduction. Angew Chem Int Ed 54(35):10102–10120. doi:10.1002/anie.201500569
47. Gupta S, Tryk D, Bae I, Aldred W, Yeager E (1989) Heat-treated polyacrylonitrile-based catalysts for oxygen electroreduction. J Appl Electrochem 19:19–27. doi:10.1007/BF01039385
48. Zhu Y, Zhang B, Liu X, Wang D-W, Su DS (2014) Unravelling the structure of electrocatalytically active Fe–N complexes in carbon for the oxygen reduction reaction. Angew Chem Int Ed 53(40):10673–10677. doi:10.1002/anie.201405314
49. Zagal JH, Koper MTM (2016) Reactivity descriptors for the activity of molecular MN_4 catalysts for the oxygen reduction reaction. Angew Chem Int Ed 55(47):14510–14521. doi:10.1002/anie.201604311
50. Watanabe M, Motoo S (1975) Electrocatalysis by ad-atoms: Part III. Enhancement of the oxidation of carbon monoxide on platinum by ruthenium ad-atoms. J Electroanal Chem 60 (3):275–283. doi:10.1016/S0022-0728(75)80262-2
51. Watanabe M, Motoo S (1976) Oxidation of CO-H_2 gas mixtures on Ru electrodes and Pt with Ru and As adatoms (in Japanese). Denki Kagaku 44:602–607
52. Ross PN (1992) Trends in the bonding of CO to the surfaces of Pt3M alloys (M = Ti Co, and Sn). J Vac Sci Technol A: Vacuum Surf Films 10(4):2546–2550. doi:10.1116/1.578096
53. Igarashi H, Fujino T, Zhu Y, Uchida H, Watanabe M (2001) CO tolerance of Pt alloy electrocatalysts for polymer electrolyte fuel cells and the detoxification mechanism. Phys Chem Chem Phys 3(3):306–314. doi:10.1039/B007768M
54. Arenz M, Stamenkovic V, Blizanac BB, Mayrhofer KJ, Markovic NM, Ross PN (2005) Carbon-supported Pt-Sn electrocatalysts for the anodic oxidation of H_2, CO, and H_2/CO mixtures: part II: the structure-activity relationship. J Catal 232(2):402–410. doi:10.1016/j.jcat.2005.03.022
55. Shi G, Yano H, Tryk DA, Watanabe M, Iiyama A, Uchida H (2016) A novel Pt-Co alloy hydrogen anode catalyst with superlative activity, CO-tolerance and robustness. Nanoscale 8 (29):13893–13897. doi:10.1039/c6nr00778c
56. Shi G, Yano H, Tryk DA, Iiyama A, Uchida H (2017) Highly active, CO-tolerant, and robust hydrogen anode catalysts: Pt-M(M = Fe Co, Ni) alloys with stabilized Pt-skin layers. ACS Catal 7(1):267–274. doi:10.1021/acscatal.6b02794
57. Strmcnik D, Uchimura M, Wang C, Subbaraman R, Danilovic N, van der Vliet D, Paulikas AP, Stamenkovic VR, Markovic NM (2013) Improving the hydrogen oxidation reaction rate by promotion of hydroxyl adsorption. Nat Chem 5(4):300–306. doi:10.1038/nchem.1574
58. Durst J, Siebel A, Simon C, Hasche F, Herranz J, Gasteiger HA (2014) New insights into the electrochemical hydrogen oxidation and evolution reaction mechanism. Energy Env Sci 7 (7):2255–2260. doi:10.1039/C4EE00440J
59. Wang Y, Wang G, Li G, Huang B, Pan J, Liu Q, Han J, Xiao L, Lu J, Zhuang L (2015) Pt-Ru catalyzed hydrogen oxidation in alkaline media: oxophilic effect or electronic effect? Energy Env Sci 8(1):177–181. doi:10.1039/C4EE02564D
60. Sheng W, Bivens AP, Myint M, Zhuang Z, Forest RV, Fang Q, Chen JG, Yan Y (2014) Non-precious metal electrocatalysts with high activity for hydrogen oxidation reaction in alkaline electrolytes. Energy Env Sci 7(5):1719–1724. doi:10.1039/C3EE43899F
61. Miller HA, Lavacchi A, Vizza F, Marelli M, Di Benedetto F, D'Acapito F, Paska Y, Page M, Dekel DR (2016) A Pd/C-CeO_2 anode catalyst for high-performance platinum-free anion exchange membrane fuel cells. Angew Chem Int Ed 55(20):6004–6007. doi:10.1002/anie.201600647
62. Serov A, Padilla M, Roy AJ, Atanassov P, Sakamoto T, Asazawa K, Tanaka H (2014) Anode catalysts for direct hydrazine fuel cells: from laboratory test to an electric vehicle. Angew Chem Int Ed 53(39):10336–10339. doi:10.1002/anie.201404734

63. Jeon T-Y, Watanabe M, Miyatake K (2014) Carbon segregation-induced highly metallic Ni nanoparticles for electrocatalytic oxidation of hydrazine in alkaline media. ACS Appl Mater Interfaces 6(21):18445–18449. doi:10.1021/am5058635
64. Shao Y, Liu J, Wang Y, Lin Y (2009) Novel catalyst support materials for PEM fuel cells: current status and future prospects. J Mater Chem 19(1):46–59. doi:10.1039/B808370C
65. Yano H, Kataoka M, Yamashita H, Uchida H, Watanabe M (2007) Oxygen reduction activity of carbon-supported Pt-M (M = V, Ni, Cr Co, and Fe) alloys prepared by nanocapsule method. Langmuir 23(11):6438–6445. doi:10.1021/la070078u
66. Chen M, Nikles DE (2002) Synthesis, self-assembly, and magnetic properties of $Fe_xCo_yPt_{100-x-y}$ nanoparticles. Nano Lett 2(3):211–214. doi:10.1021/nl015649w
67. Sun S, Anders S, Thomson T, Baglin JEE, Toney MF, Hamann HF, Murray CB, Terris BD (2003) Controlled synthesis and assembly of FePt nanoparticles. J Phys Chem B 107 (23):5419–5425. doi:10.1021/jp027314o
68. Yano H, Akiyama T, Uchida H, Watanabe M (2010) Temperature dependence of oxygen reduction activity at Nafion-coated Pt/graphitized carbon black catalysts prepared by the nanocapsule method. Energy Environ Sci 3(10). doi:10.1039/C0EE00106F
69. Yano H, Akiyama T, Bele P, Uchida H, Watanabe M (2010) Durability of Pt/graphitized carbon catalysts for the oxygen reduction reaction prepared by the nanocapsule method. Phys Chem Chem Phys 12(15):3806–3814. doi:10.1039/B923460H
70. Yano H, Akiyama T, Watanabe M, Uchida H (2013) High durability of Pt/graphitized carbon catalysts for polymer electrolyte fuel cells prepared by the nanocapsule method. J Electroanal Chem 688:137–142. doi:10.1016/j.jelechem.2012.09.028
71. Yano H, Song JM, Uchida H, Watanabe M (2008) Temperature dependence of oxygen reduction activity at carbon-supported Pt_xCo (x = 1, 2, and 3) alloy catalysts prepared by the nanocapsule method. J Phys Chem C 112(22):8372–8380. doi:10.1021/jp712025q
72. Okaya K, Yano H, Uchida H, Watanabe M (2010) Control of particle size of Pt and Pt alloy electrocatalysts supported on carbon black by the nanocapsule method. ACS Appl Mater Interf 2(3):888–895. doi:10.1021/am9008693
73. Wang J, Swain GM (2003) Fabrication and evaluation of platinum/diamond composite electrodes for electrocatalysis—preliminary studies of the oxygen-reduction reaction. J Electrochem Soc 150(1):E24–E32. doi:10.1149/1.1524612
74. Spataru N, Zhang XT, Spataru T, Tryk DA, Fujishima A (2008) Platinum electrodeposition on conductive diamond powder and its application to methanol oxidation in acidic media. J Electrochem Soc 155(3):B264–B269. doi:10.1149/1.2830857
75. La-Torre-Riveros L, Abel-Tatis E, Mendez-Torres AE, Tryk DA, Prelas M, Cabrera CR (2011) Synthesis of platinum and platinum-ruthenium-modified diamond nanoparticles. J Nanopart Res 13(7):2997–3009. doi:10.1007/s11051-010-0196-8
76. La-Torre-Riyeros L, Guzman-Bas R, Mendez-Torres AE, Prelas M, Tryk DA, Cabrera CR (2012) Diamond nanoparticles as a support for Pt and PtRu catalysts for direct methanol fuel cells. ACS Appl Mater Interf 4(2):1134–1147. doi:10.1021/am2018628
77. LaTorre-Riveros L, Tryk DA, Cabrera CR (2005) Chemical purification and characterization of diamond nanoparticles for electrophoretically coated electrodes. Rev Adv Mater Sci 3 (10):256–260
78. Chen G, Bare SR, Mallouk TE (2002) Development of supported bifunctional electrocatalysts for unitized regenerative fuel cells. J Electrochem Soc 149(8):A1092–A1099. doi:10.1149/1.1491237
79. Shintani H, Kojima Y, Kakinuma K, Watanabe M, Uchida M (2015) Novel strategy to mitigate cathode catalyst degradation during air/air startup cycling via the atmospheric resistive switching mechanism of a hydrogen anode with a platinum catalyst supported on tantalum-doped titanium dioxide. J Power Sources 294:292–298. doi:10.1016/j.jpowsour.2015.06.072
80. Parrondo J, Han T, Niangar E, Wang C, Dale N, Adjemian K, Ramani V (2014) Platinum supported on titanium–ruthenium oxide is a remarkably stable electrocatayst for hydrogen fuel cell vehicles. PNAS 111(1):45–50. doi:10.1073/pnas.1319663111

81. Chhina H, Campbell S, Kesler O (2006) An oxidation-resistant indium tin oxide catalyst support for proton exchange membrane fuel cells. J Power Sources 161(2):893–900. doi:10.1016/j.jpowsour.2006.05.014
82. Senoo Y, Kakinuma K, Uchida M, Uchida H, Deki S, Watanabe M (2014) Improvements in electrical and electrochemical properties of Nb-doped $SnO_{2-\delta}$ supports for fuel cell cathodes due to aggregation and Pt loading. RSC Adv 4(61):32180–32188. doi:10.1039/C4RA03988B
83. Chino Y, Kakinuma K, Tryk DA, Watanabe M, Uchida M (2016) Influence of Pt loading and cell potential on the HF ohmic resistance of an Nb-doped SnO_2-supported Pt cathode for PEFCs. J Electrochem Soc 163(2):F97–F105. doi:10.1149/2.0571602jes
84. Chino Y, Taniguchi K, Senoo Y, Kakinuma K, Hara M, Watanabe M, Uchida M (2015) Effect of added graphitized CB on both performance and durability of Pt/Nb-SnO_2 cathodes for PEFCs. J Electrochem Soc 162(7):F736–F743. doi:10.1149/2.0651507jes
85. Senoo Y, Taniguchi K, Kakinuma K, Uchida M, Uchida H, Deki S, Watanabe M (2015) Cathodic performance and high potential durability of Ta-$SnO_{2-\delta}$-supported Pt catalysts for PEFC cathodes. Electrochem Commun 51:37–40. doi:10.1016/j.elecom.2014.12.005
86. Chiwata M, Kakinuma K, Wakisaka M, Uchida M, Deki S, Watanabe M, Uchida H (2015) Oxygen reduction reaction activity and durability of Pt catalysts supported on titanium carbide. Catalysts 5(2):966–980. doi:10.3390/catal5020966
87. Shintani H, Kakinuma K, Uchida H, Watanabe M, Uchida M (2015) Performance of practical-sized membrane-electrode assemblies using titanium nitride-supported platinum catalysts mixed with acetylene black as the cathode catalyst layer. J Power Sources 280:593–599. doi:10.1016/j.jpowsour.2015.01.132
88. Miyatake K (2015) Membrane electrolytes, from perfluorosulfonic acid (PFSA) to hydrocarbon ionomers. In: Meyers RA (ed) Encyclopedia of sustainability science and technology. Springer Science + Business Media, New York, pp 1–32. doi:10.1007/978-1-4939-2493-6_146-3
89. Singh RK, Tsuneda T, Miyatake K, Watanabe M (2014) Theoretical investigation of local proton conductance in the proton exchange membranes. Chem Phys Lett 608:11–16. doi:10.1016/j.cplett.2014.05.076
90. Singh RK, Kunimatsu K, Miyatake K, Tsuneda T (2016) Experimental and theoretical infrared spectroscopic study on hydrated Nafion membrane. Macromolecules 49(17):6621–6629. doi:10.1021/acs.macromol.6b00999
91. Asano N, Aoki M, Suzuki S, Miyatake K, Uchida H, Watanabe M (2006) Aliphatic/aromatic polyimide ionomers as a proton conductive membrane for fuel cell applications. J Am Chem Soc 128(5):1762–1769. doi:10.1021/ja0571491
92. Tian S, Meng Y, Hay AS (2009) Membranes from poly(aryl ether)-based ionomers containing randomly distributed nanoclusters of 6 or 12 sulfonic acid groups. Macromolecules 42:1153–1160. doi:10.1021/ma802456m
93. Bae B, Yoda T, Miyatake K, Uchida H, Watanabe M (2010) Proton-conductive aromatic ionomers containing highly sulfonated blocks for high-temperature-operable fuel cells. Angew Chem Int Ed 49(2):317–320. doi:10.1002/anie.200905355
94. Savinell R, Yeager E, Tryk D, Landau U, Wainright J, Weng D, Lux K, Litt M, Rogers C (1994) A polymer electrolyte for operation at temperatures up to 200 °C. J Electrochem Soc 141(4):L46–L48. doi:10.1149/1.2054875
95. Wainright JS, Wang J-T, Weng D, Savinell RF, Litt M (1995) Acid-doped polybenzimidazoles: a new polymer electrolyte. J Electrochem Soc 142(7):L121–L123. doi:10.1149/1.2044337
96. Berber MR, Fujigaya T, Sasaki K, Nakashima N (2013) Remarkably durable high temperature polymer electrolyte fuel cell based on poly(vinylphosphonic acid)-doped polybenzimidazole. Sci Rep 3:1764. doi:10.1038/srep01764
97. Merle G, Wessling M, Nijmeijer K (2011) Anion exchange membranes for alkaline fuel cells: a review. J Membrane Sci 377(1–2):1–35. doi:10.1016/j.memsci.2011.04.043

98. Cheng J, He G, Zhang F (2015) A mini-review on anion exchange membranes for fuel cell applications: stability issue and addressing strategies. Int J Hydrogen Energy 40(23):7348–7360. doi:10.1016/j.ijhydene.2015.04.040
99. Hibbs MR, Fujimoto CH, Cornelius CJ (2009) Synthesis and characterization of poly (phenylene)-based anion exchange membranes for alkaline fuel cells. Macromolecules 42 (21):8316–8321. doi:10.1021/ma901538c
100. Luo Y, Guo J, Wang C, Chu D (2010) Quaternized poly(methyl methacrylate-co-butyl acrylate-co-vinylbenzyl chloride) membrane for alkaline fuel cells. J Power Sources 195 (12):3765–3771. doi:10.1016/j.jpowsour.2009.12.106
101. Li N, Leng Y, Hickner MA, Wang C-Y (2013) Highly stable, anion conductive, comb-shaped copolymers for alkaline fuel cells. J Am Chem Soc 135(27):10124–10133. doi:10.1021/ja403671u
102. Shimada M, Shimada S, Miyake J, Uchida M, Miyatake K (2016) Anion conductive aromatic polymers containing fluorenyl groups: effect of the position and number of ammonium groups. J Polym Sci A: Polym Chem 54(7):935–944. doi:10.1002/pola.27928
103. Bockris JOM, Cahan BD (1969) Effect of a finite-contact-angle meniscus on kinetics in porous electrode systems. J Chem Phys 50(3):1307–1324. doi:10.1063/1.1671193
104. Eikerling M, Ioselevich AS, Kornyshev AA (2004) How good are the electrodes we use in PEFC? Fuel Cells 4(3):131–140. doi:10.1002/fuce.200400029
105. Xia Z, Wang Q, Eikerling M, Liu Z (2008) Effectiveness factor of Pt utilization in cathode catalyst layer of polymer electrolyte fuel cells. Can J Chem 86(7):657–667. doi:10.1139/V08-053
106. Xie Z, Navessin T, Shi K, Chow R, Wang Q, Song D, Andreaus B, Eikerling M, Liu Z, Holdcroft S (2005) Functionally graded cathode catalyst layers for polymer electrolyte fuel cells. J Electrochem Soc 152(6):A1171–A1179. doi:10.1149/1.1904990
107. Motoo S, Watanabe M, Furuya N (1984) Gas diffusion electrode of high performance. J Electroanal Chem 160:351–357. doi:10.1016/S0022-0728(84)80139-4
108. Watanabe M, Tomikawa M, Motoo S (1985) Preparation of a high performance gas diffusion electrode. J Electroanal Chem 182(1):193–196. doi:10.1016/0368-1874(85)85453-8
109. Watanabe M, Tozawa M, Motoo S (1985) A gas diffusion electrode for oxygen reduction working at 100% utilization of catalyst clusters. J Electroanal Chem 183(1–2):391–394. doi:10.1016/0368-1874(85)85505-2
110. Song JM, Suzuki S, Uchida H, Watanabe M (2006) Preparation of high catalyst utilization electrodes for polymer electrolyte fuel cells. Langmuir 22(14):6422–6428. doi:10.1021/la060671w
111. Lee M, Uchida M, Yano H, Tryk DA, Uchida H, Watanabe M (2010) New evaluation method for the effectiveness of platinum/carbon electrocatalysts under operating conditions. Electrochim Acta 55(28):8504–8512. doi:10.1016/j.electacta.2010.07.071
112. Lee M, Uchida M, Tryk DA, Uchida H, Watanabe M (2011) The effectiveness of platinum/carbon electrocatalysts: dependence on catalyst layer thickness and Pt alloy catalytic effects. Electrochim Acta 56(13):4783–4790. doi:10.1016/j.electacta.2011.03.072
113. Watanabe M, Sei H, Stonehart P (1989) The influence of platinum crystallite size on the electroreduction of oxygen. J Electroanal Chem 261:375–387. doi:10.1016/0022-0728(89)85006-5
114. Weber AZ, Newman J (2004) Modeling transport in polymer-electrolyte fuel cells. Chem Rev 104(10):4679–4726. doi:10.1021/cr020729l
115. Uchida H, Song JM, Suzuki S, Nakazawa E, Baba N, Watanabe M (2006) Electron tomography of Nafion ionomer coated on Pt/carbon black in high utilization electrode for PEFCs. J Phys Chem B 110(27):13319–13321. doi:10.1021/jp062678s
116. Chisaka M, Daiguji H (2006) Design of ordered-catalyst layers for polymer electrolyte membrane fuel cell cathodes. Electrochem Commun 8(8):1304–1308. doi:10.1016/j.elecom.2006.06.009
117. Yano H, Watanabe M, Iiyama A, Uchida H (2016) Particle-size effect of Pt cathode catalysts on durability in fuel cells. Nano Energy 29:323–333. doi:10.1016/j.nanoen.2016.02.016

118. Takahashi K, Kakinuma K, Uchida M (2016) Improvement of cell performance in low-Pt-loading PEFC cathode catalyst layers prepared by the electrospray method. J Electrochem Soc 163(10):F1182–F1188. doi:10.1149/2.0611610jes
119. Park Y-C, Tokiwa H, Kakinuma K, Watanabe M, Uchida M (2016) Effects of carbon supports on Pt distribution, ionomer coverage and cathode performance for polymer electrolyte fuel cells. J Power Sources 315:179–191. doi:10.1016/j.jpowsour.2016.02.091
120. Zhang XF, Kamino T (2006) Imaging gas-solid interactions in an atomic resolution environmental TEM. Microsc Today 14(5):16–18
121. Axnanda S, Zhu Z, Zhou W, Mao B, Chang R, Rani S, Crumlin E, Somorjai G, Liu Z (2014) In situ characterizations of nanostructured SnO_x/Pt(111) surfaces using ambient-pressure XPS (APXPS) and high-pressure scanning tunneling microscopy (HPSTM). J Phys Chem C 118(4):1935–1943. doi:10.1021/jp409272j
122. Beden B, Lamy C, Bewick A, Kunimatsu K (1981) Electrosorption of methanol on a platinum electrode. IR spectroscopic evidence for adsorbed CO species. J Electroanal Chem 121:343–347. doi:10.1016/S0022-0728(81)80590-6
123. Sato T, Kunimatsu K, Uchida H, Watanabe M (2007) Adsorption/oxidation of CO on highly dispersed Pt catalyst studied by combined electrochemical and ATR-FTIRAS methods: Part 1. ATR-FTIRAS spectra of CO adsorbed on highly dispersed Pt catalyst on carbon black and carbon un-supported Pt black. Electrochim Acta 53(3):1265–1278. doi:10.1016/j.electacta.2007.05.007
124. Kunimatsu K, Sato T, Uchida H, Watanabe M (2008) Adsorption/oxidation of CO on highly dispersed Pt catalyst studied by combined electrochemical and ATR-FTIRAS methods: oxidation of CO adsorbed on carbon-supported Pt catalyst and unsupported Pt black. Langmuir 24(7):3590–3601. doi:10.1021/la702441x
125. Watanabe M, Sato T, Kunimatsu K, Uchida H (2008) Temperature dependence of co-adsorption of carbon monoxide and water on highly dispersed Pt/C and PtRu/C electrodes studied by in-situ ATR-FTIRAS. Electrochim Acta 53:6928–6937. doi:10.1016/j.electacta.2008.02.023
126. Kunimatsu K, Yoda T, Tryk DA, Uchida H, Watanabe M (2010) In situ ATR-FTIR study of oxygen reduction at the Pt/Nafion interface. Phys Chem Chem Phys 12(3):621–629. doi:10.1039/B917306D
127. Hanawa H, Kunimatsu K, Watanabe M, Uchida H (2012) In situ ATR-FTIR analysis of the structure of Nafion-Pt/C and Nafion-Pt_3Co/C interfaces in fuel cell. J Phys Chem C 116(40):21401–21406. doi:10.1021/jp306955q
128. Kunimatsu K, Bae B, Miyatake K, Uchida H, Watanabe M (2011) ATR-FTIR study of water in Nafion membrane combined with proton conductivity measurements during hydration/dehydration cycle. J Phys Chem B 115(15):4315–4321. doi:10.1021/jp112300c
129. Hara M, Inukai J, Bae B, Hoshi T, Miyatake K, Uchida M, Uchida H, Watanabe M (2012) Micro-Raman study on water distribution Inside a Nafion membrane during operation of polymer electrolyte fuel cell. Electrochim Acta 82:277–283. doi:10.1016/j.electacta.2012.04.099
130. Hara M, Hattori D, Inukai J, Hara M, Miyatake K, Watanabe M (2014) Reversible/irreversible increase in proton-conductive areas on proton-exchange-membrane surface by applying voltage using current-sensing atomic force microscope. J Electroanal Chem 716:158–163. doi:10.1016/j.jelechem.2013.11.035
131. Hara M, Hara M, Miyatake K, Inukai J, Watanabe M (2014) Effects of hot liquid-water treatment on local proton conductivity at surfaces of sulfonated poly(arylene ketone) block copolymer membrane for fuel cells studied by current-sensing atomic force microscopy. Electrochim Acta 143:383–389. doi:10.1016/j.electacta.2014.08.031
132. Hara M, Kimura T, Nakamura T, Shimada M, Ono H, Shimada S, Miyatake K, Uchida M, Inukai J, Watanabe M (2016) Effect of surface ion conductivity of anion exchange membranes on fuel cell performance. Langmuir 32(37):9557–9565. doi:10.1021/acs.langmuir.6b01747

133. Ishigami Y, Waskitoaji W, Yoneda M, Takada K, Hyakutake T, Suga T, Uchida M, Nagumo Y, J.Inukai, Nishide H, Watanabe M (2014) Oxygen partial pressures on gas-diffusion layer surface and gas-flow channel wall in polymer electrolyte fuel cell during power generation studied by visualization technique combined with numerical simulation. J Power Sources 269:556–564. doi:10.1016/j.jpowsour.2014.07.017
134. Nagase K, Suga T, Nagumo Y, Uchida M, Inukai J, Nishide H, Watanabe M (2015) Real-time visualization of oxygen partial pressures in straight channels of running polymer electrolyte fuel cell with water plugging. J Power Sources 273:873–877. doi:10.1016/j.jpowsour.2014.09.169
135. Nagase K, Motegi H, Yoneda M, Nagumo Y, Suga T, Uchida M, Inukai J, NIshide H, Watanabe M (2015) Visualization of oxygen partial pressure and numerical simulation of a running polymer electrolyte fuel cell with straight flow channels to elucidate reaction distributions. ChemElectroChem 2(10):1495–1501. doi:10.1002/celc.201402385
136. Kordesch K, Gsellmann J, Cifrain M, Voss S, Hacker V, Aronson RR, Fabjan C, Hejze T, Daniel-Ivad J (1999) Intermittent use of a low-cost alkaline fuel cell-hybrid system for electric vehicles. J Power Sources 80(1–2):190–197. doi:10.1016/S0378-7753(98)00261-4
137. Kordesch K, Hacker V, Gsellmann J, Cifrain M, Faleschini G, Enzinger P, Fankhauser R, Ortner M, Muhr M, Aronson RR (2000) Alkaline fuel cells applications. J Power Sources 86 (1–2):162–165. doi:10.1016/S0378-7753(99)00429-2
138. Hejze T, Besenhard JO, Kordesch K, Cifrain M, Aronsson RR (2008) Current status of combined systems using alkaline fuel cells and ammonia as a hydrogen carrier. J Power Sources 176(2):490–493. doi:10.1016/j.jpowsour.2007.08.117
139. Information Distribution Centre CaMB, Industry Canada (2003) The practice of innovation: seven canadian firms in profile
140. Ballard News Releases (2017) http://ballard.com/about-ballard/newsroom/news-releases/news-releases-2017.aspx. Accessed January 2017
141. Kröger H (2016) The fuel cell gets a plug https://www.mercedes-benz.com/en/mercedes-benz/next/e-mobility/the-fuel-cell-gets-a-plug/. Accessed January 2017
142. Edelstein S (2016) Nikola one hydrogen range-extended electric truck to be unveiled tonight. http://www.greencarreports.com/news/1107560_nikola-one-hydrogen-range-extended-electric-truck-to-be-unveiled-tonight. Accessed January 2017
143. Omata T (2016) Specific country reports: Japan. In: Fuel cells: data, facts and figures. Wiley-VCH Verlag GmbH & Co. KGaA, pp 270–275. doi:10.1002/9783527693924.ch27

On the Theory of Electrocatalysis

Wolfgang Schmickler

Abstract A theory of electrocatalysis developed in our group is presented and related to other theories of electrochemical electron transfer. As an example, the theory is applied to the first step in oxygen reduction on silver in alkaline media. It is shown, that this step occurs in the outer sphere mode.

1 Introduction

In the first approximation, scientists can be grouped into two classes: specialists, who work in a small field that they analyze profoundly, and generalists, who cover a broad area, and are less concerned with small details. Prof. John O'M. Bockris was a generalist, and, what is more important, a generalist with a vision. The breadth of his work is exemplified by his large number of publications, and by his seminal books on *Surface Electrochemistry* [1] and *Quantum Electrochemistry* [2] (both with S. Khan), each encompassing between 500 and 100 pages. His textbook on Modern Electrochemistry [3] (with K.N. Reddy) educated generations of electrochemists, and contrasts in style and spirit with the equally influential *Electrochemical Methods* by Bard and Faulkner [4]. As early as 1976, he presented his vision of the hydrogen economy based on solar energy and electrochemical energy conversion, which he later published as a book [5]; he returned to this topic in several of his later books aimed at a general audience. When he presented his ideas, he was a lonely prophet, but now, about 50 years later, they belong to the mainstream.

The theory of electrocatalysis was among the many topics on which he worked. At that time, the theory of electrochemical reactions was limited to outer sphere electron transfer, and he pointed out correctly, that these could not be applied to catalytic reactions. Throughout his life he worked on various topics of electrocatalysis. Obviously this is not the place to review his work, but we would like to draw attention to one of his early works, together with Brian Conway, entitled: *Electrolytic hydrogen evolution kinetics and its relation to electronic and adsorptive properties of metals*

W. Schmickler (✉)
Institute of Theoretical Chemistry, Ulm University, 89069 Ulm, Germany
e-mail: wolfgang.schmickler@uni-ulm.de

K. Uosaki (ed.), *Electrochemical Science for a Sustainable Society*,
DOI 10.1007/978-3-319-57310-6_4

[6],which discusses in an intelligent way the relation between the kinetics and the energy of adsorption of hydrogen, and related quantities. It precedes the works of Gerischer [7] and Parsons [8] on volcano plots by about a year, and the standard work by Trasatti [9] by 15 years. Nowadays, the most cited work on this topic seems to be the article by Nørskov et al. [10], who provided DFT data for this venerable topic. Conway and Bockris did not only discuss the Sabatier principle, but made the useful distinction between *sp* and *d* metals, and furthermore pointed out the importance of the filling of the *d* band, which at that time was called *d* character—all these topics were rediscovered at the beginning of this millennium. In addition, they discussed current-potential relationships in terms of potential energy curves for the transition of the proton. Unfortunately, the extensive work of Bockris and his school on electrocatalysis never resulted in a quantitative theory, because the computational tools were missing at that time, and even the experimental values were not very reliable.

In this chapter, we review our own theory of electrocatalysis, which, we are sure, John O'M. Bockris would have approved, because it is based on the type of molecular description which he favored during his lifetime.

2 Elements for a Theory of Electrocatalysis

Before presenting our own theory, we would like to discuss a few concepts pertinent to electrocatalysis. The first quantitative theory for electrochemical reactions was for outer sphere electron transfer. It came in two flavors: The work of Levich, Dogonadze, and their school [11, 12] was primarily based on perturbation theory and weak interactions. The theories of Marcus [13] and Hush [14], which preceded the Soviet works, concern the weakly adiabatic limit, in which the interaction between the reactant and the electrode is strong enough to make the reaction adiabatic, but so weak that it does not affect the reaction barrier. A characteristic feature of the latter class of reactions is that the rate does not depend on the electrode material [15, 16]. Neither version is applicable to electrocatalysis, where the interactions are strong, and where often the rate on various materials can vary over eight orders of magnitudes [1]. Already in 1986, I had proposed a version of electron transfer theory based on Green's functions [17], which could be applied to interactions of arbitrary strengths, but in absence of a way to calculate strong electronic interactions this did not result in a theory of electrocatalysis. Nowadays, with density functional theory we have the computational means to calculate such interactions. So one essential aspect of theories of electrocatalysis is, that they must be able to treat strong interactions, and this will usually imply that DFT plays an important role.

However, even though the classical electron transfer theories cannot be applied to electrocatalysis, we must not forget the most important lesson that they taught us, the role of solvent reorganization. By definition, all electrochemical reactions involve charge transfer, and thus at least one of the reactants changes its charge, and hence its solvation. The accompanying changes in solvation energy are usually of the order of a few electron volts; in the case of the discharge of the proton it

reaches about 11.3 eV! The concomitant energy of solvent reorganization makes an important contribution to the activation energy—indeed, in outer sphere electron transfer it alone determines the barrier height—and fluctuations of the solvent trigger the reaction. Therefore theories of electrocatalysis must contain an explicit treatment of the solvent, which must include statistical fluctuations. A simple model of a water bilayer at zero temperature is not enough.

As a reacting ion moves toward an electrode surface, its energy of solvation changes. The magnitude of this effect depends on the ion under consideration; for small ions such as Ag^+ and Li^+, which fit well into the structure of water, it is quite small [18], while it can be appreciable for larger ions like I^- [19]. In any case, it is an effect which must be considered. If both the reactant and the product are solvated, we require the energy of solvation as a function of position for both of them.

Finally, a rather trivial point: electrochemical reactions are governed by the electrode potential, which determines the rate, the activation energy, and even the direction. Since so far there is no consistent way to include the electrode potential in DFT calculations, a treatment that is based on DFT alone lacks a fundamental aspect.

3 Our Model for Electrocatalytic Reactions

We have presented our theory for electrocatalytic reactions in various publications [20–22], where we also give the mathematical details. Here we want to demonstrate the various effects that enter, and present our model Hamiltonian step by step. In order to focus on the main points, we present the version where spin plays no role, such as in the Volmer reaction or in the deposition of monovalent ions like Ag^+. Thus we consider one orbital labeled a on the reactant, and a continuum of states k on the metal. Generally, the index k runs both over the *sp* band and the *d* band of the metal. Denoting electronic energies by ϵ, and the operator for the occupation number by n, the electronic terms without interactions are:

$$H_1 = \epsilon_a n_a + \sum_k \epsilon_k n_k \tag{1}$$

Electron exchange between reactant and electron is effected by a combination of annihilation c and creation operators c^* for the electronic states:

$$H_2 = \sum_k \left(V_k c_k^* c_a + V_k^* c_a^* c_k \right) \tag{2}$$

The first term transfers an electron from the reactant to the metal state k with an amplitude of V_k, the second term effects the reverse process. The sum $H_1 + H_2$ describes the spinless version of the Anderson–Newns theory [23, 24].

Next we introduce the coupling with the solvent. Electron transfer theory distinguishes between two kinds of modes: slow modes, which in the case of water

correspond to the motion of the molecular dipole moment, and the fast modes, which correspond to the electronic polarizability of the molecule, and which follow any charge transfer almost instantaneously. Electron transfer is triggered by thermal fluctuations of the slow modes, which are described as a bath of harmonic oscillators—in fact, any other model based on a harmonic approximation gives identical results. There is an infinite number of such oscillator modes, but in the harmonic approximation the minima for the initial state, the activated state, and the final states lie on a straight line, and this can be used to define a single solvent coordinate q; details are given in Ref. [25]. It is convenient to normalize q in such a way that the minima occur at integral values. Specifically, we normalize q in such a way that a solvent configuration characterized by q would be in equilibrium with a charge number of $-q$ on the reactant. For simplicity, we assume that the initial state with $\langle n_a \rangle = 0$ carries unit positive charge, and the final state is an adsorbed neutral atom, whose energy of solvation we neglect. Then the corresponding terms in our Hamiltonian are:

$$H_{\text{sol}} = \lambda q^2 + 2(z - n_a)\lambda q \tag{3}$$

The first term describes the slow solvent modes when the charge on the reactant is zero; the second term is a linear coupling of these modes with the charge. λ is the energy of reorganization familiar from Marcus theory, and z is the charge number of the reactant when the orbital a is empty. We have left out the kinetic energy, since it plays no role in the determination of the saddle point. To be specific, we discuss the case where $z = 1$, so that the reaction is the transfer of one electron to a cation.

Since we neglect the solvation of the final state, the interaction with the fast solvent modes affects only the energies of the initial state i, which is the cation. We denote the corresponding solvation energy by G^i_{fast}, and it contributes a term:

$$H_{\text{fast}} = (1 - n_a)\Delta G^i_{\text{fast}} \tag{4}$$

As a reactant approaches the electrode, its solvation energy changes; this effect can be obtained by molecular dynamics simulations, and the corresponding change is called the *potential of mean force* (pmf). In terms of the notation of Marcus theory, the potentials of mean force correspond to work terms, so we denote them by w_i and w_f, and introduce a term $n_a w_f + (1 - n_a)w_i$. Since in the case considered here the final state is an adsorbed atom, $w_f = 0$; however, we shall first keep this term in order to show the correspondence with Marcus theory for the case of weak interactions.

Finally we include the electrode potential ϕ, which simply shifts the energy of the ion, and gives a term $(1 - n_a)e_0\phi$. Collecting the various terms gives:

$$\begin{aligned} H = {} & (\epsilon_a - e_0\phi - \Delta G^i_{\text{fast}} + w_f - w_i - 2\lambda q)n_a + \lambda q^2 + 2\lambda q \\ & + \Delta G^i_{\text{fast}} + w_i + \sum_k \epsilon_k n_k + \sum_k (V_k c^*_k c_a + V^*_k c^*_a c_k) \end{aligned} \tag{5}$$

In the limit of weak interactions, the coupling to the metal has no effect on the energy, and we should retrieve Marcus theory. In this case, the initial state with $\langle n_a \rangle = 0$ has its minimum at $q = -1$, with an energy:

$$G_i = w_i - \lambda + \Delta G^i_{\text{fast}} = \Delta G_{\text{sol}} + w_i \tag{6}$$

where we have used the fact that $-\lambda$ is the slow part of the total solvation energy ΔG_{sol}. The interpretation is obvious: the only energy is the solvation energy modified by the work term.

In the final state $\langle n_a \rangle = 1$, the minimum is at $q = 0$, with an energy:

$$G_f = \epsilon_a - e_0\phi + w_f \tag{7}$$

This is the electronic energy shifted by the electrode potential, plus the work term. This gives the following free energy difference for the electron transfer step:

$$\Delta G^{\text{el}} = \epsilon_a - e_0\phi + w_f - \Delta G^i_{\text{sol}} - w_i \tag{8}$$

The free energy difference for the overall reaction does not contain the work terms:

$$\Delta G = \epsilon_a - e_0\phi - \Delta G^i_{\text{sol}} \tag{9}$$

The energy of activation is easily obtained calculating the value of q where the energies for the two states are equal. This results in the Marcus expression [13] for the reaction rate, which we will discuss below when we relate our theory to other works.

3.1 Density of States

When the reactant is far from the electrode, its valence level is sharp and characterized solely by its energy ϵ_a. However, when it approaches the surface, it begins to interact with the electronic states of the metal, with which it can exchange electrons. Consequently the valence level is no longer sharp, but characterized by a *density of states* (DOS). In the simplest case, which we shall discuss below, this takes on the shape of a Lorentzian, and the DOS can be considered as a consequence of the lifetime broadening.

The mathematical analysis of our model in based on the consideration of the Green's function, which is defined as $G(z) = \frac{1}{z-H}$, where z is the energy variable and H the Hamiltonian of Eq. (5). The calculations are facilitated if we split the Hamiltonian in two parts: The non-interactive part H_0, which comprises all of the terms of Eq. (5) except the last sum, which in the interacting part denoted by V. The Green's function can then be obtained via the identity:

$$G(z) = G_0(z) + G(z)VG_0(z), \tag{10}$$

where $G_0(z)$ is the Green's function pertaining to the Hamiltonian H_0.

The density of states can be calculated exactly from the Green's function, and expressed in terms of the two so-called *chemisorption functions* which describe the interaction [26]:

$$\Delta(\epsilon) = \pi \sum_k |V_k|^2 \delta(\epsilon - \epsilon_k) \qquad \Lambda(\epsilon) = \frac{1}{\pi} \mathcal{P} \int \frac{\Delta(\epsilon')}{\epsilon - \epsilon'} \, d\epsilon', \tag{11}$$

where $\mathcal{P}$ denotes the principle part. The corresponding density of states of the reactant is:

$$\rho_a(\epsilon) = \frac{1}{\pi} \frac{\Delta}{\left[\epsilon - (\tilde{\epsilon}_a - \Lambda - 2\lambda q)\right]^2 + \Delta^2}, \tag{12}$$

where we have collected the terms that modify ϵ_a:

$$\tilde{\epsilon}_a = \epsilon_a - e_0\phi - \Delta G^i_{\text{fast}} + w_f - w_i \tag{13}$$

In the simplest case, which we shall discuss in more detail below, Δ and Λ are constant. In this case the density of states $\rho_a(\epsilon)$ takes the form of a Lorentzian of width Δ, whose center has been shifted by Λ. In addition, the center fluctuates with the solvent coordinate q. In the general case, Δ and Λ depend on the energy ϵ, and the form is more complicated.

The occupancy of the valence state a is obtained by integrating the DOS up to the Fermi level E_F:

$$\langle n_a \rangle = \int_{-\infty}^{E_F} \rho_a(\epsilon) \, d\epsilon \tag{14}$$

From now on, we shall set $E_F = 0$. The electronic part of the energy is obtained by multiplying the DOS with the energy ϵ and integrating again to the Fermi level:

$$E_{\text{el}} = \int_{-\infty}^{0} \epsilon \, \rho_a(\epsilon) \, d\epsilon \tag{15}$$

3.2 Wide Band Approximation

As already mentioned, in the simplest case Δ does not depend on the energy; in this case $\Lambda = 0$. This is known as the *wide band approximation*, because physically it corresponds to the interaction of the reactant with a wide, structureless band of the electrode. The integrals in Eqs. (14) and (15) can be performed explicitly. This gives for the occupancy:

$$\langle n \rangle = \frac{1}{\pi} \operatorname{arccot} \frac{\epsilon_a - 2\lambda q}{\Delta} \tag{16}$$

This simple approximation can be used to nicely explain a basic effect of catalysis due to the width Δ of the reactant's DOS. For this purpose, we ignore the fast solvation and the work terms for the moment—they become important for quantitative calculations on real systems—and focus on electron transfer and solvent reorganization. Then the energy can be written as a function of the solvent coordinate q:

$$E(q) = \lambda q^2 + 2\lambda q + (\epsilon_a - 2\lambda q)\langle n \rangle + \frac{\Delta}{2\pi} \ln \frac{\left[\epsilon_a - 2\lambda q\right]^2 + \Delta^2}{\epsilon_a^2 + \Delta^2} \tag{17}$$

It is easy to verify that equilibrium occurs for $\epsilon_a = -\lambda$, and this is the case we shall now consider. The corresponding free energy curve has been examined in detail in [17]. For not too strong interactions, for $\Delta < 2\lambda/\pi$, the curve has two minima corresponding to the initial and the final state, separated by a maximum at the transition state. The corresponding energy of activation is:

$$E_{\text{act}} = \lambda/4 + \frac{\Delta}{2\pi} \ln \frac{\Delta^2}{\lambda^2 + \Delta^2} \tag{18}$$

For $\Delta \to 0$, we recover the Marcus result of $\lambda/4$; for finite values of Δ, the argument of the logarithmic term is smaller than unity, and hence this terms decreases the energy of activation. The reason can be visualized in Fig. 1: According to Eq. 15, the electronic energy is obtained by integrating $\epsilon \rho_a(\epsilon)$ up to the Fermi level. At the activated state, the DOS is centered directly at the Fermi level, which is the energy at which the electron transfer takes place. For a sharp DOS, i.e., for $\Delta \approx 0$, the electronic energy at the saddle point would be equal to E_F, and hence equal zero with our

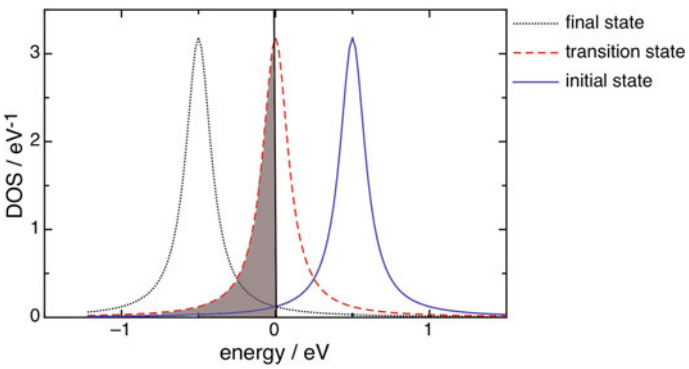

Fig. 1 DOS for the initial, the activated, and the final state for the case of equilibrium; parameter: $\lambda = 0.5$ eV. The shaded portion of the DOS for the transition state reduces the energy of activation. After [25]

choice of reference energy. For a finite width Δ, the shaded part which lies below the Fermi level contributes to the energy of the activated state. Obviously, it is smaller than zero, and the lower, the greater Δ. In this way, a strong interaction with the metal lowers the activation energy, and thus catalyzes the reaction. We shall meet the same effect when we discuss electrocatalysis in real system.

4 Relation to Other Theories

4.1 Marcus Theory

Marcus theory corresponds to the weakly adiabatic case: The interaction with the metal is strong enough, to make the electron transfer adiabatic, but too weak to have an effect on the activation energy. The latter is easily derived by calculating the intersection point between energy curves of the initial ($\langle n_a \rangle = 0$) and the final ($\langle n_a \rangle = 1$) states, both considered as a function of the solvent coordinate q. The result is:

$$E_{\text{act}} = w_i + \frac{(\lambda + \Delta G + w_f - w_i)^2}{4\lambda} \tag{19}$$

which is familiar from Marcus theory. The properties of the metal and its interaction with the reactant do not enter; so there is no catalysis. Indeed, experimental results show that in this case the rate is independent of the nature of the metal [15, 16]. We shall not discuss the pre-exponential factor, which is usually obtained from Kramers theory [27].

4.2 Levich and Dogonadze Theory

The first quantum mechanical theory of electrochemical electron transfer was developed by the Soviet group led by Levich and Dogonadze [11]. In essence, it is based on a Hamiltonian like ours, but without the work terms. However, the interacting part V is considered as weak and treated by first-order perturbation theory. A systematic perturbation theory can be based on an iteration of Eq. (10), which results in a series in terms of V:

$$G(z) = G_0(z) + G_0(z)VG_0(z) + G_0VG_0(z)VG_0(z) + \cdots \tag{20}$$

In the first-order perturbation only the first two terms are retained. As a consequence, the width Δ and the shift Λ do not figure in the theory. The standard procedure is to perform a Fourier transform, from which Fermi's golden rule is obtained after some calculations. The final expression for the rate constant contains the same energy of activation as Marcus theory, though without the work terms. However, the

pre-exponential factor contains the matrix element of V_{if} between the initial and final states, and is given by $|V_{if}|^2/h$. The element V_{if} has the meaning of an effective value of V_k.

In Marcus theory as well as in ours the reactant shares its electrons with the metal. In contrast, in perturbation theory electron transfer is a rare event, and the theory traces the transition of a single electron with a definite energy. Thus one obtains an *energy resolved rate* $W(\epsilon)$ for the transfer an electron of an energy ϵ, to the metal, and a corresponding expression for the reverse direction. Since electron transfer from the reactant can only occur to empty levels, the total rate k_r of reduction is obtained by multiplying with the probability of finding an empty level, and integrating over energy:

$$k_\mathrm{a} = \int [1 - f(\epsilon)] W_a(\epsilon, \eta)\, d\epsilon, \tag{21}$$

where we have expressed the fact that the rate depends on the overpotential η as well; $f(\epsilon)$ is the Fermi–Dirac distribution. The index 'a' indicates that this is the rate for the anodic reaction, which is the oxidation. The energy resolved rate takes the form:

$$W_a(\epsilon, \eta) \propto (4\pi\lambda kT)^{-1/2} \exp - \frac{(\lambda - \epsilon + e_0\eta)^2}{4\lambda kT} \tag{22}$$

The term $(-\epsilon + e_0\eta)$ is the free energy for the transfer of an electron of energy ϵ to the electrode. Thus, the energy of activation is given by the Marcus expression of Eq. (19), but without the work terms. The pre-exponential factor contains the perturbation $|V_{if}|^2$, and a factor which converts normal concentrations to surface concentrations [25].

For the cathodic reaction, the free energy of the reaction in the energy resolved rate takes the opposite sign:

$$W_c(\epsilon, \eta) \propto (4\pi\lambda kT)^{-1/2} \exp - \frac{(\lambda + \epsilon - e_0\eta)^2}{4\lambda kT} \tag{23}$$

and this has to be multiplied with the probability to find an occupied state on the metal from which the electron can be transferred:

$$k_\mathrm{a} = \int f(\epsilon) W_c(\epsilon, \eta)\, d\epsilon \tag{24}$$

4.3 Gerischer's Theory

Gerischer's theory [28] is essentially a re-interpretation of the theories of Marcus and of Levich and Dogonadze. Just like the latter, it considers electron exchange with specific energy levels ϵ. For the anodic direction, we introduce the electronic density

of states $\rho_e(\epsilon)$ of the electrode; the product $\rho_e(\epsilon)[1-f(\epsilon)]$ is then the probability of finding an empty state on the electrode. The term:

$$W_{\text{red}}(\epsilon,\eta) = (4\pi\lambda kT)^{-1/2} \exp -\frac{(\lambda - \epsilon + e_0\eta)^2}{4\lambda kT} \tag{25}$$

is then interpreted as the *density of reduced states* of the reactant. Apart from the pre-exponential factor, this is the same as the energy reduced rate of Eq. (22) given above. The total rate is then obtained by multiplying the density of empty states on the electrode with the density of reduced states of the reactant, and integrating over energy:

$$k_a = \int \rho_e(\epsilon)[1-f(\epsilon)]W_{\text{red}}(\epsilon,\eta)d\epsilon \tag{26}$$

Since at room temperature the Fermi–Dirac distribution is almost a step function, in practice the integral is taken from the Fermi level to the top of the conduction band; the upper limit can be extended to infinity, since the integrand drops off rapidly for high energies.

Similarly, the density of oxidized states of the reactants is introduced as:

$$W_{\text{ox}}(\epsilon,\eta) = (4\pi\lambda kT)^{-1/2} \exp -\frac{(\lambda + \epsilon - e_0\eta)^2}{4\lambda kT} \tag{27}$$

and the cathodic rate is given by:

$$k_a = \int \rho_e(\epsilon)f(\epsilon)W_{\text{ox}}(\epsilon,\eta)d\epsilon \tag{28}$$

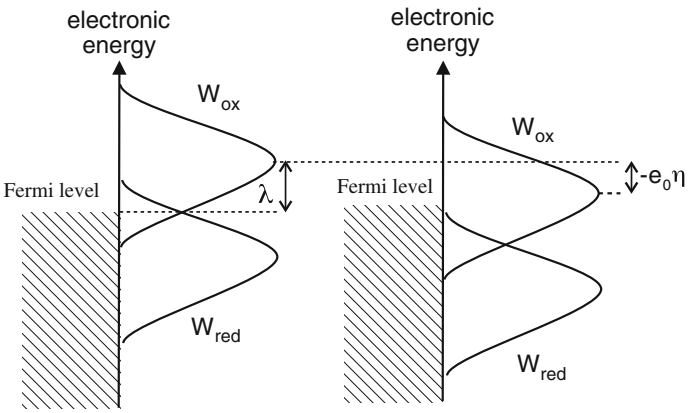

Fig. 2 Densities of reduced and oxidized states at equilibrium (*left*) and after the application of a cathodic overpotential (*right*). After [25]

In practice, the integral goes from minus infinity to the Fermi level. Gerischer's theory is for adiabatic transitions, since the perturbation $|V_{if}|$ does not enter into the rate equation. On the other hand, it uses the concept of electron exchange with specific energy levels of the metal. Equations (26) and (28) have a nice graphical representation shown in Fig. 2. In this picture, the application of an overpotential simply shifts the densities of states of the redox couple with respect to the Fermi level of the metal. This model has the further advantage that it can be readily applied to semiconductors. Equations (26) and (28) stay the same, but the electronic density of states $\rho_e(\epsilon)$ of the electrode now has a band gap.

5 Application to Real Systems: Oxygen Reduction in Alkaline Media

We now return to our theory of electrocatalysis as presented in Sect. 2, and show how it can be applied to real systems, where simple approximations like the wide band approximation do not hold. For this purpose, we need a number of quantities, which we obtain from DFT and from molecular dynamics. We start with the parameters that relate to the interaction of the reactant with the metal. As a concrete example, we chose the first step in oxygen reduction on Ag(100) in alkaline media [29], which occurs according to:

$$O_2 + e^- \rightarrow O_2^- \tag{29}$$

The reasons for choosing this particular reaction are the following: The rate of reaction (29) is very similar on a variety of electrode materials. It has therefore been suggested, that it occurs by an outer sphere mechanism, in which neither the reactant nor the product are adsorbed [30]. On the basis of our theory, we have recently shown that on Au(100) it indeed occurs in the outer sphere mode [31]. However, gold is special in that the oxygen molecule is not adsorbed on the surface. In contrast, silver is much more reactive to oxygen; in the vacuum the molecule adsorbs with an energy of about −0.4 eV [32]. We therefore want to investigate, if the reaction mechanism on Ag(100) is inner or outer sphere.

5.1 Interaction with the Metal

The parameters for the interaction with the metal can be determined by DFT. Calculations for a slab of metal performed with one of the common packages yield the electronic structure of the metal surface. For most metal of interest, this consists of a *sp*- and a *d* band. Usually, it is a good approximation to assume that the interaction of the reactant is constant for each band. Therefore we can write:

$$\Delta = \pi |V_{\mathrm{sp}}|^2 \rho_{\mathrm{sp}}(\epsilon) + \pi |V_{\mathrm{d}}|^2 \rho_{\mathrm{d}}(\epsilon), \tag{30}$$

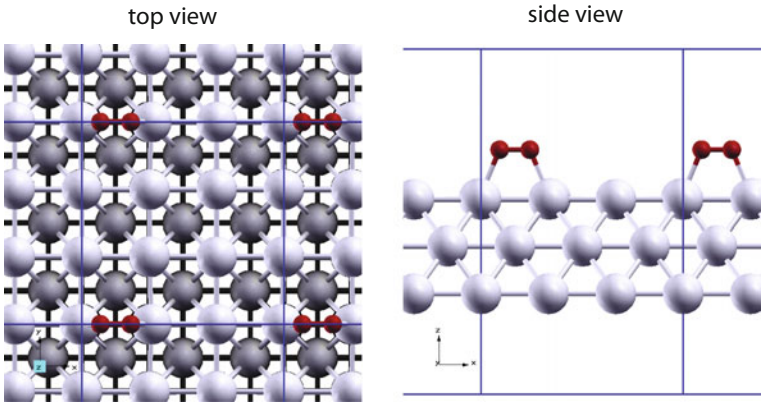

Fig. 3 Configuration of O_2 adsorbed on Ag(100). After [29]

where $\rho_{sp}(\epsilon)$ and $\rho_d(\epsilon)$ are the electronic densities of states of the metal *sp* and *d* bands. The function $\Lambda(\epsilon)$ is then obtained by integration according to Eq. (11). In addition, we need the energy ϵ_a of the reactant. In order to construct the free energy surface for the reaction, we require these three parameters as a function of the distance. For this purpose, we perform DFT calculations for the O_2 molecule in front of the Ag(100) surface at various distances. This gives us the energy as a function of the distance, and also the densities of states of the molecule. In order to obtain V_{sp}, V_d and ϵ_a for a given distance, we fit the theoretical density of states as given by Eq. (12), taken at $q = 0$, to the DOS obtained by DFT. The technical details are given in [29].

In our example, the approaching O_2 molecule has two empty antibonding spin orbitals; only the one which is directed perpendicularly to the metal surface interacts with the silver surface. As it approaches Ag(100), it becomes partially filled, and acquires a charge of about $-0.7\ e_0$ when it is adsorbed. The configuration of the adsorbed molecule is shown in Fig. 3. As an example of the fitting procedure, we show the DOS when the molecule is adsorbed, and the theoretical DOS according to Eq. (12) with the fitted values in Fig. 4. The fit is excellent, and this is true for larger separations as well. We must admit that the fitting procedure does not always work quite as well as in this example. In a few cases, for example, for the adsorption of OH on Pt(111), we have to introduce an energy dependence of the coupling constants [33].

5.2 *Solvent and Work Terms*

The energy of reorganization and the work terms are obtained from the energies of solvation of the reactant and the product. The bulk values of these energies are known

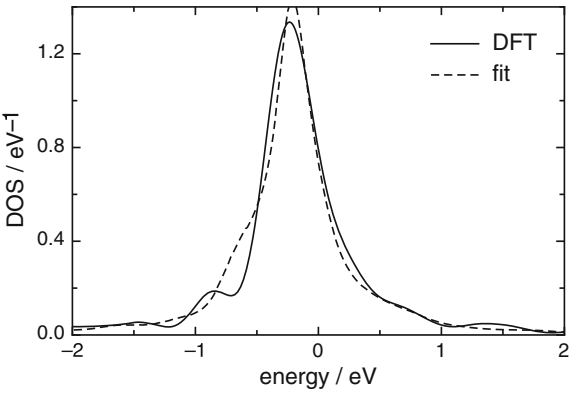

Fig. 4 DOS of the O_2 antibonding orbital that binds to the Ag(100) surface; the full curve has been obtained by DFT, the *dashed curve* by fitting. The fitted parameters are: $|V_{sp}|^2 = 0.96$ eV^2, $|V_d|^2 = 0.09$ eV^2, $\epsilon_a = -0.33$ eV. After [29]

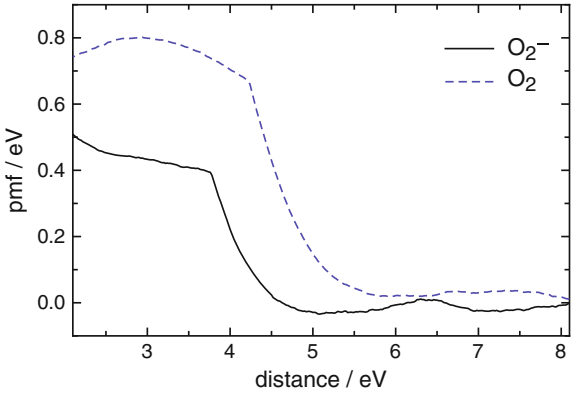

Fig. 5 Potentials of mean force for the approach of O_2^- and O_2 to the electrode surface. These curves are the same for Ag(100) and Au(100). After [29]

from experiment; as these particles approach the electrode surface they lose a part of their solvation sheets. The concomitant change in energy is known as the *potential of mean fore* (pmf), and can be obtained by molecular dynamics. For the details, we refer to the literature [29, 33].

We have calculated the pmf of both the molecule and the anion for the approach to the Ag(100). As expected, both increase toward the surface, as their hydration becomes weaker—see Fig. 5. This effect is stronger for the molecule, where the pmf begins to rise at about 6 Å, than for the anion, where it even has a slight minimum near 5 Å before it starts to rise. Considering that the hydration energy of the anion is about −3.9 eV, the rise in energy toward the surface is moderate.

The energy of solvation must be split into two parts: the slow part, which determines the energy of reorganization, and the fast part, which enters into the work terms. For this purpose, we note that the Marcus expression for the energy of reorganization is related to the energy of solvation, as given by Born's theory, by the relation:

$$\lambda = -\frac{1/\epsilon_\infty - 1/\epsilon_s}{1 - 1/\epsilon_s}\Delta G_{\text{sol}}, \tag{31}$$

where ϵ_∞ is the optical dielectric constant of the solvent, and ϵ_s the static constant. For aqueous solutions, λ is about one half of the absolute value of the energy of solvation.

5.3 The First Step in Oxygen Reduction on Ag(100)

We now have the ingredients which we need to calculate the free energy surface for reaction (1). In Fig. 6 we present the surface for the potential, when the reaction is in equilibrium in the outer sphere. As usual, we have plotted the free energy as a function of the distance d of the reactant from the surface and of the solvent coordinate [25]. A quick reminder: The solvent coordinate characterizes the state of the solvent; it takes on the value q, when the solvent would be in equilibrium with a reactant of charge $-q$. At $d = 5$ Å and $q = 0$, we see a minimum that corresponds to the uncharged O_2 molecule; toward the bulk of the solution this extends into a valley. We have chosen the energy zero such that the energy is zero at this minimum. Likewise at large distances, but at $q = 1$, lies the minimum for the anion; again this extends into a valley toward the bulk, but it does have a real shallow minimum which corresponds to the slight minimum in the pmf observed in Fig. 5. These two minima are separated by a saddle point with an energy of 0.5 eV. A transition between these minima corresponds to an outer sphere electron transfer, so according to Marcus

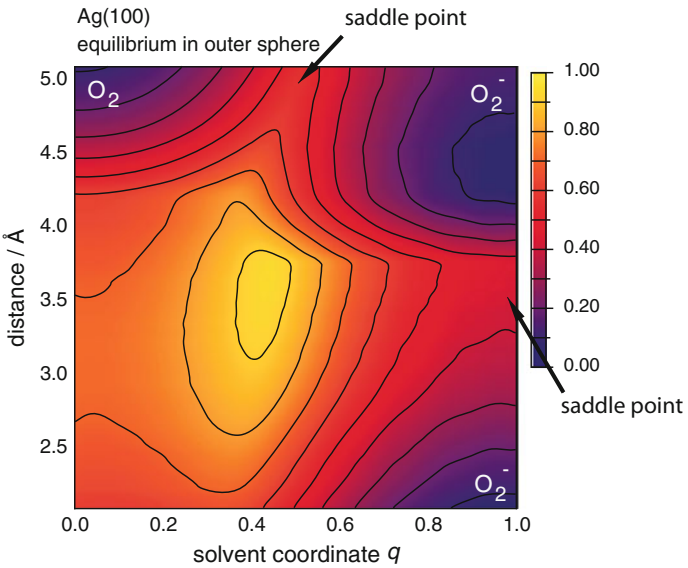

Fig. 6 Free energy surface for the reaction $O_2 + e^- \rightarrow O_2^-$ on Ag(100). The electrode potential is for equilibrium in the outer sphere mode. After [29]

theory [13], its activation energy should correspond to $\lambda/4$, where λ is the energy of reorganization. As we have argued above [20, 21], in aqueous solutions λ is half the absolute value of the energy of hydration (−3.9 eV in the bulk), so this activation energy agrees with Marcus theory. We note that close to the surface, λ decreases a little as the absolute value of energy of solvation becomes smaller in accord with the pmf for the anion.

Right on the electrode surface, at $q = 1$, there is a third minimum corresponding to the adsorbed state. Due to the effect of solvation, which favors charged particles, its charge is −1, somewhat lower than for the adsorbed state in the vacuum. Its energy is practically the same as that of the other two minima. This is the result of a compensation effect: The interaction with the metal lowers the energy by 0.4 eV, but the pmf is higher than that in the bulk by about 0.5 eV (see Fig. 5). A little bit of extra energy is gained by the change in the charge. The saddle point that separates the ionic state in the bulk from the one at the surface has an activation energy of about 0.4 eV. Within the accuracy of our calculations, this is of the same order of magnitude as the saddle point for the outer sphere step.

We have also performed calculations for a cathodic overpotential of $\eta = 0.2$ V making the reduction more favorable. The effect on the outer sphere pathway is straightforward: The energy of the ion is lowered by $-e_0\eta$, that of the molecule is unchanged, and the saddle point is lowered by the order of 0.1 V, giving a transfer coefficient of $\alpha \approx 0.5$. The effect on the rest of the surface requires a model for the variation of the potential near the surface. We have chosen a simple model in which the effect of the overpotential decays linearly between $d = 5.1$ Å, and the electrode surface, where its effect vanishes. However, the qualitative conclusions are independent of the details of this decay. The corresponding surface is shown in Fig. 7. Since the effect of the overpotential vanishes right on the surface, the energy of the adsorbed state is unchanged, and is now higher than that of the anion in the solution.

Blizanac et al. [34] have performed a thorough investigation of oxygen reduction on single crystal silver in alkaline solutions. They observed onset potentials of the order of 0.9 V RHE, which is compatible with an outer sphere mechanism. The onset potential should be close to the potential at which the outer sphere transfer is in equilibrium. From the temperature dependence of the currents, they determined the activation energies. For an electrode potential of 0.8 V RHE, which translates into an overpotential of about 0.1 V for the outer sphere reaction, they observed activation energies of the order of 0.3 eV, which are quite compatible with our theoretical values. The measured transfer coefficients are close to 0.5, in agreement with our results and typical for an outer sphere mechanism.

Thus our results suggest the following pathway: At equilibrium, the first step in oxygen reduction takes place in the outer sphere mode. The energy of the adsorbed species is about the same as that of the anion in solution, so the two species can interchange. The direct pathway from O_2 to the adsorbed anion is not favorable because of the strong rise of the pmf of the molecule near the surface (see Fig. 5). Application of a cathodic overpotential favors the anion in the solution, so that the adsorbed state becomes less favorable.

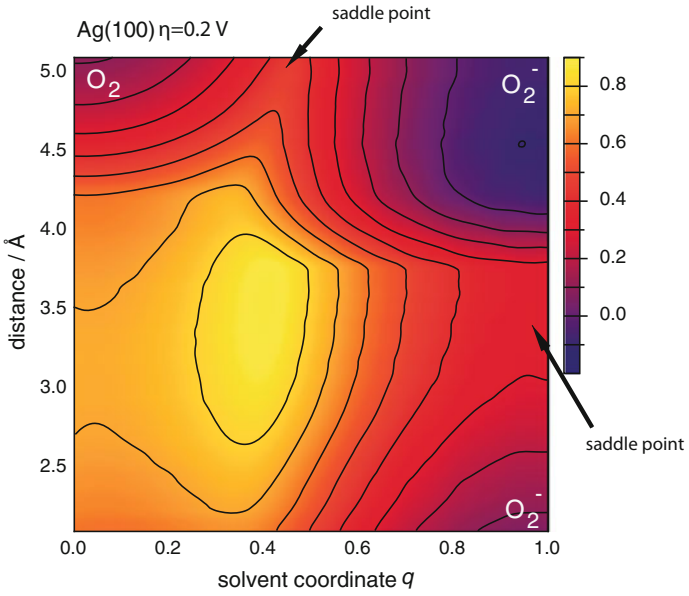

Fig. 7 Free energy surface for the reaction $O_2 + e^- \rightarrow O_2^-$ on Ag(100) for a cathodic overpotential of $\eta = 0.2$ V. After [29]

6 Conclusions

In this article, we have briefly reviewed the theory of electrocatalysis as developed in our group. It is related to older theories for outer sphere electron transfer. The new feature is that we have developed the theory so that it applicable to strong interactions between the electrode and the reactants, and are able to extract the system parameters from DFT calculations and molecular dynamics. As an example, we have presented recent results for oxygen reduction in alkaline media. For applications to other reactions, in particular to hydrogen evolution, we refer to our published works [20–22].

So far, we have mainly performed model calculations for the case where a single atom or molecule reacts. Obviously, the application of our method becomes more complicated when the number of reactants is larger. We have taken first step in this direction in our investigation of the Heyrovsky reaction on Ag(111) [35].

Acknowledgements I gratefully acknowledge financial support by the Deutsche Forschungsgemeinschaft (FOR 1376), and thank CONICET for continued support. I am also grateful for a generous grant of computing time from the Baden-Württemberg grid.

References

1. Bockris JOM, Khan SUM (1993) Surface electrochemistry: a molecular level approach. Plenum Press, New York
2. Bockris JOM, Khan SUM (1979) Quantum electrochemistry. Plenum Press, New York
3. Bockris JOM, Reddy AKN (1973) Modern electrochemistry, vol 1 and 2. Plenum Press, New York
4. Bard AJ, Faulkner LR (1980) Electrochemical methods: fundamentals and applications. Wiley, New York
5. Bockris JOM (1980) Energy options: real economics and the solar-hydrogen system energy: solar hydrogen alternative. Wiley, New York
6. Conway BE, Bockris JOM (1957) J Phys Chem 26:532
7. Gerischer H (1958) Bull Soc Chim Belg 67:506
8. Parsons R (1958) Trans Farad Soc 54:1053
9. Trasatti S (1973) J Electroanal Chem 39:163
10. Norskøv JK, Bligaard T, Logadottir A, Kitchin JR, Chen JG, Pandelov S, Stimming U (2005) J Electrochem Soc 152:J23. See also the comment on this paper: Schmickler W, Trasatti S (2006) J Electrochem Soc 153:L31
11. Levich VG (1970) Kinetics of reactions with charge transfer. In: Eyring H, Henderson D, Jost W (eds) Physical chemistry, and advanced treatise, vol. Xb. Academic Press, New York
12. Kuznetsov AM (1995) Charge transfer in physics, chemistry and biology. Gordon and Breach, New York
13. Marcus RA (1956) J Chem Phys 24:966
14. Hush NS (1958) J Chem Phys 28:962
15. Iwasita T, Schmickler W, Schultze JW (1985) Ber. Bunsenges. Phys Chem 89:38. J Electroanal Chem 194:355
16. Santos E, Iwasita T, Vielstich W (1986) Electrochim Acta 31:431
17. Schmickler W (1986) J Electroanal Chem 204:31
18. Pinto LMC, Spohr E, Quaino P, Santos E, Schmickler W (2013) Angewandte Chemie Int Ed 52:7883
19. Pecina O, Schmickler W, Spohr E (1995) J Electroanal Chem 394:29
20. Santos Elizabeth, Lundin Angelica, Pötting Kay, Quaino Paola, Schmickler Wolfgang (2009) Phys Rev B 79:235436
21. Santos E, Quaino P, Schmickler W (2012) PCCP 14:11224
22. Santos E, Schmickler W (2009) Electrochemical electron transfer: from Marcus theory to electrocatalysis. In: Koper M (ed) Cell fuel, catalysis: a surface science approach. Wiley, Hoboken
23. Anderson PW (1961) Phys Rev 124:41
24. Newns DM (1969) Phys Rev 178:1123
25. Schmickler W, Santos E (2010) Interfacial electrochemistry. Springer, Heidelberg
26. Davison S, Sulston K (2006) Green-Function theory of chemisorption. Springer, Dordrecht
27. Kramers HA (1940) Physica 7:284
28. Gerischer H (1960) Z Phys Chem NF 26:223; 27: 40,48
29. Goduljan A, Pinto L, Santos E, Juarez F, Schmickler W (2016) ChemPhysChem 17:500
30. Ramaswamy N, Mukerjee S (2012) Adv Chem Phys. doi:10.1155/2012/491604
31. Quaino P, Luque NB, Nazmutdinov R, Santos E, Schmickler W (2012) Angew Chem Int Ed 52:12459
32. Buatier de Mongeot F, Rocca M, Cupolillo A, Valbusa U, Kreuzer HJ, Payne SH (1997) J Chem Phys 106:711
33. Pinto Leandro MC, Quaino LP, Arce MD, Santos E, Schmickler W (2014) ChemPhysChem 15:2003
34. Blizanac BB, Ross PN, Markovic NM (2006) J Phys Chem 110:4735
35. Santos E, Hindelang P, Quaino P, Schmickler W (2011) PCCP 13:6992

Kinetics at Single Crystal Electrodes

Enrique Herrero and Juan M. Feliu

Abstract In this chapter, an approach to kinetic studies on single crystal platinum electrodes is attempted. The selected reactions are those called structure-sensitive, involving chemisorption steps of reactants and/or intermediates that clearly reflect site-dependent adsorption energies. For this reason, it is important to define the type of sites involved in the reaction and describe how it is possible to characterize them under electrochemical conditions. The reactivity of the different surfaces is tested against a classical probe reaction: the CO stripping in acidic and alkaline solutions. The changes observed when dissolved CO is also present are also shown. The oxidation of formic acid is then discussed, taking into account the existence of a dual-path mechanism that leads to surfaces poisoned by CO. In order to extract relevant kinetic information, the two reactions should be separated, in such a way that the experimental current could be safely assigned to the active intermediate route alone. This is discussed for different orientations and different acidic solutions. The more complex case of ethanol oxidation, which also involves CO poisoning as a result of the C–C bond breaking, a reaction step that is sensitive to the surface structure, anion adsorption and pH, is briefly described. Finally, ammonia oxidation in alkaline solution, an extreme electrocatalytic reaction that only occurs at surfaces having platinum sites with square symmetry, is addressed.

1 Introduction

The Electrodic Electrochemistry is, by definition, the part of the Electrochemistry that deals on reactions in which electrons are exchanged across interphases and is now the most important part of the Electrochemistry [1]. Initially, almost all studies on the kinetics of electron transfer reactions dealt with outer sphere processes in which species were close to the electrode surface but not necessarily adsorbed. This research line has produced a lot of works dealing with the electrode kinetics and

E. Herrero · J.M. Feliu (✉)
Instituto de Electroquímica, Universidad de Alicante, Apdo. 99, 03080 Alicante, Spain
e-mail: juan.feliu@ua.es

K. Uosaki (ed.), *Electrochemical Science for a Sustainable Society*,
DOI 10.1007/978-3-319-57310-6_5

contributed to the development of many electrochemical techniques, but single crystals were generally not used in this research. On the other hand, the studies of the heterogeneous process involving electron transfer to/from adsorbed species, usually related to the catalysis of these processes, also called electrocatalysis, are directly related with the heterogeneous catalysis, due to the presence of two phases [2–6] and we will deal with this kind of reactions in the following.

As in any heterogeneous catalysis processes, the interaction between the reactant species (in electrochemistry the species present generally in a liquid and ion conducting phase) and the catalyst (in electrochemistry, the electrode which is an electronic conducting phase) is the key element for the change in the reaction rate. This interaction should have the appropriate energy so that the global activation energy for the process is lowered. If the interaction between the reactant species and the catalysts is very weak, the energetics of the reaction path will not change much. On the other hand, if the interaction is very strong, the complex formed between the catalyst and the reactant species will have an extra stabilization energy that will make difficult any evolution from that point to the final products. Thus, the interaction between the catalyst and the reactant species should have the right energy, as enunciated in the Sabatier principle, which should involve all the relevant species at the interphase [7].

For a heterogeneous catalysis, it is easy to determine whether the added phase to the reaction is acting as a true catalyst. The reaction rate should increase in the presence of the additional phase. Thus, for a given reaction, it is possible to classify the possible catalysts according to the absolute increase of the reaction rate in the presence of the catalysts with respect to that measured in the absence of it. In Electrocatalysis, such a classification is not so simple, since the additional phase (the electrode) is always required to accept or donate the electrons needed in the desired reaction. The ideal situation, however, can be easily calculated: the thermodynamics can supply the equilibrium for a given experimental process and also can predict the conditions for a Nernstian electron transfer. In this way, if the current-potential curve follows that of a reversible transport-controlled process, the reaction would be as fast as possible under these experimental conditions. Separation from this ideal behavior will define the kinetic limitations that could be eventually corrected by choosing the appropriate electrocatalysts. The goal of the electrocatalyst will be then to achieve the conditions for which the electrodic reaction is always controlled by the transport of the reactants to the electrode surface in the whole current-potential curve.

If the key element in the heterogeneous catalysts and electrocatalysis is the interaction between the electrode and the reactant species, it is clear that the composition and the surface structure of the electrode should play a role in the electrocatalysis [3]. In a naïve approach, a change in surface composition would lead to modifications in the interaction between the reactant species and the electrode, giving rise to different reactivity. On the other hand, the different arrangements of the surface atoms of the electrode can also lead to different reactivity (see as an example reference [8]). The surface atoms have an energy that differ from that of the bulk atoms due to the different environment, and the energy of the surface

atoms is different depending on the local arrangement of the atoms. Additionally, distances between atoms in the surface can differ from those found in the bulk metal. For bidentate interactions of the species with the surface (those in which the species bonds to two atoms in the surface), the change of the distances can also alter the interaction between them due to geometrical reasons. Thus, clear differences in reactivity can be observed for some reactions depending on the surface structure.

In a usual polyoriented surface, there will be several types of sites and arrangements or sites, each of them will have a different reactivity. The measured reactivity will be the result of this complex surface, in which each site contributes in a different way. However, the total reactivity is not a simple linear combination of the reactivity of each site. Thus, it is possible that some type of site, even in very small ratio, dominates the reactivity of the surface, masking the reactivity of the rest of the sites. This could be the case when a small fraction of sites has a high activity for the reaction but the detailed mechanism of the reaction is different than that observed for the rest of the sites. When the mechanism is studied in this material, it may seem that it takes place through a well-defined mechanism. However, the reaction is occurring through, at least. two different mechanisms in the different types of sites present on the electrode surface. Another problem may appear when the onset potential of the reaction is different for the different sites or areas, as nanopatches, present on the electrode surface. It may happen that when the second type of area reaches its activation potential, the first one (which has much higher activity) is already under diffusion controlled conditions for the reaction. In this case, this second area will never operate properly for the desired reaction, since almost all of the incoming species are consumed in the most active areas. In this case, the boundary conditions for the less active areas will be disturbed by the consumption of reactants in the more active areas of the polycrystalline material [9–12]. These examples would lead to incorrect conclusions regarding the activity of these materials. Thus, the only way to measure and determine the true activity of the surface and the reaction mechanism is the use of surfaces with a well-defined surface structure, i.e., single crystal electrodes.

Single crystal surfaces have an ordered and well-defined arrangement of atoms that allow a better understanding of the nature of the reaction process. The simplest surface structures are those having a single type of site in a long range-ordered arrangement. Those are the low index planes in the face centered cubic (fcc) lattice. Since the surface structure of a practical electrode is generally very complicated, having a different types of sites and arrangements, the surface structure of the low index planes can be modified by adding a regular series of steps with a defined geometry and even further, including kinks within the steps. The systematic studies of how all these modifications affect the electrochemical reactivity allow understanding how real electrodes behave and designing better electrocatalysts. This work will review recent results of how the surface structure of the catalysts affects the electrochemical reactivity, focusing in studies with single crystal electrodes. These studies are similar to those carried out in ultra-high vacuum (UHV). However, there is a major difference, the presence of the solvent (generally water) and the ions in the solution. Thus, in the study of the interactions of the reactant

species and the electrode surface, the presence of the solvent and the ions should always be taken into account. Consequently, the interactions between the surface and the reactant species should always be stronger than those of the solvent or ions in solution to find an effective electrocatalytic behavior.

2 Nomenclature of Single Crystal Surfaces

Single crystal surfaces of platinum, gold, palladium, and iridium are the most studied because their catalytic activity. Those metals have an fcc structure. For fcc metals, the so-called low index planes have a single type of site arranged in a theoretically infinite long range 2D structure. These surfaces are the (111), (110) and (100) surfaces (Fig. 1) and the atoms are arranged with a hexagonal, rectangular and square symmetry, respectively. The (111) surface has the highest atomic packing density of all the surfaces and also the surface atoms have the highest number of nearest neighbors 9, compared to 12 nearest neighbors of a bulk atom in a fcc lattice. For this reason, this surface has the lowest surface energy (the energetic environment of the surface atoms is the closest to the bulk in any possible surface) and, for several electrochemical reactions, the behavior is different from the rest. The surface atoms of the (100) plane have 8 nearest neighbors and the (110) plane 6. Due to the lower coordination number, these surface atoms are generally more reactive to adsorption than those of the (111) surface.

The low index surfaces are located in the vertices of the stereographic triangle (Fig. 2). In the edges of this stereographic triangle, the stepped surfaces are found. The ideal structure of these surfaces combines terraces of different width with the surface structure of the closest vertex and monoatomic steps with the symmetry of the second vertex. Thus, in the line connecting the (111) and (100) surfaces in the stereographic triangle, the step surfaces having (111) symmetry terraces and (100) monoatomic steps and (100) symmetry terraces and (111) monoatomic step are found. The closer to the (111) vertex, the longer the terrace with the (111) symmetry will be. In this line, the (311) surface is the so-called turning point, since it can be considered that this surface has monoatomic terraces with (111) symmetry separated by a (100) monoatomic step or, equally, monoatomic

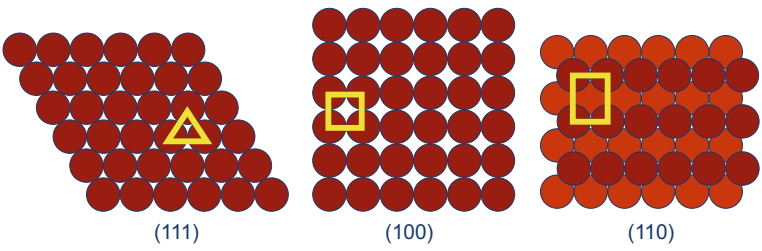

Fig. 1 Scheme of the (111), (100) and (110) surfaces of a fcc metal

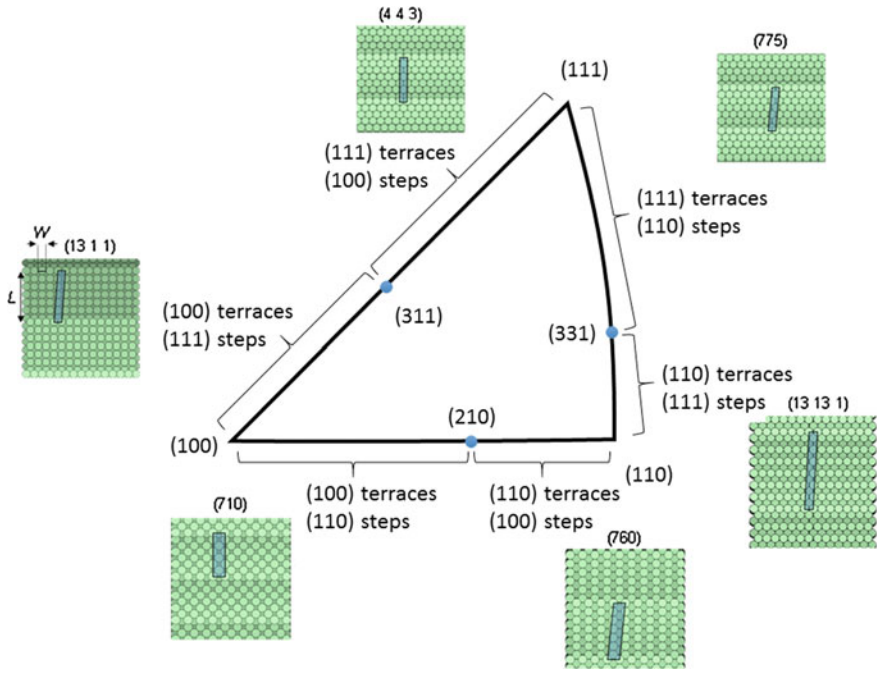

Fig. 2 Stereographic triangle for a fcc metal showing the low index planes and the different stepped surfaces

terraces with (100) symmetry and a (111) monoatomic step. For the other edges of the stereographic triangle the situation is similar. However, it should be always taken into account that the (110) surface can also be considered as a stepped surface with (111) monoatomic terraces and a (111) monoatomic step or a stepped surface with (100) monoatomic terraces and a (100) monoatomic step.

The Miller indices of these surfaces are normally used for their notation. However, it is generally more convenient the use of the Lang, Joyner and Somorjai (LJS) [13] nomenclature, which gives the information on the symmetry and length of the terrace and the symmetry of the monoatomic step. In this notation the surfaces are named as:

$$\mathrm{M(hkl)} = \mathrm{M(S)}\left[n\left(\mathrm{h'k'l'}\right) \times \left(\mathrm{h''k''l''}\right)\right], \tag{1}$$

where M is the symbol of the metal, S stands for stepped surface, (hkl), (h′k′l′), and (h″k″l″) are the Miller indices of the stepped surface, the terrace, and the step orientations, respectively, and n indicates the number of atomic rows in the terrace. Table 1 gives the relationship between Miller indices and the LJS notation. For the surfaces with (110) steps, both notations using a (110) or the corresponding (100) or (111) steps are given.

Table 1 Notations for the stepped surfaces platinum

Zone	LJS notation	Miller indices
[1$\bar{1}$0]	Pt(S)[n(111) × (111)] ≡ Pt(S)[(n–1)(111) × (110)]	Pt(n, n, n − 2)
	Pt(S)[n(110) × (111)]	Pt(2n − 1, 2n − 1, 1)
[01$\bar{1}$]	Pt(S)[n(111) × (100)]	Pt(n + 1, n − 1, n − 1)
	Pt(S)[n(100) × (111)]	Pt(2n − 1, 1, 1)
[001]	Pt(S)[n(100) × (100)] ≡ Pt(S)[(n–1)(100) × (110)]	Pt(n, 1, 0)
	Pt(S)[n(110) × (100)]	Pt(n, n − 1, 0)110

3 Electrochemical Characterization of the Pt Single Crystal Electrodes

When the electrocatalysis is to be studied, it is important to determine what are the species adsorbed on the electrode surface, since those species can affect the reactivity of the surface toward the desired reaction. In this sense, the electrochemical techniques provide tools for their characterization. The use of the flame annealing technique in the process of ordering and cleaning of the Pt electrodes gave the first evidence that the voltammograms of the Pt single crystal electrodes have significant differences from the typical voltammograms recorded for a polycrystalline sample [14, 15]. This fact implies that surface processes that give rise to those voltammetric profiles are very dependent on the surface structure. For this reason, the voltammograms of the electrodes can be used as fingerprints to determine the quality and cleanliness of the surface. As can be seen in Fig. 3, the voltammograms of the different well-ordered surfaces show distinct features in perchloric and, sulfuric acid as well as sodium hydroxide solutions, which allow, by a simple visual inspection to establish the type of Pt surface under scope. In order to obtain these well-ordered surfaces, the annealing conditions, especially the atmosphere in which the electrodes are cooled, have to be carefully controlled [16–19]. The signals presented in this figure clearly correspond to reversible adsorption processes on the Pt surfaces; they are symmetrical and the currents are proportional to the scan rate.

Although voltammetry is a powerful technique for the assessment of the quality of the surface, it presents some problems in the determination of the nature of the species involved in the charge transfer processes observed in the voltammograms. The features sown in Fig. 3 can be assigned to oxidation or reduction processes, according to the sing of the current, but nothing can be said regarding the species involved in the processes. Thus, the signals recorded in the positive scan direction are associated to oxidation processes (currents are positive), but they can correspond to the hydrogen desorption process according to the reaction

$$\mathrm{Pt - H \rightarrow Pt + H^+ + e^-} \tag{2}$$

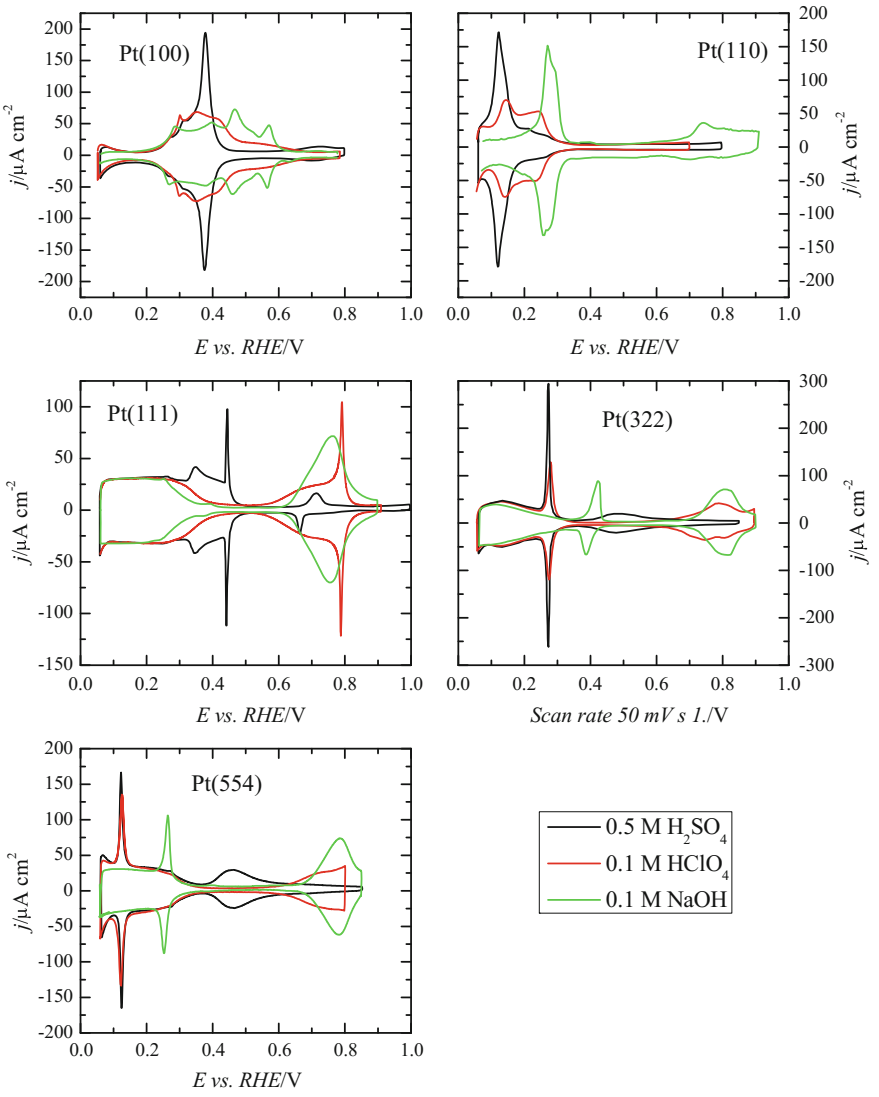

Fig. 3 Voltammetric profiles of different platinum single crystal electrodes in different supporting electrolytes. Scan rate: 50 mV/s

or to an anion adsorption process with a charge transfer:

$$Pt + A^- \rightarrow Pt - A + e^- \quad (3)$$

After several years, the charge displacement experiments at constant potential using a neutral adsorbing probe (for instance with CO or I) provide the first evidence on the nature of the species [20–26]. Thus, when the currents recorded in a

charge displacement experiment are positive, they correspond to the replacement of adsorbed hydrogen by CO according to:

$$\mathrm{Pt-H+CO \rightarrow Pt-CO+H^+ + e^-}, \tag{4}$$

whereas negative currents correspond to the displacement of an anion

$$\mathrm{Pt-A+CO+e^- \rightarrow Pt-CO+A^-} \tag{5}$$

This simple experiment then allowed determining whether the adsorbed species at a given potential was either hydrogen or the corresponding anion present in the solution. The assignment of the signal to the different processes has been confirmed later by other chemical sensitive techniques, as XPS or Raman [27].

Although a detailed description of the behavior of these surfaces processes can be found elsewhere [28–34], here the main features that can be important in the discussion of the electrocatalysis of these surfaces will be presented. At potential close to hydrogen evolution, hydrogen is adsorbed in all the surfaces with different degrees of coverage. If the potential is increased, hydrogen is desorbed. For the Pt (111) electrode (Fig. 3a), this desorption process results in currents that decay at ca. 0.30 V, potential at which the hydrogen coverage is close to zero. In perchloric and alkaline solutions, currents diminish at this potential value to reach those typical of the double layer of Pt at ca. 0.4 V. In these supporting solutions, current increase again due to the OH adsorption processes at ca. 0.6 V, to give rise to a single wave (with a shoulder) in alkaline solutions or two different processes in perchloric acid solutions [35]. In sulfuric acid solutions, the signal appearing between 0.35 and 0.5 V is related to the adsorption of sulfate, which give rise to the formation of an ordered ($\sqrt{3} \times \sqrt{7}$) sulfate adlayer after the spike at 0.45 V [36–38].

For the stepped surfaces with (111) terraces, the presence of the step can be visualized by the appearance of an additional peak in the hydrogen region, whose potential depends on the nature of the electrolyte and the step symmetry. The charge under the peak is directly proportional to the step density [28, 29, 39]. The other features related to the (111) terrace appear at ca. the same potentials than those measured for the Pt(111) surface, but their charge diminishes as the step density increases. Thus, the (110) steps give raise to a peak at 0.125 V in perchloric and sulfuric solutions and at 0.27 V in alkaline solutions, whereas the peak for the (100) steps appears at 0.32, 0.26, and 0.45 V in perchloric, sulfuric, and alkaline solutions, respectively. Regarding the nature of the species adsorbed on the step, at potentials negative to the peak, the step is covered by hydrogen. However, it is still not clear whether the step has adsorbed anions at positive potentials. For the (100) steps, the peak shift when sulfuric acid is added with respect to that observed in perchloric acid solutions indicates that sulfates could be adsorbed on the step. On the other hand, for the (110), the constancy of the peak potential in these solutions would suggest that anions are not adsorbed. The peak shift to positive potentials in

alkaline solutions would suggest a possible difference regarding the chemical nature of the adsorbed species at high pH values with respect to acid solutions [40]. However, a simpler option is that the peak positions are simply reflecting the change of lateral interaction between adsorbates and water present on the surface before and after the electron transfer processes generating the species involved in a particular peak [41]. New experiments are required to determine the nature of the species involved in these processes.

For the Pt(111) electrode, hydrogen and anion adsorption processes in perchloric and alkaline solutions are well separated. However, for the other two basal planes, both processes overlap. In perchloric acid solutions, the signals for the Pt(100) electrode below 0.4 V correspond to hydrogen adsorption-desorption processes, whereas the wave that appears between 0.4 and 0.5 V is related to adsorbed OH [42–44]. Although the overall shape of the voltammograms is different, the potential regions where H and OH are adsorbed in alkaline solutions are very similar to those in perchloric acid for this electrode [32]. In the presence of strong adsorbing anions, such as sulfate, an intense peak appears which is related to the competitive adsorption process of hydrogen and sulfate [45]. Thus, at potentials positive to the peak, anions are adsorbed, whereas at negative values, hydrogen is the specie on the surface.

The behavior of the Pt(110) electrode is qualitatively similar to the Pt(100) plane [43]. In perchloric and alkaline solutions, the main signal can be ascribed to the hydrogen adsorption-desorption process, whereas, the small features that appear at a shoulder of the main peak at positive values can be assigned to OH processes. Again, the peak in sulfuric acid solution can be associated to the competitive adsorption process between sulfate and hydrogen. Recently, a CO cooling treatment has been proposed, and the reactivity associated with the resulting surface is under scope, although the nature of the adsorbed species is the same [19, 46].

Regarding the behavior of the electrodes in perchloric acid and alkaline solutions, one would expect that, a priori, the voltammograms in both media where the same in the RHE scale, since the involved species in the adsorption processes are the same: hydrogen and OH. Although the stability ranges are very similar, the clear changes in the voltammograms between both media indicate that there are changes in the interaction of these species, especially OH, with the surface as the pH changes. These changes can be related to the effect of the modifications in the interaction between the adsorbed species with the interfacial water as pH varies [41] or, even, to a different nature of the adsorbed species (OH and O) as has been proposed for the (100) and (110) steps on the (111) terraces [40]. As will be shown later, these changes will affect the reactivity of the surfaces with respect to the studied reaction. It is clear that the control of the surface structure and composition in the whole experiment is a prerequisite to perform kinetic studies. If the employed surfaces are disordered or contaminated, the interpretation of the experimental data would be misleading.

4 Kinetics of Adsorbed CO Oxidation on Pt(h k l) Surfaces

CO oxidation may look as a rather simple reaction since it involves the exchange of only two electrons, according to the general reaction:

$$CO + H_2O \rightarrow CO_2 + 2H^+ + 2e^- \quad (6)$$

However, the oxidation process on platinum electrodes has several complications. First, CO is strongly adsorbed on Pt due to the well-known donation/back donation mechanism. Filled 5σ orbital of CO donates electrons to the metal paired with a back donation of electrons from the metal to the 2π orbital of CO [47]. This donation/back donation process is surface and potential dependent [48]. Second, the oxidation process to CO_2 requires the transfer of an oxygen atom to the CO to form a second C–O bond. This step is normally the rate determining step in the process. Thus, two possible oxidation mechanisms can be envisaged: Langmuir–Hinslewood (L-H) or Eley–Rideal (E-R) mechanisms, depending whether the species transferring the oxygen atom is adsorbed or in solution, respectively.

The oxidation of adsorbed CO layers on platinum electrodes in acidic solutions normally gives rise to a single oxidation peak, with the presence of occasional shoulders and pre-peaks (Fig. 4). The reactivity order is Pt(110) > Pt(100) > Pt (111) [49]. On Pt(111) electrodes, a single peak is normally obtained and the charge associated to the oxidation of CO, after the appropriate corrections related to double layer and anions readsorption, corresponds to a coverage of ca. 0.68 [25, 50]. This coverage value is related to the formation of an ordered structure $(\sqrt{19} \times \sqrt{19})$ R23.4° $- \Theta_{CO} = 0.68$ [51]. For the CO adlayer on Pt(111) electrodes, two additional structures have been also identified, the $(2 \times 2) - \Theta_{CO} = 0.75$ adlayer [51, 52] with a higher coverage, which is only stable when CO is dissolved in the electrolytic solution [53] and the $(\sqrt{7} \times \sqrt{7})$ R19.1° $- \Theta_{CO} = 0.56$ [51], with a lower coverage, close to the $c(4 \times 2) - \Theta_{CO} = 0.5$ adlayer observed in UHV environments at room temperature [54].

When the kinetics of this oxidation process is analyzed for the Pt(111) single crystal electrode in acid solution it was found that the oxidation mechanism followed a L-H mean field mechanism [55, 56], according to the reaction mechanism

$$Pt + H_2O \rightleftarrows Pt - OH + H^+ + e^- \quad (7)$$

$$Pt - CO + Pt - OH \rightarrow 2Pt + CO_2 + H^+ + e^- \qquad \text{r.d.s} \quad (8)$$

in which the first step is fast and the second one is the rate determining step (r.d.s). The mean field mechanism assumes a random distribution of CO and OH species on the electrode surface. Since the reaction occurs when two neighboring adsorbed OH and CO species react, the random distribution implies that the mobility of OH and/or CO on the surface is fast, much faster than the reaction rate, so that a random

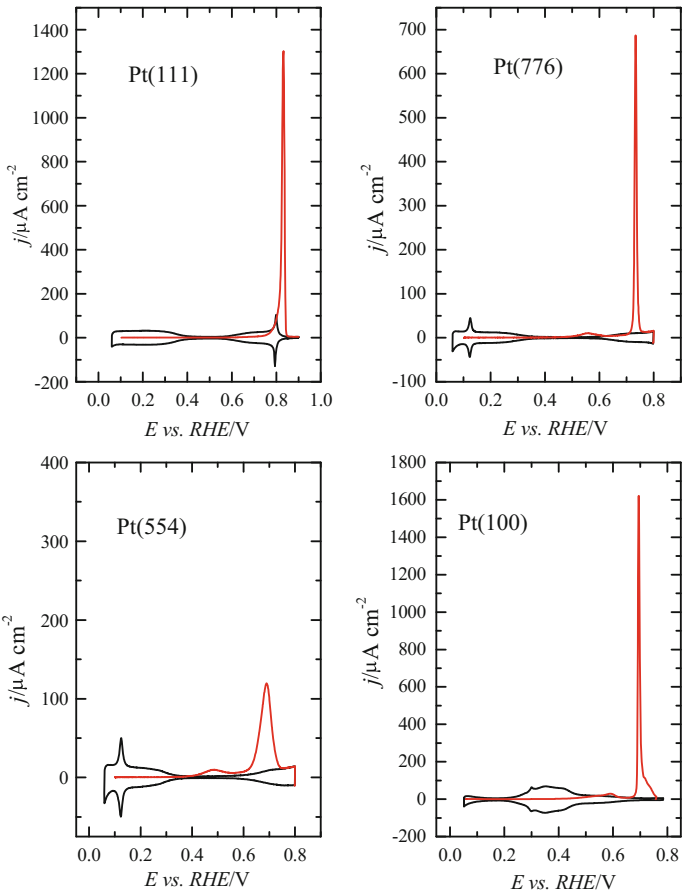

Fig. 4 CO stripping profiles on different Pt single crystal electrodes in 0.1 M $HClO_4$. Scan rate: 50 mV s^{-1}

distribution is always attained [57]. This mean field mechanism allowed determining the activation energy of the oxidation process on Pt(111) and Pt(100) electrodes, which is in the range between 110 and 140 kJ mol^{-1} [49, 58]. Also, this oxidation mechanism helped to explain the Tafel slope measured in acid solutions, which stands for ca. 70 mV [49, 55, 56, 58–61]. Typically, a Tafel slope close to 60 mV is associated to a mechanism in which the r.d.s. is a chemical reaction after the first electron transfer, which is not in agreement with the mechanism of Eqs. (7) and (8). For a mechanism in which the r.d.s is the second electron transfer, a Tafel slope value of 40 is normally expected, but this is only strictly true when, in the first electron transfer reaction, adsorption processes of the different species are not involved. When adsorption processes appear (as happens in Eq. 7), the Tafel slope value will depend on the actual coverage and on the adsorption isotherm. For these

reasons, a value of ca. 60–70 mV is experimentally obtained, although the second electron transfer is the r.d.s. [62].

When the oxidation is studied on stepped surfaces with (111) terraces, a clear catalytic effect of the presence of the (110) steps is obtained. In voltammetry, the oxidation peak shifts to lower potential values (Fig. 4). When the reaction rate is determined using chronoamperometric experiments, it is found that the oxidation rate is directly proportional to the step density [56]. In fact, the extrapolation of the results obtained with stepped surfaces to a perfect (111) indicates that the reaction rate for this perfect surface would be negligible. This reactivity trend for a perfect Pt (111) surface is in agreement with the proposed L-H mechanism. On a prefect and well-ordered ($\sqrt{19} \times \sqrt{19}$) R23.4° − $\Theta_{CO} = 0.68$ structure, there is no possible OH adsorption, so that the reaction cannot be initiated. When steps or defects are present on the surface, they act as initiators of the reaction, so that it can proceed until the eventual oxidation of the CO adsorbed layer. The (100) steps on (111) terraces also catalyze the CO oxidation reaction, but to a lower extent than (110) steps [63, 64]. Additional experiments highlight the role of the step in the mechanism. Step decoration with a foreign adatom (leaving the terrace free) leads to a significant diminution of the reaction rate [63, 64]. Moreover, it has been proposed that the inner corner of the step is the reactive site of the process, where OH adsorption takes place to activate the mechanism [61]. This fact explains the deactivation when adatoms decorate the step, since the adatom is preferentially adsorbed at this site in the initial deposition stages [65, 66]. Thus, it can be proposed that the CO oxidation reaction on these step surfaces is initiated on the lower part of the step. Once the initial holes on the adalyer are created, CO molecules diffuse over the terrace and create new holes where OH can adsorb, so that the reaction progresses through the mean field mechanism.

For the stepped surfaces with (100) terraces, the presence of (111) steps catalyze the oxidation of CO [67], with a behavior qualitatively similar to that found for (111) surfaces. However, it should be always taken into account that the prepared (100) surfaces have higher amount of defects due to the lifting of the hex reconstruction to the (1 × 1) structure when the electrode is put in contact with the electrolytic solution [19]. At the annealing temperatures, the Pt(100) surface reconstructs to form an hexagonal structure, which has a higher atomic density. When the reconstruction is lifted during the immersion of the electrode in the solution, the extra atoms present on the surface form monoatomic-high islands, which increase the defect density. For the surfaces having (110) terraces, the presence of the steps leads to a complex behavior, probably related to the possible reconstruction of these surfaces [68].

When the CO oxidation process is studied in alkaline media, the oxidation charges and peak potentials are very similar. However, two main differences are observed. The first one is the appearance of multiple peaks in the CO oxidation process when stepped surfaces with (111) terraces are studied [69, 70]. Two peaks are observed, one at low potentials, whose charge is proportional to the step density, and the second one that appear at potentials similar to that observed for the Pt(111) surfaces (Fig. 5). Moreover, the peak related to the presence of (110) steps appear at

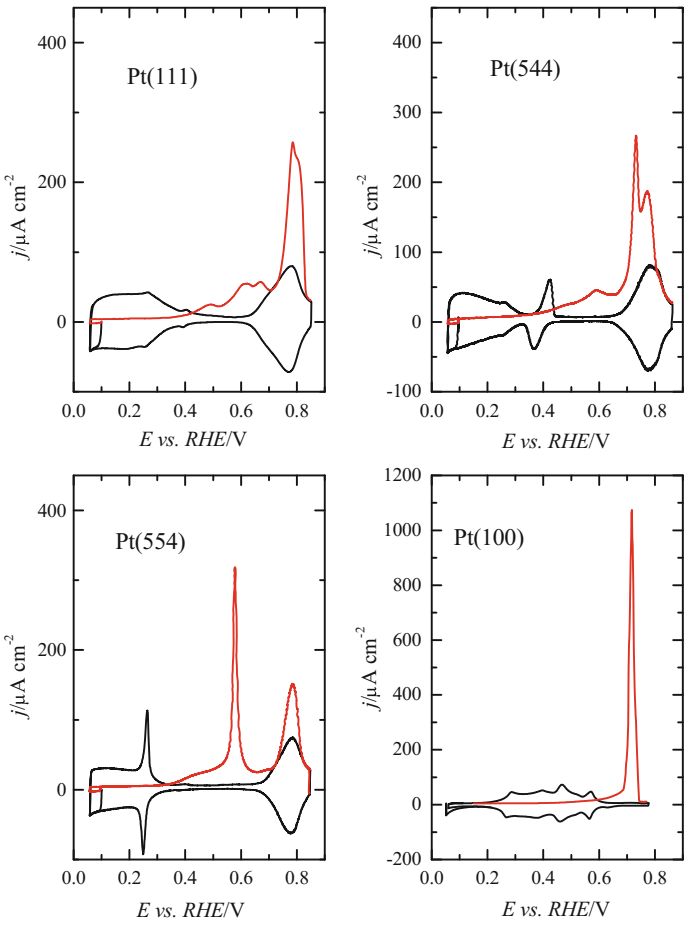

Fig. 5 CO stripping profiles on different Pt single crystal electrodes in 0.1 M NaOH. Scan rate: 50 mV s^{-1}

potentials lower than that associated to the presence of (100) steps. Additionally, for kinked surfaces, the peaks associated to terrace, step and kink are clearly visible. The appearance of peak multiplicity indicates changes in the oxidation mechanism in alkaline solution with respect to that described in acidic solutions. In order to study the kinetics of the process, chronoamperometric transients where recorded [71, 72]. The transients have a bell shape, similar to that recorded in acidic conditions, but with a characteristic tailing at the end of the process. Two different models have been used to fit the transients: a mean field L-H kinetics superimposed with an exponential decay related to the oxidation of CO on the steps [71], and a nucleation and growth kinetics coupled with anisotropic effects [72]. This two kinetic models corresponds to two situations which differ on the mobility of CO on

the surface. The mean field L-H kinetics implies that CO is very mobile on the surface and the appearance of the two peaks in stepped surfaces is related to the blockage of the reactive sites after the initial oxidation of CO on these sites [70]. On the other hand, the nucleation and growth kinetics means that the CO is not mobile. Since the presence of the specie which is blocking the reactive sites after the initial oxidation has not been detected [72], the low mobility of CO on the surface seems to be the most probable cause of the peak multiplicity. Thus, the oxidation mechanism on these surfaces is also initiated at the low part of the step leading to the oxidation of all CO molecules directly neighboring these sites, which give rise to the peak at low potentials. Unlike the situation observed in acid, since the CO diffusion rate is slow, no holes are created in the terrace, and the oxidation process stops until the electrode potential reaches the value at which CO is oxidized on the (111) terrace [73]. This oxidation process gives rise to the peak at high potentials. The last CO molecules to be oxidized are those adsorbed on the top of the steps.

Conversely, a single peak is always observed for surfaces having (100) terraces, and the presence of the step is catalyzing the oxidation of CO for terraces with $n > 4$ [32]. The presence of a single peak in this case is probably related to the small difference in the adsorption energies of the step and terraces for the surfaces having (100) terraces [66]. These small differences normally imply that the reactivity of the (100) terraces and steps on those surfaces are very similar, unlike what it is observed for the surfaces with (111) terraces. Thus, processes on both type of sites cannot be resolved. In the surfaces with (111) terraces, the higher difference between the adsorption energies of (111) terraces and steps [74] leads to a clear separation of both processes, as has been experimentally observed.

The second important difference is the usual appearance of an oxidation pre-peak at low potentials for all the surfaces (Fig. 4). These pre-peaks were first occasionally observed in acid solutions and its appearance depends on the CO adsorption conditions [75–79]. In alkaline solutions, the pre-peak is normally very prominent. As happens in acidic solutions, the CO adsorption conditions, essentially, the electrode potential at which CO is adsorbed, are the key element in the appearance of the pre-peak [80]. When CO is adsorbed at 0.1 V versus RHE in acidic solutions and then transferred to an alkaline solution, the pre-peak is absent [81] (Fig. 6). Moreover, CO oxidation peaks are narrower and shift to higher potential values, indicating that the CO adlayer has lower amount of defects. If the electrode potential is reversed after the pre-peak, it can be observed that hydrogen adsorption is still blocked by the presence of the CO layer [70, 81]. Thus it has been proposed that the pre-peak corresponds always to the initial stage of the CO oxidation process to form a less compact adlayer. This oxidation process is triggered by the presence of defects in the adlayer. If the adlayer is formed in acidic solutions, the high mobility of CO on these environments leads to the formation of a more ordered adlayer with a lower amount of defects. Thus, in acid solutions or when the electrode is transferred to alkaline solutions, no pre-peak is observed [81]. On the other hand, when the adlayer is formed in alkaline solutions, the low mobility of CO necessarily implies the formation of CO adlayers with a higher number of defects. Those defects trigger the oxidation of CO at low potential to form a more

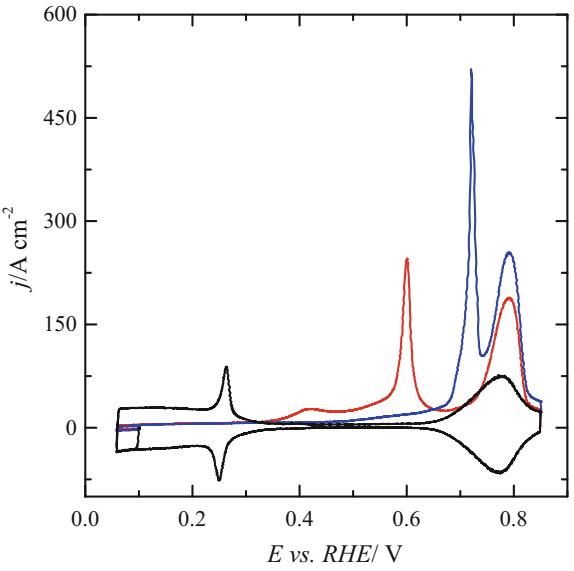

Fig. 6 Voltammetric profile on a Pt(776) electrode for CO stripping in 0.1 M NaOH when CO adsorbed at 0.1 V in 0.5 M H_2SO_4 (*blue line*) and when CO adsorbed at 0.1 V in 0.1 M NaOH (*red line*). The *black curve* is the blank voltammetry. Scan rate: 0.05 V s^{-1} (Color figure online)

relaxed adlayer. It should be stressed that the CO coverage attained in acidic and alkaline solutions is very similar [81], which highlights the role of a relatively low number of the defects in the oxidation mechanism.

The behavior of the CO oxidation process when CO is present on the solution responds to the same rules, that is, the initial stages of the oxidation depends on the number of defects in the CO adalyer, and CO mobility and anion adsorption form electrolyte play significant roles in the process [62, 82, 83]. The typical voltammograms under these conditions are shown in Fig. 6. In these voltammograms, no current in the positive scan direction is observed up to ca. 0.85 V, where a sharp spike appears. The onset potential for the oxidation is higher than that recorded in the absence of CO in solution due to the "healing effect" of solution CO. In the initial stages of the oxidation, when the potential dependent oxidation rate is still low, the free sites created by the incipient CO oxidation are immediately covered by CO adsorption, retarding the oxidation process. As the potential increases, the reaction rate increases, reaching a potential where all CO adsorbed molecules are oxidized giving rise to the spike. It should be noted that the charge of this spike contains not only the contribution form the initially adsorbed CO molecules, but also those corresponding to bulk CO molecules that have been adsorbed and oxidized. After the spike, the CO oxidation process is controlled by the diffusion of CO to the surface, giving rise to the limiting diffusion current. In the negative scan direction, this limiting current is maintained until the CO adsorption rate is faster than the CO oxidation rate. As aforementioned, the spike potential in the positive scan direction and the potential for decay in the negative scan direction depends on the number of defects. This effect can be readily observed in Fig. 7, where both potentials shift to lower values as the step density increases [82], as happen in the

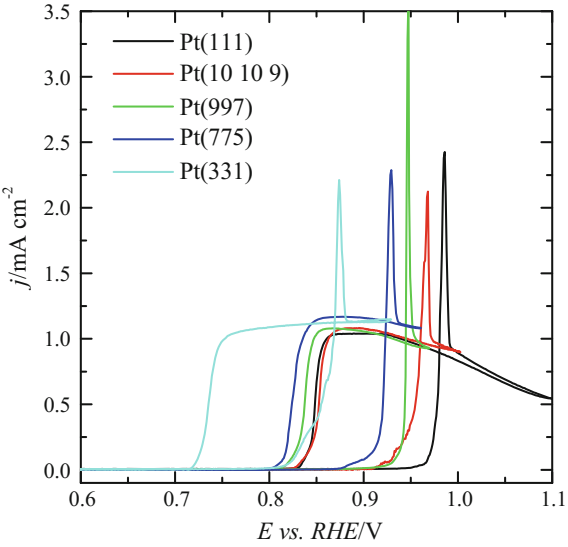

Fig. 7 Saturated CO-bulk oxidation voltammograms for the Pt(111) and vicinal electrodes 0.1 M H_2SO_4 at 20 mV s^{-1} and 600 rpm

absence of CO in solution. Also, strong anion adsorption (sulfate or chloride) leads to higher potential values [83].

5 Kinetics of Formic Acid Oxidation on Pt(h k l) Electrodes

Formic acid has the same oxidation state than CO, e.g., its oxidation only requires the transfer of two electrons. However, the catalysis of the oxidation reaction is different. Here, to obtain CO_2, one C–H bond and one O–H bond have to be broken but no new bonds have to be formed a priori, because the reactant contains all oxygen atoms to generate the product. The second bond to be broken is that involved in the acid–base equilibrium of formic acid, and thus it is rather simple process. For the C–H bond breaking, which can be regarded as dehydrogenation step, platinum or palladium electrodes are very active [84], and thus the oxidation of formic acid takes place at lower overpotentials than those required for the CO oxidation reaction. Additionally, formic acid is adsorbed on the electrode surface as formate [85], but this adsorption process is weaker than that CO. According to that, the oxidation mechanism on platinum electrodes should have been simpler. However, the voltammograms indicate the presence of a poisoning species [84], which is identified by IR as adsorbed CO [86]. The presence of CO implies an additional complication to the mechanism. A C–O bond has been broken, which imposes the necessity of an extra step in the oxidation mechanism to form a new C–O bond and yield CO_2. As aforementioned in previous section, CO is strongly adsorbed and its

oxidation is difficult, so that CO can be considered as a poison intermediate. Thus, in the oxidation mechanism on platinum electrodes, there is a reaction path through a poison intermediate, i.e., adsorbed CO. The presence of a second path, going through a different intermediate, was confirmed using isotopically labeled CO and differential electrochemical mass spectrometry (DEMS) [87]. This reaction path is also called the active intermediate path, since it is active to yield CO_2 at low potentials. Thus the mechanism can be summarized as:

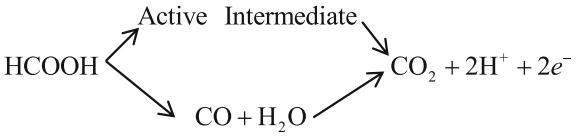

(9)

The step leading to the formation of adsorbed CO is a dehydration step in which no electrons are transferred, and thus it is expected that is not affected by the electrode potential. On the other hand, the nature of the active intermediate is still under discussion. However, it is clear that formate from solution is the active species in the oxidation reaction [88–91] and that adsorbed formate is also involved in the reaction mechanism [85, 92–101]. The existence of a reaction path going through CO requires a complex strategy in order to catalyze the reaction on Pt. Since CO blocks the surface and prevents the oxidation of the molecule through the active intermediate, this reaction path is not desirable. Thus, the different strategies for increasing the activity of the catalysts seek the enhancement of the reaction rate through the active intermediate path and the inhibition of the CO formation.

The initial studies of the effect of the surface structure on this reaction revealed that it was very sensitive to the surface structure [102], as shown in Fig. 8. Additionally, there was a clear hysteresis between the positive and negative scan directions. In the positive scan direction, currents were smaller due to the formation of adsorbed CO at low potentials, which partially blocks the surface [103–105] and hinders the reaction through the active intermediate. As shown in the previous section, CO is only oxidized above 0.7 V. From that potential, the surface becomes free from CO and the reaction in the negative scan direction is free from CO, so currents are higher. Thus, the higher difference between the currents in the positive and negative scan directions, the higher activity for CO formation. As can be seen in Fig. 8, the order of activity for the formic acid oxidation is Pt(100) > Pt (110) > Pt(111). The same reactivity order is obtained for the CO formation step, that is, the Pt(100) electrode is the one showing higher poisoning rate.

When studying the CO dehydration step on platinum single crystal electrodes modified by the presence of adatoms, the first significant differences appeared between the Pt(111) electrodes and the rest. Very low adatom coverages were required to completely inhibit poison formation on the Pt(111) electrode [104, 106, 107], whereas on the Pt(100) electrode, the dehydration step was only prevented at high coverage values [105, 108, 109]. At these coverage values, only isolated sites were present on the surface, which suggested that the dehydration path requires, at least, two contiguous Pt sites to occur, more than those involved in the direct

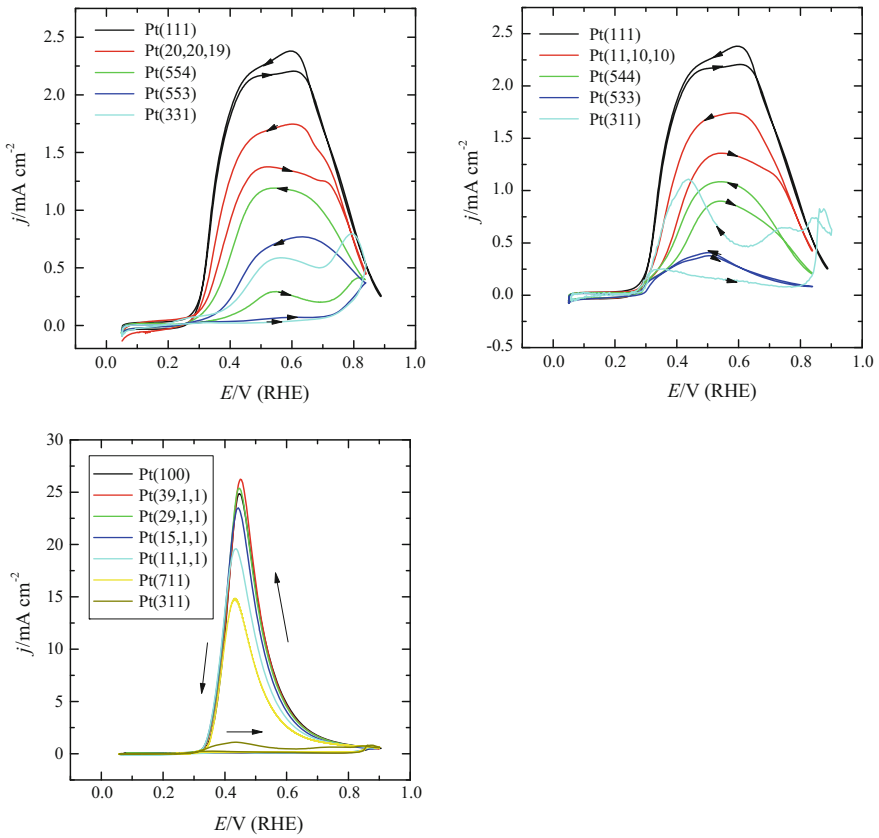

Fig. 8 Voltammetric profile of different Pt single crystal electrodes in 0.1 M HCOOH + 0.5 M H_2SO_4. Scan rate: 50 mV s^{-1}

oxidation. The origin of such prominent difference was explained when adatom decorated stepped surfaces with (111) terraces were used. It was found that CO formation was completely inhibited on decorated surfaces [110–112], which clearly evidenced that the dehydration step on the Pt(111) surfaces only takes place on defects. Since adatoms adsorb preferentially on the defects on the Pt(111) electrode [65], very small amount of adatoms were required to completely block the small fraction of reactive sites for the dehydration reaction on the real Pt(111) electrode.

The quantitative analysis of the kinetics of the oxidation reaction has been made using the transients obtained the pulsed voltammetry first used by Clavilier [113]. In this technique, a pulse to potentials above 0.85 V is superimposed to the voltammetric ramp. In this pulse, all the CO molecules accumulated on the surface are oxidized, so that when the electrode returns to the previous potential value, the surface is free from adsorbed CO. A general scheme of the pulse can be seen in the

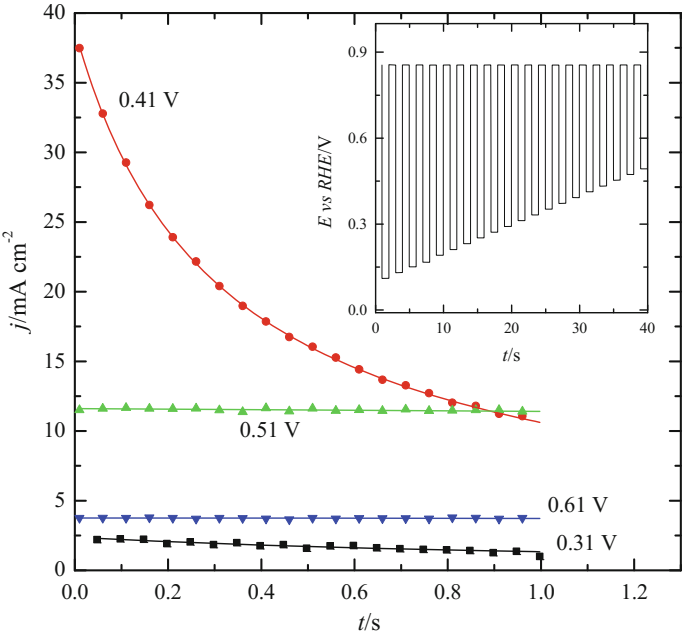

Fig. 9 Transients recorded during the pulsed voltammetry for the Pt(100) electrode in 0.5 M H_2SO_4 + 0.1 M HCOOH. Inset: Potential program of the pulsed voltammetry

inset of Fig. 9 [114]. Normally, the transient currents show a decay (Fig. 9), which, in absence of transport limitations, is due to the formation of CO. Additionally, the currents at $t = 0$ represents the activity of the surface for the reaction path through the active intermediate. If the potential of the transient is lower than 0.6 V, it can be considered that CO oxidation rate is negligible, and the transient will contain the information on the active intermediate path and the dehydration step, but not on the CO oxidation step. The recorded transients obtained after the pulse at high potentials can be then modeled to obtain the relevant parameters of the oxidation mechanism, that is, the activity of the reaction for the active intermediate by the extrapolation of the transient to $t = 0$, and the rate for formation of CO through the dehydration path, which is related to the rate of decay in the current [114–116]. The analysis of the parameters obtained from the model has allowed to verify that the dehydration step takes place in a narrow potential window. In fact, the narrow region where measurable rates are obtained is centered around the local potential of zero total charge of the considered site, as can be seen in Fig. 10 [114, 115, 117]. Thus, the reactivity order for the dehydration step on the different sites is the following:

(100) terraces ≈ steps on (100) terraces > (110) steps on (111) terraces > (100) steps on (111) terraces having (111) terraces a negligible activity for this reaction.

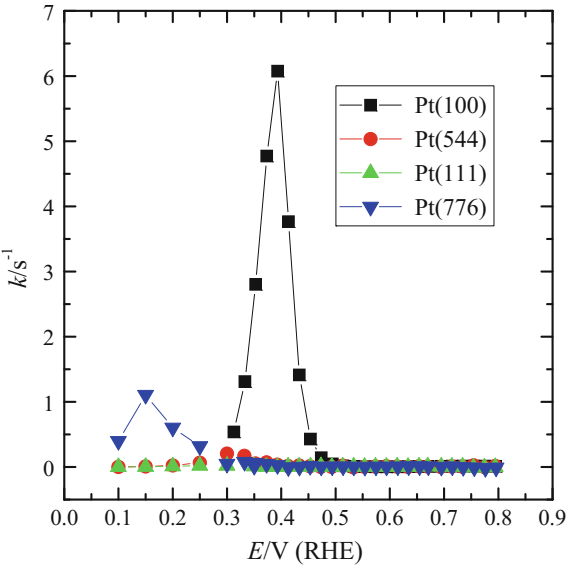

Fig. 10 Reaction rate for the dehydration step on different platinum surfaces in 0.5 M H_2SO_4 + 0.1 M HCOOH

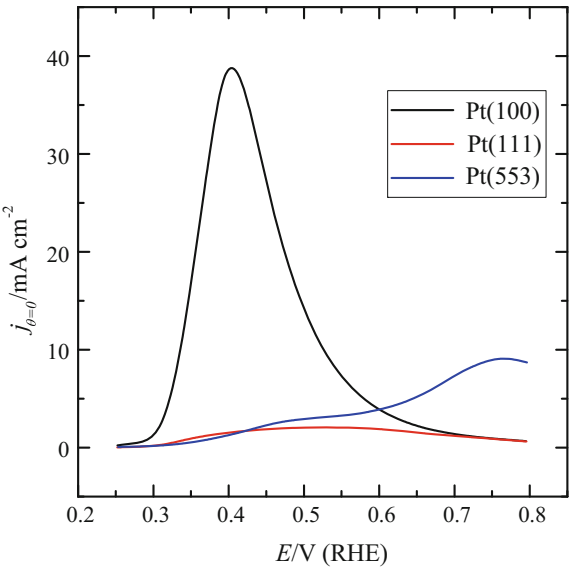

Fig. 11 Currents at t = 0 for the active intermediate path on different platinum surfaces in 0.5 M H_2SO_4 + 0.1 M HCOOH

On the other hand, the reactivity order for the active intermediate path, measured as the extrapolated current at $t = 0$ (Fig. 11) at low potentials is

(100) terraces ≈ steps on (100) terraces > (111) terraces > (110) steps on (111) terraces > (100) steps on (111) terraces

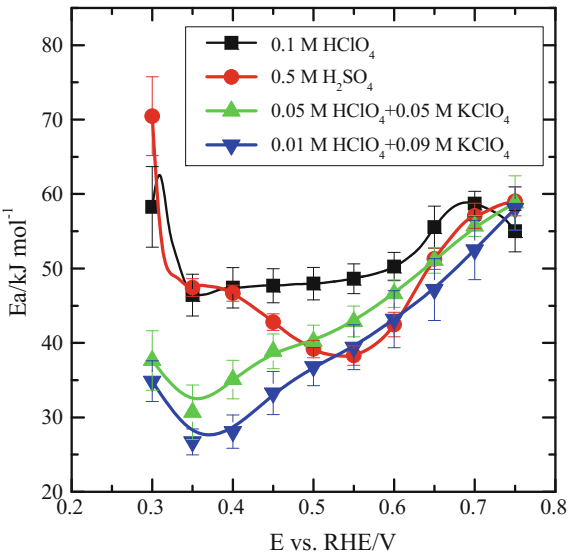

Fig. 12 Activation energies for the active intermediate path on a Pt(111) electrode in different supporting electrolytes with 0.1 M HCOOH

The reactivity orders obtained with the analysis of the transients is compatible with the voltammetric curves shown in Fig. 7.

Additional information on the oxidation mechanism can be obtained when the activation energy for the different paths is calculated from the temperature dependence of the reaction rates [116, 118, 119]. Activation energies range between 50–60 kJ mol^{-1} for the active intermediate path and 20–120 kJ mol^{-1} for the dehydration path and show a complex behavior which is very dependent on the anion adsorption, formate or other possible anions present on the electrolyte (i.e., sulfate), on the surface and pH (Fig. 12). For the Pt(100) electrode, oscillatory behavior can be observed, both in potentiostatic and galvanostatic conditions [119–121] due to the presence of the CO formation path. The complex behavior of the activation energy for both reaction paths leads to an oscillatory regime that is temperature dependent [119].

Regarding the nature of the active species in the oxidation, pH dependent studies clearly indicate that solution formate is the active species, since reaction rates increase as pH increases for pH values lower than the pK_a of formic acid [88, 91, 118]. On the other hand, bidentate adsorbed formate can be detected on polycrystalline electrodes by attenuated total reflection FTIR experiments [85, 93, 122, 123] and also by fast voltammetry on Pt(111) [124], which suggests that adsorbed formate plays an important role in the oxidation mechanism. All these data allowed to proposed a reaction mechanism for the reactive intermediate path that is able to reproduce the experimental results [116, 118]. In this model, an adsorbed anion (formate or sulfate) facilitates the positioning of a second formate species from solution, which is the active species, with the C–H bond pointing toward the surface. In this configuration, the cleavage of the C–H bond is possible, as has been

proposed due to the low activation energy predicted from DFT calculations [98], facilitating the formation of CO_2. Using a kinetic equation associated with this model, the calculated currents from this equation can be compared with those measured in the voltammetry, and a very good agreement was found [118]. In order to calculate the currents for the oxidation of formic acid, formate coverage values estimated from fast voltammetric experiments were used [124].

This type of configuration for the formate, in which he C–H bond points to the surface also explain the high catalytic activity of the Pt electrodes modified with some adatoms of groups 14–16. The presence of some adatoms on the surface, such as Pb, Bi or Te catalyze the oxidation of formic acid, not only by inhibiting the formation of CO, but also by increasing the oxidation rate through the active intermediate [104, 106, 107, 125–141]. Recent DFT calculations have allowed to establish the activation mechanism of these adatoms [142, 143]. The adatoms that catalyze the oxidation are those that have a partial positive charge when adsorbed, (i.e., Pb or Bi) whereas those that have a negative charge (S or Se) do not show any enhancement. Moreover, the positive charge, which is proportional to the electronegativity difference between the adatom and Pt, is a good descriptor of the catalytic effect, that is, the lower electronegativity of the adatom, the higher catalytic enhancement is found. The surface dipole with partial positive charge on the adatom facilitates the adsorption of the formate through an oxygen atom, locating the C–H pointing out to the surface. Once the formate species is adsorbed, the neighboring platinum atoms assist in the C–H bond cleavage in a barrierless process. DFT calculations also show that thee adatom mediated process has a lower activation energy, as has been experimentally found [142, 143].

6 Ethanol Oxidation on Pt(h k l) Electrodes

Ethanol oxidation is a complex reaction in which 12 e^- should be exchanged in the complete oxidation to CO_2. The complexity of the reaction and the requirements that the electrocatalyst has to fulfill to achieve the total oxidation can be easily understood when the tasks to be performed in the oxidation are enumerated: 5 C–H bonds, an O–H bond and a C–C bond have to be broken and 3 O containing groups have to be transferred to the carbon atoms. As it will be shown, from all these processes, the key step is the C–C bond breaking.

For the oxidation mechanism of ethanol, the following scheme has been proposed [144, 145]:

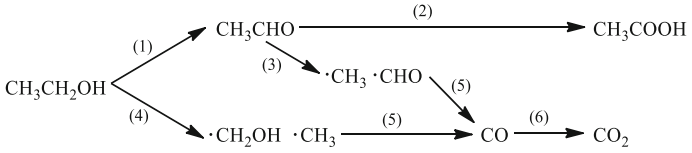

Two main routes can be found in these mechanisms, the one leading to the formation of acetic acid and that conducting to CO_2. Since acetic acid is very difficult to oxidize at room temperature [146], and only four electrons are exchanged in the oxidation to acetic acid, this reaction path is to be avoided, since two-thirds of the total possible energy accumulated on the electrode is lost. Thus, to achieve the complete oxidation of the ethanol molecule to CO_2 the electrocatalysts

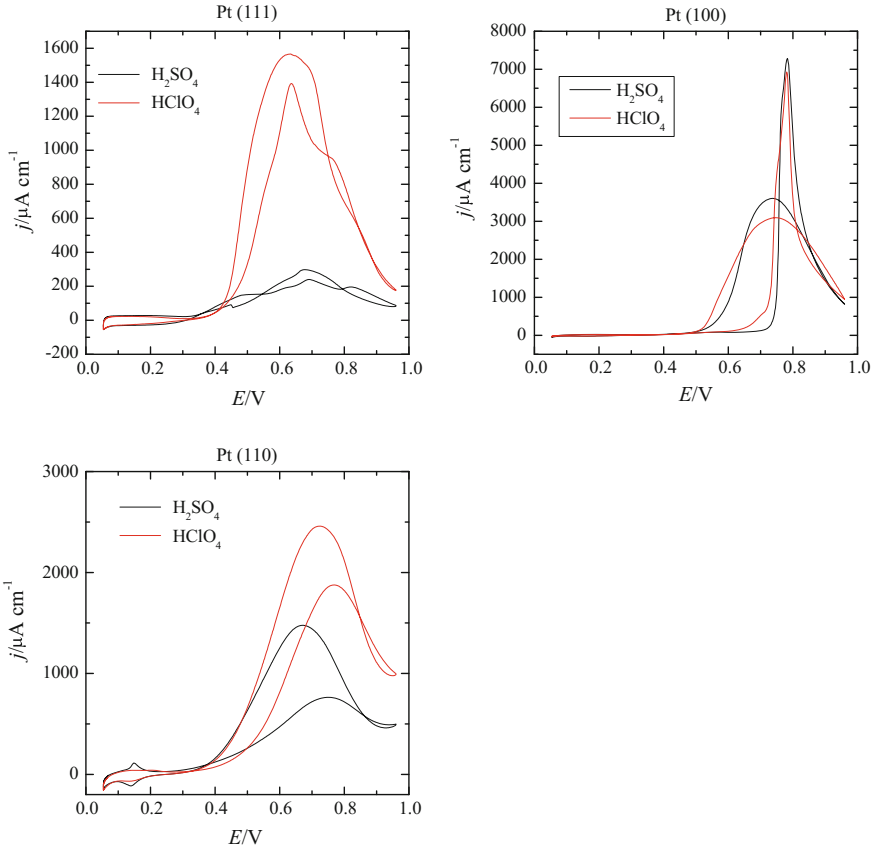

Fig. 13 Voltammetric profile of different Pt single crystal electrodes in 0.1 M HCOOH + 0.5 M H_2SO_4. Scan rate: 50 mV s^{-1}

should activate the cleavage of the C–C bond. When the C–C bond is broken, the two fragments eventually yield adsorbed CO to finally produce CO_2.

It is not surprising that the oxidation of ethanol is also a structure-sensitive reaction, as shown in Fig. 13. In a complex reaction in which several products can be formed, spectroscopic techniques provide the necessary complement to the electrochemical techniques. Thus, the combination of voltammetry, chronoamperometry and FTIR have allowed to determine the preferential paths in oxidation mechanism for the different electrodes and its dependence with the potential [144]. On the Pt(111) electrode in acidic media, the only products detected are acetaldehyde and acetic acid, indicating that this electrode is inactive for the C–C bond breaking. Moreover, in perchloric acid solutions, very high currents for the oxidation are measured in transients at $E > 0.5$ V showing that the electrode is very active for the oxidation to acetic acid. However, the activity decays very fast due to the adsorption of acetate (from the produced acetic acid) which act as a poison for the oxidation of ethanol [144, 147]. Thus, acetic acid is not only undesirable because part of the energy accumulated on ethanol is lost, but also because deactivates the surface. For the other two low index electrodes, Pt(100) and Pt(110), CO can be detected at low potentials, and the oxidation ethanol at $E > 0.5$ V produces a mixture of CO_2, acetaldehyde and acetic acid.

As before, the Pt(111) electrode represents a special case, and the modification of this electrode with steps significantly alters the reactivity. In this case, FTIR experiments show that the presence of steps catalyze the C–C bond breaking [148–150]. Moreover, studies with isotopically labeled ethanol ($^{12}CH_3$ $^{13}CH_2OH$) show that the cleavage takes place at low potentials and the $^{13}CH_2OH$ fragment rapidly evolves to yield adsorbed ^{13}CO [151, 152]. The other fragment is only partially transformed to adsorbed ^{12}CO at $E > 0.5$ V, since the production of $^{13}CO_2$ is always higher than that of ^{12}CO.

The behavior of the oxidation of ethanol in alkaline solution has significant differences with that measured in acidic conditions. First, the reactivity order is almost the opposite of that found in acidic solutions [153]. In alkaline solutions, Pt(111) shows higher peak currents than the rest of electrodes but the highest onset, which is the opposite behavior of that found in sulfuric or perchloric acid solutions. The second and most important difference is that the oxidation is taking place through the acetic acid path, since carbonate cannot be detected [153, 154]. Moreover, a strong inhibition upon cycling is observed, due to the polymerization of acetaldehyde, which occurs spontaneously in alkaline solutions. The inhibition is directly proportional to the measured currents [153].

7 Ammonia Oxidation

Ammonia oxidation reaction in alkaline media is also a reaction very sensitive to the surface structure. Ideally, the oxidation should yield N_2 as final product. According to the mechanism proposed by Gerischer [155], the reaction proceeds

through several dehydrogenation steps, to give adsorbed NH_x species. These species could dimerize, which facilitates the formation of N_2 or further dehydrogenate to give adsorbed N. This latter species is considered as a poison, since it is strongly adsorbed on the electrode surface [156]. The formation of N_2H_x species, and its role as active species in the oxidation mechanism has been supported by the detection of N_3^- ions from the reaction of N_2H_x with ammonia [157]. On polycrystalline Pt electrodes, NO and other nitrogen oxide species have been observed at high potentials, which suggest the elimination of the adsorbed N species in the presence of adsorbed OH on the electrode surface [158].

When this reaction was studied on platinum single crystal electrodes, it was found that it was very sensitive to the presence of (100) domains [159–161]. In fact, the reaction only took place at significant current densities when (100) domains were present in the sample. The maximum current densities for the reaction were obtained for the Pt(100) surface, and the introduction of steps in this low index plane led to a diminution of the current density [160]. As reaction products, N_2, NO and N_2O have been detected [161], where NO and N_2O are probably the oxidation products of the adsorbed poisoning species formed at low potentials. The high activity of the Pt(100) surface for this oxidation reaction has been explained as due to the ability of the (100) surface to stabilize adsorbed NH_2 species, which dimerizes to yield N_2, whereas the Pt(111) surface stabilizes NH and N adsorbed species, which are not active for the dimerization [162].

The extreme sensitivity of the ammonia oxidation reaction to the presence of (100) well-ordered domains has allowed to use this reaction to characterize the presence of those domains on the surface of nanoparticles [163–165] and to determine the quality of those ordered domains [166, 167].

Acknowledgements This work has been financially supported by the MCINN-FEDER (Spain) and Generalitat Valenciana through projects CTQ2016-76221-P and PROMETEO/2014/013, respectively.

References

1. Bockris JOM, Reddy AKN (1970) Modern electrochemistry. Plenum, New York
2. Lipkowski J, Ross PN (1998) Electrocatalysis. Wiley-VCH, New York
3. Herrero E, Feliu JM, Aldaz A (2003) In: Bard AJ, Stratmann M (eds) Encyclopedia of electrochemistry—interfacial kinetics and mass transport, vol 2. Wiley-VCH Verlag, Weinheim, Germany, pp 443–465
4. Wieckowski A, Savinova ER, Vayenas CG (2003) Catalysis and electrocatalysis at nanoparticle surfaces. CRC Press, New York
5. Climent V, García-Aráez N, Feliu JM (2008) In: Fuel cell catalysis. Wiley, pp 209–244. doi:10.1002/9780470463772.ch7
6. Vayenas CG (2011) In: White RE, Vayenas CG, Gamboa-Aldeco ME (eds) Modern aspects of electrochemistry, vol 51. Springer, New York. doi:10.1007/978-1-4419-5580-7
7. Sabatier P (1911) Announcement. Hydrogenation and dehydrogenation for catalysis. Ber Dtsch Chem Ges 44:1984–2001

8. Bond GC (1966) Adsorption and co-ordination of unsaturated hydrocarbons with metal surfaces and metal atoms. Discuss Faraday Soc 41:200–214
9. Menshykau D, Streeter I, Compton RG (2008) Influence of electrode roughness on cyclic voltammetry. J Phys Chem C 112:14428–14438
10. Menshykau D, Compton RG (2008) The influence of electrode porosity on diffusional cyclic voltammetry. Electroanalysis 20:2387–2394
11. Streeter I, Baron R, Compton RG (2007) Voltammetry at nanoparticle and microparticle modified electrodes: theory and experiment. J Phys Chem C 111:17008–17014
12. Chevallier FG, Jiang L, Jones TGJ, Compton RG (2006) Mathematical modelling and numerical simulation of cyclic voltammetry at an electrode covered with an insulating film containing cylindrical micropores. J Electroanal Chem 587:254–262
13. Lang B, Joyner RW, Somorjai GA (1972) LEED studies of high index crystal surfaces of platinum. Surf Sci 30:440
14. Clavilier J, Chauvineau JP (1979) Chemical characterization by auger-electron spectroscopy and voltammetry of platinum-electrode surfaces prepared in the gas-phase. J Electroanal Chem 100:461–472
15. Clavilier J (1980) The role of anion on the electrochemical behaviour of a {111} platinum surface; an unusual splitting of the voltammogram in the hydrogen region. J Electroanal Chem 107:211–216
16. Clavilier J, Elachi K, Petit M, Rodes A, Zamakhchari MA (1990) Electrochemical monitoring of the thermal reordering of platinum single-crystal surfaces after metallographic polishing from the early stage to the equilibrium surfaces. J Electroanal Chem 295:333–356
17. Rodes A, Zamakhchari MA, Elachi K, Clavilier J (1991) Electrochemical-behavior of pt (100) in various acidic media. On a new voltammetric profile of Pt(100) in perchloric-acid and effects of surface-defects. J Electroanal Chem 305:115–129
18. Rodes A, Clavilier J, Orts JM, Feliu JM, Aldaz A (1992) Electrochemical-behavior of pt (100) in various acidic media.2. On the relation between the voltammetric profiles induced by anion specific adsorption studied with a transfer technique preserving surface cleanliness and structure. J Electroanal Chem 338:317–338
19. Kibler LA, Cuesta A, Kleinert M, Kolb DM (2000) In-situ STM characterisation of the surface morphology of platinum single crystal electrodes as a function of their preparation. J Electroanal Chem 484:73–82
20. Clavilier J, Albalat R, Gómez R, Orts JM, Feliu JM, Aldaz A (1992) Study of the charge displacement at constant potential during CO adsorption on Pt(110) and Pt(111) electrodes in contact with a perchloric acid solution. J Electroanal Chem 330:489–497
21. Clavilier J, Albalat R, Gómez R, Orts JM, Feliu JM (1993) Displacement of adsorbed iodine on platinum single-crystal electrodes by irreversible adsorption of CO at controlled potentia. J Electroanal Chem 360:325–335
22. Clavilier J, Albalat R, Gomez R, Orts JM, Feliu JM (1993) Displacement of adsorbed iodine on platinum single-crystal electrodes by irreversible adsorption of Co at controlled potential. J Electroanal Chem 360:325–335
23. Orts JM, Gómez R, Feliu JM, Aldaz A, Clavilier J (1994) Potentiostatic charge displacement by exchanging adsorbed species on Pt(111) electrodes—acidic electrolytes with specific anion adsorption. Electrochim Acta 39:1519–1524
24. Herrero E, Feliu JM, Wieckowski A, Clavilier J (1995) The unusual adsorption states of Pt (111) electrodes studied by an iodine displacement method: comparison with Au(111) electrodes. Surf Sci 325:131–138
25. Gómez R, Feliu JM, Aldaz A, Weaver MJ (1998) Validity of double-layer charge-corrected voltammetry for assaying carbon monoxide coverages on ordered transition metals: comparisons with adlayer structures in electrochemical and ultrahigh vacuum environments. Surf Sci 410:48–61

26. Gómez R, Climent V, Feliu JM, Weaver MJ (2000) Dependence of the potential of zero charge of stepped platinum (111) electrodes on the oriented step-edge density: Electrochemical implications and comparison with work function behavior. J Phys Chem B 104:597–605
27. Wakisaka M, Udagawa Y, Suzuki H, Uchida H, Watanabe M (2011) Structural effects on the surface oxidation processes at Pt single-crystal electrodes studied by X-ray photoelectron spectroscopy. Energy Environ Sci 4:1662–1666
28. Clavilier J, Elachi K, Rodes A (1990) In situ probing of step and terrace sites on Pt(S)-n(111) x(111) electrodes. Chem Phys 141:1–14
29. Rodes A, Elachi K, Zamakhchari MA, Clavilier J (1990) Hydrogen probing of step and terrace sites on Pt(S)-[n(111) × (100)]. J Electroanal Chem 284:245–253
30. Rodes A, Elachi K, Zamakhchari MA, Clavilier J (1991) In: Brongersma HH, Vansanten RA (eds) Fundamental aspects of heterogeneous catalysis studied by particle beams, vol 265. Nato advanced science institutes series, Series B, Physics, pp 75–82
31. Clavilier J, Rodes A (1993) Electrochemical detection and characterization at pt(n, n, n-2) oriented electrodes of multiatomic step formation induced by quenching at high-temperatures. J Electroanal Chem 348:247–264
32. Arán-Ais RM, Figueiredo MC, Vidal-Iglesias FJ, Climent V, Herrero E, Feliu JM (2011) On the behavior of the Pt(100) and vicinal surfaces in alkaline media. Electrochim Acta 58:184–192
33. Souza-Garcia J, Climent V, Feliu JM (2009) Voltammetric characterization of stepped platinum single crystal surfaces vicinal to the (110) pole. Electrochem Commun 11:1515–1518
34. Souza-Garcia J, Angelucci CA, Climent V, Feliu JM (2013) Electrochemical features of Pt (S) n(110) x (100) surfaces in acidic media. Electrochem Commun 34:291–294
35. Berna A, Climent V, Feliu JM (2007) New understanding of the nature of OH adsorption on Pt(111) electrodes. Electrochem Commun 9:2789–2794
36. Itaya K (1998) In-situ scanning-tunneling-microscopy in electrolyte-solutions. Prog Surf Sci 58:121–247
37. Funtikov AM, Linke U, Stimming U, Vogel R (1995) An in-situ STM study of anion adsorption on Pt(111) from sulfuric acid solutions. Surf Sci 324:L343–L348
38. Funtikov AM, Stimming U, Vogel R (1997) Anion adsorption from sulfuric acid solutions on Pt(111) single crystal electrodes. J Electroanal Chem 428:147–153
39. Clavilier J, Elachi K, Rodes A (1989) In situ characterization of the Pt(S)-[n(111) × (111)] electrode surfaces using electrosorbed hydrogen for probing terrace an step sites. J Electroanal Chem 272:253–261
40. van der Niet MJTC, Garcia-Araez N, Hernández J, Feliu JM, Koper MTM (2013) Water dissociation on well-defined platinum surfaces: the electrochemical perspective. Catal Today 202:105–113
41. Gómez-Marín AM, Feliu JM (2016) Thermodynamic properties of hydrogen–water adsorption at terraces and steps of Pt(111) vicinal surface electrodes. Surf Sci 646:269–281
42. Gómez R, Orts JM, Alvarez-Ruiz B, Feliu JM (2004) Effect of temperature on hydrogen adsorption on Pt(111), Pt(110), and Pt(100) electrodes in 0.1 M HClO4. J Phys Chem B 108:228–238
43. Tanaka H, Sugawara S, Shinohara K, Ueno T, Suzuki S, Hoshi N, Nakamura M (2015) Infrared reflection absorption spectroscopy of OH adsorption on the low index planes of Pt. Electrocatalysis 6:295–299
44. Huang Y-F, Kooyman PJ, Koper MTM (2016) Intermediate stages of electrochemical oxidation of single-crystalline platinum revealed by in situ Raman spectroscopy. Nat Commun 7:12440
45. Gamboaaldeco ME, Herrero E, Zelenay PS, Wieckowski A (1993) Adsorption of bisulfate anion on a Pt(100) electrode—a comparison with Pt(111) and Pt(Poly). J Electroanal Chem 348:451–457

46. Attard GA, Brew A (2015) Cyclic voltammetry and oxygen reduction activity of the Pt{1 1 0}-(1 × 1) surface. J Electroanal Chem 747:123–129
47. Blyholder G (1964) Molecular orbital view of chemisorbed carbon monoxide. J Phys Chem 68:2772–2777
48. Koper MTM, van-Santen RA, Wasileski SA, Weaver MJ (2000) Field-dependent chemisorption of carbon monoxide and nitric oxide on platinum-group (111) surfaces: quantum chemical calculations compared with infrared spectroscopy at electrochemical and vacuum-based interfaces. J Chem Phys 113:4392–4407
49. Herrero E, Alvarez B, Feliu JM, Blais S, Radovic-Hrapovic Z, Jerkiewicz G (2004) Temperature dependence of the COads oxidation process on Pt(111) Pt(100), and Pt(110) electrodes. J Electroanal Chem 567:139–149
50. Weaver MJ (1998) Potentials of zero charge for platinum(111)-aqueous interfaces: a combined assessment from in-situ and ultrahigh-vacuum measurements. Langmuir 14:3932–3936
51. Villegas I, Weaver MJ (1994) Carbon-monoxide adlayer structures on platinum(111) electrodes—a synergy between in-situ scanning-tunneling-microscopy and infrared-spectroscopy. J Chem Phys 101:1648–1660
52. Markovic NM, Grgur BN, Lucas CA, Ross PN (1999) Electrooxidation of CO and H_2/CO mixtures on Pt(111) in acid solutions. J Phys Chem B 103:487–495
53. Rodes A, Gómez R, Feliu JM, Weaver MJ (2000) Sensitivity of compressed carbon monoxide adlayers on platinum(III) electrodes to long-range substrate structure: influence of monoatomic steps. Langmuir 16:811–816
54. Kiskinova M, Szab A, Yates JT (1988) Compressed CO overlayers on Pt(111)—evidence for tilted CO species at high coverages by digital ESDIAD. Surf Sci 205:215–229
55. Bergelin M, Herrero E, Feliu JM, Wasberg M (1999) Oxidation of CO adlayers on Pt(111) at low potentials: an impinging jet study in H_2SO_4 electrolyte with mathematical modeling of the current transients. J Electroanal Chem 467:74–84
56. Lebedeva NP, Koper MTM, Herrero E, Feliu JM, van Santen RA (2000) CO oxidation on stepped Pt n(111) × (111) electrodes. J Electroanal Chem 487:37–44
57. Petukhov AV, Akemann W, Friedrich KA, Stimming U (1998) Kinetics of electrooxidation of a CO monolayer at the platinum/electrolyte interface. Surf Sci 402:182–186
58. Herrero E, Feliu JM, Blais S, Radovic-Hrapovic Z, Jerkiewicz G (2000) Temperature dependence of CO chemisorption and its oxidative desorption on the Pt(111) electrode. Langmuir 16:4779–4783
59. Koper MTM, Lukkien JJ, Lebedeva NP, Feliu JM, van Santen RA (2001) Adsorbate interactions and phase transitions at the stepped platinum/electrolyte interface: experiment compared with Monte Carlo simulations. Surf Sci 478:L339–L344
60. Lebedeva NP, Koper MTM, Feliu JM, van Santen RA (2002) Role of crystalline defects in electrocatalysis: Mechanism and kinetics of CO adlayer oxidation on stepped platinum electrodes. J Phys Chem B 106:12938–12947
61. Lebedeva NP, Rodes A, Feliu JM, Koper MTM, van Santen RA (2002) Role of crystalline defects in electrocatalysis: CO adsorption and oxidation on stepped platinum electrodes as studied by in situ infrared spectroscopy. J Phys Chem B 106:9863–9872
62. Angelucci CA, Herrero E, Feliu JM (2010) Modeling CO oxidation on Pt(111) electrodes. J Phys Chem C 114:14154–14163
63. Chen QS, Berna A, Climent V, Sun SG, Feliu JM (2010) Specific reactivity of step sites towards CO adsorption and oxidation on platinum single crystals vicinal to Pt(111). Phys Chem Chem Phys 12:11407–11416
64. Chen QS, Feliu JM, Berna A, Climent V, Sun SG (2011) Kinetic study of CO oxidation on step decorated Pt(111) vicinal single crystal electrodes. Electrochim Acta 56:5993–6000

65. Herrero E, Climent V, Feliu JM (2000) On the different adsorption behavior of bismuth, sulfur, selenium and tellurium on a Pt(775) stepped surface. Electrochem Commun 2:636–640
66. Ferre-Vilaplana A, Gisbert R, Herrero E (2014) On the electrochemical properties of platinum stepped surfaces vicinal to the (100) pole. A computational study. Electrochim Acta 125:666–673
67. Domke K, Herrero E, Rodes A, Feliu JM (2003) Determination of the potentials of zero total charge of Pt(100) stepped surfaces in the 01(-1) zone. Effect of the step density and anion adsorption. J Electroanal Chem 552:115–128
68. Vidal-Iglesias FJ, Solla-Gullón J, Campina JM, Herrero E, Aldaz A, Feliu JM (2009) CO monolayer oxidation on stepped Pt(S) (n-1)(100) × (110) surfaces. Electrochim Acta 54:4459–4466
69. Garcia G, Koper MTM (2008) Stripping voltammetry of carbon monoxide oxidation on stepped platinum single-crystal electrodes in alkaline solution. Phys Chem Chem Phys 10:3802–3811
70. Garcia G, Koper MTM (2009) Dual reactivity of step-bound carbon monoxide during oxidation on a stepped platinum electrode in alkaline media. J Am Chem Soc 131: 5384–5385
71. Garcia G, Koper MTM (2009) Mechanism of electro-oxidation of carbon monoxide on stepped platinum electrodes in alkaline media: a chronoamperometric and kinetic modeling study. Phys Chem Chem Phys 11:11437–11446
72. Herrero E, Chen Q-S, Hernandez J, Sun S-G, Feliu JM (2011) Effects of the surface mobility on the oxidation of adsorbed CO on platinum electrodes in alkaline media. The role of the adlayer and surface defects. Phys Chem Chem Phys 13:16762–16771
73. Farias MJS, Herrero E, Feliu JM (2013) Site selectivity for CO adsorption and stripping on stepped and kinked platinum surfaces in alkaline medium. J Phys Chem C 117:2903–2913
74. Buso-Rogero C, Herrero E, Bandlow J, Comas-Vives A, Jacob T (2013) CO oxidation on stepped-Pt(111) under electrochemical conditions: insights from theory and experiment. Phys Chem Chem Phys 15:18671–18677
75. Kita H, Shimazu K, Kunimatsu K (1988) Electrochemical oxidation of CO on Pt in acidic and alkaline solutions. Part I. voltammetric study on the adsorbed species and effects of aging and Sn(IV) pretreatment. J Electroanal Chem 241:163–179
76. López-Cudero A, Cuesta A, Gutiérrez C (2005) Potential dependence of the saturation CO coverage of Pt electrodes: The origin of the pre-peak in CO-stripping voltammograms. Part 1: Pt(1 1 1). J Electroanal Chem 579:1–12
77. Cuesta A, Couto A, Rincón A, Pérez MC, López-Cudero A, Gutiérrez C (2006) Potential dependence of the saturation CO coverage of Pt electrodes: the origin of the pre-peak in CO-stripping voltammograms. Part 3: Pt(poly). J Electroanal Chem 586:184–195
78. López-Cudero A, Cuesta Á, Gutiérrez C (2006) Potential dependence of the saturation CO coverage of Pt electrodes: the origin of the pre-peak in CO-stripping voltammograms. Part 2: Pt(1 0 0). J Electroanal Chem 586:204–216
79. Yan Y-G, Yang Y-Y, Peng B, Malkhandi S, Bund A, Stimming U, Cai W-B (2011) Study of CO oxidation on polycrystalline Pt electrodes in acidic solution by ATR-SEIRAS. J Phys Chem C 115:16378–16388
80. Spendelow JS, Goodpaster JD, Kenis PJA, Wieckowski A (2006) Mechanism of CO oxidation on Pt(111) in alkaline media. J Phys Chem B 110:9545–9555
81. Farias MJS, Busó-Rogero C, Gisbert R, Herrero E, Feliu JM (2013) Influence of the CO adsorption environment on its reactivity with (111) terrace sites in stepped Pt electrodes under alkaline media. J Phys Chem C 118:1925–1934
82. Angelucci CA, Herrero E, Feliu JM (2007) Bulk CO oxidation on platinum electrodes vicinal to the Pt(111) surface. J Solid State Electrochem 11:1531–1539
83. Angelucci CA, Nart FC, Herrero E, Feliu JM (2007) Anion re-adsorption and displacement at platinum single crystal electrodes in CO-containing solutions. Electrochem Commun 9:1113–1119

84. Parsons R, Vandernoot T (1988) The oxidation of small organic molecules: a survey of recent fuel cell related research. J Electroanal Chem 257:9–45
85. Samjeske G, Osawa M (2005) Current oscillations during formic acid oxidation on a Pt electrode: insight into the mechanism by time-resolved IR spectroscopy. Angew Chem Int Ed 44:5694–5698
86. Sun SG, Clavilier J, Bewick A (1988) The mechanism of electrocatalytic oxidation of formic acid on Pt (100) and Pt (111) in sulphuric acid solution: an emirs study. J Electroanal Chem 240:147–159
87. Willsau J, Heitbaum J (1986) Analysis of adsorbed intermediates and determination of surface potential shifts by DEMS. Electrochim Acta 31:943–948
88. Joo J, Uchida T, Cuesta A, Koper MTM, Osawa M (2013) Importance of acid-base equilibrium in electrocatalytic oxidation of formic acid on platinum. J Am Chem Soc 135:9991–9994
89. Joo J, Uchida T, Cuesta A, Koper MTM, Osawa M (2014) The effect of pH on the electrocatalytic oxidation of formic acid/formate on platinum: a mechanistic study by surface-enhanced infrared spectroscopy coupled with cyclic voltammetry. Electrochim Acta 129:127–136
90. Brimaud S, Solla-Gullon J, Weber I, Feliu JM, Behm RJ (2014) Formic acid electrooxidation on noble-metal electrodes: role and mechanistic implications of pH, surface structure, and anion adsorption. ChemElectroChem 1:1075–1083
91. Perales-Rondón JV, Brimaud S, Solla-Gullón J, Herrero E, Jürgen Behm R, Feliu JM (2015) further insights into the formic acid oxidation mechanism on platinum: pH and anion adsorption effects. Electrochim Acta 180:479–485
92. Chen YX, Ye S, Heinen M, Jusys Z, Osawa M, Behm RJ (2006) Application of in-situ attenuated total reflection-Fourier transform infrared spectroscopy for the understanding of complex reaction mechanism and kinetics: Formic acid oxidation on a Pt film electrode at elevated temperatures. J Phys Chem B 110:9534–9544
93. Samjeske G, Miki A, Ye S, Osawa M (2006) Mechanistic study of electrocatalytic oxidation of formic acid at platinum in acidic solution by time-resolved surface-enhanced infrared absorption spectroscopy. J Phys Chem B 110:16559–16566
94. Miyake H, Okada T, Samjeské G, Osawa M (2008) Formic acid electrooxidation on Pd in acidic solutions studied by surface-enhanced infrared absorption spectroscopy. Phys Chem Chem Phys 10:3662–3669
95. Cuesta A, Cabello G, Gutierrez C, Osawa M (2011) Adsorbed formate: the key intermediate in the oxidation of formic acid on platinum electrodes. Phys Chem Chem Phys 13:20091–20095
96. Osawa M, Komatsu K, Samjeske G, Uchida T, Ikeshoji T, Cuesta A, Gutierrez C (2011) The role of bridge-bonded adsorbed formate in the electrocatalytic oxidation of formic acid on platinum. Angew Chem Int Ed 50:1159–1163
97. Cuesta A, Cabello G, Osawa M, Gutiérrez C (2012) Mechanism of the electrocatalytic oxidation of formic acid on metals. ACS Catal 2:728–738
98. Wang H-F, Liu Z-P (2009) Formic acid oxidation at Pt/H_2O interface from periodic DFT calculations integrated with a continuum solvation model. J Phys Chem C 113:17502–17508
99. Zhang H-X, Wang C, Wang J-Y, Zhai J-J, Cai W-B (2010) Carbon-supported pd − pt nanoalloy with low Pt content and superior catalysis for formic acid electro-oxidation. J Phys Chem C 114:6446–6451
100. Gao W, Keith JA, Anton J, Jacob T (2010) Theoretical Elucidation of the competitive electro-oxidation mechanisms of formic acid on Pt(111). J Am Chem Soc 132:18377–18385
101. Peng B, Wang H-F, Liu Z-P, Cai W-B (2010) Combined surface-enhanced infrared spectroscopy and first-principles study on electro-oxidation of formic acid at Sb-modified Pt electrodes. J Phys Chem C 114:3102–3107
102. Clavilier J, Parsons R, Durand R, Lamy C, Leger JM (1981) Formic acid oxidation on single crystal platinum electrodes. Comparison with polycrystalline platinum. J Electroanal Chem 124:321–326

103. Clavilier J, Sun SG (1986) Electrochemical study of the chemisorbed species formed from formic-acid dissociation at platinum single-crystal electrodes. J Electroanal Chem 199: 471–480
104. Herrero E, Fernández-Vega A, Feliu JM, Aldaz A (1993) Poison formation reaction from formic acid and methanol on Pt(111) electrodes modified by irreversibly adsorbed Bi and As. J Electroanal Chem 350:73–88
105. Herrero E, Feliu JM, Aldaz A (1994) Poison formation reaction from formic acid on Pt(100) electrodes modified by irreversibly adsorbed bismuth and antimony. J Electroanal Chem 368:101–108
106. Herrero E, Llorca MJ, Feliu JM, Aldaz A (1995) Oxidation of formic acid on Pt(111) electrodes modified by irreversibly adsorbed tellurium. J Electroanal Chem 394:161–167
107. Climent V, Herrero E, Feliu JM (1998) Electrocatalysis of formic acid and CO oxidation on antimony-modified Pt(111) electrodes. Electrochim Acta 44:1403–1414
108. Herrero E, Llorca MJ, Feliu JM, Aldaz A (1995) Oxidation of formic acid on Pt(100) electrodes modified by irreversibly adsorbed tellurium. J Electroanal Chem 383:145–154
109. Leiva E, Iwasita T, Herrero E, Feliu JM (1997) Effect of adatoms in the electrocatalysis of HCOOH oxidation. A theoretical model. Langmuir 13:6287–6293
110. Maciá MD, Herrero E, Feliu JM, Aldaz A (1999) Formic acid self-poisoning on bismuth-modified Pt(755) and Pt(775) electrodes. Electrochem Commun 1:87–89
111. Maciá MD, Herrero E, Feliu JM, Aldaz A (2001) Formic acid self-poisoning on bismuth-modified stepped electrodes. J Electroanal Chem 500:498–509
112. Maciá MD, Herrero E, Feliu JM (2002) Formic acid self-poisoning on adatom-modified stepped electrodes. Electrochim Acta 47:3653–3661
113. Clavilier J (1987) Pulsed linear sweep voltammetry with pulses of constant level in a potential scale, a polarization demanding condition in the study of platinum single-crystal electrodes. J Electroanal Chem 236:87–94
114. Grozovski V, Climent V, Herrero E, Feliu JM (2010) Intrinsic activity and poisoning rate for HCOOH oxidation on platinum stepped surfaces. Phys Chem Chem Phys 12:8822–8831
115. Grozovski V, Climent V, Herrero E, Feliu JM (2009) Intrinsic activity and poisoning rate for HCOOH oxidation at Pt(100) and vicinal surfaces containing monoatomic (111) steps. ChemPhysChem 10:1922–1926
116. Perales-Rondón JV, Herrero E, Feliu JM (2015) On the activation energy of the formic acid oxidation reaction on platinum electrodes. J Electroanal Chem 742:90–96
117. Grozovski V, Solla-Gullon J, Climent V, Herrero E, Feliu JM (2010) Formic acid oxidation on shape-controlled Pt nanoparticles studied by pulsed voltammetry. J Phys Chem C 114:13802–13812
118. Perales-Rondon JV, Herrero E, Feliu JM (2014) Effects of the anion adsorption and pH on the formic acid oxidation reaction on Pt(111) electrodes. Electrochim Acta 140:511–517
119. Angelucci CA, Varela H, Herrero E, Feliu JM (2009) Activation energies of the electrooxidation of formic acid on Pt(100). J Phys Chem C 113:18835–18841
120. Strasser P, Eiswirth M, Ertl G (1997) Oscillatory instabilities during formic acid oxidation on Pt(100), Pt(110) and Pt(111) under potentiostatic control. 2 Model calculations. J Chem Phys 107:991–1003
121. Strasser P, Lubke M, Raspel F, Eiswirth M, Ertl G (1997) Oscillatory instabilities during formic acid oxidation on Pt(100), Pt(110) and Pt(111) under potentiostatic control. 1. Experimental. J Chem Phys 107:979–990
122. Chen YX, Heinen M, Jusys Z, Behm RJ (2006) Bridge-bonded formate: active intermediate or spectator species in formic acid oxidation on a Pt film electrode? Langmuir 22: 10399–10408
123. Chen Y, Heinen M, Jusys Z, Behm R (2006) Kinetics and mechanism of the electrooxidation of formic acid—spectroelectrochemical studies in a flow cell. Angew Chem Int Ed 45:981–985

124. Grozovski V, Vidal-Iglesias FJ, Herrero E, Feliu JM (2011) Adsorption of formate and its role as intermediate in formic acid oxidation on platinum electrodes. ChemPhysChem 12:1641–1644
125. Watanabe M, Horiuchi M, Motoo S (1988) Electrocatalysis by ad-atoms. 23. Design of platinum ad-electrodes for formic acid fuel cells with ad-atoms of the 4th group and the 5th group. J Electroanal Chem 250:117–125
126. Clavilier J, Fernández-Vega A, Feliu JM, Aldaz A (1989) Heterogeneous electrocatalysis on well-defined platinum surfaces modified by controlled amounts of irreversibly adsorbed adatoms. 3. Formic-acid oxidation on the Pt(100)-Bi system. J Electroanal Chem 261: 113–125
127. Clavilier J, Fernández-Vega A, Feliu JM, Aldaz A (1989) Heterogeneous electrocatalysis on well defined platinum surfaces modified by controlled amounts of irreversibly adsorbed adatoms. 1. Formic-acid oxidation on the Pt (111)—Bi system. J Electroanal Chem 258:89–100
128. Fernández-Vega A, Feliu JM, Aldaz A, Clavilier J (1989) Heterogeneous electrocatalysis on well defined platinum surfaces modified by controlled amounts of irreversible adsorbed adatoms. 2. Formic acid oxidation on the Pt(100)-Sb system. J Electroanal Chem 258: 101–113
129. Fernández-Vega A, Feliu JM, Aldaz A, Clavilier J (1991) Heterogeneous electrocatalysis on well-defined platinum surfaces modified by controlled amounts of irreversibly adsorbed adatoms: part IV. Formic acid oxidation on the Pt(111)-As system. J Electroanal Chem 305:229–240
130. Xia XH, Iwasita T (1993) Influence of underpotential deposited lead upon the oxidation of HCOOH in HClO4 at platinum electrodes. J Electrochem Soc 140:2559–2565
131. Llorca MJ, Herrero E, Feliu JM, Aldaz A (1994) Formic acid oxidation on Pt(111) electrodes modified by irreversibly adsorbed selenium. J Electroanal Chem 373:217–225
132. Lei HW, Hattori H, Kita H (1996) Electrocatalysis by Pb adatoms of HCOOH oxidation at Pt (111) in acidic solution. Electrochim Acta 41:1619–1628
133. Smith SPE, Ben-Dor KF, Abruna HD (1999) Structural effects on the oxidation of HCOOH by bismuth-modified Pt(111) electrodes with (100) monatomic steps. Langmuir 15: 7325–7332
134. Smith SPE, Abruna HD (1999) Structural effects on the oxidation of HCOOH by bismuth modified Pt(111) electrodes with (110) monatomic steps. J Electroanal Chem 467:43–49
135. Maciá MD, Herrero E, Feliu JM (2003) Formic acid oxidation on Bi-Pt(111) electrode in perchloric acid media. A kinetic study. J Electroanal Chem 554:25–34
136. Buso-Rogero C, Perales-Rondon JV, Farias MJS, Vidal-Iglesias FJ, Solla-Gullon J, Herrero E, Feliu JM (2014) Formic acid electrooxidation on thallium-decorated shape-controlled platinum nanoparticles: an improvement in electrocatalytic activity. Phys Chem Chem Phys 16:13616–13624
137. Casado-Rivera E, Gal Z, Angelo ACD, Lind C, DiSalvo FJ, Abruna HD (2003) Electrocatalytic oxidation of formic acid at an ordered intermetallic PtBi surface. ChemPhysChem 4:193–199
138. Roychowdhury C, Matsumoto F, Mutolo PF, Abruna HD, DiSalvo FJ (2005) Synthesis, characterization, and electrocatalytic activity of PtBi nanoparticles prepared by the polyol process. Chem Mater 17:5871–5876
139. Blasini DR, Rochefort D, Fachini E, Alden LR, DiSalvo FJ, Cabrera CR, Abruna HD (2006) Surface composition of ordered intermetallic compounds PtBi and PtPb. Surf Sci 600: 2670–2680
140. Alden LR, Han DK, Matsumoto F, Abruña HD, DiSalvo FJ (2006) Intermetallic PtPb nanoparticles prepared by sodium naphthalide reduction of metal-organic precursors: electrocatalytic oxidation of formic acid. Chem Mater 18:5591–5596
141. Matsumoto F, Roychowdhury C, DiSalvo FJ, Abruna HD (2008) Electrocatalytic activity of ordered intermetallic PtPb nanoparticles prepared by borohydride reduction toward formic acid oxidation. J Electrochem Soc 155:B148–B154

142. Perales-Rondon JV, Ferre-Vilaplana A, Feliu JM, Herrero E (2014) Oxidation mechanism of formic acid on the bismuth adatom-modified Pt(111) surface. J Am Chem Soc 136: 13110–13113
143. Ferre-Vilaplana A, Perales-Rondon JV, Feliu JM, Herrero E (2015) Understanding the effect of the adatoms in the formic acid oxidation mechanism on Pt(111) electrodes. ACS Catal 5:645–654
144. Colmati F, Tremiliosi-Filho G, Gonzalez ER, Berna A, Herrero E, Feliu JM (2008) Surface structure effects on the electrochemical oxidation of ethanol on platinum single crystal electrodes. Faraday Discuss 140:379–397; 417–337
145. Koper MTM, Lai SCS, Herrero E (2009) In: Koper MTM (ed) Fuel cell catalysis, A surface science approach. Wiley, Hoboken, NJ, pp 159–208
146. Rodes A, Pastor E, Iwasita T (1994) An ftir study on the adsorption of acetate at the basal planes of platinum single-crystal electrodes. J Electroanal Chem 376:109–118
147. Prieto MJ, Tremiliosi-Filho G (2011) The influence of acetic acid on the ethanol electrooxidation on a platinum electrode. Electrochem Commun 13:527–529
148. Tarnowski DJ, Korzeniewski C (1997) Effects of surface step density on the electrochemical oxidation of ethanol to acetic acid. J Phys Chem B 101:253–258
149. Colmati F, Tremiliosi G, Gonzalez ER, Berna A, Herrero E, Feliu JM (2009) The role of the steps in the cleavage of the C-C bond during ethanol oxidation on platinum electrodes. Phys Chem Chem Phys 11:9114–9123
150. Del Colle V, Berna A, Tremiliosi G, Herrero E, Feliu JM (2008) Ethanol electrooxidation onto stepped surfaces modified by Ru deposition: electrochemical and spectroscopic studies. Phys Chem Chem Phys 10:3766–3773
151. Souza-Garcia J, Herrero E, Feliu JM (2010) Breaking the C-C bond in the ethanol oxidation reaction on platinum electrodes: effect of steps and ruthenium adatoms. ChemPhysChem 11:1391–1394
152. Del Colle V, Souza-Garcia J, Tremiliosi G, Herrero E, Feliu JM (2011) Electrochemical and spectroscopic studies of ethanol oxidation on Pt stepped surfaces modified by tin adatoms. Phys Chem Chem Phys 13:12163–12172
153. Busó-Rogero C, Herrero E, Feliu JM (2014) Ethanol oxidation on Pt single-crystal electrodes: surface-structure effects in alkaline medium. ChemPhysChem 15:2019–2028
154. Christensen PA, Jones SWM, Hamnett A (2012) In situ FTIR studies of ethanol oxidation at polycrystalline Pt in alkaline solution. J Phys Chem C 116:24681–24689
155. Gerischer H, Mauerer A (1970) Untersuchungen zur anodischen oxidation von ammoniak an platin-elektroden. J Electroanal Chem 25:421–433
156. de Vooys ACA, Koper MTM, van Santen RA, van Veen JAR (2001) The role of adsorbates in the electrochemical oxidation of ammonia on noble and transition metal electrodes. J Electroanal Chem 506:127–137
157. Vidal-Iglesias FJ, Solla-Gullon J, Perez JM, Aldaz A (2006) Evidence by SERS of azide anion participation in ammonia electrooxidation in alkaline medium on nanostructured Pt electrodes. Electrochem Commun 8:102–106
158. Wasmus S, Vasini EJ, Krausa M, Mishima HT, Vielstich W (1994) DEMS-cyclic voltammetry investigation of the electrochemistry of nitrogen compounds in 0.5 M KOH. Electrochim Acta 39:23–31
159. Vidal-Iglesias FJ, Garcia-Araez N, Montiel V, Feliu JM, Aldaz A (2003) Selective electrocatalysis of ammonia oxidation on Pt(100) sites in alkaline medium. Electrochem Commun 5:22–26
160. Vidal-Iglesias FJ, Solla-Gullón J, Montiel V, Feliu JM, Aldaz A (2005) Ammonia selective oxidation on Pt(100) sites in an alkaline medium. J Phys Chem B 109:12914–12919
161. Vidal-Iglesias FJ, Solla-Gullón J, Feliu JM, Baltruschat H, Aldaz A (2006) DEMS study of ammonia oxidation on platinum basal planes. J Electroanal Chem 588:331–338
162. Rosca V, Koper MTM (2006) Electrocatalytic oxidation of ammonia on Pt(111) and Pt(100) surfaces. Phys Chem Chem Phys 8:2513–2524

163. Vidal-Iglesias FJ, Solla-Gullón J, Rodríguez P, Herrero E, Montiel V, Feliu JM, Aldaz A (2004) Shape-dependent electrocatalysis: ammonia oxidation on platinum nanoparticles with preferential (100) surfaces. Electrochem Commun 6:1080–1084
164. Solla-Gullón J, Vidal-Iglesias FJ, Rodríguez P, Herrero E, Feliu JM, Clavilier J, Aldaz A (2004) In situ surface characterization of preferentially oriented platinum nanoparticles by using electrochemical structure sensitive adsorption reactions. J Phys Chem B 108: 13573–13575
165. Rodríguez P, Herrero E, Solla-Gullón J, Vidal-Iglesias FJ, Aldaz A, Feliu JM (2005) Specific surface reactions for identification of platinum surface domains—surface characterization and electrocatalytic tests. Electrochim Acta 50:4308–4317
166. Bertin E, Roy C, Garbarino S, Guay D, Solla-Gullon J, Vidal-Iglesias FJ, Feliu JM (2012) Effect of the nature of (100) surface sites on the electroactivity of macroscopic Pt electrodes for the electrooxidation of ammonia. Electrochem Commun 22:197–199
167. Berlin E, Garbarino S, Guay D, Solla-Gullon J, Vidal-Iglesias FJ, Feliu JM (2013) Electrodeposited platinum thin films with preferential (100) orientation: characterization and electrocatalytic properties for ammonia and formic acid oxidation. J Power Sources 225:323–329

Novel In Situ Techniques

Takuya Masuda and Kohei Uosaki

Abstract To understand how electrochemical processes proceed at electrode/electrolyte interfaces and to improve the efficiencies of these processes, it is essential to probe these processes in situ real time. Thus, the developments of in situ techniques have been carried out very intensively for a long time. Thanks to the technological advancement in electronics, optics, quantum beams, and nanomaterials, various in situ techniques, which are capable of determining molecular, geometric, and electronic structures at electrochemical interfaces, have been developed in the last several decades and they are applied to a wide range of electrochemical interfaces from both fundamental and practical points of view. Here, various in situ techniques are described with historical aspects, several key innovations related to the techniques, and a few examples for the techniques to be applied.

1 Introduction

Many important processes, both fundamentally and practically, such as crystal growth, corrosion, electrochemical reactions, and biological processes, are taking place at solid/liquid interfaces. These processes consist of many elementally steps including mass/electron transfer, adsorption/desorption, oxidation/reduction, deposition/dissolution, and formation/cleavage of chemical bonds [1]. Many efforts have been devoted to understand how these processes proceed not only because of fundamental interests but also because of practical importance to improve the efficiencies of electrochemical energy conversion reactions in batteries, fuel cells, etc. Although in situ real time clarifications of the geometric, electronic, and molecular structures at solid/liquid interfaces with atomic and molecular resolution are essential to understand how these processes proceed, the presence of the liquid inhibits the use of the various tools utilizing electrons as a probe such as electron microscopy,

T. Masuda · K. Uosaki (✉)
National Institute for Materials Science (NIMS), Tsukuba, Japan
e-mail: Uosaki.kohei@nims.go.jp

K. Uosaki (ed.), *Electrochemical Science for a Sustainable Society*,
DOI 10.1007/978-3-319-57310-6_6

low-energy electron diffraction (LEED), and X-ray photoelectron spectroscopy (XPS), which are very powerful in determining the geometric and electronic structures of solid surfaces in vacuum. Thus, earlier studies on structures of electrode surfaces employed these techniques ex situ by transferring an electrode from an electrochemical cell to a measuring equipment without or minimal exposure to air. Real "in situ" measurements of the electrochemical processes were, however, also carried out even in the 1960s, utilizing photon as a probe [2]. Various in situ optical techniques used in the earlier stage such as ellipsometry and Raman scattering are well-documented previously [3]. Thanks to the dramatic advances in optics, electronics, quantum beams, and nanotechnology, applications of the surface analysis techniques towards "in situ" observations of electrochemical processes at solid/liquid interfaces have been considerably progressed in the last several decades [4–9].

Scanning probe microscopy (SPM) including scanning tunneling microscopy (STM) and atomic force microscopy (AFM) enables to directly monitor the geometric structure of solid surfaces with an atomic resolution not only in ultrahigh vacuum (UHV) but also in gas and liquid phases. Actually, studies of electrochemical surface are revolutionized by the developments of SPM and a new preparation method of single crystalline surfaces of precious metals such as Au, Pt, Rh, Ir, and Pd developed by Clavilier [10]. An atomically flat, clean surface of a specific face can be obtained by melting one end of a wire of desired metal to form a single crystalline bead, followed by cutting and polishing the bead along with the desired face. These techniques make atomic resolution surface studies possible without expensive vacuum equipment.

As the advanced synchrotron radiation sources with very high brightness, high directionality, tunable polarization, and variability of wavelength become available, various x-ray-based techniques have been applied to electrochemical interfaces. While SPM can provide the surface geometric structure of the outermost layer in real space in very small area, surface x-ray scattering (SXS) is capable of determining the atomic arrangement of a few top layers of single crystal surfaces averaged in a relatively large area under electrochemical potential control. Hence, SPM and SXS are often complementarily used to determine the three-dimensional atomic arrangement of electrochemical interfaces in situ. SXS is only applicable to crystalline surfaces with a long-range order because this technique is based on diffraction induced by periodic structure but x-ray absorption fine structure (XAFS) can be applied to investigate the local geometric structure and the electronic structure of samples without a long-range order such as polycrystalline surfaces, nanoparticles, metal complexes, and biomolecules on solid substrates or in solutions.

Vibrational spectroscopies such as infrared reflection absorption spectroscopy (IRAS) and Raman scattering are widely used to investigate the molecular structure of chemical species such as reactants, intermediates, products, solvents, and reaction inhibitors at the interfaces. Various unique measurement modes and arrangements that make use of total reflection, potential/polarization modulation, and plasmonic enhancement induced by nanostructured substrates have been developed to track a trace amount of surface species with a high surface sensitivity. Nonlinear optical spectroscopies such as sum frequency generation spectroscopy (SFG) and

second harmonic generation spectroscopy (SHG) are intrinsically surface sensitive and are successfully utilized to probe the molecular and electronic structures of the electrochemical interfaces.

Although techniques utilizing electrons as a probe cannot be applied to solid/liquid interfaces as mentioned above, a UHV apparatus equipped with an electrochemical chamber and, at least, one spectrometer/detector was developed [11, 12]. In this set-up, electrochemically treated samples can be directly transferred into the analysis chamber after the removal of electrolyte solutions by pumping down the electrochemical chamber. This technique has been widely used not only in fundamental electrochemical science but also in various applications such as manufacturing process for semiconductor devices [13] and electrocatalysts for fuel cells [14]. Most serious drawback of this method is that the electrochemical potential cannot be maintained because electrolyte solutions are removed prior to the measurements. Recently, techniques using (photo)electrons [15–17] and soft x-rays [18, 19] have been utilized for in situ observation of electrochemical processes by using room temperature ionic liquids (RTILs), near ambient pressure (NAP-) XPS, and ultrathin films as a separator/window between vacuum and liquid.

In addition to the surface analysis techniques mentioned above, real time detection of chemical species near the electrode is required to fully understand electrochemical processes and a system combined an electrochemical cell with a quadrupole mass spectrometer (QMS), which is known as differential electrochemical mass spectroscopy (DEMS), has been developed [20, 21]. In this technique, chemical species near the electrode are transferred through a porous PTFE membrane by using a differentially pumped vacuum system to QMS and mass ion currents are monitored simultaneously with Faradaic current.

In the following sections, various important analysis techniques applicable to in situ analysis of electrochemical interfaces are described with brief introductions followed by a few application examples.

2 Scanning Probe Microscopy

The development of STM by Binning and Rohrer of IBM Zurich Research Laboratory in 1982 has revolutionized the researches at surfaces and interfaces [22]. After the development of AFM by Binning [23], not only conductors but also a wide variety of solid surfaces including insulators have been the subjects of the SPM studies. Microscopic distribution of versatile physical properties at solid surfaces has been investigated by simultaneously measuring the current, magnetic force, modulation of frequency/force, and electrostatic interaction induced by AC bias, together with the surface force between the probe and surface. SPM is now utilized for a wide variety of solid surfaces not only in UHV but also in ambient atmosphere, insulating liquids and even electrolyte solutions under the electrochemical potential control, and made a significant impact on fundamental surface science and nanotechnology.

2.1 Scanning Tunneling Microscopy

In STM, a bias is applied between an atomically sharp tip and a (semi)conductor surface with a distance of typically less than one nm, and tunneling current, which flows between the tip and the surface, is used as a probe. When the tip is scanned over the sample surface, tunneling current is dramatically varied as the tip-surface distance changes, reflecting the surface topography. For the electrochemical STM measurement, reference and counter electrodes should be placed in an electrochemical cell so that the electrochemical potential can be individually applied to the tip and the sample by a bipotentiostat. In this case, the Faradaic current flows between the sample and the counter electrode and tunneling current flows between the tip and the sample. An inert material should be used as a tip, which must be coated with an insulating resin or glass except for the very end, so that the leakage current and electrochemical reaction at the tip can be suppressed.

In situ structural change of a Au(111) surface in sulfuric acid solution has been widely studied using an atomically flat surface prepared by the Clavilier method [10]. Various techniques including SHG [24], SXS [25, 26] and STM [27] have been utilized to monitor the potential-induced structural change. After a flame-annealing, a thermally induced reconstructed herringbone structure representing ($\sqrt{3} \times 23$) structure was observed at −0.2 V vs. Ag/AgCl (Fig. 1a) [28]. In the potential range between 0.4 and 0.8 V, the reconstructed ($\sqrt{3} \times 23$) structure was lifted to the (1×1) phase and (hydrogen-) sulfate anions adsorbed on the (1×1) surface (Fig. 1b, left) [28]. When the potential was scanned to more positive than 0.85 V, phase transition of the disordered sulfate anions into the ordered ($\sqrt{3} \times \sqrt{7}$) structure took place at the Au(111)-(1×1) surface (Fig. 1b, right) [28]. The quality of the STM images has been drastically improved since the first report of STM observation on structural changes of Au(111) electrode surface long time ago as clearly seen in Fig. 1 [28].

Recently, not only the spatial resolution but also the time constant has been significantly advanced up to the "video-rate" so that fast electrochemical processes can be monitored [29–32].

2.2 Atomic Force Microscopy

Since STM uses the tunneling current between the tip and the sample as a probe, it cannot be applied for insulating materials such as polymers, ceramics and metal oxides. Potential range for observing semiconductor surfaces is also limited due to the space-charge layer in a reverse bias region. On the other hand, AFM, in which the force between the tip and the sample surface is used as a probe, is capable of imaging not only the conductor surfaces but also insulating surfaces with a high

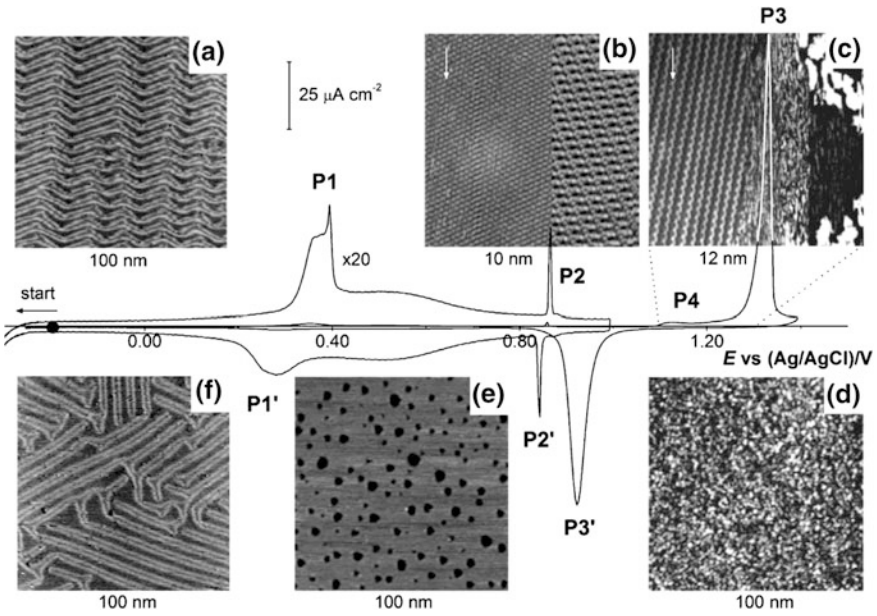

Fig. 1 Cyclic voltammograms and potential-dependent STM images of an Au(111) single crystal electrode in 50 mM H_2SO_4 [28]

spatial resolution similar to that of STM. Moreover, AFM has a few advantages over STM; (1) electrochemical reactions at the tip do not affect the measurement, (2) distribution of various physical properties such as friction, magnetism, surface potential, viscoelasticity and conductivity can be measured simultaneously with the surface topography, and (3) AFM can be used in combination with other surface analysis techniques such as fluorescent, IR, and Raman spectroscopy.

Although contact and tapping modes were used in the early stage, an extremely high spatial resolution of frequency modulation (FM-) AFM, which is a class of non-contact modes, has made it an indispensable tool for the studies on electrified interfaces [33, 34]. Figure 2A shows a mica surface in contact with water with a true atomic resolution [33]. FM-AFM has brought a significant impact not only on imaging studies because of its high spatial resolution but also on electric double layer because of its 2D/3D force mapping capability in liquid phases. In fact, hydration structures as well as that of local electric double layer forces have been discussed with a molecular-scale on the basis of 3D mapping of frequency shift as shown in Fig. 2B [35].

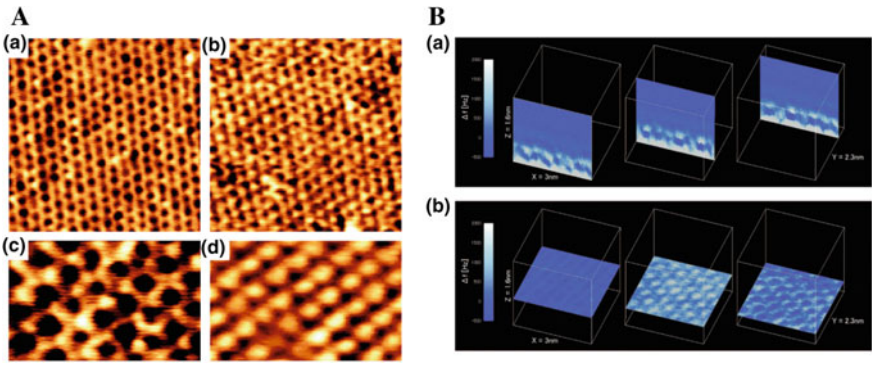

Fig. 2 **A** FM-AFM images of the cleaved mica surface in water [33]. **B** *a* z–x slices and *b* x–y slices of a 3D force mapping of mica in aqueous solution [35]

3 Vibrational Spectroscopy

Vibrational spectroscopies such as IR spectroscopy and Raman scattering provide the information about the molecular composition, structure and interactions within samples by measuring vibrational energy of the chemical bonds. IR spectroscopy and Raman scattering are complementary because their selection rules are different. Although vibrational spectra can be obtained from the samples in solid, liquid and gas phases, they are not intrinsically surface sensitive. Thus, a large number of techniques to extract/enhance the information of surfaces and interfaces have been developed using nanostructured substrates and modulation of electrochemical potential and polarization.

3.1 Infrared Spectroscopy

IR spectroscopy is one of the most widely used techniques to investigate the molecular structures not only in liquid and gas phases but also at solid/liquid interfaces under electrochemical potential control. There is one major difficulty in its utilization for solid/liquid interfaces. The signal originated from the molecules at the interface is often buried within the much stronger signals of the bulk species such as gas, electrolyte and solvent molecules. In the 1980s, Bewick developed an electrochemically modulated IR spectroscopy (EMIRS), in which an electrochemical potential is alternately modulated by square wave and change in reflectivity at the different potentials is detected by a phase sensitive detector with a grating spectrometer to yield a difference spectrum [36–39]. In their

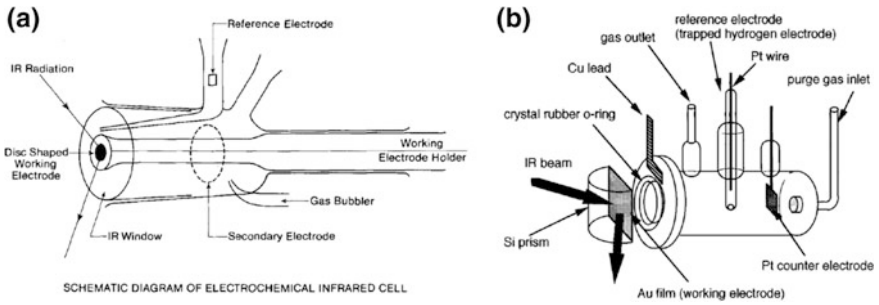

Fig. 3 Schematic diagrams of the spectroelectrochemical cells in **a** the external-reflection [38] and **b** the internal-reflection configuration [42]

external-reflection configuration shown in Fig. 3a, IR spectra were accumulated by using a grating spectrometer and IR absorption due to the solvent was minimized by pressing the electrode against an optical window to maintain the thickness of solution layer to a micro-meter scale [38]. They have applied this technique to study a variety of electrode/electrolyte interfaces including CO adsorption on various metal surfaces [40], which is still of a great interest, especially in relation to the fuel cell research. In addition, they have used Fourier transform (FT-) IR spectroscopy and proposed its advantages over the conventional grating spectrometer [41]. While the grating spectrometer records only over a narrow spectral range, FT-IR spectrometer enables to record spectra in a wide frequency range with a high resolution without extension of the data acquisition time, although the absolute sensitivity was often less than that of the grating spectrometer.

Soon after, thanks to the advancement of the autoscaling analog-to-digital (A/D) converter with a greater dynamic range, FT-IR spectrometers began to spread rapidly and subtractively normalized interfacial Fourier transform IR spectroscopy (SNIFTIRS) was established as a surface-sensitive technique [43–45]. In SNIFTIRS, interferrograms are alternately measured at two potentials and a difference spectrum can be obtained with a high sensitivity after repeating the interchangeable measurements for certain time.

Figure 4 shows SNIFTIRS spectra of Au(100) surface modified with a self-assembled monolayer of 2-(11-mercaptoundecyl)hydroquinone ($H_2QC_{11}SH$) in 0.1 M $HClO_4$ solution [46]. In the potential region more positive than 0.6 V, three upward and downward peaks were observed and the intensities increased as the potential became more positive. Since the upward and downward peaks are corresponding to the species disappearing and appearing at the applied electrode potential, upward and downward peaks should be due to the hydroquinone and its oxidized form, respectively. The upward peak observed at 1206 cm^{-1} is assignable to the C-O stretching and those at 1456 and 1508 cm^{-1} are assignable to the benzene ring stretch. The downward peaks observed at 1303, 1600, and 1660 cm^{-1} are assignable to the C-C stretching, C=C stretching and C=O stretching vibration

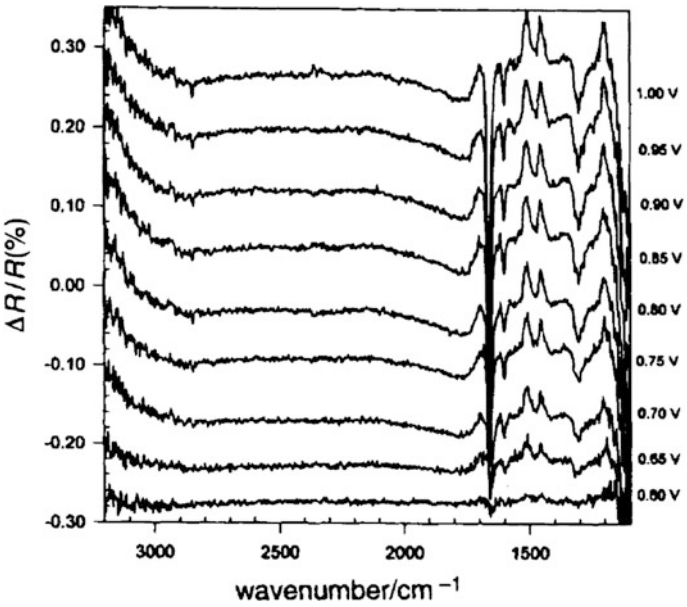

Fig. 4 In situ FT-IRRAS spectra of the $H_2QC_{11}SH$ SAM-modified gold electrode measured at various potentials in 0.1 M $HClO_4$ solution with p-polarization. The spectra measured at 0 V was used as a Ref. [46]

of quinone ring of the oxidize form, respectively. This result clearly shows that the structural change of mono-molecular layer can be detected by in situ SNIFTIRS.

The electrochemical modulation techniques such as EMIRS and SNIFTIRS cannot be used when the structure of adsorbed species is changed irreversibly with the potential because the electrode potential is alternately modulated in those techniques. Another approach to obtain the surface-sensitive spectra is utilization of polarized IR light as a probe. When p-polarized light, of which the electric field vector is normal to the sample surface, is incident, absorption due to the surface species is significantly enhanced by the strong electric field perpendicular to the surface formed by the interference between the incident and reflected light. In contrast, when the s-polarized light, of which the electric field vector is parallel to the sample surface, is incident, the electric fields of the incident and reflected light are canceled each other due to their phase difference, resulting in a relatively small absorption. In the case of metal substrates, information of the adsorbed species perpendicular to the sample surface is selectively detected in the spectra measured at p-polarization and the maximum sensitivity can be achieved when the incident angle of IR light is 80–85°. Thus, the reflection absorption spectra of adsorbed species can be obtained by rapidly switching the polarization of the incident light between s- and p-polarizations with a photoelastic modulator under a constant potential, that is, polarization modulation IR reflection absorption spectroscopy (PM-IRRAS) [47].

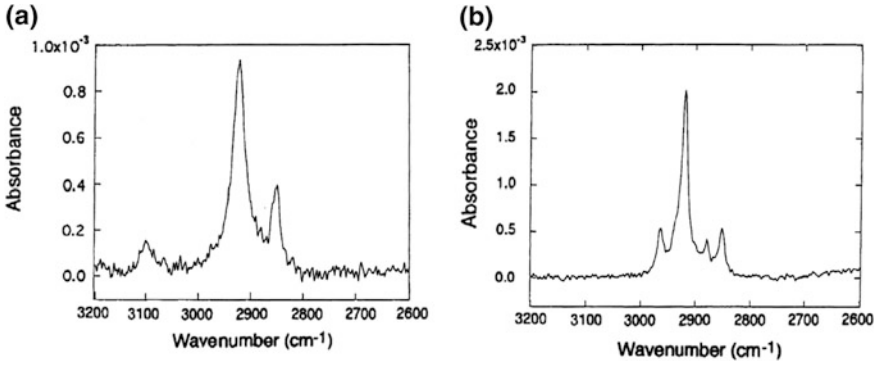

Fig. 5 PM-IRRAS spectra in the CH stretching region for gold electrodes modified with self-assembled monolayers of **a** FcC11SH and **b** C18SH [47]

Figure 5 shows PM-IRRAS spectra in the C-H stretching region for gold electrodes modified with self-assembled monolayers of (a) 11-ferrocenyl-1-undecanethiol (FcC11SH) and (b) 1-octadecanethiol (C18SH) [47]. Peaks corresponding to the CH stretching vibration of the ferrocene ring, asymmetric and symmetric CH stretching vibrations of methylene groups were observed at 3100, 2923 and 2851 cm^{-1} in Fig. 5a. Instead of the ferrocene ring, asymmetric and symmetric CH stretching vibrations of methyl groups were observed at 2960 and 2870 cm^{-1}, as well as those of methylene groups, in Fig. 5b. Although these spectra were obtained in air, PM-IRRAS measurements can be performed at the solid/liquid interfaces under the electrochemical potential control. Thus, the molecular structural change can be discussed at a mono-molecular level by this method.

The sensitivity can be further enhanced by a factor of two orders of magnitude when the above-mentioned techniques are used in combination with the surface-enhanced IR absorption spectroscopy (SEIRAS). SEIRAS can be easily combined with various experimental configurations including both internal- and external-reflection without any significant change of optical design since such a surface enhancement of the IR absorption is achieved by using roughened surfaces of various metals such as gold, silver, copper and platinum as is the case of Raman spectroscopy (see below). After the finding of SEIRA effect by Hartstein in 1980 [48], a significant progress has been made to monitor the potential-induced structural change of the molecules at the electrode surfaces, as well as the understanding of the enhancement mechanism of SEIRA [49, 50]. Since the enhancement factor rapidly decays with the distance from the surface, very high sensitivity to the surface molecular species can be obtained by SEIRA. Recently, SEIRA in an internal-reflection configuration is widely used for solid/liquid interfaces as in situ IRRAS measurements can be performed with a thick solution layer using a prism coated with a thin metal layer as a working electrode as shown in Fig. 3b [42], since IR light is irradiated from the backside of the IR-transparent prism. This

configuration has several advantages over external-reflection configuration including surface sensitivity, smaller time constant, and easier mass transport. Upon the reflectance of the IR light incident from the prism side, some of the IR light penetrates into the solution side and interacts with the molecules at the interface, so that surface-sensitive IRRAS spectra can be obtained. Because thick solution layer can be used in the internal-reflection configuration in contrast to the external-reflection configuration, in which the electrode should be pressed to an optical window to avoid the absorption of IR light due to the solvent, smaller time constant for potential application, more uniform potential distribution, and easier mass transfer can be expected.

3.2 Raman Spectroscopy

When visible light with a given frequency, ν_0, is incident on materials, in addition to elastically scattered light with the original frequency (Rayleigh scattering), scattered light with an energy smaller and larger than that of the incident light by the frequency of ν is generated due to inelastic scattering; Stokes and anti-Stokes Raman scattering, respectively. Raman spectroscopy, in which intensities of Raman scattering are plotted as a function of ν, is capable of determining the vibrational states because ν corresponds to the vibrational energy of chemical bonds and lattice. Unlike the IR spectroscopy, which needs to avoid the significant loss of IR in the solution phase, information of electrodes in contact with a thick solution layer can be obtained in both the external- and internal-reflection configurations because visible light can be used for both excitation and detection light in the Raman spectroscopy. The origin of the surface enhancement effect of Raman scattering has been studied since its discovery [51] both theoretically and experimentally on the basis of two mechanisms, an electromagnetic effect and a short-range chemical effect. Meanwhile, Raman spectroscopy with surface enhancement effect has been rapidly spread to be used as a surface vibrational spectroscopy referred to as surface-enhanced Raman spectroscopy (SERS) because the intensity of Raman scattering is enhanced by a factor of more than 10^{10}, although Raman spectroscopy is inherently a surface-insensitive technique.

Figure 6 shows potential-dependent SERS spectra during the electrochemical reduction of nitrobenzene at gold electrode surfaces in acidic and alkaline solutions [52]. When the potential was made more positive than 0 V in the acidic solution, Raman bands corresponding to the ring breathing (ν_{12}), ring stretching (ν_{8b}), and NO_2 symmetric stretching modes of nitrobenzene were observed at 998, 1108, and 1330 cm^{-1}, respectively. As the potential was made more negative, the peak at 1330 cm^{-1} gradually decreased and three new bands assignable to adsorbed nitrosobenzene appeared at around 1145, 1390, and 1590 cm^{-1}, suggesting that nitrosobenzene is a surface reaction intermediate. In the alkaline solution, when the potential more positive than −0.4 V was applied, features corresponding to nitrobenzene were observed as was the case in the acidic solution. However, unlike

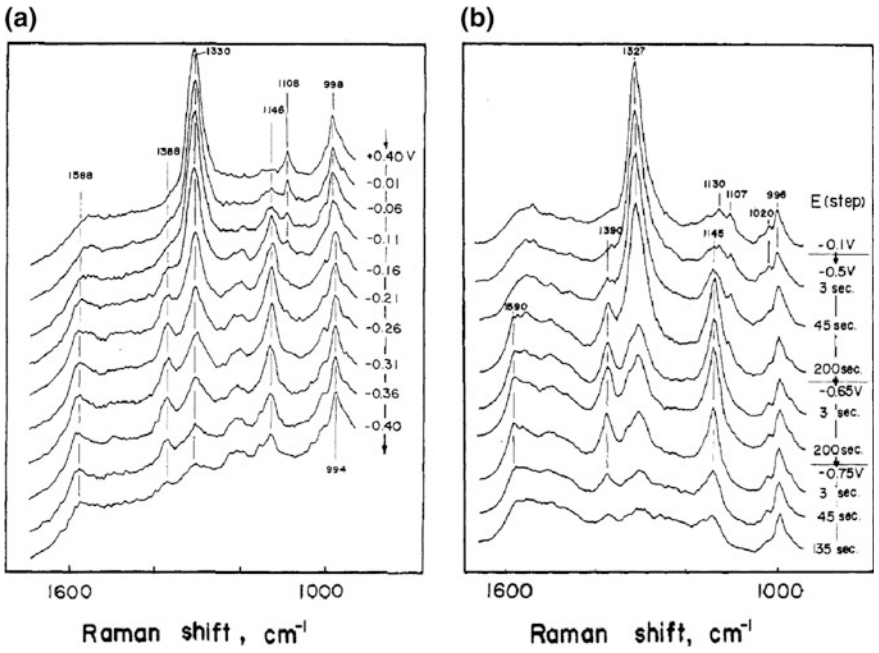

Fig. 6 Potential-dependent SERS spectra measured during linear sweep voltammetric reduction of nitrobenzene at gold electrode in aqueous solutions of **a** 0.1 M H_2SO_4 plus 3 mM nitrobenzene and **b** 0.1 M NaOH plus 3 mM nitrobenzene [52]

in the acidic solution, no band due to nitrosobenzene was observed in the potential region up to −0.7 V, although the spectral features of nitrobenzene disappeared. These results demonstrate that the reaction pathways of electrochemical processes at electrode surfaces can be discussed on the basis of the in situ SERS detection of intermediate species.

The enhancement of Raman scattering was first found at a roughened silver surface and, to date, SERS has been extended into various metal surfaces such as gold, silver, copper and platinum. Although SERS used to be only applicable for roughened surfaces of SERS-active materials, a significant enhancement of Raman intensities by a factor of approximately 10^6 is also achieved at atomically flat surfaces including single crystal surfaces not only of SERS-active but also of non-SERS-active materials by depositing gold nanoparticles on top of a molecular layer formed on a metal surface as shown in Fig. 7a [53]. This technique, which was first developed by Ikeda [54–57] and then extended by Tian [58] and Wandlowski [59], is referred as gap-mode Raman spectroscopy since the Raman scattering enhancement originates in the gap between the gold nanoparticle and the metal surface.

Figure 7b shows normalized Raman spectra of 4-aminobenzenethiol (ABT) monolayer formed on Au(111) and Au(100) surfaces measured at various electrochemical potentials in the presence of gold nanoparticles on top of the

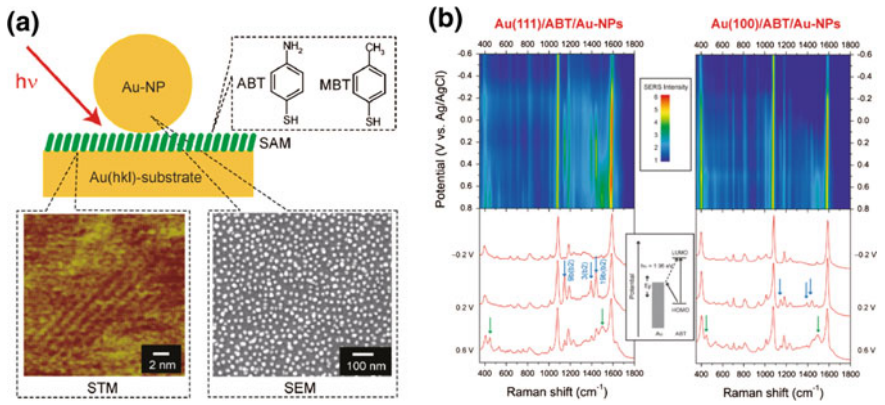

Fig. 7 **a** A schematic illustration of Au–NPs/SAMs/Au(hkl) system in a gap-mode configuration. An STM image of MBT-SAM/Au(111) and a SEM image of Au-NPs adsorbed on the SAM are also presented. **b** Potential dependence of sphere-plane SERS spectra of ABT at **a** Au(111) and **b** Au(100) surfaces. The overall signal intensity is normalized by the 7a(a1) intensity to focus on the ratios of b2 lines with respect to a1 lines. The cross-section spectra at 0.6, 0.2 and −0.2 V vs. Ag/AgCl electrode are also presented. Blue and green arrows indicate b2 modes and dimerization-related modes, respectively [53]

monolayer, i.e., the gap-mode Raman configuration [53]. Peaks due to the b2 modes are observed only in the potential range more positive than −0.2 V and 0 V for Au (111) and Au (100), respectively, and the intensities are clearly dependent on the electrode potential. This potential dependence is attributed to the alignment of energy states. Since b2 modes are corresponding to the metal-to-molecule charge transfer resonance as illustrated by dashed line in the energy diagram of Fig. 7b, the significant enhancement of Raman scattering is obtained when the energy of excitation light is matched with the energy difference between the molecular affinity level and Fermi level of the electrode, which is represented by electrode potential. Raman spectra are dependent not only the potential but also crystal-face. For example, the threshold potentials are different between Au(111) and Au(100). This difference is caused by the adsorbed amount of ABT. The work function can be modulated by the formation of dipoles between metal and molecule and the degree of modulation depends on the density and directions of the interfacial dipoles. In fact, the adsorbed amount of ABT was higher at Au(100) than at Au(111) by 20%, leading to the different molecular orientation between the facets.

4 Nonlinear Spectroscopy

Nonlinear spectroscopies such as SFG and SHG are powerful tools for surface-sensitive analysis of molecular and electronic structures because those phenomena take place not in isotropic media such as gas and liquid phases but only

at the surfaces and interfaces where the inversion symmetry/centrosymmetry is broken. In conjunction with the advances of optics, laser systems and theory, significant contributions have been made by SFG and SHG studies to understand the molecular and electronic structures at the surfaces and interfaces, although still only limited groups can carry out the SFG and SHG measurements due to the complexities in the experimental set-ups and interpretation of data.

4.1 Second Harmonic Generation

When intense light is incident on solid surfaces, light with twice the energy of the incident light is generated at the interface where the inversion symmetry is broken, that is one of the second-order nonlinear optical phenomena and is called second harmonic generation (SHG) [60]. When the SHG intensity is measured as a function of the incident photon energy, it is resonantly enhanced when either the photon energy of SHG or incident light coincides with the transition energy between two states at the interface, so that a surface-sensitive electronic spectrum can be obtained. Since the photon energy in the UV/visible region can be used as an incident light, absorption of incident and SHG light in the solution layer is generally not a problem.

Figures 8A and B show a schematic illustration of a spectroelectrochemical cell and an experimental set-up, respectively, used for in situ SHG measurement for electrochemical processes [8, 61]. The potential-dependent current response and the

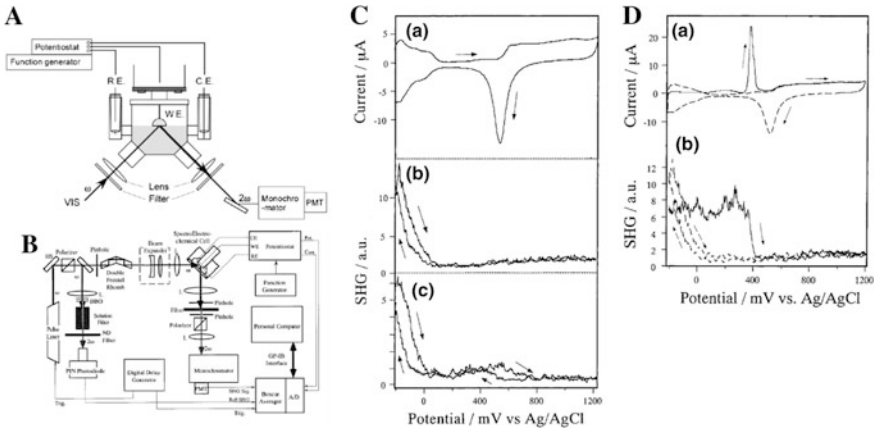

Fig. 8 **A** A spectroelectrochemical cell [8] and **B** an experimental set-up [61] for in situ SHG measurements at solid/liquid interfaces under potential control. **C** Potential dependent *a* current and SHG signals at *b* 532 nm and *c* 1064 nm excitation of a Pt electrode in a 0.1 M $HClO_4$ solution [61]. **D** Potential dependent *a* current and *b* SHG signals at 532 nm excitation of a CO-adsorbed Pt electrode in a 0.1 M $HClO_4$ solution [61]

SHG signals of the surface in contact with the electrolyte solution can be spontaneously measured. Laser light through a polarizer and a filter is incident on the electrode surface through the electrolyte solution layer and SHG light generated coaxially with the reflected light is detected using a photomultiplier through a filter and a spectroscope. Figure 8C shows the potential-dependent current response and spontaneously recorded SHG signals of a Pt electrode in 0.1 M $HClO_4$ [61]. As the potential was scanned negatively, current due to hydrogen adsorption started to flow from *ca.* 100 mV vs. Ag/AgCl reference electrode and SHG signals were significantly enhanced. In the reverse scan, SHG signals reversibly decreased upon desorption of hydrogen. In addition, Fig. 8D shows that the SHG signal enhanced by the pre-adsorbed CO drastically decreased at around 400 mV where oxidative desorption peak was observed in the current response [61]. This enhancement was attributable to the electronic transition from the Fermi level of Pt to an anti-bonding orbital of the adsorbed CO ($2\pi^*$). An anisotropic feature of the surface electronic structure can be also determined by measuring the anisotropy of the SHG intensity as a function of the azimuthal angle by rotating the sample with respect to the surface normal [62]. This method was applied to determine the surface chirarity of naturally chiral gold single crystalline surfaces [63].

4.2 Sum Frequency Generation

When two photons with different energies are incident, a photon with the sum of those energies is generated at the interface where the centrosymmetry is broken. This phenomenon is called sum frequency generation, SFG [60, 64]. If visible light with a fixed energy and IR light with a variable energy are focused on a sample surface, a surface-sensitive vibrational spectrum can be obtained by measuring the SFG response as a function of the energy of IR because SFG intensity is resonantly enhanced when the energy of IR coincides with the vibration energy of surface adsorbed species. Despite the complexity of the experimental set-up and data analysis, SFG spectroscopy is a very suitable technique to investigate the electrochemical processes with a very high surface sensitivity from the view point of molecular structure because solution species in the bulk, a centrosymmetric environment, do not contribute to the SFG spectra. For electrochemical SFG study, a spectroelectrochemical cell similar to those of in situ IRRAS can be used, which can avoid the absorption of IR due to the solution species. Internal-reflection configuration can be employed also in SFG; the IR and visible light incident from the back side of the prism are totally reflected at the solution/prism interface, and the SF light filtered from the reflected light is detected by a photomultiplier through a filter and monochromator.

Figure 9 shows SFG spectra in the OH stretching region of a gold and a platinum electrode measured in a 0.1 M $HClO_4$ solution [65]. While a broad peak around 3500 cm^{-1} is dominant at the gold electrode, two peaks at around 3200 and 3450 cm^{-1} were observed at the platinum electrode. This difference is attributed to

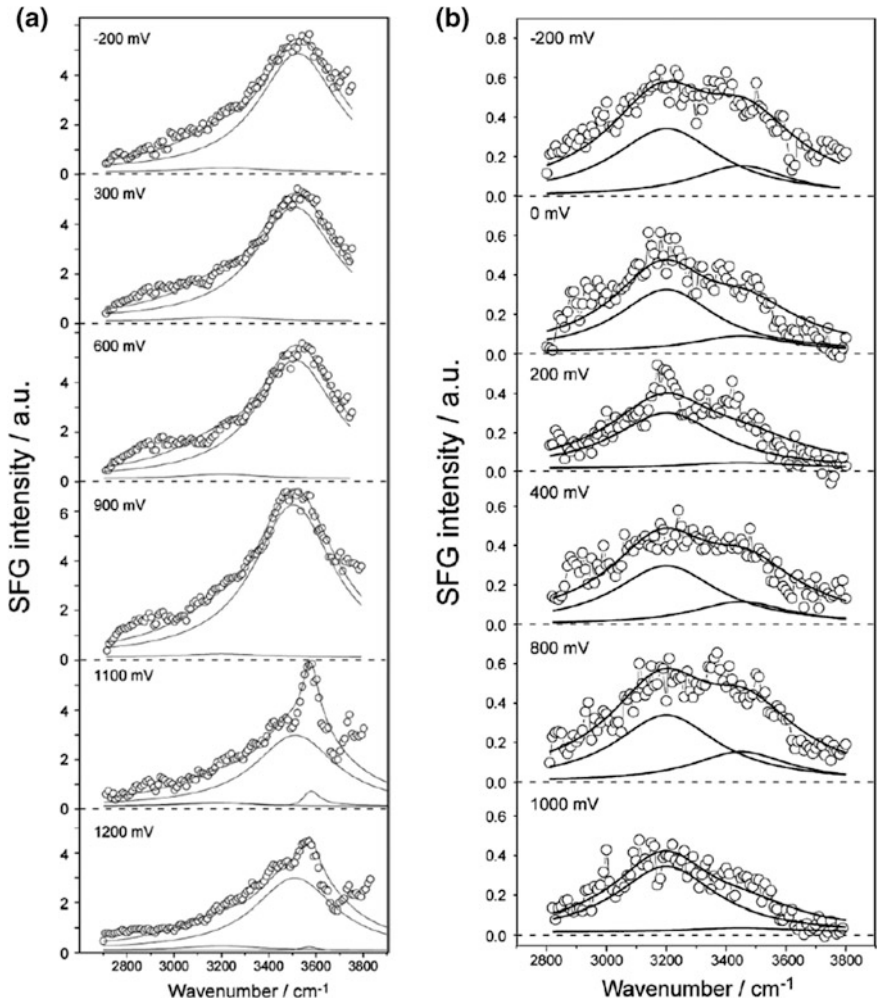

Fig. 9 SFG spectra in the OH stretching region at **a** a gold and **b** a platinum electrode at various potentials in 0.1 M $HClO_4$ solution [65]

the interactions between water molecules and the gold and platinum surfaces as water layer is more ordered at a platinum surface than at a gold surface. The SFG intensity due to the interfacial water was significantly affected by the electrode potential, although their shapes did not change much. The SFG intensity becomes minimum at around 300 mV and 200 mV for the gold and platinum electrode, respectively, which are close to the potential of zero charge of each electrode in this solution.

The SFG intensity can be enhanced not only by the resonance of IR light with vibration energy of surface species but also by the resonance of visible light with

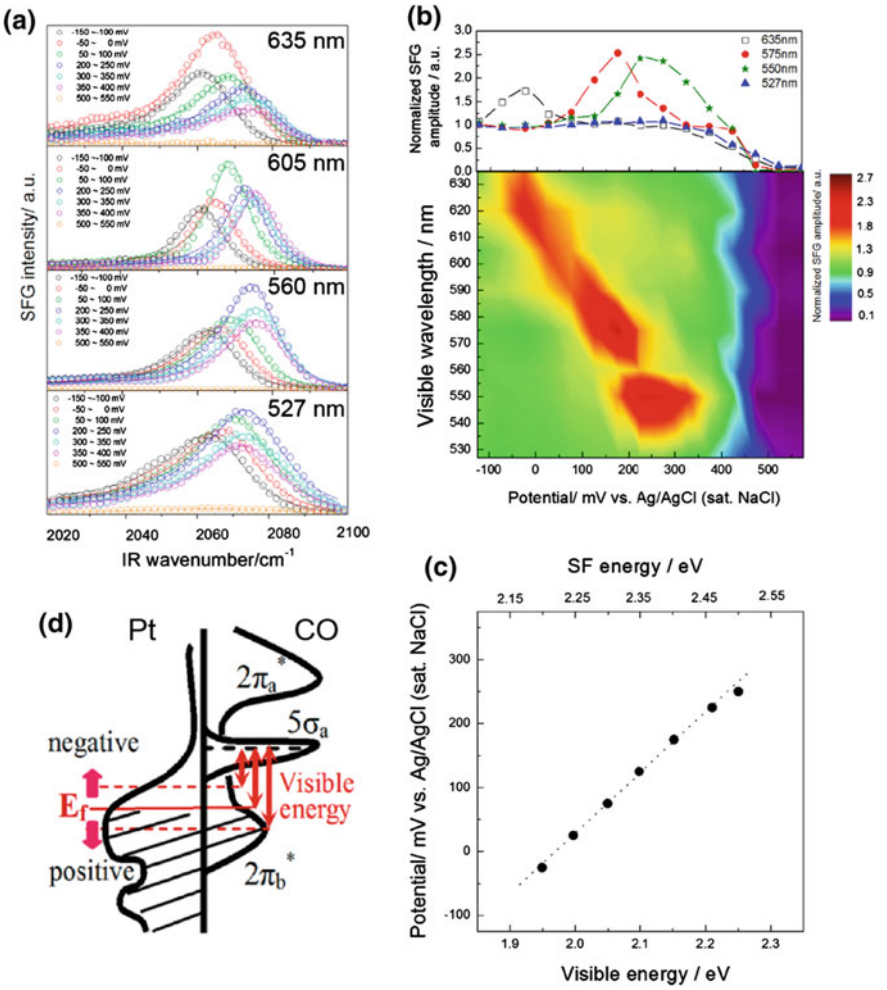

Fig. 10 **a** Potential-dependent SFG spectra of the CO-adsorbed Pt(111) electrode in 0.5 M H_2SO_4 solution measured by visible light at 635, 605, 560 and 527 nm. **b** Normalized peak height of the CO stretching vibration obtained from the SFG spectra shown in **a** as a function of potential and a contour plot of the peak amplitude as functions of the potential and wavelength of visible light. **c** Peak potential as a function of the energy of incident visible light. **d** A proposed model of electronic structure of the CO-adsorbed Pt(111) electrode [66]

the electronic transition between two energy states at the surface. When both IR and visible lights are in resonant, it is called double resonant (DR-) SFG. Recently, DR-SFG was applied to determine the electronic structure of the CO-adsorbed Pt (111) electrode in an electrolyte solution [66]. Figure 10a shows potential-dependent SFG spectra measured by visible light with various wavelength [66]. In all the spectra except for those measured at the potential more positive than

500 mV where the oxidative decomposition of CO starts to take place, peaks corresponding to the CO stretching vibration were observed and, interestingly, the peaks blue-shifted as the potential was made more positive. In addition, intensities of the CO stretching peaks are dependent not only on the electrode potential but also on the energy of visible light, although the amount of adsorbed CO is constant in this potential range. Thus, the SFG intensity was affected by both the electrode potential and wavelength of visible light; the electrode potential and wavelength where the highest SFG intensity is obtained have a linear relationship as can be seen in Fig. 10b, c. This linear relation between the potential and energy of visible light with a slope of 1 eV/V can be explained by the model proposed in Fig. 10d. The SFG peak attributed to the CO stretching vibration is further enhanced by the resonance of visible light with the transition energy between the Fermi level, E_f, which can be varied linearly with the electrode potential, and $5\sigma_a$ of the adsorbed CO. As the potential becomes more negative, the transition energy between E_f and $5\sigma_a$ becomes smaller and, therefore, resonance occurs with lower photon energy.

5 Synchrotron Radiation X-Ray Based Techniques

Although the surface geometric structure can be directly imaged by STM and AFM at an atomic scale, information is obtained only from the outermost layer of the sample surfaces. X-rays are considered to be an ideal probe for the structural analysis at solid/liquid interfaces at an atomic scale, because (1) they transmit through the solution layers without significant loss in intensity due to absorption and scattering in the liquid phases, (2) the energy is high enough to excite electrons at core levels of various atoms and (3) the wavelength is equivalent to the size of atoms and ions (0.01–10 Å), although lateral resolution is not high. In the early stage, applications of x-ray-based techniques to the electrochemical science were rather very limited because it was very difficult to obtain the information at the electrochemical interface buried within the electrolyte solution layer with a high signal-to-noise (S/N) ratio owing to the severe limitations of x-ray sources in laboratories, such as low intensity, low directionality and restriction of wavelength. In contrast, x-rays from synchrotron radiation source have an extremely high brilliance, directionality and a continuous wavelength distribution and thus, utilization of synchrotron radiation light as the x-ray source has brought an innovation in the use of x-rays in the field of surface science, especially at the surfaces and interfaces buried within electrolyte solutions.

5.1 Surface X-Ray Scattering

Surface x-ray scattering (SXS) is a generic term for crystal truncation rod (CTR) and surface x-ray diffraction (SXRD). The information of

the interfacial structures both perpendicular and parallel to the surface can be obtained by combining both techniques. In the "ordinary" powder x-ray diffraction, incident angles much higher than the critical angle are used to yield an intensity distribution of the diffracted x-rays as a function of the angle, and the bulk crystal structure can be analyzed from the position and width of diffraction peaks. In the SXRD, however, x-rays are incident onto the sample surfaces below the critical angle, typically less than 2–3 mrad, so that penetration depth of the incident x-rays is only 1–10 nm and most of the x-rays are specularly reflected. The penetrated x-rays can be diffracted by the two dimensionally ordered structure at the sample surface, so that the two-dimensional structure can be determined from the distribution of diffraction intensities. SXRD profiles can be measured by monitoring the intensity of diffracted/scattered x-rays with scanning the azimuthal angle of the sample and detector and fixing the grazing angle of incident x-rays.

CTR scattering occurs at the surfaces and interfaces since the diffraction condition is eliminated in the surface normal due to the breaking of the crystal periodicity, i.e., truncation of the surfaces. Distribution of the intensity can be expressed along with the rods vertical to the two dimensionally ordered surface in a reciprocal lattice space. Using a set of H and K, which represent the two-dimensional plane, each rod is referred as an (H K) rod. CTR profiles can be measured by monitoring the intensity of scattered x-rays with changing the polar angles at given azimuthal angles of the sample and detector. Since SXRD and CTR measurements can be carried out in the same experimental set-up with a multi-axis diffractometer, their complementary use allows to determine the three-dimensional geometric structure of the single crystalline surfaces at an atomic resolution.

Figure 11 shows schematic drawings of the spectroelectrochemical cells for in situ SXS measurements at the solid/liquid interfaces. Although highly intense x-rays from synchrotron radiation are utilized as a light source, the SXS measurements are carried out in a thin layer type cell [67], where the thickness of the solution layer is controlled to be less than a few tens of micrometers by an x-ray

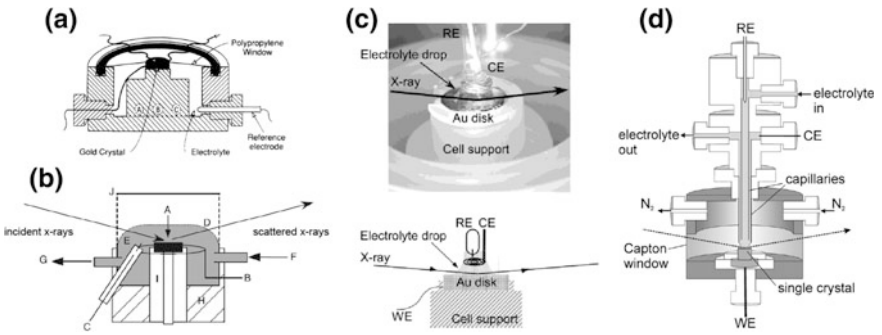

Fig. 11 Schematic illustrations of various spectroelectrochemical cells for in situ SXS measurements. **a** Thin layer type [67], **b** tunable type [68], **c** drop type [69], and **d** meniscus type configurations [70]

window, typically, a thin polyester or polyimide film, to minimize the absorption of the incident and scattered x-ray by the solution layer (Fig. 11a). This configuration often causes the nonuniform potential distribution and prevents the effective mass transfer to the electrode surfaces. Hence, an advanced cell, in which the thickness of the electrolyte solution between the polymer window and electrode can be tuned during the potential sweeping, was designed (Fig. 11b) [68]. Another approach is a transmission configuration, where a droplet of an electrolyte solution is kept on the single crystalline electrode surface with counter and reference electrodes such as a drop [69] and meniscus type cell [70] (Fig. 11c, d). In the transmission configuration, as long as the grazing angle of the incident x-rays is almost parallel to the surface, the travel distance for x-rays through the solution layer is almost the same as that for the thin layer configuration. In addition, since sufficiently thick solution layer can be ensured for uniform potential distribution and effective mass transfer, in situ dynamic measurements can be performed with a relatively high time resolution. However, it is sufferred from a few technical difficulties such as arrangement of counter and reference electrodes in the droplet and maintaining the droplet on the sample surface in any arrangement of the diffractometer.

As mentioned above, Au(111) surfaces in contact with electrolyte solutions have been one of the most studied systems. Atomic arrangements of the thermally induced reconstructed structure, lifting of the reconstruction, adsorption of sulfate and its phase transformation have been determined in situ not only by STM but also by SXS. Figure 12a shows a series of CTR profiles of the Au(111) surface measured in a sulfuric acid solution at various electrode potentials by using the tunable type cell [26]. As a result of the least-square fitting of the CTR profiles with a

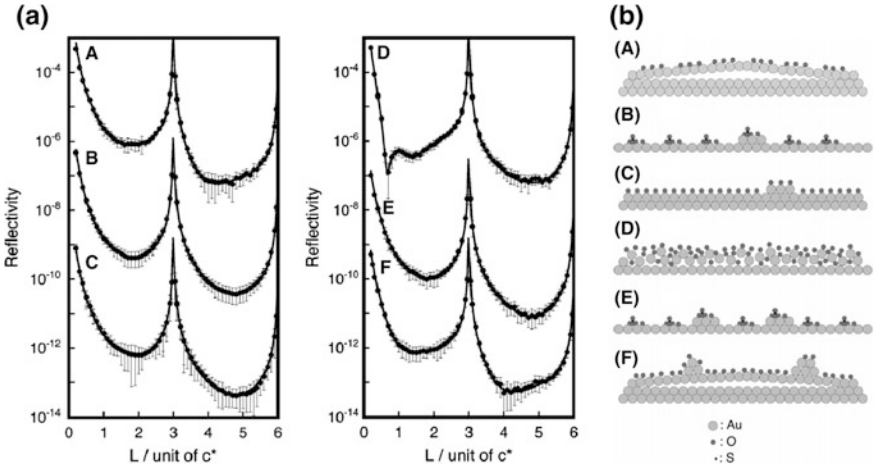

Fig. 12 **a** CTR profiles of the Au(111) measured in 50 mM H_2SO_4 solution at *A* 0 V upon immersion, *B* 0.95 V, *C* 1.05 V, *D* 1.40 V, *E* 0.65 V and *F* 0 V after the potential cycle and **b** corresponding schematic models of the Au(111) on the basis of fitting analysis using three layers model [26]

kinematical calculation based on a specific interfacial model, three-dimension structures of top a few layers of the Au(111)/0.5 M H_2SO_4 interface were quantitatively determined as Fig. 12b.

It is worth noting that, although SPM is capable of direct imaging of the surface atomic arrangement in real space, the interpretation of SXS results is often very difficult since the data is acquired in reciprocal space. On the other hand, although SPM provides the atomic arrangement of only the outermost layer in a microscopic region, SXS clarifies the information of top few atomic layers in a relatively large area. Thus, in situ structural changes at the electrode/electrolyte interfaces have been often investigated by complementarily use of SPM and SXS [71–73].

5.2 *X-Ray Absorption Spectroscopy*

Whereas SXS is only applicable to single crystalline surfaces with a long-range order, XAFS is applicable not only to single crystalline surfaces but also to materials without a long-range order, such as polycrystalline surfaces, nanoparticles, metal complexes including those in solutions and on solid surfaces. XAFS is composed of two regions; x-ray absorption near-edge structure (XANES) which is an approximately ±50 eV range from the absorption edge and extended x-ray absorption fine structure (EXAFS) which is an oscillatory structure observed over an energy range of approximately 1000 eV from the absorption edge. XANES is originated from the electron transition from a core level to an unoccupied state, and provides the information of the electronic structure of the x-ray absorbing atoms with a very high elemental selectivity. EXAFS oscillation is caused by the interference between electrons emitted by x-ray absorption and backscattered by neighboring atoms, and provides the information of the local structure including neighboring atomic species, their coordination number and distance from the x-ray absorbing atoms. Although XAFS is not inherently the surface sensitive techniques due to the relatively long attenuation length of the x-rays, various spectroelectrochemical cells which enable to perform in situ measurements have been developed to selectively extract the signal from the surfaces and interfaces.

A basic configuration of the spectroelectrochemical cell in the transmission mode, in which the intensities of x-rays are monitored before and after the transmission through the sample as a function of incident energy of x-rays, is shown in Fig. 13 [74]. In this cell, a material of interest such as thin metal films is deposited on the x-ray window, which is typically a polyester or polyimide film, as a working electrode. A fluorescence mode, in which the intensities of the incident and fluorescence x-rays are measured to obtain the quasi-absorption spectrum, is beneficial for low concentration materials and thick samples through which x-rays cannot transmit. The spectroelectrochemical cell with a thin-layer configuration used for in situ SXS measurements shown in Fig. 11a can be also employed for in situ XAFS measurements in the fluorescence mode. The sample is pushed to the x-ray windows to maintain the thickness of the solution layer to be several tens of

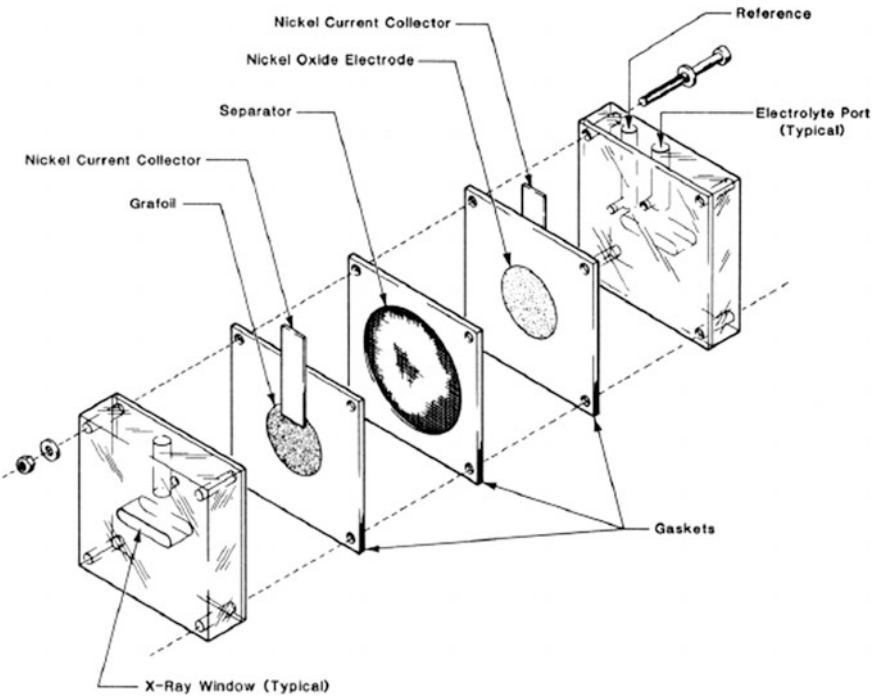

Fig. 13 A spectroelectrochemical cell for in situ XAFS measurements in the transmission mode [74]

micrometers to minimize the intensity loss of fluorescence x-rays and noise due to the scattering and absorption.

Figure 14 shows potential-dependent XANES spectra and EXAFS oscillations at the Pt LIII absorption edge of a Si(111) electrode modified with viologen moieties and Pt complexes measured in an Ar-saturated 0.1 M Na_2SO_4 solution using the spectroelectrochemical cell for the fluorescence mode in a total-reflection configuration together with those for K_2PtCl_4 and Pt foil as references [75, 76]. After a viologen-modified Si(111) surface was immersed in an aqueous solution containing K_2PtCl_4, both XANES spectrum (Fig. 14A (a)) and EXAFS oscillation (Fig. 14B (a)) became almost identical to those of K_2PtCl_4 pellet, showing that $PtCl_4^{2-}$ were incorporated into the viologen layer as a counter anion by ion exchange reaction. As the potential was made more negative in the 0.1 M Na_2SO_4 solution, intensities of near-edge peaks at around 11560 eV, that is called white line, gradually increased in the XANES spectra (Fig. 14A (b–e)) and period of the EXAFS oscillations significantly changed (Fig. 14B (b–e)). As a result from the curve fittings of Fourier transform and the FEFF simulations for various possible structures, Pt–Cl bonds were shown to be gradually replaced by oxygenated species such as water molecules and/or hydroxide groups as the potential was swept more negatively to promote hydrogen evolution reaction. Thus, it was found that Pt

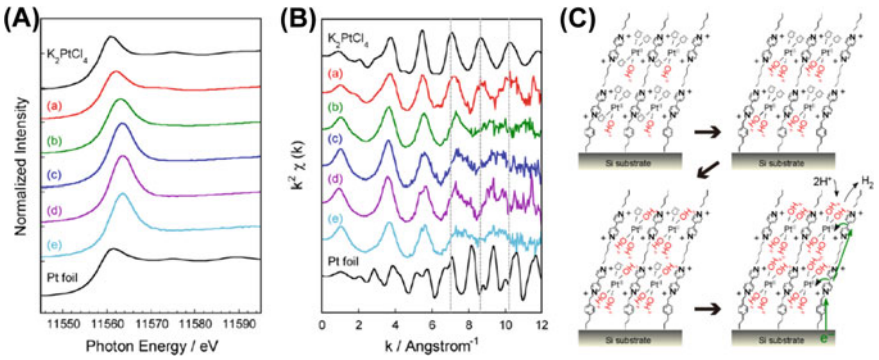

Fig. 14 **A** XANES spectra and **B** EXAFS oscillations at the Pt L_{III} absorption edge of the Si(111) electrode modified with viologen moieties and Pt complexes measured *a* in air immediately after the metal incorporation and in a 0.1 M Na_2SO_4 solution at *b* open circuit potential, *c* −0.4 V, *d* −0.6 V and *e* −0.8 V, together with results of a K_2PtCl_4 pellet diluted in a fine boron nitride powder and Pt foil as standard [75, 76]. **C** Schematic illustrations of the Si(111) electrode modified with viologen moieties and Pt complexes

complexes incorporated within the molecular layer acted as well-dispersed "molecular catalysts" without being reduced to nanoclusters, although the potential was made much more negative than the reduction potential of Pt complexes to Pt metal, e.g., 0.51 V vs. Ag/AgCl electrode for $PtCl_4^{2-}$.

Recently, not only hard x-ray XAFS but also soft x-ray absorption spectroscopy (XAS) [18, 77] and soft x-ray emission spectroscopy (XES) [19, 78] have been extended to the electrochemical interfaces. In these systems, spectroelectrochemical cells with a thin membrane window for x-rays of a thickness of an order of 100 nm were used in the UHV apparatus combined to beamlines of synchrotron facilities.

5.3 X-Ray Photoelectron Spectroscopy

X-ray photoelectron spectroscopy is a powerful technique to determine the elemental composition of the surface and oxidation state of each element with very high surface sensitivity [79]. Although the utilization of XPS for in situ analysis of electrochemical processes at solid/liquid interfaces has been a longstanding dream of electrochemists, it had not been established because of the requirement of vacuum.

Since the 1970s, various surface analysis apparatus equipped with an electrochemical chamber, from which an electrochemically treated specimen can be transferred to a UHV chamber for surface analysis such as LEED, AES and XPS without exposure to ambient air, have been developed [7] and are currently utilized not only for fundamental surface electrochemistry but also to study a wide range of electrode processes related to energy conversion [14]. In this "electrochemical-XPS

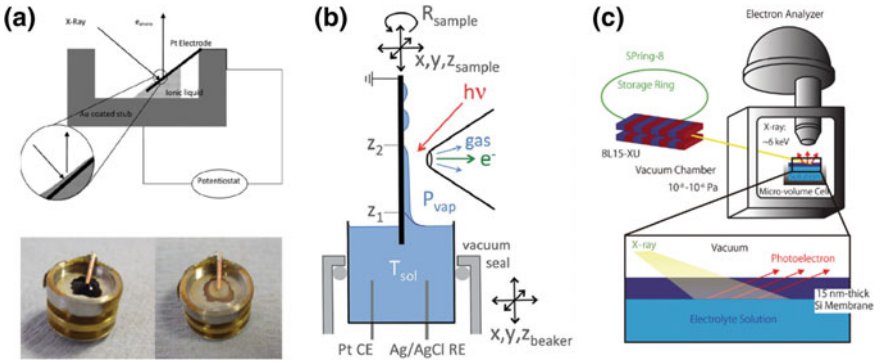

Fig. 15 Schematic illustrations of various in situ XPS cells using **a** room temperature ionic liquid [87, 88], **b** NAP-XPS [17] and **c** ultrathin membrane type cell [16]

apparatus," however, in situ electrochemical processes cannot be studied under the potential control because the electrolyte solutions are evacuated from the electrode surface prior to the sample transfer. By using RTILs as an electrolyte, in situ XPS measurements can be performed in UHV under the electrochemical potential control (Fig. 15a) [15]. Another approach for in situ XPS measurements is the utilization of near ambient pressure (NAP-)XPS (Fig. 15b) [17, 80]. In this system, photoelectrons ejected from the sample surface, which is kept in relatively low vacuum, can be collected by utilizing a differential pumping system and an electrostatic lens system [81].

Recent advances in nanofabrication technology for silicon-based thin films and other two-dimensional materials have enabled not only in situ SEM/TEM observations but also in situ XPS measurements [82] of materials kept in gas [83, 84] and liquid phases [16, 85, 86] by using environmental-controlled cell, which is filled with gas or liquid under ambient pressure and is separated from the UHV by the ultrathin membrane, typically silicon [16] or graphene-based materials [82]. Recently, we have carried out in situ electrochemical XPS measurement based on this concept for the first time [16]. XPS spectra of a sample placed in the cell can be obtained by collecting the electrons transmitted through the membrane (Fig. 15c).

6 Conclusion

In this chapter various novel in situ techniques to investigate the electrochemical processes taking place at solid/liquid interfaces developed in the last several decades are introduced with their advantages/disadvantages in their applications to various electrochemical systems. It must be stressed that an integrated approach using multiple complementary techniques is essential to understand the structure of electrode/electrolyte interfaces [89] and electrochemical processes.

References

1. Bockris JOM, Reddy AKN (1970) Modern electrochemistry, vol 1. Plenum Press, New York
2. Conway BE (1993) A tribute and survey of his research over 47 years on the occasion of his 70th anniversary—John O'M Bockris. J Electroanal Chem 357(1–2):1–46
3. Bockris JOM, Rand DA, Welch BJ (1976) Trends in electrochemistry. Plenum Press, New York
4. Abruña HD (1991) Electrochemical interfaces: modern techniques for in-situ interface characterization. VCH Publishers, New York-Weinheim-Cambridge
5. Lipkowski J, Ross PN (1992) Adsorption of molecules at metal electrodes. Frontiers of electrochemistry. VCH Publishers, New York-Weinheim-Cambridge
6. Lipkowski J, Ross PN (1993) Structure of electrified interfaces. Frontiers of electrochemistry. VCH Publishers, New York-Weinheim-Cambridge
7. Wieckowski A (1999) Interfacial electrochemistry: experimental, theory and applications. Marcel Dekker, New York
8. Uosaki K (2015) In situ real-time monitoring of geometric, electronic, and molecular structures at solid/liquid interfaces. Jpn J Appl Phys 54(3):030102
9. Gewirth AA, Feliu JM, Kuwabata S, Murakoshi K (2016) The Kohei Uosaki Festschrift: electrochemistry of ordered interfaces—design, construction, and interrogation of functional electrochemical interphases with atomic/molecular resolution. J Phys Chem C 120:15527. http://pubs.acs.org/doi/abs/10.1021/acs.jpcc.6b05243
10. Clavilier J, Faure R, Guinet G, Durand R (1980) Preparation of mono-crystalline Pt microelectrodes and electrochemical study of the plane surfaces cut in the direction of the (111) and (110) planes. J Electroanal Chem 107(1):205–209
11. Ishikawa RM, Hubbard AT (1976) Study of platinum-electrodes by means of thin-layer electrochemistry and low-energy electron-diffraction. 1. Electrode surface-structure after exposure to water and aqueous-electrolytes. J Electroanal Chem 69(3):317–338
12. Gerischer H, Tobias CW (1990) Advances in electrochemical science and engineering, vol 1. VCH, Weinheim-New York
13. Mayer T, Lebedev MV, Hunger R, Jaegermann W (2006) Synchrotron photoemission analysis of semiconductor/electrolyte interfaces by the frozen-electrolyte approach: interaction of HCl in 2-propanol with GaAs(100). J Phys Chem B 110(5):2293–2301
14. Wakisaka M, Udagawa Y, Suzuki H, Uchida H, Watanabe M (2011) Structural effects on the surface oxidation processes at Pt single-crystal electrodes studied by X-ray photoelectron spectroscopy. Energy Environ Sci 4(5):1662–1666
15. Lovelock KRJ, Villar-Garcia IJ, Maier F, Steinruck HP, Licence P (2010) Photoelectron spectroscopy of ionic liquid-based interfaces. Chem Rev 110(9):5158–5190
16. Masuda T, Yoshikawa H, Noguchi H, Kawasaki T, Kobata M, Kobayashi K, Uosaki K (2013) In situ x-ray photoelectron spectroscopy for electrochemical reactions in ordinary solvents. Appl Phys Lett 103(11):111605
17. Karslioglu O, Nemsak S, Zegkinoglou I, Shavorskiy A, Hartl M, Salmassi F, Gullikson EM, Ng ML, Rameshan C, Rude B, Bianculli D, Cordones AA, Axnanda S, Crumlin EJ, Ross PN, Schneider CM, Hussain Z, Liu Z, Fadley CS, Bluhm H (2015) Aqueous solution/metal interfaces investigated in operando by photoelectron spectroscopy. Faraday Discuss 180: 35–53
18. Nagasaka M, Yuzawa H, Horigome T, Hitchcock AP, Kosugi N (2013) Electrochemical reaction of aqueous iron sulfate solutions studied by Fe L-edge soft X-ray absorption spectroscopy. J Phys Chem C 117(32):16343–16348
19. Niwa H, Kiuchi H, Miyawaki J, Harada Y, Oshima M, Nabae Y, Aoki T (2013) Operando soft X-ray emission spectroscopy of iron phthalocyanine-based oxygen reduction catalysts. Electrochem Commun 35:57–60
20. Jusys Z, Behm RJ (2009) Methanol, formaldehyde, and formic acid adsorption/oxidation on a carbon-supported Pt nanoparticle fuel cell catalyst: a comparative quantitative DEMS study.

In: Koper MTM (ed) Fuel cell catalysis a surface science approach. Wiley series on electrocatalysis and electrochemistry. Wiley, Hoboken, New Jersey, pp 411–464
21. Ashton SJ (2012) Design, construction and research application of a differential electrochemical mass spectrometer (DEMS). Springer theses. Springer, Heidelberg
22. Binnig G, Rohrer H, Gerber C, Weibel E (1982) Surface studies by scanning tunneling microscopy. Phys Rev Lett 49(1):57–61
23. Binnig G, Quate CF, Gerber C (1986) Atomic force microscope. Phys Rev Lett 56(9): 930–933
24. Friedrich A, Pettinger B, Kolb DM, Lupke G, Steinhoff R, Marowsky G (1989) An in situ study of reconstructed gold electrode surfaces by second harmonic-generation. Chem Phys Lett 163(2–3):123–128
25. Wang J, Davenport AJ, Isaacs HS, Ocko BM (1992) Surface-charge induced ordering of the Au(111) surface. Science 255(5050):1416–1418
26. Kondo T, Morita J, Hanaoka K, Takakusagi S, Tamura K, Takahasi M, Mizuki J, Uosaki K (2007) Structure of Au(111) and Au(100) single-crystal electrode surfaces at various potentials in sulfuric acid solution determined by in situ surface X-ray scattering. J Phys Chem C 111(35):13197–13204
27. Kolb DM (1996) Reconstruction phenomena at metal-electrolyte interfaces. Prog Surf Sci 51 (2):109–173
28. Zhumaev U, Rudnev AV, Li JF, Kuzume A, Vu TH, Wandlowski T (2013) Electro-oxidation of Au(111) in contact with aqueous electrolytes: new insight from in situ vibration spectroscopy. Electrochim Acta 112:853–863
29. Labayen M, Magnussen OM (2004) In situ Video-STM study of the potential-induced (1 x 1) -> "hex" transition on Au(100) electrode surfaces in Cl- containing solution. Surf Sci 573 (1):128–139
30. Matsushima H, Taranovskyy A, Haak C, Gründer Y, Magnussen OM (2009) Reconstruction of Cu(100) electrode surfaces during hydrogen evolution. J Am Chem Soc 131(30):10362–10363
31. Suto K, Magnussen OM (2010) In situ Video-STM studies of sulfate dynamics on Au(1 1 1). J Electroanal Chem 649(1–2):136–141
32. Matsushima H, Haak C, Taranovskyy A, Gründer Y, Magnussen OM (2010) In situ video STM studies of the hydrogen-induced reconstruction of Cu(100): potential and pH dependence. Phys Chem Chem Phys 12(42):13992–13998
33. Fukuma T, Kobayashi K, Matsushige K, Yamada H (2005) True atomic resolution in liquid by frequency-modulation atomic force microscopy. Appl Phys Lett 87(3):034101
34. Fukuma T, Kobayashi K, Matsushige K, Yamada H (2005) True molecular resolution in liquid by frequency-modulation atomic force microscopy. Appl Phys Lett 86(19):193108
35. Kobayashi K, Oyabu N, Kimura K, Ido S, Suzuki K, Imai T, Tagami K, Tsukada M, Yamada H (2013) Visualization of hydration layers on muscovite mica in aqueous solution by frequency-modulation atomic force microscopy. J Chem Phys 138(18):184704
36. Bewick A, Kunimatsu K, Pons BS (1980) Infrared-spectroscopy of the electrode-electrolyte interphase. Electrochim Acta 25(4):465–468
37. Bewick A, Kunimatsu K, Robinson J, Russell JW (1981) IR vibrational spectroscopy of species in the electrode-electrolyte solution interphase. J Electroanal Chem 119(1):175–185
38. Bewick A, Kunimatsu K, Pons BS, Russell JW (1984) Electrochemically modulated infrared-spectroscopy (EMIRS)—experimental details. J Electroanal Chem 160(1–2):47–61
39. Avramovivic M, Adzic RR, Bewick A, Razaq M (1988) An investigation of the oxidation of formaldehyde on noble-metal electrodes in alkaline-solutions by electrochemically modulated infrared-spectroscopy (EMIRS). J Electroanal Chem 240(1–2):161–169
40. Beden B, Bewick A, Kunimatsu K, Lamy C (1982) Infrared study of adsorbed species on electrodes—adsorption of carbon-monoxide on Pt, Rh and Au. J Electroanal Chem 142(1–2): 345–356

41. Davidson T, Pons BS, Bewick A, Schmidt PP (1981) Vibrational spectroscopy of the electrode-electrolyte interface—use of fourier-transform infrared-spectroscopy. J Electroanal Chem 125(1):237–241
42. Ataka K, Yotsuyanagi T, Osawa M (1996) Potential-dependent reorientation of water molecules at an electrode/electrolyte interface studied by surface-enhanced infrared absorption spectroscopy. J Phys Chem 100(25):10664–10672
43. Pons S (1983) The use of fourier-transform infrared-spectroscopy for insitu recording of species in the electrode electrolyte solution interphase. J Electroanal Chem 150(1–2):495–504
44. Habib MA, Bockris JOM (1983) In situ FT-IR spectroscopic study of electrochemical adsorption of phosphoric acid on platinum. J Electrochem Soc 130(12):2510–2512
45. Habib MA, Bockris JOM (1984) FT-IR spectrometry for the solid-solution interface. J Electroanal Chem 180(1–2):287–306
46. Ye S, Yashiro A, Sato Y, Uosaki K (1996) Electrochemical in situ FT-IRRAS studies of a self-assembled monolayer of 2-(11-mercaptoundecyl) hydroquinone. J Chem Soc, Faraday Trans 92(20):3813–3821
47. Sato Y, Frey BL, Corn RM, Uosaki K (1994) Polarization modulation fourier-transform infrared studies of the effects of self-assembly time on the order and orientation of 11-Ferrocenyl-1-Undecanethiol monolayers on gold. Bull Chem Soc Jpn 67(1):21–25
48. Hartstein A, Kirtley JR, Tsang JC (1980) Enhancement of infrared-absorption from molecular monolayers with thin metal overlayers. Bull Am Phys Soc 25(3):425–425
49. Osawa M (1997) Dynamic processes in electrochemical reactions studied by surface-enhanced infrared absorption spectroscopy (SEIRAS). Bull Chem Soc Jpn 70 (12):2861–2880
50. Osawa M (2001) Surface-enhanced infrared absorption. Top Appl Phys 81:163–187
51. Fleischmann M, Hendra PJ, Mcquillan AJ (1974) Raman-spectra of pyridine adsorbed at a silver electrode. Chem Phys Lett 26(2):163–166
52. Gao P, Gosztola D, Weaver MJ (1988) Surface-enhanced raman-spectroscopy as a probe of electroorganic reaction pathways. 1. Processes involving adsorbed nitrobenzene, azobenzene, and related species. J Phys Chem 92(25):7122–7130
53. Ikeda K, Suzuki S, Uosaki K (2011) Crystal face dependent chemical effects in surface-enhanced raman scattering at atomically defined gold facets. Nano Lett 11 (4):1716–1722
54. Ikeda K, Fujimoto N, Uehara H, Uosaki K (2008) Raman scattering of aryl isocyanide monolayers on atomically at Au(111) single crystal surfaces enhanced by gap-mode plasmon excitation. Chem Phys Lett 460(1–3):205–208
55. Ikeda K, Sato J, Fujimoto N, Hayazawa N, Kawata S, Uosaki K (2009) Plasmonic enhancement of raman scattering on Non-SERS-Active platinum substrates. J Phys Chem C 113(27):11816–11821
56. Jung U, Muller M, Fujimoto N, Ikeda K, Uosaki K, Cornelissen U, Tuczek F, Bornholdt C, Zargarani D, Herges R, Magnussen O (2010) Gap-mode SERS studies of azobenzene-containing self-assembled monolayers on Au(111). J Colloid Interface Sci 341 (2):366–375
57. Ikeda K, Sato J, Uosaki K (2011) Surface-enhanced Raman scattering at well-defined single crystalline faces of platinum-group metals induced by gap-mode plasmon excitation. J Photoch Photobio A 221(2–3):175–180
58. Li JF, Li SB, Huang YF, Ren B, Tian ZQ (2010) Shell-isolated nanoparticle-enhanced raman spectroscopy for inspecting pesticide residues. In: Xxii international conference on Raman spectroscopy, vol 1267, pp 1049–1049
59. Cui L, Liu B, Vonlanthen D, Mayor M, Fu YC, Li JF, Wandlowski T (2011) In situ gap-mode Raman spectroscopy on single-crystal Au(100) electrodes: tuning the torsion angle of 4,4 '-Biphenyldithiols by an electrochemical gate field. J Am Chem Soc 133(19):7332–7335
60. Shen YR (1989) Surface properties probed by second harmonic and sum frequency generation. Nature 337(6207):519–525

61. Yagi I, Nakabayashi S, Uosaki K (1997) Excitation wavelength dependent three-wave mixing at a CO-covered platinum electrode. J Phys Chem B 101(38):7414–7421
62. Yagi I, Nakabayashi S, Uosaki K (1998) In situ optical second harmonic rotational anisotropy measurements of an Au(111) electrode during electrochemical deposition of tellurium. J Phys Chem B 102(15):2677–2683
63. Yagi I, Chiba M, Uosaki K (2005) Optical recognition of surface chirality at Au(hkl) single crystalline surfaces by second harmonic generation rotational anisotropy. J Am Chem Soc 127 (36):12743–12746
64. Zhu XD, Suhr H, Shen YR (1987) Surface vibrational spectroscopy by infrared-visible sum frequency generation. Phys Rev B 35(6):3047–3050
65. Noguchi H, Okada T, Uosaki K (2008) Molecular structure at electrode/electrolyte solution interfaces related to electrocatalysis. Faraday Discuss 140:125–137
66. Yang S, Noguchi H, Uosaki K (2015) Electronic structure of the CO/Pt(111) electrode interface probed by potential-dependent IR/visible double resonance sum frequency generation spectroscopy. J Phys Chem C 119(46):26056–26063
67. Wang J, Ocko BM, Davenport AJ, Isaacs HS (1992) In situ X-ray-diffraction and X-ray-reflectivity studies of the Au(111) electrolyte interface—reconstruction and anion adsorption. Phys Rev B 46(16):10321–10338
68. Kondo T, Zegenhagen J, Takakusagi S, Uosaki K (2015) In situ real-time study on potential induced structure change at Au(111) and Au(100) single crystal electrode/sulfuric acid solution interfaces by surface x-ray scattering. Surf Sci 631:96–104
69. Tamura K, Wang JX, Adzic RR, Ocko BM (2004) Kinetics of monolayer Bi electrodeposition on Au(111): surface X-ray scattering and current transients. J Phys Chem B 108(6):1992–1998
70. Magnussen OM, Krug K, Ayyad AH, Stettner J (2008) In situ diffraction studies of electrode surface structure during gold electrodeposition. Electrochim Acta 53(9):3449–3458
71. Chen CH, Kepler KD, Gewirth AA, Ocko BM, Wang J (1993) Electrodeposited bismuth monolayers on Au(111) electrodes—comparison of surface X-ray-scattering, scanning-tunneling-microscopy, and atomic-force microscopy lattice structures. J Phys Chem 97(28):7290–7294
72. Uosaki K, Ye S, Naohara H, Oda Y, Haba T, Kondo T (1997) Electrochemical epitaxial growth of a Pt(111) phase on an Au(111) electrode. J Phys Chem B 101(38):7566–7572
73. Takahasi M, Hayashi Y, Mizuki J, Tamura K, Kondo T, Naohara H, Uosaki K (2000) Pseudomorphic growth of Pd monolayer on Au(111) electrode surface. Surf Sci 461(1–3): 213–218
74. McBreen J, O'Grady WE, Pandya KI, Hoffman RW, Sayers DE (1987) EXAFS study of the nickel-oxide electrode. Langmuir 3(3):428–433
75. Masuda T, Fukumitsu H, Takakusagi S, Chun WJ, Kondo T, Asakura K, Uosaki K (2012) Molecular catalysts confined on and within molecular layers formed on a Si(111) surface with direct Si-C bonds. Adv Mater 24(2):268–272
76. Masuda T, Sun Y, Fukumitsu H, Uehara H, Takakusagi S, Chun WJ, Kondo T, Asakura K, Uosaki K (2016) Various active metal species incorporated within molecular layers on Si (111) electrodes for hydrogen evolution and CO_2 reduction reactions. J Phys Chem C 120 (29):16200–16210
77. Nagasaka M, Yuzawa H, Horigome T, Kosugi N (2014) In operando observation system for electrochemical reaction by soft X-ray absorption spectroscopy with potential modulation method. Rev Sci Instrum 85 (10):104105/104101-104105/104107
78. Asakura D, Hosono E, Niwa H, Kiuchi H, Miyawaki J, Nanba Y, Okubo M, Matsuda H, Zhou H, Oshima M, Harada Y (2015) Operando soft x-ray emission spectroscopy of $LiMn_2O_4$ thin film involving Li–ion extraction/insertion reaction. Electrochem Commun 50:93–96
79. Siegbahn K (1974) Electron-spectroscopy—outlook. J Electron Spectrosc Relat Phenom 5 (Nov-D):3–97
80. Axnanda S, Crumlin EJ, Mao BH, Rani S, Chang R, Karlsson PG, Edwards MOM, Lundqvist M, Moberg R, Ross P, Hussain Z, Liu Z (2015) Using "Tender" X-ray ambient

pressure X-ray photoelectron spectroscopy as a direct probe of solid-liquid interface. Sci Rep 5:9788
81. Salmeron M, Schlogl R (2008) Ambient pressure photoelectron spectroscopy: a new tool for surface science and nanotechnology. Surf Sci Rep 63(4):169–199
82. Kolmakov A, Dikin DA, Cote LJ, Huang JX, Abyaneh MK, Amati M, Gregoratti L, Gunther S, Kiskinova M (2011) Graphene oxide windows for in situ environmental cell photoelectron spectroscopy. Nat Nanotechnol 6(10):651–657
83. Ma T, Miyazaki K, Ariga H, Takakusagi S, Asakura K (2015) Investigation of the cleanliness of transferred graphene: the first step toward its application as a window material for electron microscopy and spectroscopy. Bull Chem Soc Jpn 88(8):1029–1035
84. Tsunemi E, Watanabe Y, Oji H, Cui YT, Son JY, Nakajima A (2015) Hard x-ray photoelectron spectroscopy using an environmental cell with silicon nitride membrane windows. J Appl Phys 117(23):234902
85. Kraus J, Reichelt R, Gunther S, Gregoratti L, Amati M, Kiskinova M, Yulaev A, Vlassiouk I, Kolmakov A (2014) Photoelectron spectroscopy of wet and gaseous samples through graphene membranes. Nanoscale 6(23):14394–14403
86. Velasco-Velez JJ, Pfeifer V, Havecker M, Weatherup RS, Arrigo R, Chuang CH, Stotz E, Weinberg G, Salmeron M, Schlogl R, Knop-Gericke A (2015) Photoelectron spectroscopy at the graphene-liquid interface reveals the electronic structure of an electrodeposited cobalt/graphene electrocatalyst. Angew Chem Int Ed 54(48):14554–14558
87. Taylor AW, Qiu FL, Villar-Garcia IJ, Licence P (2009) Spectroelectrochemistry at ultrahigh vacuum: in situ monitoring of electrochemically generated species by X-ray photoelectron spectroscopy. Chem Commun 39:5817–5819
88. Qiu FL, Taylor AW, Men S, Villar-Garcia IJ, Licence P (2010) An ultra high vacuum-spectroelectrochemical study of the dissolution of copper in the ionic liquid (N-methylacetate)-4-picolinium bis(trifluoromethylsulfonyl)imide. Phys Chem Chem Phys 12(8):1982–1990
89. Bockris JOM, Devanathan MAV, Muller K (1963) On the structure of charged interfaces. Proc R Soc Lond A 274:91–121

Large-Scale Batteries for Green Energy Society

Kiyoshi Kanamura

Abstract An extensive demand for rechargeable batteries from environmental problems due to CO_2 emission was described in the introduction. Then, general information about several kinds of batteries for energy storage and electric vehicle applications are described. Specially, lead acid battery, lithium ion battery, sodium-sulfur battery, and redox-flow battery have been discussed based on electrochemical reactions occurring in the practical cells. The energy density of each battery was also discussed in detail based on not only material sciences but also battery technologies. In the future, higher energy density is strongly required for future rechargeable batteries. In the final section, research and development of next generation batteries are involved in this chapter.

1 Introduction

A large amount of CO_2 has been released from fossil fuels by human activity. A concentration of CO_2 in atmosphere is increasing year by year. CO_2 is one of global warming gases. An average temperature of earth gradually increases, leading to serious environmental problems. In order to realize a sustainable green society, we have to reduce the consumption of fossil fuels. Recently, natural energy, such as solar and wind power energy has been developed. However, these energies are not stable, strongly depending on weather (day time and night time, season, and place). When this kind of unstable electric power is applied to a main electric power grid, the electricity supply becomes unstable. Therefore, the natural energy cannot be directly injected into a main electric power grid. One of solutions for this problem is electric energy storage by using rechargeable batteries. A major source of CO_2 is a car with thermal engine. An energy conversion efficiency of thermal engine is not so high, usually around 40%. This means that 60% of energy from gasoline is lost in order to obtain a kinetic energy for car. The lost energy is converted to heat energy

K. Kanamura (✉)
Tokyo Metropolitan University, Hachioji, Japan
e-mail: kanamura@tmu.ac.jp

K. Uosaki (ed.), *Electrochemical Science for a Sustainable Society*,
DOI 10.1007/978-3-319-57310-6_7

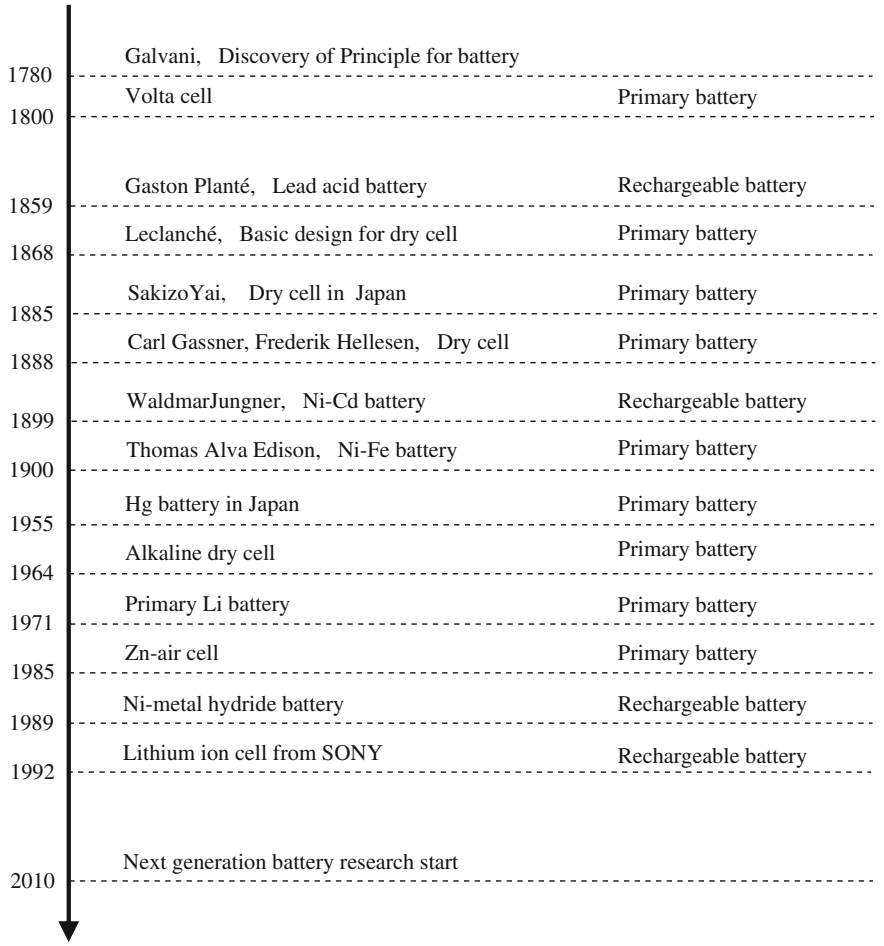

Fig. 1 History of batteries

by a heat loss of engine, a friction between tire and road, air resistance, and a breaking system. For effective use of gasoline, a hybrid car which has motor and engine has been developed and already commercialized by using high-performance battery, such as lithium ion battery.

There are so many devices including small- or middle-sized batteries. In various electric devices, such as refrigerator, computer, calculator, watch, sensor, and so on, several kinds of primary and secondary (rechargeable) batteries have been utilized to make our human life convenient.

In this chapter, the large-scale rechargeable batteries are discussed in order to construct a future green energy society with reduction of CO_2 generation from our human activities.

2 Classification of Batteries

At first, a classification of battery is described with a development history of primary and secondary ones. Figure 1 shows a history of battery development from 1780 to 2010. There are various kinds of batteries. Some of these batteries have been used in our life. The biggest event is a production of lithium ion battery by Sony in Japan.

2.1 Small Size Batteries

Several kinds of primary batteries have been used for lighting, watch, and so on. Most popular battery is a dry cell with MnO_2 cathode and Zn anode. Another important primary cell is a lithium battery for various electronic devices and camera. Ag battery and Zn-air battery have also been utilized in some specific applications. The primary cells can be discharged during their life, while impossible to be charged again. In order to utilize batteries to large-scale applications, batteries should be able to be charged many times. Ni-Cd and lead acid batteries are famous small- or middle-sized rechargeable batteries for car and electronic applications. Lead acid battery is still a main battery especially for lighting and starting of car. Ni-Cd battery is also very nice rechargeable battery, but unfortunately Cd has a high toxicity so that it has been replaced by other rechargeable batteries. These batteries have a reasonable energy density and power density. However, they cannot be applied to new applications such as cellar phone and personal computer. Instead of Ni-Cd battery, Ni-metal hydride battery has been commercialized and applied to cellar phone. This battery exhibited a relatively high energy density. By using this battery, cellar phone was produced. In 1992, Sony released a new high energy density battery that is so-called lithium ion battery. Lithium ion battery has the highest energy density among rechargeable batteries at this moment.

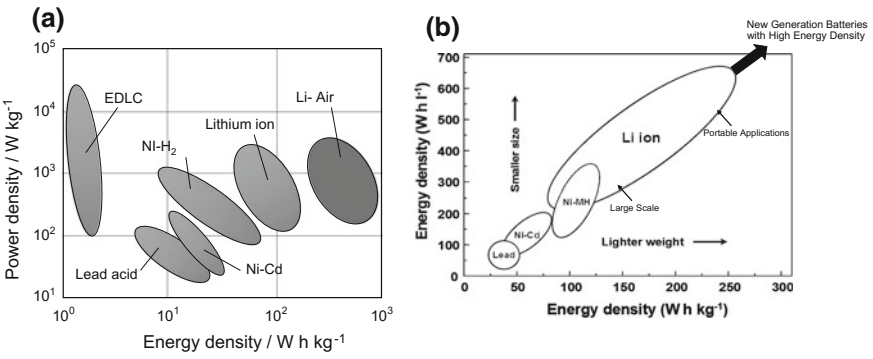

Fig. 2 **a** Power and **b** energy densities for rechargeable batteries

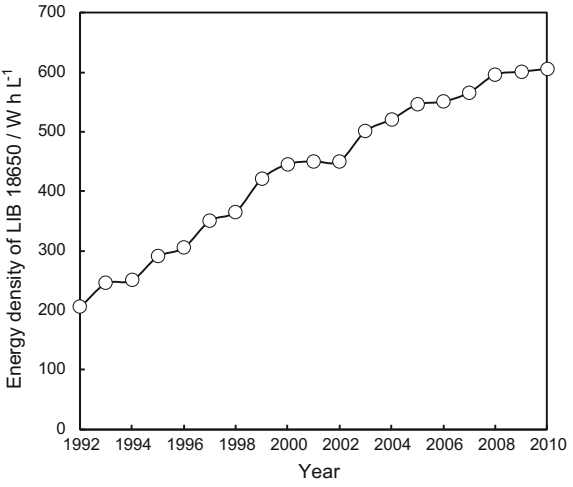

Fig. 3 Improvement of energy density of lithium ion battery (cylindrical type 18650)

Figure 2 shows a summary of energy density and power density of rechargeable batteries. Figure 3 shows an improvement of energy density of lithium ion batteries. Both energy and power densities have been improved. During this period, the materials for lithium ion battery did not change. Only the battery technology has progressed very much. The high energy density of Ni-metal hydride battery or lithium ion battery has been realized by using new electrode reaction that is an intercalation (or insertion) and de-intercalation (or extraction). For small-size applications, especially smart phone and tablet PC, lithium ion battery has a high advantage. On the other hand, the demanded energy density for rechargeable batteries increases year by year.

2.2 Large-Scale Batteries

Recently, global worming becomes a serious problem for human due to an excess emission of CO_2 and other greenhouse gases from industries, houses, and cars. A lot of CO_2 has been produced from electric power plant, steel production, and chemical industries. In addition, a thermal engine used in cars, ships, and trains produces a large amount of CO_2 due to their poor energy conversion efficiency. An ordinary engine has high energy conversion efficiency from chemical energy (fossil fuel) to kinetic energy. However, the total efficiency of thermal engine is still less than 40%. In order to improve its energy conversion efficiency, rechargeable batteries have been used in a hybrid car system. Rechargeable batteries can store the recovered heat energy from a braking system and provide electric energy to a motor. Another important point to reduce CO_2 emission is a utilization of natural energies, such as solar energy and wind energy. These energies are not stable. Therefore, rechargeable battery is required to stabilize and to use them efficiently.

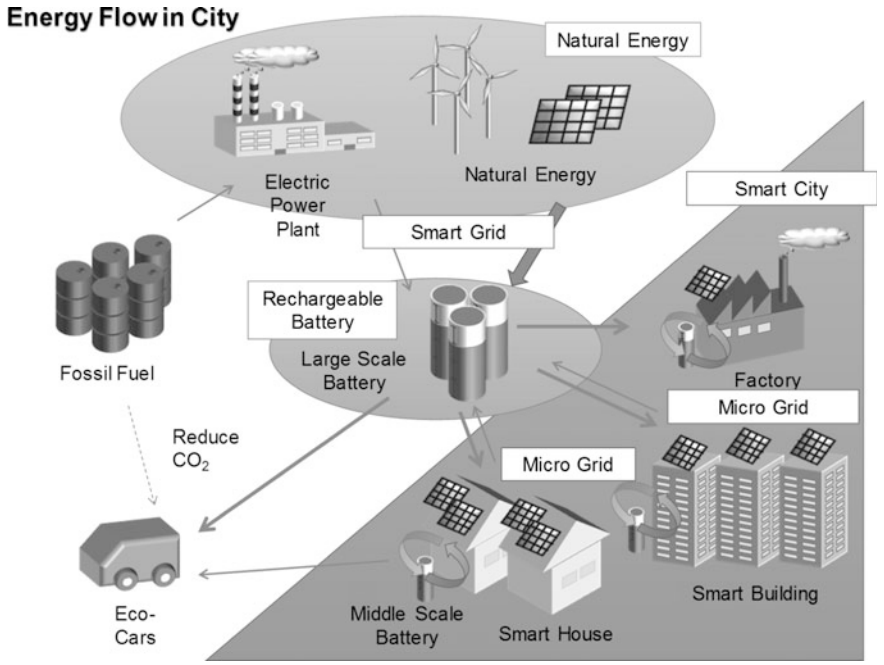

Fig. 4 Future green energy society with rechargeable batteries

On the other hand, both geothermal and tidal energies do not require rechargeable batteries, because of a stable electric power generation independent from weather and season. Solar and wind power has been already utilized partially in our society. For more effective use of natural energies, we have to select a suitable rechargeable battery with energy and power densities appropriate for this purpose. Figure 4 shows the energy system for future society.

3 Energy Density and Power Density of Batteries

An energy density of battery is indicated in Fig. 2. The energy density is calculated based on cell or battery weight or volume. For example, lead acid battery has 50 W h kg^{-1} energy density and lithium ion battery has 150 W h kg^{-1}. In lead acid battery, PbO_2 and Pb are used as cathode and anode materials, respectively, and H_2SO_4 aqueous solution is used as electrolyte. Figure 5 shows a structure of lead acid battery for car use. The battery consists of a lot of materials and parts. When the energy density of lead acid battery is calculated based on PbO_2 cathode, Pb anode, and H_2SO_4 electrolyte, its energy density is about 70 W h kg^{-1} which is larger than real energy density. In a comparison of two energy densities, it can be seen that the energy density of battery dose not only depend on active materials

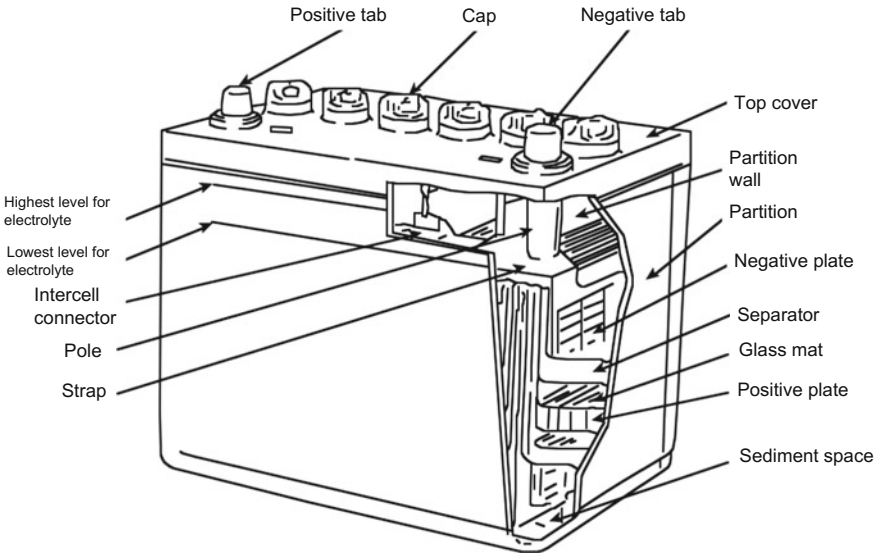

Fig. 5 Structure of lead acid battery

including electrolyte, but also is strongly influenced by parts of battery, such as current collector, separator, cell case, and so on. In the case of lithium ion battery, the energy density based on active materials is calculated to be more than 300 W h kg^{-1}. The practical energy density of lithium ion battery for large-scale applications is roughly 50% of that obtained from only active materials. From the comparison of two energy densities for lead acid battery and lithium ion battery, it can be said that the battery technology for lead acid battery is higher than that for lithium ion battery.

Recently, various kinds of new generation battery have been proposed. Li-air battery, Li-sulfur battery, Mg battery, all solid state battery, Li-metal battery, and so on. However, at this moment, real energy densities of these batteries cannot be precisely estimated due to a lack of information of practical battery structure and design. In some of previous reports, it has been claimed that the energy density of Li-air battery is more than 1000 W h kg^{-1} [1–3]. Li-sulfur battery has 600 W h kg^{-1} [4–6]. These energy densities have been estimated from only materials for cathode and anode. Figure 6 shows the estimation of energy density of next generation batteries published in several papers [7–9].

By the way, the energy density of battery has to be improved to realize pure electric vehicle which can drive more than 500 km per one charging. For this purpose, at least, 500 W h kg^{-1} energy density is needed for electric vehicles. Among practical rechargeable batteries, lithium ion battery has the highest energy density at this moment. New cathodes and new anodes have been extensively investigated to increase the energy density of lithium ion batteries. However, 300 W h kg^{-1} and 700 W h L^{-1} may be the maximum energy density.

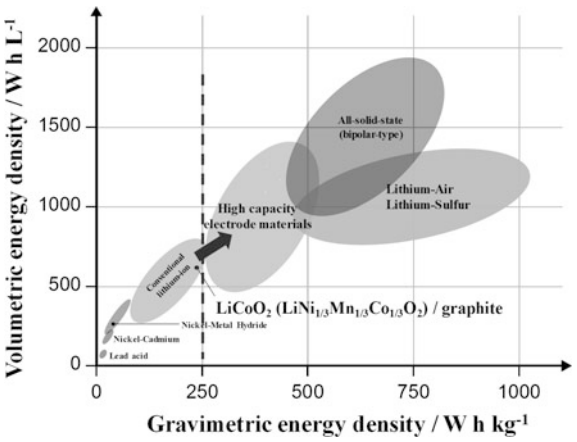

Fig. 6 Energy density of conventional and next generation batteries

Table 1 Comparison of specification of lithium ion batteries for hybrid vehicle and pure electric vehicle

	EV		HEV	
	Cell	Module	Cell	Module
Battery		8 cells in series		8 cells in series
Size	ϕ67 × 410 (L)	440(L) × 29 (W) × 180(H)	ϕ40 × 108 (L)	541(L) × 260 (W) × 160(H)
Weight/kg	3.2	30	0.3	20.2
Capacity/Ah	90	90	3.6	3.6
Voltage/V	3.8	30	3.6	170
Energy/W h	340	2700	13	610
Energy density/W h kg^{-1}	107	93	73	30
Energy density/W h L^{-1}	237	114	105	27
Power density/W kg^{-1}	470 (DOD85%)	350 (DOD85%)	2000 (DOD50%)	1350 (DOD50%)

Therefore, next generation batteries should have a practically high energy density of 500 W h kg^{-1} and 1000 W h L^{-1}.

The energy density is very important for rechargeable battery, simultaneously the power density of rechargeable battery is strongly required. Table 1 shows the specification of lithium ion batteries for pure electric vehicle and hybrid vehicle [10]. The power density of battery is determined by kinetics of electrochemical reactions taking place in cathode, anode, and electrolyte. Mostly, the maximum power density depends on the transportation of ions in porous electrode and electrolyte. Figure 7 shows the illustration for electrode reaction taking place in lithium ion cell. At high current, the diffusion of Li^+ ion in electrolyte may be a limiting process of electrode reactions. The transportation of Li^+ ion strongly depends on

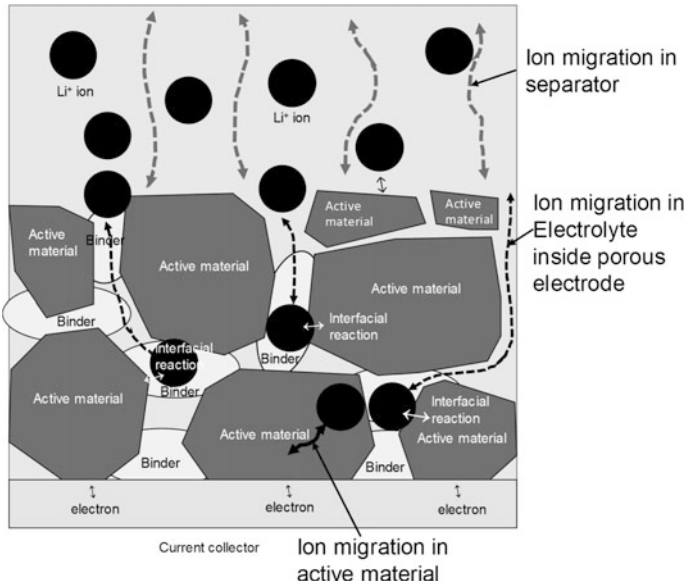

Fig. 7 Schematic illustration of porous electrodes in lithium ion battery

porous nature of electrode and separator, and also physical properties of non-aqueous electrolyte, such as ionic conductivity and Li^+ ion transportation number. In addition, the physical structure of electrode is also very important, for example, the thickness, porosity, pore distribution, pore size, and composition of electrode. In order to improve the energy density of lithium ion battery, a higher density (lower porosity) of electrode and also a thick electrode are required. However, this electrode structure increases the diffusion resistance of porous matrix filled with electrolyte, leading to lower power density of lithium ion cell. In this way, the relationship between power density and energy density is always an inverse proportion. Other kinds of cells, such as lead acid battery, Ni-metal hydride battery, and new generation batteries have the same relationship. As shown in Fig. 8, the standard structure for batteries is a sandwich type. Figure 9 shows a general relationship between energy density and power density for cell with a sandwich structure. This is very important for design of cells to realize both desired energy density and power density, simultaneously. For example, the lithium ion battery for portable application has more than 200 W h kg^{-1}. On the other hand, the lithium ion battery for electric vehicles has less than 150 W h kg^{-1}, at this moment. Both cells have the same materials and the same structure. The difference between two types of lithium ion cells is mainly a porous nature of electrodes to obtain adequate rate capability of cell. The battery for electric vehicles needs higher rate capability than that for portable application. Therefore, the energy density of lithium ion

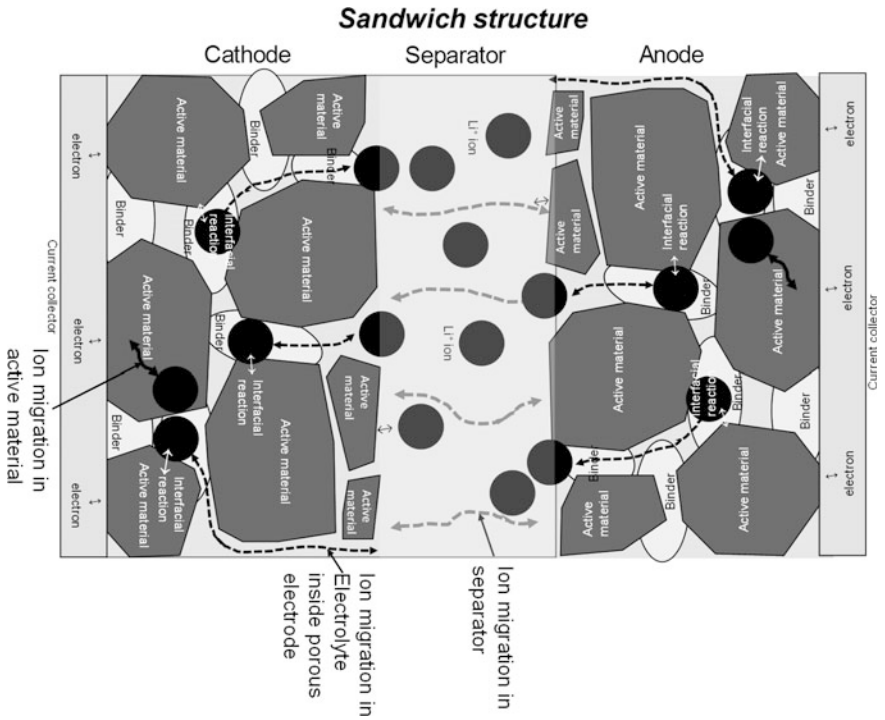

Fig. 8 Sandwich structure for lithium ion battery

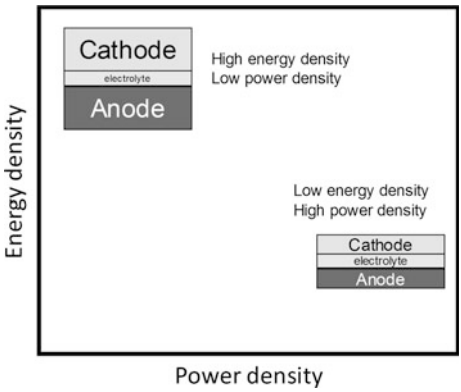

Fig. 9 Relationship between energy density and power density for sandwich structural cell

battery for electric vehicle is lower than that for portable application. When new generation batteries or other advanced batteries are developed, this relation should be taken into account, for researches.

4 Lithium Ion Battery

Lithium ion battery is the most promising battery among various kinds of rechargeable batteries. A history of lithium ion battery is more than 20 years after commercialization by Sony in Japan. Lithium ion battery chemistry was founded by Goodenough and Wittingham in USA [11, 12]. That is an intercalation or insertion of Li^+ ion into oxides or carbon materials. The first lithium ion battery was made from $LiCoO_2$ cathode and carbon anode. Figure 10 shows the structure of lithium ion battery. One is a cylindrical type and another is a prismatic type. During the discharge and charge processes, Li^+ ion is inserted or extracted to/from oxides and carbon materials, as shown in Fig. 11. In this battery, nonaqueous electrolytes have been used due to high voltage of cell, around 4 V. An aqueous electrolyte cannot be utilized because of narrow electrochemical potential window (1.23 V in theory). As shown in Fig. 7, the electrolyte is not involved in electrode reaction, it just works as Li^+ ion conductive media, so that the amount of electrolyte can be minimized based on cell design. In the case of portable application, the amount electrolyte is very small. This is suitable to obtain high energy density of cell, but is not good for high rate capability and longer cycle life of cell. On the other hand, the large-scale application of lithium ion battery requires a large amount of electrolyte in order to obtain higher rate capability and longer cycle life. In fact, the batteries for electric vehicle and natural energy utilization involve a relatively larger amount of electrolyte.

Materials used in lithium ion battery have been extensively studied to improve both energy density and power density. Figure 3 shows the improvement of cell capacity from 1992 to 2010. This improvement of cell capacity is mainly due to cell preparation technology, for example an increase in tap density of electrode and a reduction of separator thickness and other parts, but not due to material change, as discussed above. In fact, $LiCoO_2$ and graphite have been used for a long time. Recently, the energy density has reached to almost the theoretical energy density that can be expected from capacity density of materials and cell design. Therefore, other materials with high capacity density and high operation voltage should be developed and applied to advanced lithium ion cells. By the way, a safety issue for lithium ion battery also becomes very important after explosion of some lithium ion cells used in notebook computers and cellar phones. In order to improve the safety of lithium ion battery, new materials have to be also developed. Especially, the large-scale lithium ion battery must be highly safe. Figure 12 shows a summary of new materials for cathode and anode and their capacity density [13]. $LiNi_xMn_yCo_z$ (NCM) cathode is now the most promising candidates for practical lithium ion cell, which provides more than 200 mA h g^{-1} capacity density. By the way, $LiCoO_2$ has 140 mA h g^{-1} capacity density. NCM has higher capacity and also higher safety compared with those of $LiCoO_2$ cathode. Now, NCM becomes a main cathode material for lithium ion battery. In the case of anode, carbon materials, especially graphite, have been used in lithium ion cell. Recently, lithium ion battery with $Li_4Ti_5O_{12}$ (LTO) anode has been commercialized for vehicles by Toshiba [14].

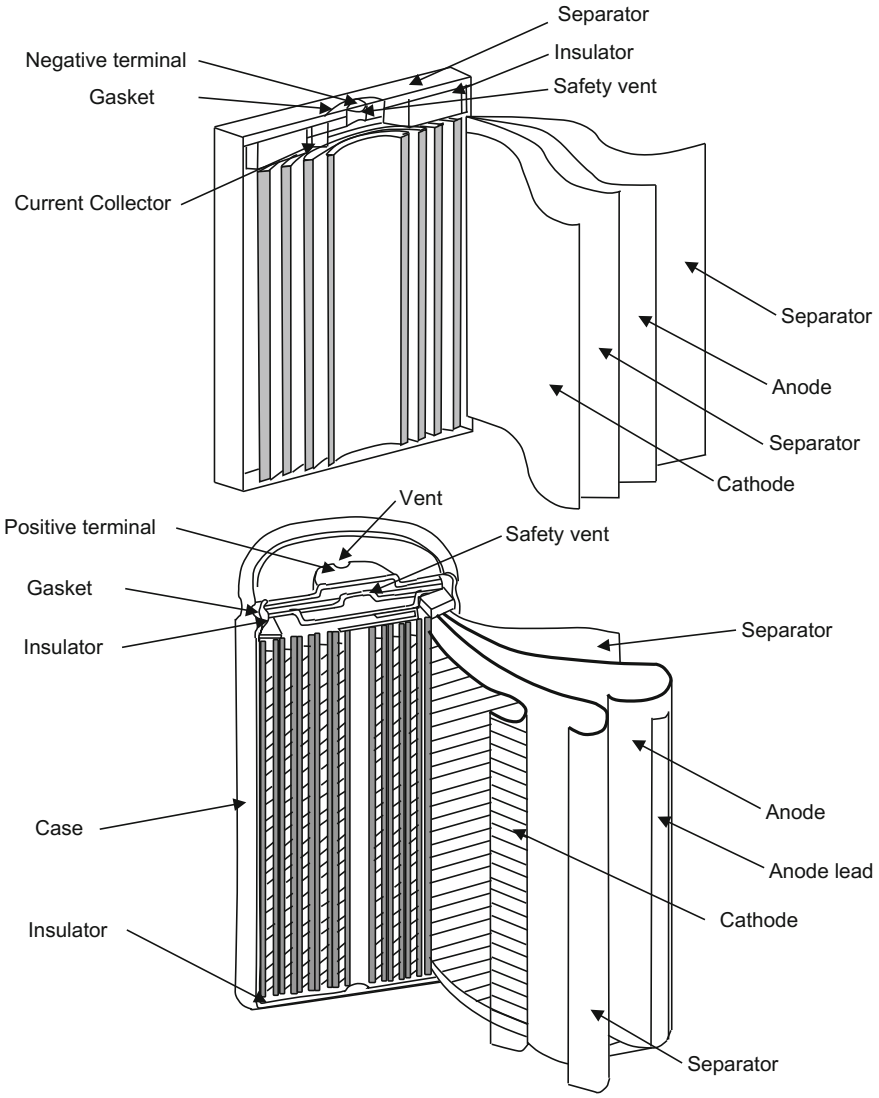

Fig. 10 Structure of lithium ion battery with prismatic or cylindrical type

LTO provides a high safety and reasonable capacity that is 50% of graphite in weight and 75% in volume. However, the electrode potential is 1.5 V versus Li/Li^+. The electrode potential of graphite is 0.05~1.0 V. When LTO is used as anode, the energy density becomes smaller, but its safety is improved very much. In addition, the charging rate of cell with LTO becomes very high. The charging rate is sometimes limited by lithium metal deposition on anode materials. The electrode potential of LTO is good for quick charge of cell. For future green energy society,

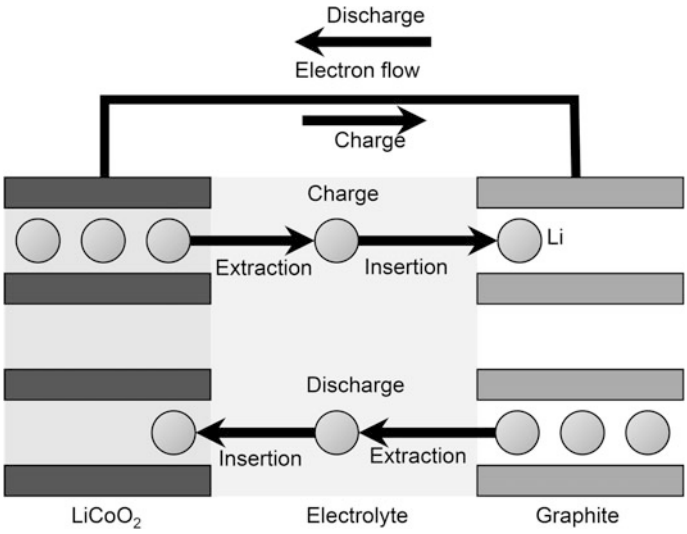

Fig. 11 Schematic illustration for Li^+ ion insertion and extraction mechanism

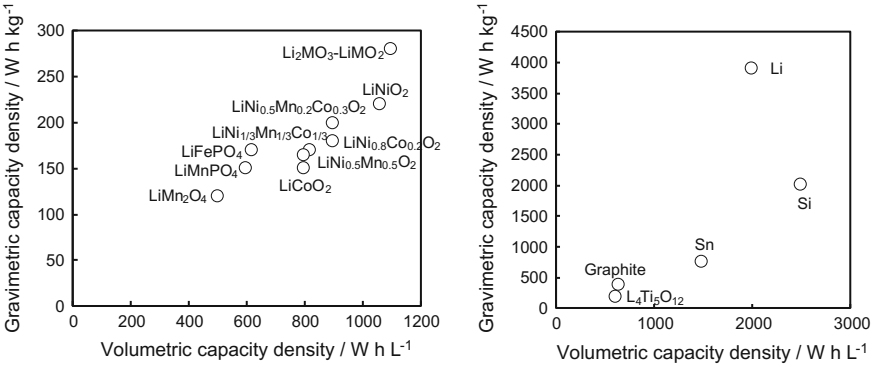

Fig. 12 Volumetric and gravimetric capacity densities for various cathode and anode materials

higher energy density is required for rechargeable batteries used in electric vehicles and other applications. Lithium ion battery has a limitation of energy density due to material problems, as discussed above. Therefore, new anode and cathode have been investigated, such as alloy type anode (Si, Sn, and other alloys with Li) and Li-rich solid solution type cathode. Si anode has a high capacity density that is 2000 mA h g^{-1} [15]. Li-rich solid solution cathode has 300 mA h g^{-1} [16]. However, most of the new materials have some problems which should be solved before utilization to practical cell. In the future, these materials would be applied to cell to develop high energy density lithium ion battery.

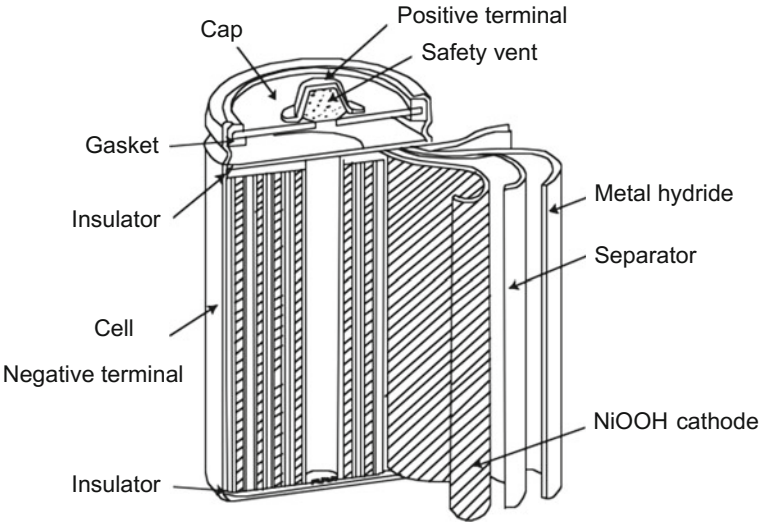

Fig. 13 Structure of Ni-metal hydride battery

5 Ni-Metal Hydride Battery

Ni-metal hydride battery was one of new rechargeable batteries for cellar phone before the development of lithium ion battery. Now, all cellar phones are operated by lithium ion battery. However, this battery is still important as power source of hybrid vehicle [17]. Figure 13 shows the schematic illustration of Ni-metal hydride battery. The cell reaction is similar to that of lithium ion battery. Instead of Li^+ ion, H^+ (H_3O^+) ion is inserted or extracted into/from NiOOH cathode or metal hydride, such as $LaNi_5$ [18]. Alkaline aqueous solution, such as KOH aqueous solution, is used as electrolyte. Only OH^- ion passes through the electrolyte during discharge and charge processes, so that the amount of electrolyte can be minimized to increase the energy density of battery. This is the same with that of lithium ion battery. Some of electric vehicles produced by Toyota utilize the Ni-metal hydride battery.

6 Na-S Battery

Solar cell or wind power generation system has been utilized in factory, buildings, and home for energy-saving by utilization of natural energy. The big factories of solar cell have been established in city area and supplied electricity instead of thermal electric power station. However, natural energy from solar and wind power is not stable. If the natural energy is injected into main electric grid, power failure problem may happen so frequently. Therefore, some control system is required,

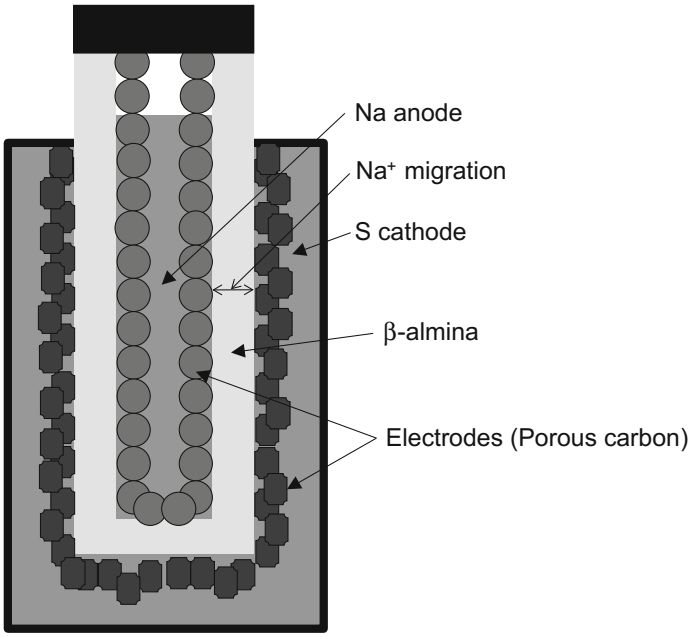

Fig. 14 Structure of Na-S battery

that is a large-scale battery. As described above, a large-scale lithium ion battery is one of possible candidates for this application. On the other hand, Na-S battery has been already used in electric power station to stabilize electric power supply [19]. Figure 14 shows the schematic illustration of Na-S battery. This battery is operated at 350 °C. Both Na anode and S cathode are liquid state at this operating temperature. β-Almina ($7Al_2O_3 \cdot 4NaO$) has been used as solid electrolyte. Porous carbon electrodes are employed at both sides of the solid electrolyte. This cell system is suitable to obtain high energy density of battery. However, a safety of Na-S battery is low due to liquid Na and S which can react with oxygen, easily. Higher safety for Na-S battery should be realized near future.

7 Others

Other rechargeable batteries, such as redox-flow battery, Ni-Fe, Zn-Cl_2, Zn-Br_2, Na-$NiCl_2$, Zn-air, and so on have been developed for large-scale applications. Among these batteries, the redox-flow battery become attractive for smart grid system, recently [20]. Figure 15 shows the schematic illustration of the redox-flow battery. The electrode reaction in this battery consists of two redox couples. Cr^{3+}/Cr^{2+} and Fe^{3+}/Fe^{2+} redox couples have been employed for this battery. However,

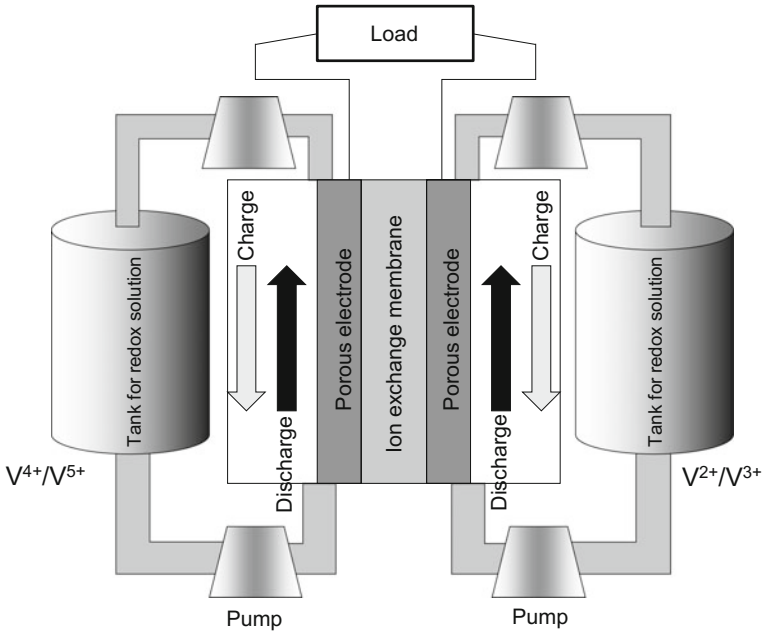

Fig. 15 Structure of redox-flow battery

a mixing of Cr and Fe species became a problem. Recently, V^{2+}/V^{3+} and V^{4+}/V^{5+} redox reactions are utilized in this battery. In this system, a mixing of redox couples is not a problem. These ions are dissolved in water and circulated in the cell by pump. The system is similar to fuel cell. The cell reactions are described below.

	Vanadium system	Fe chloride and Cr chloride system
Cathode reaction	$V^{5+} + e^- \rightarrow V^{4+}$	$FeCl_3 + e^- \rightarrow FeCl_2 + Cl^-$
Anode reaction	$V^{2+} \rightarrow V^{3+} + e^-$	$CrCl_2 + Cl^- \rightarrow CrCl_3 + e^-$
Total reaction	$V^{5+} + V^{2+} \rightarrow V^{4+} + V^{3+}$	$FeCl_3 + CrCl_2 \rightarrow FeCl_2 + CrCl_3$

As electrolyte, sulfuric acid or HCl aqueous solution has been used in the cell. A lot of cells are stacked to obtain high voltage. The capacity is determined by a volume of tanks for redox solutions. The key materials for redox-flow battery are an ion exchange membrane (polymer electrolyte separator) and conductive bipolar type separation plate. In addition, the construction of large-scale battery container is also important for practical cell. The energy conversion efficiency of redox-flow battery depends on pump system, over-potentials of anode and cathode reactions, and so on. The total system of redox-flow battery is more complicated than those of other rechargeable batteries. Recently, this battery has been applied to wind power generation plant.

8 Next Generation Batteries

A conventional rechargeable batteries including lithium ion battery provides various benefits to our life, such as a cellar phone, personal computer, and hybrid vehicle. Moreover, new applications (Radio frequency identifier, Sensor, Medical applications) are realized by using lithium ion battery. The future of portable devices is still very attractive. On the other hand, we have a serious global warming problem due to CO_2 emission by human activity. In order to suppress CO_2 emission, we have to change our energy consumption system for future green society. Figure 4 shows an illustration of future energy social system. There are many rechargeable batteries in the city area combined with solar cell, wind power station, thermal power station, buildings, homes and cars. This system involves a smart grid system, micro-grid system, home energy management system, electric vehicles. Many types of rechargeable batteries may be needed to construct such smart city. Lithium ion battery, metal hydride battery, and others can be applied to this social system. However, the performance of conventional rechargeable batteries is not enough to realize highly sophisticated smart energy grid system. Therefore, new generation rechargeable batteries are strongly required. Around the world, extensive research and development have been continued to realize high performance rechargeable batteries with higher energy and power densities. Figure 6 shows a summary of energy densities of next generation batteries. The battery or cell design for these batteries has not been determined, yet, so that the energy density and power density are not clear at this moment. Figure 16 shows the basic structure and electrochemical reaction of Li-air, Li-Sulfur, Li-metal, all solid state, and Mg (Ca or Al) batteries. These figures do not express the detailed structure of these batteries. The electrode reactions in these cells have to be investigated to determine real design of electrode structure and electrolyte system.

Li-metal battery may be similar to lithium ion battery. However, anode is changed from carbon materials to Li-metal so that cathode does not necessarily need to involve Li. Materials for Li-metal batteries are different from those for lithium ion battery. In addition, a larger volume expansion and shrink of electrodes take place during discharge and charge cycle in Li-metal battery, leading to low cycleability. Especially, a volume change of Li-metal anode is critical. In addition, a morphology of Li-metal is strongly related to safety and cycleability of cell. Figure 17a shows the scanning electron micrograph of Li-metal deposited during charge process. This is a typical dendrite form. When using Li-metal anode in next generation batteries, the deposition of dendrite Li-metal should be suppressed. A selection of electrolyte, additives, and separator is very important. For example, the electrochemical deposition of Li-metal can be controlled by using more uniform separator which provides highly uniform current distribution in macro-scale and micro-scale. Figure 17b shows the scanning electron micrograph of spherically deposited Li-metal. This type of Li-metal provides high cycleability of anode [21]. In future, this technology will be applied to Li-air and Li-sulfur batteries. In Mg battery, the dissolution and deposition of Mg metal occurs in the course of

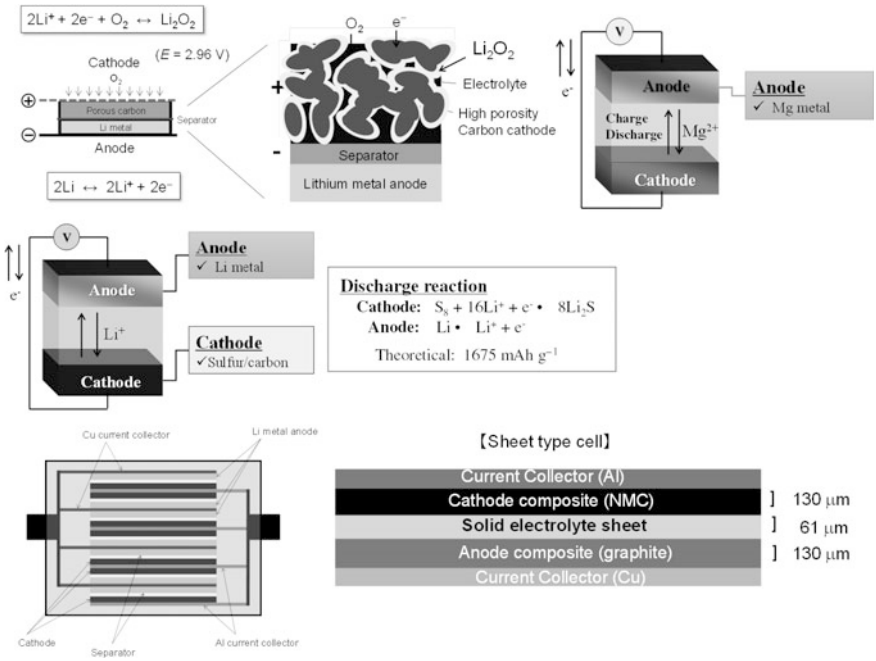

Fig. 16 Schematic illustrations for next generation batteries

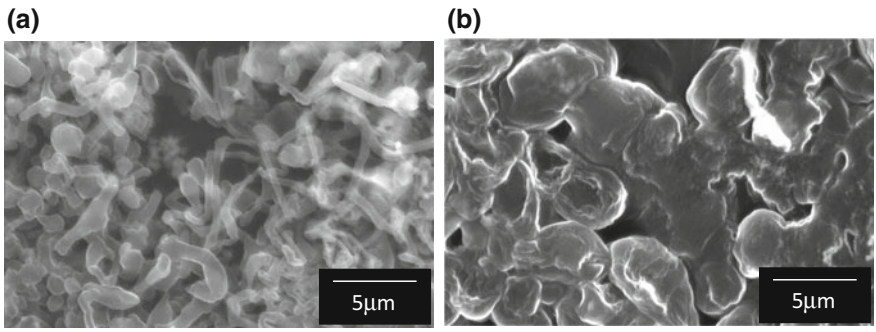

Fig. 17 Scanning electron micrographs of Li-metal deposited in **a** dendrite form and **b** spherical form

discharge and charge cycles. The dendrite formation of Mg metal does not occur [22]. Therefore, Mg battery might be easier than Li-metal battery. However, Mg electrode has another problem that is a passivation of surface resulting in an extremely large overpotential. New electrolytes have to be developed to improve a reversibility of Mg anode. Unfortunately, the performance of Mg battery is not enough at this moment.

Cathode reactions of Li-air battery and Li-sulfur battery have been extensively studied to understand reaction mechanisms [23–26]. Air cathode in Li-air battery has not been understood completely. The most possible proposed electrochemical reaction of oxygen electrode is described below.

$$\begin{array}{ll} \text{Cathode} & 2Li^+ + O_2 + 2e^- \rightarrow Li_2O_2 \\ \text{Anode} & 2Li \rightarrow 2Li^+ + 2e^- \\ \text{Total} & 2Li + O_2 \rightarrow Li_2O_2 \end{array}$$

When using nonaqueous electrolyte, the reaction product is Li_2O_2 which is two-electron reduction product. Li_2O_2 is formed from Li^+ ion in electrolyte and O_2 gas. Li_2O_2 and O_2 are not electronic conductive materials. The current collector should be needed to provide electron pathway. Therefore, the structure of air cathode should be developed for practical battery. Especially, the porous nature of current collector is very important. For example, various carbon materials have been investigated. Probably, a carbon fiber is a key material to construct three dimensional porous electrode in which Li_2O_2 forms during discharge process. The similar situation happens in Li-sulfur battery. In this case, the discharge product is Li_2S in solid state. Therefore, the porous structure of cathode should be optimized to reduce an amount of carbon material used in cell. Carbon is not active material and just works as conductive additive or network in cathode. With increasing amount of carbon, the energy density of Li-air and Li-sulfur batteries decrease. Therefore, porous carbon cathode is important to realize these batteries.

Nonaqueous electrolytes are used in Li-air and Li-sulfur batteries. The selection of electrolytes is necessary to obtain stable discharge and charge processes. For example, the oxidation of electrolyte takes place in Li-air battery during charge when using propylene carbonate electrolyte [27]. Therefore, new electrolytes have been studied. Some of electrolytes, such as glyme (glycol ether) based electrolytes, give a stability against electrochemical oxidation at charging process. In the case of Li-sulfur battery, some intermediate species are produced by the reduction of S and dissolve into electrolyte, leading to self-discharge during charging process [28, 29]. So far, various kinds of electrolytes have been investigated to prevent the dissolution of intermediates. More or less, the intermediates dissolve into even in new electrolytes. Extensive studies should be done in the future.

All solid state batteries are the most promising next generation battery. A laminated cell has been already fabricated as prototype battery. In this cell, sulfur-based solid electrolyte, such as $80Li_2S\text{-}20P_2S_5$, has been utilized [30]. The energy density of prepared all solid state battery is not so high, due to a large amount of solid electrolyte used in this cell. The electrode preparation by using solid electrolyte, active material and conductive material should be optimized to reduce amount of solid electrolyte and conductive material. The density of solid electrolyte is much higher than that of liquid one. Therefore, the energy density per unit weight of all solid state battery may not be so high, but the energy density per volume may be high. Another important aspect of all solid state battery is a safety issue. All solid state battery may be much safer than other rechargeable batteries. However, all solid

state battery with sulfur-based electrolyte has some problems. One is material problem that is a high reactivity of sulfur compounds with water and oxygen. Chemically more stable materials should be utilized in all solid state battery. The oxide-based sold electrolyte is a chemically stable, but has a low ionic conductivity [31]. There are two development ways at present. The stability of sulfur materials will be improved or the ionic conductivity of oxide materials will be enhanced. All solid state battery has not only material problem, but also a problem for mass production. The difficulty for the preparation of all solid state battery is related to a formation of interface between solid electrolyte and active material. Recently, the preparation technology for composite electrode consisting of active material and solid electrolyte has been extensively investigated to optimize electrochemical interface [32]. All solid state battery will be commercialized in near future.

Thus, various next generation batteries have been investigated by many groups around the world to realize real high energy density battery with high power density. These batteries are still on the way to a production of practical cell. An extensive study should be done to develop new materials and new design for batteries with new concepts. We are still in starting point for next generation battery development.

9 Summary

Rechargeable batteries are key devices for future energy system in urban area to save energy and utilize natural energy. Moreover, automobile will shift from thermal engine to motor driving, so that rechargeable batteries are strongly required. However, an energy density of present rechargeable batteries is not adequate for such future applications. New concepts for next generation batteries are very important. On the other hand, lithium ion battery is still the best rechargeable battery among various conventional batteries. During next 10 years, new rechargeable battery will be realized and applied to electric vehicles, stationary applications and portable applications instead of lithium ion battery. We have several possibilities for next generation batteries. We have to continue our efforts on research and development of next generation battery.

References

1. Capsoni D, Bini M, Ferrari S, Quartarone E, Mustarelli P (2012) Recent advances in the development of Li-air batteries. J Power Sources 220:253–263
2. Luntz AC, McCloskey BD (2014) Nonaqueous Li-air batteries: a status report. Chem Rev 114:11721–11750
3. Huang S, Cui Z, Zhao N, Sun J, Guo X (2016) Influence of ambient air on cell reactions of Li-air batteries. Electrochim Acta 191:473–478

4. Bruce PG, Freunberger SA, Hardwick LJ, Tarascon JM (2011) Li-O_2 and Li-S batteries with high energy storage. Nat Mater 11:19–29
5. Evers S, Nazar LF (2013) New approaches for high energy density lithium–sulfur battery cathodes. Acc Chem Res 46:1135–1143
6. Yin YX, Xin S, Guo YG, Wan LJ (2013) Lithium–sulfur batteries: electrochemistry, materials, and prospects. Angew Chem Int Ed 52:13186–13200
7. Ogasawara Y, Hibino M, Kobayashi H, Kudo T, Asakura D, Nanba Y, Hosono E, Nagamura N, Kitada Y, Honma I, Oshima M, Okuoka S, Ono H, Yonehara K, Sumida Y, Mizuno N (2015) Charge/discharge mechanism of a new Co-doped Li_2O cathode material for a rechargeable sealed lithium-peroxide battery analyzed by X-ray absorption spectroscopy. J Power Sources 287:220–225
8. Imanishi M, Yamamoto O (2014) Rechargeable lithium-air batteries: characteristics and prospects. Mater Today 17:24–30
9. Moreno N, Caballero A, Morales J, Rodriguez-Castellon E (2016) Improved performance of electrodes based on carbonized olive stones/S composites by impregnating with mesoporous TiO_2 for advanced Li-S batteries. J Power Sources 313:21–29
10. Kambe Y, Esaki K, Ishiguro Y, Inagaki A, Nozaki K, Enokishima H, Okayama S, Matsuura T, Muramatsu H, Yamada M, Kojima H (2003) Development of lithium-ion battery for vehicles. In: Abstracts of the spring conference for society of automotive engineers of Japan, Inc., March 2003, No. 19-03, p 21
11. Goodenough JB, Park KS (2013) The Li-ion rechargeable battery: a perspective. J Am Chem Soc 135:1167–1176
12. Whittingham MS (2004) Lithium batteries and cathode materials. Chem Rev 104:4271–4301
13. Nitta N, Wu F, Lee JT, Yushin G (2015) Li-ion battery materials: present and future. Mater Today 18:252–264
14. Takami N, Inagaki H, Kishi T, Harada Y, Fujita Y, Hoshina K (2009) Electrochemical kinetics and safety of 2-Volt class Li-ion battery system using lithium titanium oxide anode. J Electrochem Soc 156:A128–A132
15. Leveau L, Laik B, Pereira-Ramos JP, Gohier A, Tran-Van P, Cojocaru CS (2016) Silicon nano-trees as high areal capacity anodes for lithium-ion batteries. J Power Sources 316:1–7
16. Rozier P, Tarascon JM (2015) Review—Li-rich layered oxide cathodes for next-generation Li-Ion batteries: chances and challenges. J Electrochem Soc 162:A2490–A2499
17. Taniguchi A, Fujioka N, Ikoma M, Ohta A (2001) Development of nickel/metal-hydride batteries for EVs and HEVs. J Power Sources 100:117–124
18. Liu Y, Pan H, Gao M, Wang Q (2011) Advanced hydrogen storage alloys for Ni/MH rechargeable batteries. J Mater Chem 21:4743–4755
19. Oshima T, Kajita M, Okuno A (2004) Development of sodium-sulfur batteries. Appl Ceram Tech 1:269–276
20. Yang Z, Zhang J, Kintner-Meyer MCW, Lu X, Choi D, Lemmon JP, Liu J (2011) Electrochemical energy storage for green grid. Chem Rev 111:3577–3613
21. Kanamura K, Munakata H, Yong C (2011) Lithium secondary battery separator and method of manufacturing same. JP Patent WO2013084368 A1, 9 Dec 2011
22. Matsui M (2011) Study on electrochemically deposited Mg metal. J Power Sources 196:7048–7055
23. Mizuno F, Takechi K, Higashi S, Shiga T, Shiotsuki T, Takazawa N, Sakurabayashi Y, Okazaki S, Nitta I, Kodama T, Nakamoto H, Nishikoori H, Nakanishi S, Kotani Y, Iba H (2013) Cathode reaction mechanism of non-aqueous Li-O_2 batteries with highly oxygen radical stable electrolyte solvent. J Power Sources 228:47–56
24. Lee M, Hwang Y, Yun K-H, Chung Y-C (2016) Cathode reaction mechanism on the h-BN/Ni (111) heterostructure for the lithium-oxygen battery. J Power Sources 307:379–384
25. Zheng D, Zhang X, Wang J, Qu D, Yang X, Qu D (2016) Reduction mechanism of sulfur in lithium-sulfur battery: from elemental sulfur to polysulfide. J Power Sources 301:312–316
26. Diao Y, Xie K, Xiong S, Hong X (2013) Shuttle phenomenon—the irreversible oxidation mechanism of sulfur active material in Li-S battery. J Power Source 235:181–186

27. Freunberger SA, Chen Y, Peng Z, Griffin JM, Hardwick LJ, Bardé F, Novák P, Bruce PG (2011) Reactions in the rechargeable lithium—O_2 battery with alkyl carbonate electrolytes. J Am Chem Soc 133:8040–8047
28. Manthiram A, Fu Y, Chung SH, Zu C, Su YH (2014) Rechargeable lithium sulfur batteries. Chem Rev 114:11751–11787
29. Mikhaylik YV, Akridge JR (2004) Polysulfide shuttle study in the Li/S battery system. J Electrochem Soc 151:A1969–A1976
30. Nagao M, Hayashi A, Tatsumisago M (2011) Sulfur–carbon composite electrode for all-solid-state Li/S battery with Li_2S–P_2S_5 solid electrolyte. Electrochim Acta 56:6055–6059
31. Kim JG, Son B, Mukherjee S, Schuppert N, Bates A, Kwon O, Choi MJ, Chung HY, Park S (2015) A review of lithium and non-lithium based solid state batteries. J Power Sources 282:299–322
32. Kato T, Iwasaki S, Ishii Y, Motoyama M, West CW, Yamamoto Y, Iriyama Y (2016) Preparation of thick-film electrode-solid electrolyte composites $Li_7La_3Zr_2O_{12}$ and their electrochemical properties. J Power Sources 303:65–72

Sodium-Ion Secondary Batteries Using Ionic Liquids as Electrolytes

Rika Hagiwara

1 Preface

Ionic liquids are generally recognized as onium salts that have melting temperatures lower than 100 °C [1]. The name 'ionic liquid' does not describe the state of the substance but describes organic salts with low melting temperatures. In most cases, ionic liquids are neat onium salts with low melting temperatures. However, John O'M. Bockris gave a clearer, but different, definition of "ionic liquids" nearly a half century ago in his electrochemistry textbook, "Modern Electrochemistry [2]." He defined ionic liquids as "pure liquid electrolytes with zero solvents." This definition is simple and clear as well as appropriate from a scientific point of view. He categorized ionic crystals as *true* electrolytes. Here, "*true*" means "ionized even before they come into contact with a solvent," thus distinguishing them from "*potential* electrolytes," which are non-ionic substances only yielding ions after mixing with a solvent. Here, electrolytes are obviously ionic substances, usually solid salts. Bockris, using his categorization, continues to state that "liquid electrolytes are ionic liquids." It may be difficult to understand the profound meaning of this sentence by itself, but what he meant is if a substance in the liquid state is classified as an electrolyte, it should be made exclusively of ions without any solvents. According to this definition, there is no temperature limitation of the melting temperature to the boiling point of water at atmospheric pressure.

In this chapter, we introduce new sodium-ion secondary batteries that use ionic liquids, based on the definition of Bockris, as electrolytes. We also discuss the functionality of ionic liquids, which increase the safety and the operation temperature range of batteries.

R. Hagiwara (✉)
Graduate School of Energy Science, Kyoto University, Kyoto 606-8501, Japan
e-mail: hagiwara@energy.kyoto-u.ac.jp

K. Uosaki (ed.), *Electrochemical Science for a Sustainable Society*,
DOI 10.1007/978-3-319-57310-6_8

2 Sodium-Ion Secondary Batteries Using Ionic Liquids as Electrolytes

The introduction of renewable energy generated by solar and wind power requires large-scale power storage batteries to reduce fluctuations in output. In addition, the safety of rechargeable batteries for electric vehicles, whose demand is growing rapidly, must be improved, as well as the energy density compared to that of stationary batteries. However, it is difficult for current lithium-ion batteries to fulfill these requirements because of the significant amount of flammable organic solvents necessary for their operation. In addition, the massive production of lithium-ion batteries for energy storage may exhaust some metal resources, such as cobalt, in the future. Furthermore, lithium resources of high quality are concentrated in South America, and there is a risk of unstable supply in the future. The upper limit of the operating temperature of current lithium-ion batteries is about 333 K due to the thermal instability of the solid electrolyte interphase (SEI); this precludes the effective packing of batteries to a battery module to make the best use of their high energy density due to the need to release heat. Research and development of large-scale lithium-ion batteries has been based on the extension of technologies developed for the current generation of lithium-ion batteries for electronic devices using organic solvents as the electrolytes. Consequently, problems concerning improving the safety and thermal stability of large-scale batteries still remain. The same can be said for sodium-ion batteries, which have become a recent research focus, and have been vigorously studied for use in large-scale rechargeable batteries [3, 4]; however, sodium-ion batteries also required flammable organic solvents as electrolytes.

Ionic liquids are promising electrolytes for use in rechargeable batteries, increasing safety. Ionic liquids have excellent features such as non-flammability, non-volatility, and a wide operating temperature range; therefore, they have been studied as potential electrolytes for rechargeable lithium batteries. We have worked on developing rare metal-free rechargeable sodium-ion batteries for energy storage, and have focused on alkaline bis(fluorosulfonyl)amide (abbreviated FSA or f_2N) ionic liquids because they are electrolytes with an excellent safety [5–7]. These salts are used by combining sodium salts with other alkaline metal salts to lower the melting temperature of the ionic liquid and reduce its viscosity. These ionic liquids are made of entirely inorganic compounds, and a representative combination is the binary Na[FSA]–K[FSA] system. In addition to this inorganic system, the authors have developed inorganic–organic hybrid FSA ionic liquids as electrolytes with wide operating temperature ranges; these are aimed at applications in electric vehicles and combine sodium and quaternary ammonium salts. In this chapter, the fundamental properties of ionic liquids and performance as the electrolytes of sodium-ion batteries are described.

3 Properties of Alkaline FSA Inorganic Ionic Liquids

Figure 1 shows the anionic structures of FSA and TFSA (bis(trifluorosulfonyl) amide) anions. Alkaline FSA salts possess lower melting points and decomposition temperatures than those of TFSA salts of the same cations, limiting their stable operating temperature range [5–10]. For example, the temperature range where Na[FSA] exists in the liquid state without decomposition is only 34 K (379–413 K), whereas that of Na[TFSA] is 184 K (530–714 K). An effective way to extend the temperature range is to mix one ionic liquid with another alkaline FSA salt to lower the melting point. Figure 2 shows the phase diagram of the Na[FSA]–K[FSA] binary system, of which the eutectic point is 334 K for a composition ratio (Na[FSA]:K[FSA]) of 56:46 [7].

The ionic conductivity of Na[FSA]–K[FSA] at 363 K is 3.3 mS cm^{-1} [11], which does not seem sufficiently high for a battery electrolyte. Nevertheless, Na[FSA]–K[FSA] can still be used because the concentration of sodium ions is sufficiently high for battery operation (5.6 mol L^{-1} for the eutectic mixture). However, the ionic conductivity of this system falls sharply as the temperature decreased to the eutectic point due to the increase in viscosity.

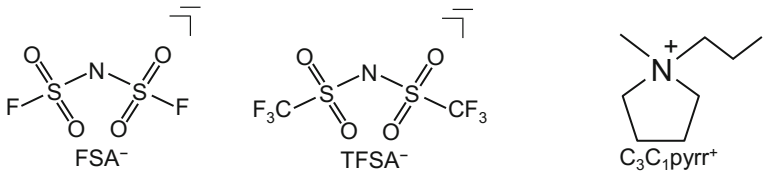

Fig. 1 Molecular structures of FSA^-, $TFSA^-$, $C_3C_1pyrr^+$

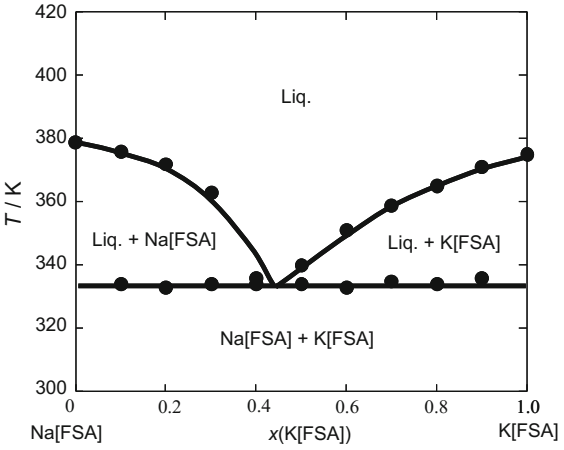

Fig. 2 Binary phase diagram of Na[FSA]–K[FSA] [7]

Cyclic voltammetry using a Cu electrode in the eutectic system shows that reversible electrodeposition and dissolution of sodium metal occurs at the cathode limit potential, that is, 0 V versus Na/Na^+ [11]. The irreversible anodic current ascribed to the decomposition of the anion was observed for a glassy carbon electrode at 5.2 V versus Na/Na^+ [11]. Therefore, the electrochemical window of the system is 5.2 V. It should be noted that, in the potentiostatic electrolysis of the Al electrode in this electrolyte at 4.5 V versus Na/Na^+, a small current flow at the very beginning of electrolysis was observed, subsequently falling to zero, indicating that effective passivation of the current collector of the positive electrode in this system.

4 Properties of FSA Inorganic–Organic Hybrid Ionic Liquids

We have studied FSA inorganic–organic hybrid systems of ionic liquids combined Na[FSA] with five organic FSA salts: *N*-Methyl-*N*-propyl pyrrolidinium (C_3C_1pyrr, Fig. 1) [12, 13], 1-ethyl-3-methylimidazolium (C_2C_1im) [14], trimethyl hexyl ammonium (TMHA) [15], dibutyl dimethylammonium (DBDM) [15], and 5-azoniaspyro [4, 5] nonane (AS [4, 5]) [15], which have been investigated as potential organic cations. All the salts exhibited shifts in the liquidus lines to lower temperatures on mixing with Na[FSA]. As an example, the phase diagram of the Na[FSA]–[C_2C_1im][FSA] system prepared based on the results of differential scanning calorimetry [14] is shown in Fig. 3. It should be noted these hybrid salts occasionally exhibit an extremely slow phase transition. Hence, the phase diagram is sometimes not at equilibrium. The liquid temperature range of FSA system is remarkably wide compared with that of the TFSA system [16].

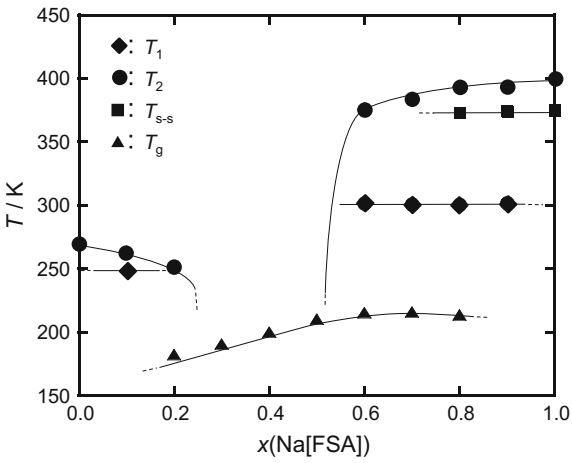

Fig. 3 Binary phase diagram of Na[FSA]–[C_2C_1im][FSA] [14]

For the system Na[FSA]:[OCat][FSA] with a ratio of 3:7, the molar concentration of Na^+ ranges from 1.3 to 1.6 mol L^{-3} which is sufficiently high for use as a battery electrolyte. Interestingly, some of the salts maintain a liquid state even at Na^+ concentrations as high as 5:5. Figures 4 and 5 show Arrhenius plots of the viscosities and conductivities of Na[FSA]:[C_3C_1pyrr][FSA] systems with different mixing ratios [13]. The plots of the viscosities and ionic conductivities are concave and convex curves, respectively, and obey the Vogel–Tamman–Fulcher (VTF) equation [17, 18]. The highest ionic conductivity is obtained for the mixture combined with C_2C_1im salt, 5.4 mS cm^{-1} at 298 K and 31 $mScm^{-1}$ at 363 K for the following composition, Na[FSA]:[C_2C_1im][FSA] = 3:7. From the viewpoint of battery operation, Na^+ ion conductivity is obtained by multiplying the sodium-ion transport number and concentration and is one of the most important parameters to measure the Na^+ ion transportability of the electrolyte. Transport numbers of Na^+ ion were measured for the Na[FSA]:[C_3C_1pyrr][FSA] system, and Na^+ conductivities were obtained to show a maximum at around 0.2–0.4 of the mole fraction of the Na^+ salt. Due to the small number of carrier ions when the Na^+ concentration is low and the increase in the viscosity when it is high, the Na^+ ion conductivity is lowered in both the cases; consequently, the optimum concentration lies somewhere in between these extremes.

The cyclic voltammograms of a nickel electrode and a glassy carbon electrode are given in Figs. 6 and 7, respectively. These hybrid salt systems have similar electrochemical windows to that found for the inorganic system, i.e., 0 to approximately 5 V versus Na/Na^+ [19]. The cathode limit reaction is the deposition

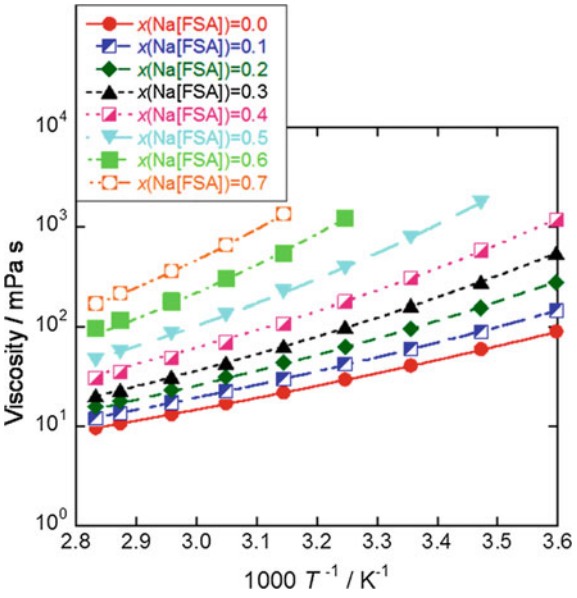

Fig. 4 Arrhenius plots of the viscosities of the Na[FSA]–[C_3C_1pyrr][FSA] ionic liquids for x(Na[FSA]) values of 0.0–0.7 [13]

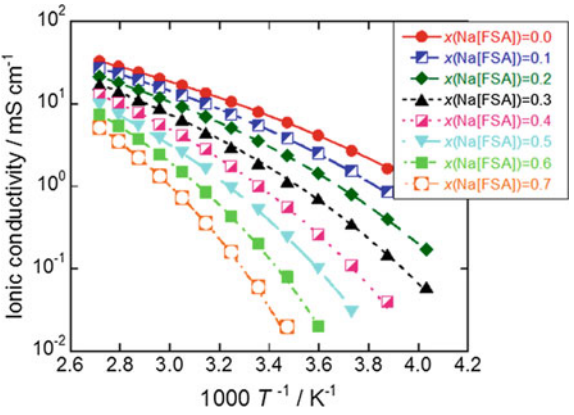

Fig. 5 Arrhenius plots of the ionic conductivities of the Na[FSA]–[C_3C_1pyrr][FSA] ionic liquids for x(Na[FSA]) values of 0.0–0.7 [13]

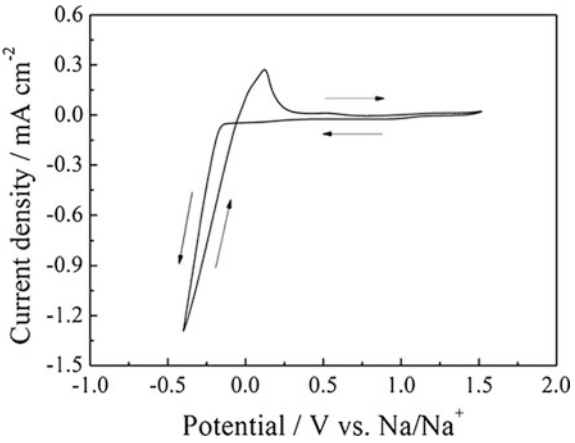

Fig. 6 Cyclic voltammogram (steady cycle) of a Ni plate electrode in NaFSA–C_3C_1pyrrFSA ionic liquid at 353 K [19]

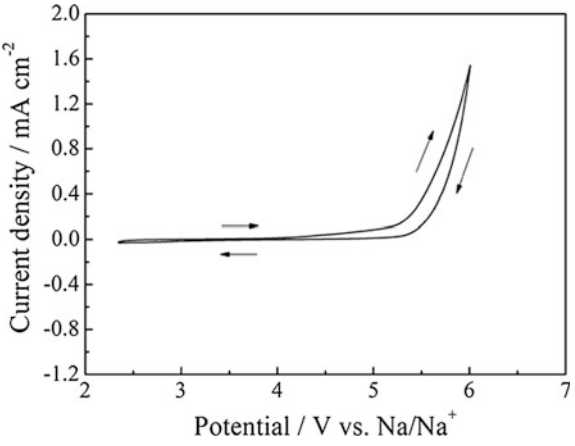

Fig. 7 Cyclic voltammogram (1st cycle) of a glassy carbon rod electrode in NaFSA–C_3C_1pyrrFSA ionic liquid at 353 K [19]

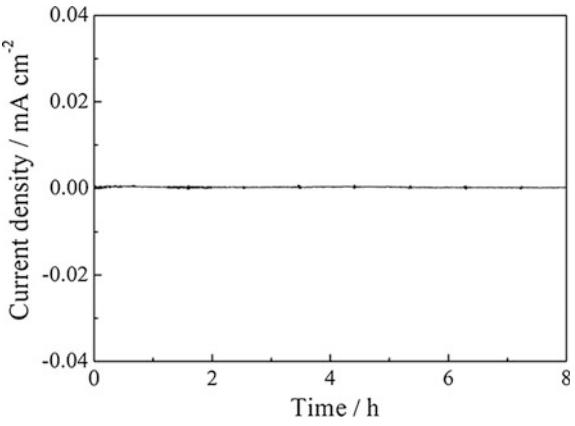

Fig. 8 Chronoamperogram of an Al plate electrode in NaFSA–C_3C_1pyrrFSA ionic liquid at 353 K. Potential: 3.8 V versus Na/Na^+ [19]

and dissolution of sodium, for which the coulombic efficiency is improved by increasing the operation temperature.

Aluminum was used as a current collector for the cathode in this study, and the stability of the aluminum plate electrode was investigated before the charge–discharge tests. Because the highest charging voltage measured in this study was 3.5 V, the stability test for the aluminum plate electrode was conducted at 3.8 V versus Na/Na^+ in the Na[FSA]–[C_3C_1pyrr][FSA] ionic liquid at 353 K. Figure 8 shows the current–time curve during the stability test. The current is negligibly small, below 0.6 mA cm^{-2}, suggesting that the aluminum plate electrode is electrochemically stable at a potential of 3.8 V versus Na/Na^+. Moreover, preliminary tests indicate that aluminum is stable even at 5.0 V versus Na/Na^+ after pretreatment by a stepwise electrolysis at lower potentials. Similar electrochemical stability of aluminum at least 4.5 V versus Na/Na^+ has been confirmed for the Na[FSA]–K[FSA] ionic liquid at 363 K [11]; this improvement is explained by the formation of a passivation film on the aluminum surface [20]. The passivation film is probably formed by the reaction between Al^{3+} and FSA^- [11].

5 Application of FSA Ionic Liquids to Rechargeable Sodium Batteries

Several positive and negative electrodes have been tested for use with the Na[FSA]–K[FSA] (56:44) and Na[FSA]–[C_3C_1pyrr][FSA] (20:80) systems. For example, in the Na[FSA]–K[FSA] system, Sn and Sn alloys as negative electrode materials [21–23] and $NaCrO_2$ [24] and $Na_2FeP_2O_7$ [25] as positive electrode materials have been tested. Figure 9 shows the charge–discharge curves of a $Na/NaCrO_2$ half-cell with different current rates at 363 K. The discharge capacity at 125 mA $(g\text{-}NaCrO_2)^{-1}$, corresponding a 1 C rate, is 113 mAh g^{-1}, close to the theoretical value. It exhibits an excellent rate performance, giving a discharge

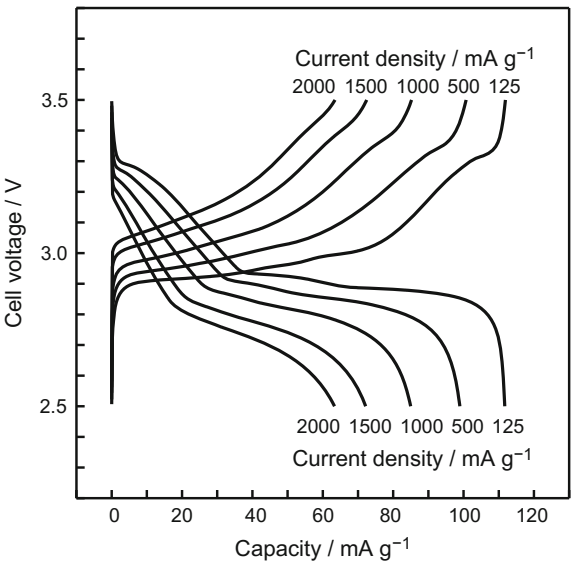

Fig. 9 Rate dependence on charge–discharge curves of Na/Na[FSA]–K[FSA]/$NaCrO_2$ cell at 363 K (The charge–discharge rate: 125, 500, 1000, 1500, 2000 mA $(g\text{-}NaCrO_2)^{-1}$) [24]. Cut-off voltages: 2.5 and 3.5 V

capacity of 63 mAh g^{-1} at 2000 mA $(g\text{-}NaCrO_2)^{-1}$ (16 C). The capacity retention ratio confirmed after 100 times of charge–discharge cycles is about 98%.

Hard carbon [26] as the negative electrode material and Na_2CrO_2 [11, 12, 19], $Na_2FeP_2O_7$ [27], and $NaMnSiO_4$ [28] as the positive electrode materials have been tested in Na[FSA]–[C_3C_1pyrr][FSA] (20:80) cells. The hard carbon negative electrodes were originally applied for sodium-ion batteries using organic electrolytes and exhibited a prominent performance [29]. The excellent charge–discharge performances are also obtained for inorganic–organic hybrid ionic liquids at 393 K, giving a discharge capacity of 260 mAh $(g\text{-}HC)^{-1}$ at a current rate of 50 mA $(g\text{-}HC)^{-1}$. $NaCrO_2$ exhibits a discharge capacity close to the theoretical value at a current rate of 20 mAg^{-1}, but the capacity decreases with the increase of the current rate. However, the capacity recovers its original value in the first cycle again with almost identical charge and discharge curves on returning to 20 mA g^{-1}, indicating that little deterioration of the positive electrode material occurred during the high rate charge–discharge tests. This ionic liquid possesses a wide temperature range for operation of a battery at temperatures below zero to medium range temperatures. Figure 10 shows the cycle performances obtained between 253 and 363 K [12]. Discharge is possible even at 253 K, although the capacity is significantly decreased at this temperature. Charge–discharge tests conducted at 363 K after the test at 253 K show that the capacity remains similar to that of the initial test at 363 K, indicating the operation at low temperatures does not cause deterioration of the electrode. The coulombic efficiency of each charge–discharge cycle is more than 99%, except just after the alteration of operation temperature. In addition, $Na_2FeP_2O_7$ has given an excellent charge–discharge performance in a wide temperature range with an outstanding rate capability.

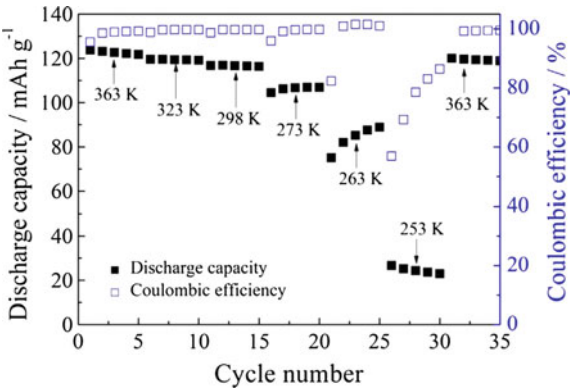

Fig. 10 The cycle performance of a Na/Na[FSA]–[C_3C_1pyrr][FSA]/$NaCrO_2$ cell operating at 253–353 K [12]. Charge–discharge rate: 20 mA (g-$NaCrO_2$)$^{-1}$. Cut-off voltage: 2.5 and 3.5 V

Fig. 11 Appearance of a 27 Ah HC/Na[FSA]–[C_3C_1pyrr][FSA]/$NaCrO_2$ prismatic full cell [30]. External size: 113 × 150 × 38 mm. Weight: 1.08 kg

6 Development of Practical Batteries

Large-scale practical sodium-ion batteries of the kWh class using ionic liquids have been developed by Sumitomo Electric Industries. One hundred sets of laminated batteries using $NaCrO_2$ as the positive electrode material and hard carbon (HC) as the negative electrode material are piled up and placed in an aluminum canister.

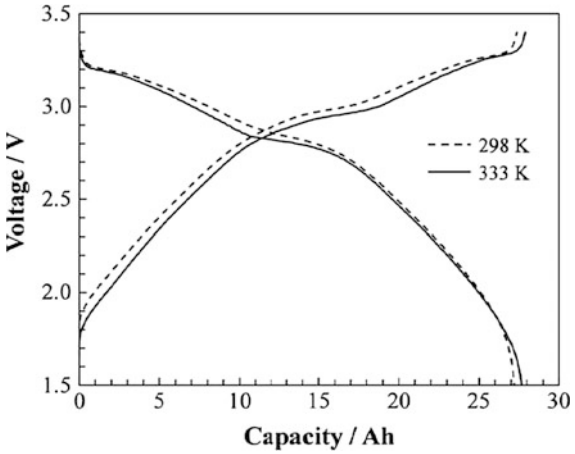

Fig. 12 Charge–discharge curves for a 27 Ah HC/Na[FSA]–[C_3C_1pyrr][FSA]/$NaCrO_2$ full cell at 298 and 333 K [30]. Charge–discharge rate: 2.7 A (298 K) and 10 A (333 K). Cut-off voltages: 1.5 and 3.35 V

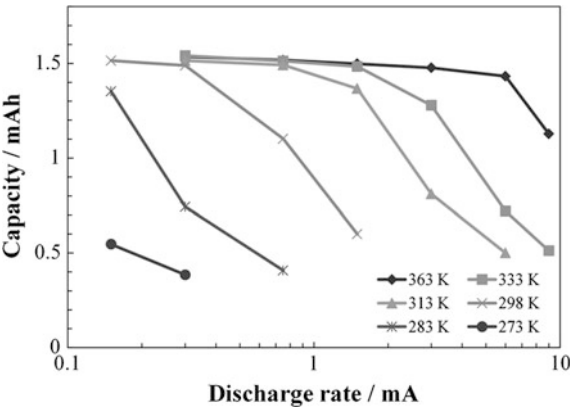

Fig. 13 Rate dependence of the discharge capacity for a 1.5 mAh HC/Na[FSA]–[C_3C_1pyrr][FSA]/$NaCrO_2$ full cell [30]. Charge condition: 0.3 mA CC (313–363 K) and 0.3 mA CC–CV (to 0.075 mA) at 298 K (273–298 K). Discharge rate: 0.15–9.0 mA. Operation temperature: 273–363 K

All the batteries are connected in parallel by welding of the lead tab. The ionic liquid electrolyte used for this battery is Na[FSA]–[C_3C_1pyrr][FSA] (20:80). This prismatic battery is shown in Fig. 11 and has a gravimetric energy density of 75 Wh kg^{-1} and volumetric energy density of 125 Wh L^{-1} [30]. These values are comparable with those of large-scale prismatic lithium-ion batteries developed in the early 2000s. Figure 12 shows the charge–discharge curves for the 27 Ah HC/$NaCrO_2$ cell at 298 and 333 K. The observed discharge capacity at a rate of 2.7 A is 27.3 Ah at 298 K, which is equal to the designed capacity. At 333 K, almost the same charge–discharge behavior is obtained, even at the higher rate of 10 A. Figure 13 shows the rate dependence of discharge capacity for the 27 Ah cell at 283, 298, 313, 333, and 363 K. In contrast, the performance at 283 K is unsatisfactory due to the lower conductivity of the ionic liquid. Figure 14 shows the cyclability of the 27 Ah cell at a rate of 10 A at 333 K. The capacity retention after 500 cycles is 87%, the same value as those of large-scale prismatic lithium-ion batteries used in the early 2000s. It should be emphasized that the 27 Ah cell has

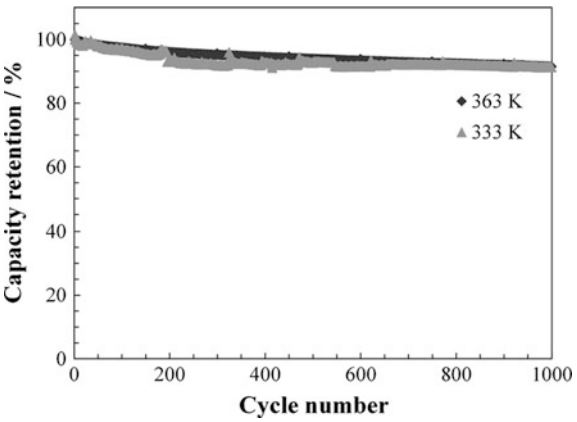

Fig. 14 Cycle property for a HC/Na[FSA]–[C_3C_1pyrr][FSA]/$NaCrO_2$ full cell. Charge–discharge rate: 1.5 mA [30]. Operation temperature: 363 and 333 K. Cut-off voltages: 1.5 and 3.35 V

been produced by an industrial process similar to that for conventional lithium-ion batteries. Therefore, it is expected that a large-sized HC/Na[FSA]–[C_3C_1pyrr][FSA]/$NaCrO_2$ cell will show further improvements in energy density, power density (rate capability), energy efficiency, and cyclability with improved manufacturing technology.

Acknowledgements This study was partly supported by Advanced Low Carbon Technology Research and Development Program (ALCA) of the Japan Science and Technology Agency (JST) and the Japanese Ministry of Education Culture, Sports, Science, and Technology (MEXT) program "Elements Strategy Initiative for Form Core Research Center."

References

1. Welton T (1999) Room-temperature ionic liquids. Solvents for synthesis and catalysis. Chem Rev 99:2071–2083
2. Bockris JOM, Reddy AKN (1970) Modern electrohemistry. Plenum Publishing Corporation, New York
3. Pan HL, Hu YS, Chen LQ (2013) Room-temperature stationary sodium-ion batteries for large-scale electric energy storage. Energy Environ Sci 6:2338–2360
4. Yabuuchi N, Kubota K, Dahbi M et al (2014) Research development on sodium-ion batteries. Chem Rev 114:11636–11682
5. Kubota K, Nohira T, Goto T et al (2008) Novel inorganic ionic liquids possessing low melting temperatures and wide electrochemical windows: binary mixtures of alkali bis(fluorosulfonyl) amides. Electrochem Commun 10:1886–1888
6. Kubota K, Nohira T, Goto T et al (2009) Binary and ternary mixtures of MFSA (M = Li, K, Cs) as new inorganic ionic liquids. ECS Trans 16:91–98
7. Kubota K, Nohira T, Hagiwara R (2010) Thermal properties of alkali bis(fluorosulfonyl) amides and their binary mixtures. J Chem Eng Data 55:3142–3146
8. Hagiwara R, Tamaki K, Kubota K et al (2008) Thermal properties of mixed alkali bis (trifluoromethylsulfonyl)amides. J Chem Eng Data 53:355–358
9. Kubota K, Nohira T, Goto T et al (2008) Ternary phase diagrams of alkali bis (trifluoromethylsulfonyl)amides. J Chem Eng Data 53:2144–2147

10. Kubota K, Tamaki K, Nohira T et al (2010) Electrochemical properties of alkali bis (trifluoromethylsulfonyl)amides and their eutectic mixtures. Electrochim Acta 55:1113–1119
11. Fukunaga A, Nohira T, Kozawa Y et al (2012) Intermediate-temperature ionic liquid NaFSA-KFSA and its application to sodium secondary batteries. J Power Sources 209:52–56
12. Ding CS, Nohira T, Hagiwara R et al (2014) Na[FSA]-[C_3C_1pyrr][FSA] ionic liquids as electrolytes for sodium secondary batteries: Effects of na ion concentration and operation temperature. J Power Sources 269:124–128
13. Matsumoto K, Okamoto Y, Nohira T et al (2015) Thermal and transport properties of Na[N($SO_2F)_2$]-[*N*-methyl-*N*-propylpyrrolidinium][N($SO_2F)_2$] ionic liquids for Na secondary batteries. J Phys Chem C 119:7648–7655
14. Matsumoto K, Hosokawa T, Nohira T et al (2014) The Na[FSA]-[C_2C_1im][FSA] ($C_2C_1im^+$:1-ethyl-3-methylimidazolium and FSA^-:Bis(fluorosulfonyl)amide) ionic liquid electrolytes for sodium secondary batteries. J Power Sources 265:36–39
15. Matsumoto K, Taniki R, Nohira T et al (2015) Inorganic-organic hybrid ionic liquid electrolytes for Na secondary batteries. J Electrochem Soc 162:A1409–A1414
16. Monti D, Jonsson E, Palacin MR et al (2014) Ionic liquid based electrolytes for sodium-ion batteries: Na^+ solvation and ionic conductivity. J Power Sources 245:630–636
17. Vogel H (1921) The temperature dependence law of the viscosity of fluids. Phys Z 22:645–646
18. Fulcher GS (1925) Analysis of recent measurements of the viscosity of glasses. II. J Am Ceram Soc 8:789–794
19. Ding CS, Nohira T, Kuroda K et al (2013) NaFSA-C_1C_3pyrFSA ionic liquids for sodium secondary battery operating over a wide temperature range. J Power Sources 238:296–300
20. Watarai A, Kubota K, Yamagata M et al (2008) A rechargeable lithium metal battery operating at intermediate temperatures using molten alkali bis(trifluoromethylsulfonyl)amide mixture as an electrolyte. J Power Sources 183:724–729
21. Yamamoto T, Nohira T, Hagiwara R et al (2012) Charge-discharge behavior of tin negative electrode for a sodium secondary battery using intermediate temperature ionic liquid sodium bis(fluorosulfonyl) amide-potassium bis(fluorosulfonyl)amide. J Power Sources 217:479–484
22. Yamamoto T, Nohira T, Hagiwara R et al (2013) Thermodynamic studies on Sn-Na alloy in an intermediate temperature ionic liquid NaFSA-KFSA at 363 K. J Power Sources 237:98–103
23. Yamamoto T, Nohira T, Hagiwara R et al (2014) Improved cyclability of Sn-Cu film electrode for sodium secondary battery using inorganic ionic liquid electrolyte. Electrochim Acta 135:60–67
24. Chen CY, Matsumoto K, Nohira T et al (2013) Electrochemical and structural investigation of $NaCrO_2$ as a positive electrode for sodium secondary battery using inorganic ionic liquid NaFSA-KFSA. J Power Sources 237:52–57
25. Chen CY, Matsumoto K, Nohira T et al (2014) Pyrophosphate $Na_2FeP_2O_7$ as a low-cost and high-performance positive electrode material for sodium secondary batteries utilizing an inorganic ionic liquid. J Power Sources 246:783–787
26. Fukunaga A, Nohira T, Hagiwara R et al (2014) A safe and high-rate negative electrode for sodium-ion batteries: hard carbon in NaFSA-C_1C_3pyrFSA ionic liquid at 363 K. J Power Sources 246:387–391
27. Chen CY, Matsumoto K, Nohira T et al (2014) Charge-discharge behavior of a $Na_2FeP_2O_7$ positive electrode in an ionic liquid electrolyte between 253 and 363 K. Electrochim Acta 133:583–588
28. Chen CY, Matsumoto K, Nohira T et al (2014) Na_2MnSiO_4 as a positive electrode material for sodium secondary batteries using an ionic liquid electrolyte. Electrochem Commun 45:63–66
29. Komaba S, Murata W, Ishikawa T et al (2011) Electrochemical na insertion and solid electrolyte interphase for hard-carbon electrodes and application to Na-ion batteries. Adv Funct Mater 21:3859–3867
30. Fukunaga A, Nohira T, Hagiwara R et al (2016) Performance validation of sodium-ion batteries using an ionic liquid electrolyte. J Appl Electrochem 46:487–496

Passivity of Iron—A Review

R. Winston Revie

Abstract The passive film on iron has provided positive benefits to the longevity of iron structures since antiquity. As the benefits of passivity of iron became recognized, debates among scientists developed over the possible mechanisms by which the very thin (2–3 nm) passive layer could impart substantive corrosion resistance. The mechanisms of passivity that impart unique properties to passive iron have been studied and debated for decades. In recent years, equipment that is sufficiently advanced for surface studies at an atomic level has been used to explore the mechanisms of passivity and, in combination with electrochemical studies, to characterize the chemical composition, physical structure, and electronic properties of the passive film on iron. The evolution of the concepts and theories of the passivity of iron are reviewed in this paper, beginning with the earliest observations and summarizing the developments that have become possible as a result of advances in instrumentation and surface analytical methods. Effects of temperature, texture, and hydrodynamics on the mechanisms of passivity of iron are discussed.

1 Introduction

The definition of 'passive' that is used in this paper is, "A metal is passive if it substantially resists corrosion in a given environment resulting from marked anodic polarization" [1]. Numerous passive metals are used successfully and economically in architectural applications and engineering systems because of the very low corrosion rates that are characteristic of these metals. For example, the passivity of iron has resulted in the long life of the Iron Pillar of Delhi, constructed around 400 A.D., and other iron artifacts that date from antiquity in different parts of India. Using modern analytical methods, studies of these ancient artifacts, exposed to atmospheric environments for more than 1,000 years, have led to insights on the composition and properties of passive films.

R.W. Revie (✉)
Ottawa, Canada
e-mail: win25@rogers.com

K. Uosaki (ed.), *Electrochemical Science for a Sustainable Society*,
DOI 10.1007/978-3-319-57310-6_9

Scientific studies on the passivity of iron that began in the 1700s have continued to the present day, with the result that mechanistic hypotheses and theories about the passivity of iron at the atomic level have continued to advance, with the benefit of modern surface analytical methods that are now available. Over many years of research [2–6], the passive film on iron has been described in many different ways, including, among others, as an oxide film, a bilayer structure consisting of two different oxides (Fe_3O_4 at the metal/oxide interface and γ-Fe_2O_3 at the oxide/solution interface), an adsorbed film, an amorphous film containing hydroxides or oxyhydroxides, and a combination of crystalline and amorphous iron oxides. As Strehblow has described in a recent review, it is necessary to use a combination of many techniques, electrochemical and surface analytical, to establish the details of corrosion processes and the passive film at an atomistic and mechanistic level [7].

2 Early Scientific Studies

James Keir discovered in 1790 that iron, after immersion in concentrated nitric acid, does not react vigorously in dilute nitric acid and does not precipitate silver from solutions of silver nitrate [8]. During the 1800s, Schönbein [9] and Faraday [10] both studied the peculiar characteristics of iron in nitric acid. Schönbein coined the term 'passive' to describe iron in its nonreactive state, and he showed that anodic polarization could be used to make iron passive. Faraday showed that a cell consisting of passive iron coupled to platinum in concentrated nitric acid produced little or no current, whereas amalgamated zinc coupled to platinum in sulfuric acid produced a high current. Passive iron corrodes only slightly in concentrated nitric acid, and amalgamated zinc corrodes only slightly in dilute sulfuric acid. Faraday reasoned that a low corrosion rate is not sufficient to imply passivity, but that the magnitude of current produced in the cell coupled with platinum is a better criterion. Accordingly, by this reasoning, iron is passive, but not zinc.

The study of the passivity of iron evolved from these early beginnings. Over the past 100+ years, a great deal of research has been carried out to characterize the passive films on which the passivity of iron depends, specifically the composition, structure, and properties of these films.

3 Oxide Film Theory

According to the oxide film theory, passive films are always diffusion barrier layers of reaction products, such as oxide films, that isolate the metal from its environment [11]. Examples of such a system would be iron immersed in aqueous hydrofluoric acid, where an iron fluoride film protects the metal from the HF environment,

or lead in sulfuric acid, where a lead sulfate film forms that is visible. On the other hand, the passive films on metals, such as iron, that are passive by the definition cited above are usually not visible and are usually about 2–3 nm in thickness.

4 Logarithmic Growth and the Place Exchange Mechanism

In the 1960s, Cohen and his colleagues at the National Research Council of Canada studied the passivity of iron in borate buffer solution of pH 8.4 [12, 13]. They calculated the thickness of the passive film on iron to range from 1 to 3 nm (10–30 A), depending on the potential within the passive region, and they found that the rate of film growth, i, could be expressed by the equation,

$$i = k' \exp(\beta E - \frac{Q_T}{B})$$

where Q_T is the film thickness, E is the potential, and k′, β, and B are constants.

At constant E,

$$i = A exp(\frac{Q_T}{B})$$

where A is a constant.

The place exchange mechanism that Sato and Cohen [13] proposed to explain the mechanism of passive film development is illustrated in Fig. 1, in which M represents a metal ion and O represents an oxygen ion. An oxygen ion adsorbed on the iron surface exchanges places with a metal ion. A second oxygen ion is adsorbed, and then the two M–O pairs rotate. As this process is repeated, the film thickens.

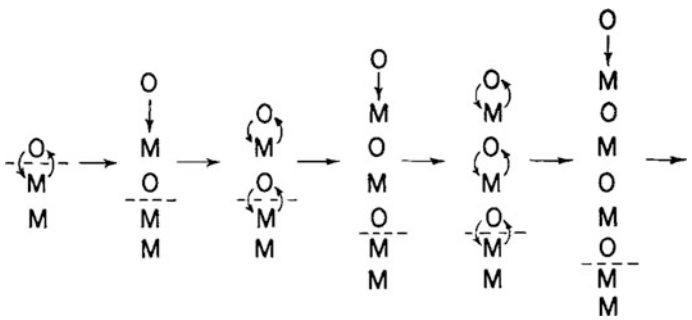

Fig. 1 Schematic illustration of the place exchange mechanism for passive film development proposed by Sato and Cohen [13] (reproduced by permission of The Electrochemical Society)

Nagayama and Cohen [12] concluded that the passive film on iron has a spinel structure, a conclusion confirmed by more recent studies, as will be discussed later in this review.

5 Adsorption and Electron Configuration Theories

According to the adsorption theory of passivity that Uhlig advanced, passive metals are covered by a chemisorbed film of, for example, oxygen, which displaces adsorbed H_2O molecules and retards anodic dissolution. Metals that are passive by the definition used here are transition metals in the periodic table. These metals contain electron vacancies or uncoupled electrons in the *d* shells of the atom. These electron vacancies in iron lead to strong bonding with oxygen, which also has uncoupled electrons. On transition metals, such as iron, the initially chemisorbed oxygen is more stable thermodynamically than is the metal oxide [14, 15].

Evidence for the adsorption theory of passivity was supported by the standard Flade potential for passive iron, which was measured to be 0.63 V versus S.H.E. [16], consistent with a chemisorbed film of oxygen on the iron surface, and about 0.6 V more noble than that of any of the known iron oxides in equilibrium with iron [14].

6 Bockris Model of Passivity of Iron

Revie et al. [17] designed and built an apparatus, unique at the time, in which an electrochemical cell and high vacuum equipment for Auger electron spectroscopy were separated by a straight-through valve. After passivating the iron electrode in a solution consisting of KOH + H_3BO_3, pH 8.1, the cell was drained, evacuated, and rinsed, the straight-through valve was opened, and the iron electrode was transferred to the Auger tube. To prevent decomposition of hydrated films under high vacuum conditions, the stage on which the electrode was mounted was cooled with liquid nitrogen. By analyzing the Auger spectra, the oxygen/iron ratio in the passive film was calculated to be 1.8 ± 0.2. Based on this result, it was concluded that $Fe_2O_3 \cdot H_2O$ was a satisfactory representation of the passive film on iron. This conclusion was in essential agreement with the results of O'Grady and Bockris who found that their Mössbauer spectroscopic results were consistent with a passive film on iron consisting of a polymeric film of hydrated iron oxide [18].

The Auger spectrum of the passive film after heating in vacuum to 150 °C was found to be characteristic of oxidized iron. It was concluded that heating the passive film in vacuum caused dehydration and the formation of an oxide, possibly γ-Fe_2O_3, which O'Grady had observed on drying passive iron [19].

7 Point Defect Model

Macdonald and his colleagues have developed the Point Defect Model for the growth and breakdown of passive films on metal surfaces in contact with aqueous solutions [20–23]. The point defect model is based on the movement of point defects to support the growth of a passive film on a metal surface. Specific assumptions of the model include the following:

1. A passive film forms on a metal surface when the externally applied potential is more noble than the Flade potential.
2. The passive film contains a high concentration of point defects, specifically, metal vacancies, oxide vacancies, electrons, and holes.
3. The passive film is characterized by high electrical fields, similar to the field required for dielectric breakdown.
4. The rate-controlling step for film growth is the transport of metal vacancies and oxide vacancies across the film.

The kinetics of film growth follows a linear logarithmic law of the form:

$$\exp(2KL) - 2KL - 1 = 2KA(B-1)t$$

where L is the film thickness, t is time, A and B are functions of the external potential, and K is a parameter that depends on the field strength and temperature [29].

Calculations using the point defect model were found to be in agreement with experimental data developed earlier in studies of the growth of the passive film on iron in borate buffer solution [13, 24, 25] and in phosphate solution [26].

8 Duplex Layer Model

Davenport et al. [27] used in situ XANES (X-ray absorption near-edge structure) to study galvanostatic reduction of the passive film on thin films of iron in borate buffer solution, pH 8.4. By studying the spectra that were obtained during the galvanostatic reduction of the passive films, these authors concluded that the average composition of the passive films that remained changed from ferric oxide to Fe_3O_4, with the implication that the passive film has an inner layer of Fe_3O_4 and an outer layer of γ-Fe_2O_3. The mechanism proposed for reductive dissolution of the passive film in the borate buffer solution was

$$Fe_2O_3 + 6H^+ + 2e^- \rightarrow 2Fe^{2+} + 3H_2O$$

In galvanostatically reducing the passive film formed in 1 M KOH, no dissolution of iron was detected. The passive film was completely reduced to ferrous oxide or hydroxide.

Schmuki et al. studied the chemical composition and thickness of passive films formed on iron in borate and phosphate buffer solutions at pH 8.4 [28]. Analysis using XPS showed that increasing the passivation potential in the borate buffer solution resulted in thicker passive films, decreased metallic iron, and increased iron oxide. By analyzing the passive layer composition after sputtering, it was found that H_2O was present only on the surface of the passive layer. By studying the XPS spectra measured at different takeoff angles, it was shown that iron hydroxide is located in the outer part of the passive film, whereas the inner part consists of iron oxides.

Although the passive films formed in borate solution contained no significant amounts of either boron or its compounds, the passive films formed in phosphate solution were shown, using XPS, to contain phosphate compounds, primarily in the outer part of the passive film. Schmuki et al. attributed this difference to the very low solubility of oxides of phosphorus compared to those of boron. Using AES depth profiling, the passive films formed in phosphate solution were shown to be thicker than those formed in borate solution of the same pH, 8.4, and at the same potential, 0.800 V versus Ag/AgCl, 5.4 nm for the former compared to 3.8 nm for the latter [28].

In both phosphate solution and borate solution, a duplex layer model is appropriate. In the borate buffer solution, the outer layer was reported to be mostly iron hydroxide, with an inner layer of iron oxide. The passive film in phosphate buffer solution consisted of an outer layer of mixed iron phosphate and oxyhydroxide and an inner layer of iron oxide [28].

Cathodic reduction of the passive film in the borate solution results in bare metal surface formation by reductive dissolution of the film. In the phosphate buffer solution, reduction of the passive film is a two-step process that does not involve dissolution. Instead, the passive film is converted into metallic iron by the formation of an intermediate Fe(II) phosphate layer.

In a scanning tunnelling microscopy (STM) study of passive films on thin films of pure iron in borate buffer solution of pH 8.4 at high anodic potentials, Ryan et al. showed the film to be crystalline and consistent with a γ-Fe_2O_3/Fe_3O_4 structure [29].

Using in situ surface X-ray diffraction, Davenport et al. identified the detailed structure of the passive film on (001) and (110) surfaces of iron single crystals in borate buffer solution at +0.4 V versus mercurous sulfate reference electrode [30]. They found that the passive film formed a nanocrystalline microstructure with an epitaxial relationship to the iron substrate and with many defects, including point defects, vacancies, interstitials, and stacking faults. The passive film was shown to be a new phase (called the LAMM phase) consisting of a spinel oxide, confirming a finding reported by Nagayama and Cohen [12] in 1962, but with a different stoichiometry, $Fe_{1.9\pm0.2}O_3$. Davenport et al. obtained the crystal structure and stoichiometry by measuring and analyzing the peak intensities. There was no evidence

found for other oxide, hydroxide, or oxyhydroxide phases, or for amorphous material. By comparing the data obtained in ex situ and in situ experiments, it was shown that the passive film formed on iron at the potential used was stable in air on removal from the electrolyte.

There were some differences in the passive films formed on (001) and (110) surfaces: films on the former had fewer defects, larger grain size, and fewer antiphase boundaries.

Strehblow and Marcus [31] used X-ray photoelectron spectroscopy (XPS) to study the passive film on iron after immersion in 1 M NaOH. In this work, the electrochemical cell was connected to the vacuum chamber required for XPS, and the specimen under study could be transferred, within the closed system, from the electrochemical cell to the vacuum chamber without exposure to the laboratory environment.

The passive film formed at potentials noble to the Flade potential was characterized as consisting of two layers, an inner Fe(II) layer and an outer Fe(III) layer of thickness d_1 and d_2, respectively [31], as illustrated schematically in Fig. 2. By analyzing the XPS data, it was concluded that Fe(II) forms a hydroxide, $Fe(OH)_2$ which converts to an oxide during oxidation to Fe(III). The result of analyzing the XPS data supported the interpretation of the Flade potential based on the reaction

$$2Fe_3O_4 + H_2O \rightarrow 3Fe_2O_3 + 2H^+ + 2e^-$$

The oxidation reactions that form passive films were found to be reversible at sufficiently negative potentials, with Fe(III) being reduced to Fe(II) and to Fe.

Using the electrochemical quartz crystal microbalance (EQCM), changes in mass of electrodes can be measured as passive films develop on the surface [32, 33]. The total current, i, at an electrode consists of the sum of the anodic and cathodic currents, i_a and i_c, respectively; i.e.,

$$i = i_a + i_c \tag{1}$$

By measuring the total current from the polarization curve and deriving the anodic current from the change in mass measured using the EQCM, Seo, Yoshida, and Noda calculated the cathodic current using Eq. (1). As expected, at the corrosion potential, where the total current is zero, the anodic and cathodic currents are equal in magnitude.

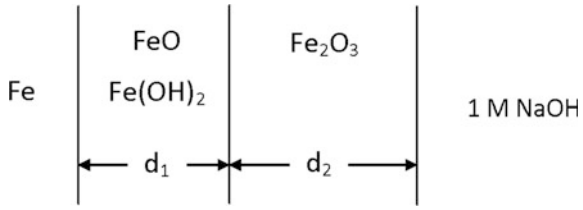

Fig. 2 Bilayer structure of the passive film on iron in 1 M NaOH. Thicknesses of the layers of Fe^{2+} and Fe^{3+} are represented by d_1 and d_2, respectively. Adapted from Strehblow and Marcus [31]

Schmutz and Landolt used the EQCM to study film growth on a Fe-25Cr alloy in 0.1 M H_2SO_4 as well as in alkaline solution [34]. By superimposing a polarization curve (current density as a function of potential) on EQCM data that indicate the mass change as a function of potential, Schmutz and Landolt were able to characterize the mass change in the potential region of passivity. In the passive region, the slope of mass change with potential is negative, indicating an increase in mass loss with rising potential (i.e., as the potential becomes more noble). Schmutz and Landolt attribute this mass loss to dissolution of iron that is oxidized at the metal/film interface, resulting in chromium enrichment of the passive film that was subsequently confirmed using XPS [35].

In alkaline solutions, iron oxide is less soluble than in acidic solutions. For this reason, in alkaline solutions, data obtained with EQCM show an increase of mass, with enrichment of iron confirmed using XPS [36].

9 Effects of Texture on Passivity of Iron

In 2014, Takabatake et al. reported the results of studies on passivity of iron single grains of a polycrystalline pure iron substrate in sulfuric acid solution [37]. Using a micro-capillary cell of diameter less than the grain size in the iron sample under study, they explored the dependence of the passivation mechanism on crystallographic orientation of iron single grains in 0.05 mol dm^{-3} sulfuric acid, pH 1.3. Crystallographic orientation of the substrate surface had a strong influence on passivation under potentiostatic polarization conditions, on the charge-transfer resistance of the passivated surface, on the chemical state of iron in the passive oxide film, and on the concentration of defects in the film. Using EIS, the charge-transfer resistance of the passive film was found to be greatest for the film formed on the substrate of orientation {101}, less on {111} orientation, and least on {001} orientation. The dependence of the passive film structure on substrate orientation was attributed to the different surface energies of the substrate surfaces of bcc iron. A further conclusion of this study was that the electric property of the passive film on iron depends on film composition rather than defect concentration.

Takabatake et al. considered that, if the passive layer formed on iron in sulfuric acid consisted of a bilayer structure, then a grain-dependent layer structure of the passive film can be assumed, an inner layer of Fe_3O_4 and an outer layer of γ-Fe_2O_3, as shown in Fig. 3. The ratio of the thicknesses of these layers was found to depend on the orientation of the substrate. On the {101} grain, the outer layer of γ-Fe_2O_3 constituted a large proportion of the passive film, the ratio of Fe^{3+}/Fe^{2+} was the highest among the three orientations that were studied, and the charge-transfer resistance was also the largest. Of the orientations that were studied, the {101} grain would be considered to have the most protective surface of the three orientations studied. This is an intriguing result that could have practical applications where the corrosion resistance of iron must be optimized.

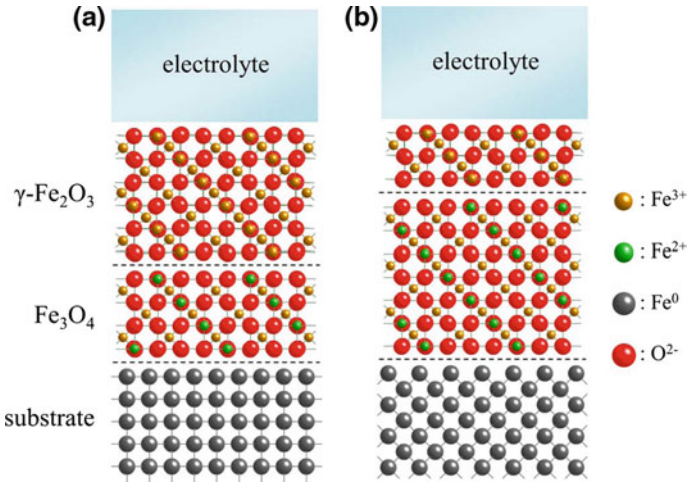

Fig. 3 Schematic diagram of iron single grain surfaces after polarization in sulfuric acid. **a** {101} surface; **b** {001} surface. Reproduced from Takabatake et al. [37]

10 Effect of Cold Work

By cold rolling pure iron plate to different thicknesses, Yamamoto et al. were able to correlate passivation characteristics of iron in pH 8.4 borate buffer solution with percent reduction and dislocation density [38]. Through analysis of etch pitting, the dislocation density on the specimen surfaces was found to be a maximum at 60% reduction in thickness. At this same reduction in thickness, both the passivation current, at 0.7 V (SHE) for 7.2 ks, and the charge consumed during the polarization were at the maximum values compared with those at other percent reductions, either greater or lesser than 60%. In addition, the critical potential for passivity was found to depend on the % reduction in thickness, being least noble at 60%. At potentials noble to the critical potential, the charge-transfer resistance was a minimum at 60% reduction in thickness. Reduction in charge-transfer resistance was interpreted to result from a less compact and/or less insulating film.

Based on EIS data, Yamamoto et al. presented the equivalent circuit shown in Fig. 4 as representative of passive iron. In this figure, R_{ct} represents the charge-transfer resistance of the passive film, C_{sc} the capacitance of the space charge layer in the passive film and R_{sol} the resistance of the solution.

By Mott–Schottky analysis, the passive film on iron was shown to have n-type semiconductive properties. The donor density of the passive film and the film thickness were both at maximum values at 60% reduction in thickness, under which conditions the thickness of the passive film was estimated to be 3.7–5.0 nm from the results of radio-frequency glow discharge optical emission spectroscopy. Yamamoto et al. noted that the dislocations in the iron substrate result in the

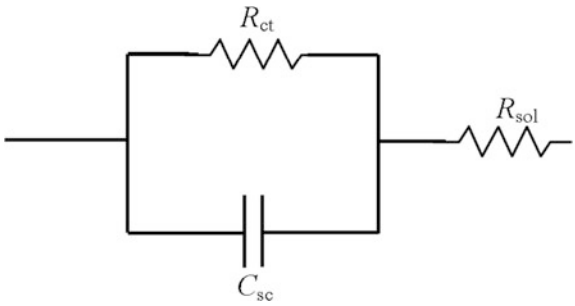

Fig. 4 Equivalent electric circuit for the passive film on iron, assumed to be homogeneous and uniform. The resistance of the solution is represented by R_{sol}. In the passive film, R_{ct} is the charge-transfer resistance, and C_{sc} is the capacitance of the space charge layer. Adapted from Yamamoto et al. [38]

formation of a passive film with a high donor density and a relatively large current to maintain passivity. They postulated that passivation of an iron substrate with no dislocations could result in a defect-free passive film with extremely high corrosion resistance. This is an intriguing view worth further study to explore the possibility of practical application.

11 Temperature Dependence

Huilhua Deng et al. studied the passivity of polycrystalline pure iron in borate buffer solution of pH 8.4 at temperatures between 25 and 60 °C and at a potential of −400 mV versus the saturated calomel reference electrode [39]. At increased temperature, both the corrosion potential and the potential noble to which passivation occurred became less noble, implying that increasing temperature accelerates dissolution of iron, the formation of the passive film, and the conversion of Fe^{2+} to Fe^{3+}. The minimum current density in the passive region also increases with temperature, confirming previous studies [40].

Using scanning tunnelling microscopy, the passive film was shown to contain fewer defects as the temperature was increased, with a defect-free structure at 60 °C. The passive film formed at 60 °C showed long-range 2-dimensional order with terraces 5 nm wide. As the temperature was increased from 25 to 60 °C, the particle size in the passive film became larger, increasing from 34 nm for passivation at 25 °C to 55 nm for passivation at 60 °C. In addition, at the higher temperatures, the surface roughness was lower.

12 Hydrodynamics

Büchler et al. [41] and Cáceres et al. [42] studied passivation under varying hydrodynamic conditions in borate buffer solutions of pH 8.4. The former investigators used pure iron (99.5% Fe) whereas the latter investigators used AISI 1020 carbon steel (99% Fe). Büchler et al. showed that hydrodynamic flow prevented the development of a deposit layer of hydroxide. In order to form this deposit layer, a sufficient surface concentration of Fe^{2+} was found to be necessary. Electrolyte convection caused by nitrogen gas bubbling was sufficient to prevent deposit layer formation. Cáceres et al. concluded that the transport of soluble ferrous ion has a major influence on potentiodynamic data obtained in borate buffer solution.

13 Summary

The chemical composition, thickness, and properties of the passive film on iron depend on the environment in which the passivation takes place. For example, as temperature increases from 25 to 60 °C, the potential noble to which passivation of iron occurs in borate buffer solution of pH 8.4 becomes less noble, and the minimum current density in the passive region increases. In addition, as the temperature increases, the passive film contains fewer defects, reported to be defect free when formed at 60 °C.

Texture has a significant effect on passivation of iron, including the charge-transfer resistance of the passivated surface, the chemical state of iron in the passive film, and the concentration of defects in the film. Of the orientations of iron surfaces studied, the {101} surface was the one on which the most protective passive film developed.

The dislocation density of cold worked iron depends on the reduction ratio and was found to be at a maximum at a 60% reduction ratio. Increasing dislocation density results in increased electric charge in passivation and increased current to maintain passivity. Dislocations exposed at the iron surface were found to increase the donor density in the passive film and to reduce the charge-transfer resistance.

Some views described in this review that may have practical application are related to the development of a defect-free passive film on iron that may offer enhanced corrosion protection, including a defect-free passive film that may be formed at 60 °C or on a dislocation-free iron substrate. It may also be useful to pursue the concept of enhanced protection claimed to result from controlling the texture of an iron substrate so that the {101} crystal surface is exposed to the passivating environment.

References

1. Revie RW, Uhlig HH (2008) Corrosion and corrosion control, an introduction to corrosion science and engineering, 4th edn. NJ, Wiley, Hoboken, p 84
2. Frankenthal RP (1971) Passivation of iron in borate buffer solution. Electrochim Acta 16:1845–1857
3. Sato N (1990) An overview on the passivity of metals. Corros Sci 31:1–19
4. Kruger J (1989) The nature of the passive film on iron and ferrous alloys. Corros Sci 29:149–162
5. Cáceres L, Soliz A, Vargas T (2016) Potentiodynamic behavior of carbon steel in borate buffer solutions under different hydrodynamic conditions. J Electrochem Soc 163(5): C171–C183
6. Revie RW, Uhlig HH (2008) Corrosion and corrosion control, an introduction to corrosion science and engineering, 4th edn. Wiley, Hoboken, NJ, pp 83–111
7. Strehblow H-H (2016) Passivity of metals studied by surface analytical methods, a review. Electrochim Acta 212:630–648
8. Keir J (1790) Philos Trans 80:374
9. Schönbein C (1836) About the behavior of tin and iron from the nitric acid. Pogg Ann 37:390–399
10. Schönbein C, Faraday M (1836) Phil Mag 9(53):56
11. Revie RW, Uhlig HH (2008) Corrosion and corrosion control, an introduction to corrosion science and engineering, 4th edn. Wiley, Hoboken, p 92
12. Nagayama M, Cohen M (1962) The anodic oxidation of iron in a neutral solution. I. The nature and composition of the passive film. J Electrochem Soc 109(2):781–790
13. Sato N, Cohen M (1964) The kinetics of anodic oxidation of iron in neutral solution. I. Steady growth region. J Electrochem Soc 111(5):512–519
14. Uhlig H (1967) Structure and growth of thin films on metals exposed to oxygen. Corros Sci 7:325–339
15. Revie RW, Uhlig HH (2008) Corrosion and corrosion control, an introduction to corrosion science and engineering, 4th edn. Wiley, Hoboken, NJ, pp 92–96
16. Franck UF (1949) The anodic behavior of iron in sulfuric acid. Z Naturforschung 4A:378–391
17. Revie RW, Baker BG, Bockris JO'M (1975) The passive film on iron: an application of Auger electron spectroscopy. J Electrochem Soc 122(11):1460–1466
18. O'Grady WE, Bockris JO'M (1973) Interpretation of Mössbauer spectra of passive films on metals. Surface Sci 38:249–251
19. O'Grady WE (1973) Ph.D. Thesis, University of Pennsylvania
20. Chao CY, Lin LF, Macdonald DD (1981) A point defect model for anodic passive films. I. Film growth kinetics. J Electrochem Soc 128(6):1187–1194
21. Macdonald DD, Biaggio SR, Song H (1992) Steady-State passive films: interfacial kinetic effects and diagnostic criteria. J Electrochem Soc 139(1):170–177
22. Macdonald DD (1992) The point defect model for the passive state. J Electrochem Soc 139(12):3434–3449
23. Macdonald DD (1999) Passivity—the key to our metals-based civilization. Pure Appl Chem 71(6):951–978
24. Goswami KN, Staehle RW (1971) Growth kinetics of passive films on Fe, Fe-Ni, Fe-Cr, Fe-Cr-Ni alloys. Electrochim Acta 16:1895–1907
25. Lukac C, Lumsden JB, Smialowska S, Staehle RW (1975) Effects of temperature on the kinetics of passive film growth on iron. J Electrochem Soc 122:1571–1579
26. Sato N, Noda T, Kudo K (1974) Thickness and structure of passive films on iron in acidic and basic solution. Electrochim Acta 19:471–475
27. Davenport AJ, Bardwell JA, Vitus CM (1995) In situ XANES study of galvanostatic reduction of the passive film on iron. J Electrochem Soc 142(3):721–724

28. Sieber IV, Hildebrand H, Virtanen S, Schmuki P (2006) Investigations on the passivity of iron in borate and phosphate buffers, pH 8.4. Corros Sci 48:3472–3488
29. Ryan MP, Newman RC, Thompson GE (1995) J Electrochem Soc 142(10):L177–L179
30. Davenport AJ, Oblonsky LJ, Ryan MP, Toney MF (2000) J Electrochem Soc 147(6):2162
31. Strehblow H-H, Marcus P (2006) X-ray photoelectron spectroscopy in corrosion research. In: Marcus P, Mansfeld F (eds) Analytical methods in corrosion science and engineering. CRC Taylor & Francis, Boca Raton, FL, pp 1–37
32. Olsson C-OA, Landolt D (2006) Electrochemical quartz crystal microbalance. In: Marcus P, Mansfeld F (eds) Analytical methods in corrosion science and engineering. CRC Taylor & Francis, Boca Raton, FL, pp 733–751
33. Seo M, Yoshida K, Noda K (1995) An EQCM study on corrosion of iron thin film in deaerated neutral solutions. Mat Sci Forum 192–194:755–764
34. Schmutz P, Landolt D (1999) In-situ microgravimetric studies of passive alloys: potential sweep and potential step experiments with Fe-25Cr and Fe-17Cr-33Mo in acid and alkaline solution. Corros Sci 41:2143–2163
35. Hamm D, Ogle K, Olsson C-OA, Weber S, Landolt D (2002) Passivation of Fe-Cr alloys studied with ICP-AES and EQCM. Corros Sci 44:1443–1456
36. Schmutz P, Landolt D (1999) Electrochemical quartz crystal microbalance study of the transient response of passive Fe-25Cr alloy. Electrochim Acta 45:899–911
37. Takabatake Y, Fushimi K, Nakanishi T, Hasegawa Y (2014) Grain-dependent passivation of iron in sulfuric acid solution. J Electrochem Soc 161(14):C594–C600
38. Yamamoto T, Fushimi K, Miura S, Konno H (2010), Influence of substrate dislocation on passivation of pure iron in pH 8.4 borate buffer solution. J Electrochem Soc 157(7): C231–C237
39. Deng H, Qian P, Sanada N, Yoneya M, Nanjo H (2003) Temperature dependence of surface crystal structures of iron passivated at −400 mV in a borate buffer solution. J Electrochem Soc 150(7):B336–B341
40. Lukac C, Lumsden JB, Smialowska S, Staehle RW (1975) Effects of temperature on the kinetics of passive film growth on iron. J Electrochem Soc 122(12):1571–1579
41. Büchler M, Schmuki P, Böhni H (1998) Iron passivity in borate buffer: formation of a deposit layer and its influence on the semiconducting properties. J Electrochem Soc 145(2):609–614
42. Cáceres L, Soliz A, Vargas T (2016) Potentiodynamic behavior of carbon steel in borate buffer solutions under different hydrodynamic conditions. J Electrochem Soc 163(5): C171–C183

Solar Fuels

S.P.S. Badwal, A.P. Kulkarni, H. Ju and S. Giddey

Abstract Global demand for energy is increasing at a fast rate especially in developing economies such as India, China, and Indonesia with heavy reliance on fossil fuels. The CO_2 levels in the atmosphere have increased to over 400 ppm. This combined with increase in the intensity of other pollutants (NO_x, SO_x, CO, methane, particulate matter, etc.) in the atmosphere is a real concern for the environment. With the major objective of reducing concentration of greenhouse gases and other pollutants and to increase reliability and security of energy supply for a sustainable future, significant progress is being made in the development and deployment of technologies and processes around renewable energy with solar and wind playing a dominant role. However, solar energy is not available in high intensity all around the word and thus there is a need for transporting energy from one place to other. Solar fuels are energy carriers and means of transporting solar energy in the form of easily transportable fuels and these are generated by embedding solar energy in the form of heat or electricity or both in water, CO_2, and fossil fuels. A number of different technologies and processes (electrolytic, solar thermal, solar thermochemical cycles, chemical looping, solar assisted reforming of natural gas, solar assisted coal/biomass gasification, photo-electrochemical, and photo-biological) for the production of major solar fuels (H_2, CO, syngas, methanol, and ammonia) are briefly discussed and reviewed in this chapter.

Keywords Hydrogen · Ammonia · Methanol · Syngas · Dimethyl ether · CO_2 conversion

List of acronyms

BSCF	$Ba_xSr_{1-x}Co_yFe_{1-y}O_{3-\delta}$
CAWE	Carbon assisted water electrolysis
CCS	Carbon capture and storage
CGO	Gadolinia-doped ceria

S.P.S. Badwal (✉) · A.P. Kulkarni · H. Ju · S. Giddey
CSIRO Energy, Private Bag 10, 3169 Clayton South, VIC, Australia
e-mail: Sukhvinder.Badwal@csiro.au

K. Uosaki (ed.), *Electrochemical Science for a Sustainable Society*,
DOI 10.1007/978-3-319-57310-6_10

CNG	Compressed natural gas
CRS	Central receiver systems
CSP	Concentrated solar power
DME	Dimethyl ether
DMR	Dry-methane reforming
F–T	Fischer–Tropsch
GHG	Greenhouse gas
HHV	High heating value
HT	High temperature
ICE	Internal combustion engine
LFR	Linear Fresnel reflector
LHV	Low heating value
LPG	Liquefied petroleum gas
LSC	$La_xS_{1-x}CoO_3$
LSCF	$La_xSr_{1-x}Co_yFe_{1-y}O_{3-\delta}$
LSCM	Chromium doped lanthanum strontium manganite
LSM	Lanthanum strontium manganite ($La_xSr_{1-x}MnO_{3-\delta}$)
LST	Lanthanum-doped strontium titanate
MAWE	Methanol assisted water electrolysis
MCFC	Molten carbonate fuel cell
NG	Natural gas
PAFC	Phosphoric acid fuel cell
PBI	Polybenzoimidazol
PEM	Polymer electrolyte membrane
PT	Parabolic-troughs
PV	Photovoltaic
R&D	Research and development
RT	Room temperature
ScSZ	Scandia-stabilized zirconia
SFCN	$SmFe_{0.7}Cu_{0.3-x}Ni_xO_{3-\delta}$
SMR	Steam-methane reforming
SOE	Solid Oxide Electrolyte
SOFC	Solid oxide fuel cell
YSZ	Yttria stabilized zirconia

1 Introduction

Currently most of our transport, stationary, and industrial energy needs are met by energy carriers such as electricity, coal, syngas, compressed or liquefied natural gas, petrol, diesel, kerosene, and liquefied petroleum gas (LPG) and to a lesser extent by methanol, ethanol, dimethyl ether (DME), and hydrogen. Fossil fuels are the major

source of these energy carriers. Power generation and industrial processes contribute to over 35 billion tons of CO_2 generation per annum now and increasing at an alarming level [1]. With CO_2 levels increasing above 400 ppm in the atmosphere and increase in the emissions of pollutants (NO_x, SO_x, CO, methane, particulate, etc.) there is a real concern about global warming and ill effect of pollutants on human health resulting from poor air quality. A number of different energy solutions, technologies, and strategies are under development to reduce the intensity of greenhouse gas and pollutant emissions which include development of high efficiency energy conversion technologies based on fossil fuels, efficient utilization of resources and increased penetration of renewable energy sources in the overall energy mix for transport, domestic, embedded generation, and large-scale applications. However, as the renewable energy component increases, the energy security and reliability become real issues due to intermittent nature of many renewable energy sources, and the need for energy storage becomes critical. Similarly, and more so in the transport area, new transport technologies such as hybrid, plug-in and electric or hydrogen fuel cell/battery hybrid vehicles are being introduced at an increasing rate and require renewable energy sources for energy/fuel supply, otherwise GHG emissions levels remain high and are only shifted to a different location. Thus a new infrastructure is required for low or zero-emission energy carriers for transition away from fossil fuel-based electricity (electric, plugin vehicles) and liquid fuels (petrol, diesel, kerosene, and LPG for internal combustion engine) for the new horizon transport sector.

As dependency on fossil fuel derived energy carriers cannot continue too long into the future, the mix of energy carrier will change and solar fuels would play an increasingly dominant role. In search for future energy carriers, consideration has to be given not only to cost but also to their impact on environment, sustainable economic growth, public health, and security of energy supply. Hydrogen is emerging as one of the most popular energy carriers. In fact Professor John Bockris was one of the very early proposers of the solar hydrogen economy going as far back as 1970s. The early work of Bockris presented a holistic overview of future energy supply chain based on hydrogen and is a comprehensive introduction to the hydrogen economy with hydrogen being an attractive fuel with its generation coupled to solar energy as the primary energy source [2, 3]. The author had discussed in detail the benefits and drawbacks of hydrogen as a fuel for power generation, technologies for its production, distribution and utilization and economics as compared to conventional sources such as oil, natural gas, and coal.

Currently 60 million tons per annum of hydrogen is produced, mostly from fossil fuels (coal, natural gas, and oil) with only 4% produced via electrolysis of water with renewable energy as the main input. Most of the hydrogen produced is used for ammonia production, in oil refineries for converting crude or heavy oil to lighter fractions) and pharmaceutical and methanol industries with small quantities used in other applications. A very small percentage of total hydrogen production is used in the energy chain. A future scenario for hydrogen as the sustainable future is shown in Fig. 1 where low emission hydrogen is generated from a range of sources.

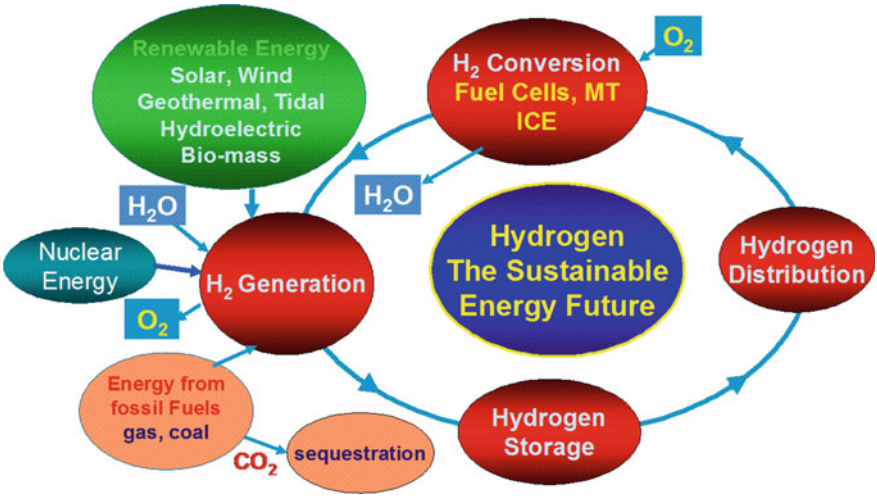

Fig. 1 A future scenario for hydrogen as the sustainable energy storage and transportation media

Other major and potential renewable/solar energy carriers include methanol and ammonia which being liquids at room temperature and under low or mild pressures in comparison to hydrogen, are easy to store and transport. However, over 200 million tons of ammonia and over 80 million tons of methanol is produced per annum mostly from NG and coal as also is the case with hydrogen production. Ammonia is used mainly in the fertilizer, chemical, and explosives industries and methanol is mainly used for chemical production (formaldehyde, acetic acid, methylamines, dimethyl ether, solvents, olefins, etc.) in addition to its use as a transport fuel.

Only a fraction of hydrogen, ammonia or methanol is used as a fuel or an energy carrier, however, there will be increasing emphasis on utilization of renewable energy sources such as solar and wind for production of energy carriers in which renewable energy can be easily stored for extensive periods of time and transported to end use sites. In the sections to follow, solar fuels are defined and a number of technologies currently under development for the production of solar fuels are discussed.

2 Solar Fuels

The incident radiation from the sun on earth has many orders of magnitude higher energy embedded in it than that is required to fulfil all global energy needs. A small fraction of this form of renewable energy can produce fuels in sufficiently large quantities to make an impact on our current and future energy needs as well as for the production of many commodity chemicals (ammonia, methanol, cement,

plastics, fertilizers, pharmaceuticals, etc.). Solar energy is already harnessed for food production, crop drying, solar heating and cooling, hot water production, water distillation and desalination, cooking, and many other processes. However, currently, in the global energy mix, the solar energy contribution to useful energy generation is relatively minor (<1%).

"Solar fuels" is a terminology which refers to the production of fuels using solar energy sources which can store energy and on combustion/conversion/oxidation provide heat for power generation or heat and electricity, e.g., in fuel cells, internal combustion engine or turbines. Often flexibility is required so that these fuels can be easily transported to end use sites. Thus solar fuels are energy storage media and carriers for transporting solar energy as the raw resource from locations with high solar intensity to locations where the solar energy intensity is low. The major aim of a transition towards solar fuels is to reduce GHG intensity and increase reliability and security of energy supply for a sustainable future. Solar fuel production may involve, in addition to water as feed stock, utilization of CO_2 (from chemical industries, power plants and refineries), and embedding solar energy in products from fossil fuels such as carbon (biomass, coal) or NG to generate hydrogen or syngas which can then be used as energy carriers or used for the production of liquid fuels. The solar processes include concentrated solar power plants (CSP) for providing heat for solar fuel generation or electricity via solar photovoltaic (PV), or both heat and electricity. Solar fuels may include H_2, CO, syngas, methane, methanol, formic acid, ammonia, dimethyl ether (DME), and diesel.

A number of different technologies and processes are at various stages of development and include both low (direct water or hydrocarbon assisted water electrolysis) and high temperature electrolysis (water/CO_2 electrolysis); solar thermal (direct water splitting, solar thermochemical cycles, chemical looping); solar assisted reforming (natural gas), solar assisted gasification (coal, biomass); photo-electrochemical; and photo-biological processes. An overview of solar fuels and processes is given in Fig. 2.

Fuels produced by embedding solar heat into carbon-based fuels (via reforming of natural gas or gasification of coal or biomass) consist mainly of hydrogen and carbon monoxide which can be used as precursors to produce methanol or DME, diesel, other liquid fuels, or generate hydrogen by converting CO to CO_2 and H_2 in a water gas shift reactor. Hydrogen formed by a range of processes (using totally renewable energy or through solar assisted fossil fuel reforming/gasification) can be used directly as a fuel or converted to easily transportable fuels such as ammonia (via Haber–Bosch process or methanol in a chemical reactor over a catalyst (Fischer–Tropsch process) [4, 5]. The methanol formed can be used as a fuel or converted to dimethyl ether (CH_3–O–CH_3–) or other liquid fuels as a low emission substitute for diesel in transport vehicles or blended into LPG for domestic cooking. Further information on solar fuels can be found in a number of references [6–11].

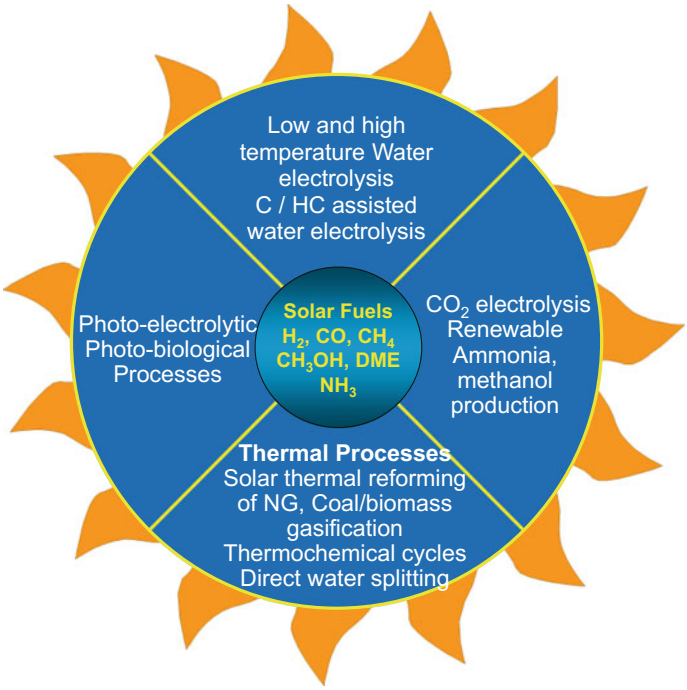

Fig. 2 An overview of solar fuels and processes

3 Solar–Electrochemical Processes

3.1 Low Temperature Electrolytic Processes

A number of technologies are at various stages of development for the production of solar fuels by low temperature electrolytic processes which can be easily integrated with intermittent renewable energy sources especially solar PV. These are discussed in the following sections.

3.1.1 Water Electrolysis

Worldwide around 4% hydrogen is produced from water electrolysis and 96% from fossil fuels (NG, coal, oil). Two main technologies used for low temperature water electrolysis are alkaline solution-based electrolysis and polymer electrolyte membrane (PEM)-based electrolysis. Both these technologies can be coupled with solar PV to provide renewable energy input for hydrogen generation. In PEM systems a proton conducting membrane based on perfluorosulfonic acid (Nafion) or hydrocarbon (polybenzoimidazol—PBI) is used as the electrolyte. In alkaline systems

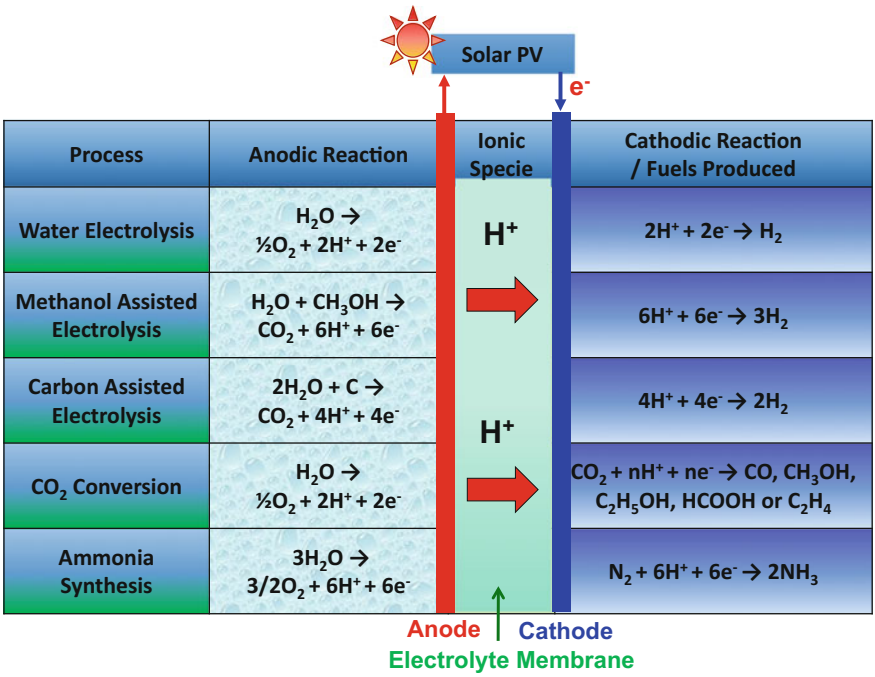

Fig. 3 Schematic of various PEM cells

20–40% KOH or NaOH solution is used as the electrolyte, and a diaphragm based on polymer or composite material is used to keep gases produced separate in the anode and cathode chambers to maintain the efficiency and safety. The electrodes used in alkaline system are Ni-based materials either coated with Pt or Ni for the cathode and with metal oxides (Ni, Co) for the anode. In PEM systems, the cathode is a Pt/C catalyst supported on a carbon paper (or cloth) and anode is Pt/Ir coated on Ti mesh. Figure 3 shows a schematic view of the electrolysis cell and the associated anodic and cathodic reactions for a PEM-based system.

In a PEM electrolysis cell, water supplied to the anode chamber is dissociated into oxygen and protons, and protons transported through the membrane are reduced at the cathode to hydrogen. In alkaline electrolysis, water supplied to the cathode chamber is dissociated into hydrogen and hydroxyl ions, and hydroxyl ions transported through the diaphragm to cathode are converted into oxygen and water. The minimum cell voltage to start electrolysis reaction is 1.48 V, called thermo-neutral voltage. Based on this cell voltage, the theoretical charge required to produce 1 Nm^3 of hydrogen is 2,393 Ah (equivalent to 3.54 kWh) [12]. However, due to various resistive losses (electrolyte membrane, resistance of cell components—electrodes, interconnects, connection wires and contact resistance

Table 1 Performance comparison of PEM and alkaline electrolyzer

Feature	Alkaline	PEM
Technical maturity	Commercial	Early commercial
Electrolyte	KOH solution	Polymer membrane
Current density (A cm^{-2})	0.3–0.5	1–2
Flexibility, min. load	20–40% most systems and some down to 5%	0
Response	Ramp up (min. to max.): 10 min. (10 s new models) Cold start: 30–60 min	Standby to full: <10 s (1 s for best models) Cold start: <10 min
Operating pressure (bars)	2–10	15–30
Max. stack capacity (kW_{ch})	3,000	100
System capital costs ($/$kW_{ch}$)	850	1000–2000
System efficiency (%HHV) (at BOL)	68–77	62–77
Annual degradation (%)	2–4	2–4
System life (years)	10–20 proven	5 proven

kW_{ch} Chemical energy of hydrogen (HHV), *BOL* Beginning of Life [13]

between components) and electrode overpotential losses (due to sluggish hydrogen and oxygen evolution reactions and reactant/products transport), the actual cell voltage for practical hydrogen production rates (current densities) is in the range 1.8–2.2 V. Thus actual power input required for water electrolysis is in the range 4.3–5.3 kWh Nm^{-3} of hydrogen produced.

Both alkaline and PEM electrolysis systems operate at 60–80 °C and produce hydrogen with purity >99.9%. Table 1 compares various features of the alkaline and PEM electrolysis systems [13]. Hydrogen generation by alkaline electrolysis is fully commercialized technology with systems installed in the MW range, however PEM-based system are at an early stage of commercialization with many systems over 100 kW in operation. Figure 4 shows images of a commercial alkaline system (Titan EL from Teledyne Energy Systems) capable of producing 80 Nm^3 h^{-1} hydrogen and a commercial PEM system (SILYZER 200 from Siemens) capable of producing 225 Nm^3 h^{-1} hydrogen [14, 15]. Siemens stack module is rated at 1.25 MW with indicated lifetimes of over 80,000 h and produces hydrogen at 35 bar. Siemens are now looking at the next generation system with much improved efficiency (SILYZER 300) and higher hydrogen output.

The alkaline electrolyzers offer low cost and larger size modules, however, these suffer from issues such as the use of corrosive electrolyte and low current densities. Further, these systems may be somewhat difficult for direct coupling to solar PV and other renewables due to poor load following capability (reactivity) and requirement to maintain a minimum load (~20%). On the other hand PEM systems offer excellent load following capability (for coupling to solar PV) and startup from

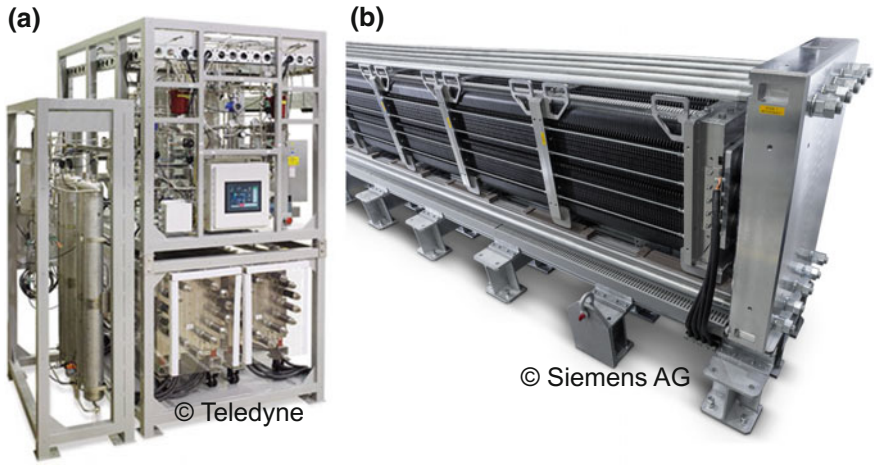

Fig. 4 Pictures of **a** a commercial alkaline system (Titan EL from Teledyne Energy Systems) and **b** a commercial PEM system (SILYZER 200 from Siemens) [14, 15]. Images reproduced with permission from Teledyne and Siemens

zero load condition, but these systems are at present expensive (precious metal catalysts, high cost of membrane and interconnects) and membrane lifetime is an issue. The average solar to electricity efficiencies of 14.5% have been demonstrated by the commercial solar PV systems, thus making it possible to achieve overall solar to hydrogen efficiency around 10% (based on 70% HHV electrolyzer system efficiency) [8].

3.1.2 Carbon Assisted Water Electrolysis

Hydrogen is produced mainly by NG reforming and coal gasification involving a number of high temperature (>500 °C) reactors. Following fuel cleaning, the entire process involves reforming/gasification, water gas shift reaction of products with steam to convert CO to CO_2 and more hydrogen, and finally hydrogen separation from CO_2 produced in the process. While simpler in terms of process steps, water electrolysis for hydrogen production is energy intensive requiring electric input of more than 5 kWh Nm^{-3} of hydrogen for commercial systems. However, if chemical energy of carbon can be used in water electrolysis, the electric energy input can be substantially reduced for hydrogen generation. In a carbon assisted water electrolysis (CAWE), carbon (coal, biomass) slurry is fed to the anodic chamber of the cell. Carbon participates in the anodic reaction to produce protons and CO_2 and protons transported through the membrane to cathode form hydrogen. Figure 3 shows the associated electrochemical reactions in the PEM-based electrolysis process. The participation of carbon in the electrolysis process reduces the thermo-neutral voltage of the process from 1.48 to 0.45 V, thus reducing the

electric input required for the electrolysis process by 66%. An overall energy balance performed on the CAWE has demonstrated that the hydrogen produced from the CAWE at practical flow rates, will require only 40% electric input with 60% contributed by the carbon in the form of chemical energy [16]. This type of system thus allows the hydrogen generation and CO_2 separation process in a single low temperature reactor as opposed to multiple reactors operating at high temperatures to produce hydrogen from fossil fuels. Furthermore, the system allows for coupling with a solar PV system of less than half the size compared to the one required for a normal water electrolysis system.

Carbon assisted electrolysis technology, although having great potential, is at an early R&D stage with a number of technical issues still to be resolved before the technology can be commercialized. Most of the research has concentrated on aqueous electrolyte (H_2SO_4, NaOH, H_3PO_4) systems in a single compartment cell or using a separator (glassy fiber or proton conducting membrane) between the electrode chambers. Coal slurries prepared from various types of coals have been investigated, however, the carbon anodic reaction has been observed to be very sluggish at the operating temperatures up to 100 °C with current densities of around 10 mA cm^{-2} achieved. With addition of Fe^{2+}/Fe^{3+} species, current densities of up to 100 mA cm^{-2} have been achieved at higher temperature (180 °C) and higher pressure (150 psi) [17]. The mechanism proposed here is that the presence of iron species (Fe^{3+}) assists in the oxidation of carbon ($C + 2H_2O + 4Fe^{3+} \rightarrow 4Fe^{2+} + 4H^+ + CO_2$) at voltages lower than required for oxygen evolution. The Fe^{2+} species formed in the above reaction are then oxidized as an anodic reaction ($Fe^{2+} \rightarrow Fe^{3+} + e^-$).

3.1.3 Methanol Assisted Water Electrolysis

Methanol is a high energy density liquid fuel (12.6 wt% H_2) and can be easily transported using existing infrastructure. Further, if hydrogen can be extracted from methanol efficiently, this can be a good source for on-site on-demand hydrogen generation. Methanol mixed with water supplied to the anodic chamber of the electrolysis cell results in a significant drop in the required cell voltages for electrolysis, similar to the carbon assisted electrolysis discussed in Sect. 3.1.2. In this case the minimum cell voltage required for hydrogen production drops from thermo-neutral voltage of 1.48 V for conventional water electrolysis to 0.22 V for methanol assisted electrolysis. Figure 3 schematically shows the respective anodic and cathodic reactions in a PEM type system. The net reaction is the formation of carbon dioxide in the anode chamber and hydrogen in the cathode chamber. The practical cell voltages to produce reasonable current densities (hydrogen flow rate) due to various voltage losses in the cell are observed to be 0.8–1 V. Thus power consumption in the methanol assisted water electrolysis (MAWE) cell is expected to be 1.9–2.4 kWh Nm^{-3} (Theoretical value: 0.53 kWh Nm^{-3}) of hydrogen produced, which represents over 55% savings on electric input required for conventional water electrolysis.

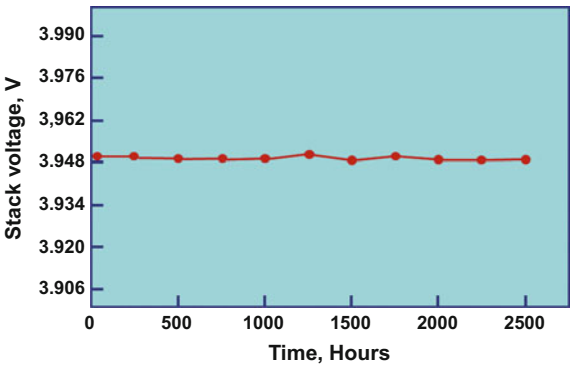

Fig. 5 Long-term performance of methanol assisted 5-cell PEM-based electrolysis stack operated at 1 A cm^{-2}, 80 °C [18]

Methanol assisted electrolysis process development is in the R&D phase. Several investigations have been reported in the literature on PEM-based electrolyte cells typically with Pt–Ru/C as the anode catalyst and Pt/C as the cathode catalyst. The variables studied include the effect of molar concentration of methanol solution (1–10 M), cell temperature (RT to 120 °C), and the use of alternative anode catalysts on cell performance, hydrogen production rates and cell stability. Figure 5 shows the performance of a 5-cell stack (consisting of Pt catalyzed 50 cm^2 active area cells and the largest system tested so far) that was operated at 1 A cm^{-2} current density for 2500 h with negligible change in the stack voltage (3.95 V) [18]. The stack produced H_2 gas flow rate of 102 L h^{-1} at 50 psi pressure (4 M methanol at 80 °C). This corresponds to an energy consumption of 1.89 kWh Nm^{-3} and shows about 60% saving in electric energy input to the electrolyzer (60% smaller size of the solar PV coupled to the MAWE system). Although significant progress has been made in the technology development, further studies are required to reduce methanol cross-over to cathode that results in cathode catalyst poisoning and loss of methanol, systems design, life time demonstration, technology up-scaling and economic viability of the entire process from methanol production to hydrogen generation. In terms of reducing CO_2 emissions, methanol obtained from biomass is more attractive for the MAWE process for hydrogen generation, although it may require considerable advances in small-scale gas to liquid process to make such an approach economically viable.

3.1.4 Electro-Catalytic CO_2 Conversion

The electro-catalytic reduction of CO_2 is carried out at low temperatures by co-electrolysis of water and CO_2. Both PEM-based and alkaline systems are being investigated. In the case of PEM, the water is supplied to the anode to produce oxygen and protons similar to the water electrolysis process, however, the protons transported through the PEM are made to react over a catalyst with CO_2 supplied to the cathode chamber to form value-added fuels. In an alkaline system, CO_2 and

water, both supplied to the cathode are reduced to hydroxyl ions and value-added fuels, and hydroxyl ions transported through the diaphragm are converted to oxygen and water similar to the alkaline electrolysis system. Figure 3 shows schematically the anodic and cathodic reactions in the case of a PEM system. Hydrogen formation and CO_2 conversion are competing reactions in both PEM and alkaline systems and therefore cathode catalyst plays a crucial role in the selectivity of the reaction and products formed. Moreover, kinetically much higher cathodic overpotentials are required to drive the electro-catalytic conversion of CO_2 resulting in poor Faradaic efficiencies for hydrocarbon fuel generation especially at high current densities. Various types of catalysts, including metal oxides, metal complexes, and transition metals are being investigated and fuels produced are methanol, CO, methane, ethylene or formic acid or a combination of these. Copper metal-based electro-catalyst has been reported to favor CO_2 reduction to hydrocarbons, while copper and other oxides (Ru) have been found to favor methanol formation [8]. The production of syngas has been demonstrated by Delacourt et al. [19] in a slightly modified design of the PEM electrolysis cell where membrane and the cathode catalyst layer (silver-based) are kept separate by a potassium bicarbonate buffer solution that enhances the selectivity for CO_2 reduction to CO in preference to hydrogen evolution.

This technology is at an early R&D stage and several issues need to be resolved for commercial realization of low temperature CO_2 reduction process to form value-added fuels. These issues are mainly related to poor CO_2 conversion rates to value-added fuels, low Faradaic efficiencies due to competing hydrogen evolution reaction and high overvoltage losses in the cell due to poor catalytic activity and catalyst poisoning over time. Although the motivation is to store renewable energy, the overall benefits (cost, energy efficiency) of coupling such a technology to solar PV has to be justified for converting an already valuable fuel (hydrogen) and almost freely available CO_2 to another fuel.

3.1.5 Ammonia Production by Electrochemical Routes

Ammonia is commercially produced by the highly energy intensive Haber–Bosch process (~500 °C, 200–300 bar), and is mainly utilized in the production of fertilizers and explosives. Ammonia possesses high energy density (3.4 kWh L^{-1} for liquid ammonia and 17.6 wt% H_2 compared to 2.36 kWh L^{-1} for liquid H_2), and thus can be used for energy storage and transport especially if produced from renewable sources of energy. In a low temperature electrochemical ammonia synthesis process, hydrogen can be sourced from natural gas reforming (or coal gasification) and supplied to the electrochemical cell. In a totally renewable ammonia production system, hydrogen can be produced in situ by electrolysis of water or from renewable fuels such as ethanol or methanol with electric power provided by solar PV. Both liquid as well as solid electrolyte systems operating

near room temperature have been investigated for ammonia synthesis. In liquid electrolytes organic solvents (lithium perchlorate in tetrahydrofuran with ethanol as the hydrogen source), ionic liquids, and aqueous solutions (lithium sulfate or lithium perchlorate in sulfuric acid with methanol as source of hydrogen) are the common electrolytes investigated. The current efficiencies of up to 58% are reported at 60 bar pressure of nitrogen supplied to the cathode, however, ammonia yield has been found to be poor, in the range 10^{-10}–10^{-9} mol cm^{-2} s^{-1} [4, 20]. In a PEM-based system where hydrogen is produced in situ, water supplied to the anode chamber is electrolyzed to protons and oxygen, and protons transported through the membrane are made to react at the cathode with nitrogen supplied to the cathode chamber. Figure 3 shows schematically the anodic and cathodic reactions associated with the process. In most of the PEM-based investigations, Nafion has been used as the proton conducting membrane, and cathode catalysts investigated are Ru on carbon felt, $SmFe_{0.7}Cu_{0.3-x}Ni_xO_{3-\delta}$ (SFCN), $Sm_{1.5}Sr_{0.5}MO_4$ (M is Ni, Co or Fe), $SmBaCuMO_{5+\delta}$ (M is Ni, Co or Fe) and Pd-based bi-metallic catalysts at temperatures up to 90 °C [4]. The peak synthesis rates achieved with PEM-based system are 1.13×10^{-8} mol cm^{-2} s^{-1} by Xu et al. [21] using humidified hydrogen supplied to the anode (SFCN as catalyst) and dry nitrogen to the cathode. The current efficiency achieved from this cell was 90% at 2 V with cell operating at 80 °C.

Ammonia produced from solar PV coupled to an electrochemical ammonia synthesis reactor is very attractive technology for renewable energy storage and transport in the form of liquid ammonia; however, the synthesis rates and power to ammonia conversion efficiencies (current efficiency) are significantly lower for a commercial system. Further, the stability of acidic polymer membranes in the presence of ammonia is an issue and new membranes tolerant to ammonia are required.

3.1.6 Ammonia Electrolysis

The two main methods of obtaining hydrogen from ammonia are ammonia cracking and ammonia electrolysis. Ammonia cracking that occurs at temperatures above 400 °C over a catalyst (usually Ru-based) is itself an energy intensive process with a significant part of the energy (at least 15% of the energy of hydrogen produced) consumed within this process. Low temperature ammonia electrolysis on the other hand if coupled to solar PV can be an attractive proposition for hydrogen generation. Two basic technologies for ammonia electrolysis are liquid ammonia electrolysis and ammonia electrolysis in alkaline solution, and later being more developed and most investigated technology. The main application of the ammonia electrolysis at present is for removing ammonia from the waste water and industrial effluents, however, technology can be exploited for hydrogen generation for energy purposes. In a typical ammonia electrolysis process the reactions involved are as follows.

$$\text{At anode:} \quad 2NH_3 + 6OH^- \rightarrow N_2 + 6H_2O + 6e^- \tag{1}$$

$$\text{At cathode:} \quad 6H_2O + 6e^- \rightarrow 3H_2 + 6OH^- \tag{2}$$

$$\text{Overall reaction:} \quad 2NH_3 \rightarrow N_2 + 3H_2 \tag{3}$$

The reversible voltage for reaction (3) is 0.059 V compared to 1.23 V for the electrolysis of water, however, the actual cell voltages where ammonia electrolysis starts is ~0.3 V, thus requiring electric power input 8 kWh kg^{-1} of hydrogen produced [22]. Noble metal catalysts have been investigated for the anode electrode and the most effective catalyst has been found to be Pt–Ir due to its low affinity for the nitrogen adsorption, which is the main cause of poisoning of the catalyst. The technology is still at early stage of development with only small cells and stacks tested so far. The largest stack tested is a 9 cell stack with 4 cm^2 active area of each cell [22]. The cells consisted of Pt–Ir alloy electroplated on carbon paper as both anode and cathode electrodes separated by a proprietary Teflon membrane. The anode side of the cells was supplied with 1 M ammonium hydroxide in 1 M KOH solution and cathode side was filled with 1 M KOH solution. The stack was operated at 4.5 A current (125 mA cm^{-2} current density) and produced a current efficiency of 97.55%. The stack was found to utilize 17.36 kWh kg^{-1} at 25 °C and 15.36 kWh kg^{-1} at 55 °C. Although the technology is promising in terms of hydrogen production from ammonia at distributed sites using solar PV, the overall economic viability of the technology has not been demonstrated (ammonia synthesis itself is an energy intensive process). In addition, technical issues such as process stability issues with the anode catalyst poisoning due to the reaction intermediates and nitrogen adsorption on the catalyst resulting in poor cell performance, technology up-scaling and life time demonstration are required to be addressed. In addition, logistics of hydrogen versus ammonia production and reconversion to hydrogen, even with considerably reduced renewable energy footprint, need to be justified.

3.2 High Temperature Electrolytic Processes

High temperature (HT) electrolytic reactors are based on oxygen ion (O^{2-}) or a proton conducting dense ceramic electrolyte membrane and operate between 400 and 1000 °C. There is a small activity involving alkaline electrolytic systems in which a molten alkaline electrolyte (e.g., NaOH/KOH with OH^- conducting specie) is held in a porous ceramic matrix and typical operating temperature is between 250 and 300 °C [23].

Amongst these systems, the solid oxide electrolytic reactors, in particularly those based on oxygen ion conducting electrolytes have been more widely studied with the established solid oxide fuel cell (SOFC) technology as the base for material selection. The key advantages of high temperature systems over low temperature

electrochemical reactors are faster reaction kinetics leading to high yield and conversion rates, high feedstock impurity tolerance, and applicability of cheaper metal or oxide catalysts as compared to precious metals required in low temperature systems. Furthermore high temperature operation enables embedding solar heat or waste heat from industrial processes to reduce the electrical energy input. In principle such systems are capable of producing several different chemicals, however, the main solar fuels under consideration are; hydrogen, syngas (mixture of H_2 and CO), methanol and ammonia. In the following sections, the HT electrolytic processes for production of these fuels have been discussed.

3.2.1 High Temperature Steam Electrolysis

The concepts for using solid electrolyte membrane reactors for various electrolytic processes, including hydrogen generation, were demonstrated over four decades ago in late 1970s [24]. With hydrogen being considered as a key energy carrier for a future low carbon economy, the research and development has increased in recent years especially where the electrolysis process is integrated with solar energy.

The basic principle of HT electrolytic membrane reactor and associated reactions for hydrogen production are shown in Fig. 6. The typical electrolysis cell consists of a solid state electrolyte membrane sandwiched between two electrodes; anode and cathode. In oxygen ion conducting electrolyte cells, under influence of an electric field, water (steam) molecule on the cathode side (−ve electrode) splits into hydrogen and oxygen ions. The oxygen ions thus generated migrate through the electrolyte to recombine at the anode (+ve electrode) to produce pure oxygen. The overall reaction is: $2H_2O \rightarrow 2H_2 + O_2$.

In HT electrolytic cells with the proton conducting electrolyte membranes, the water molecules split to form protons, which migrate through the electrolyte in a similar fashion as in low temperature water electrolysis cells described in Sect. 3.1.1. The typical operating temperature is 400–800 °C. This high operating temperature is beneficial in that it allows heat to be embedded in the electrolysis process thus reducing the electrical energy input. Figure 7 shows thermodynamic energy requirements as a function of temperature for electrolytic water splitting. The total energy input required increases only slightly; however, the electrical input is significantly reduced with increasing temperature as a part of the energy required comes from the heat.

A small part of heat required for endothermic HT electrolysis process may come from Joule heating of the cell due to passage of electric current and rest can be supplied externally by solar concentrators, or as waste heat from industrial processes or nuclear power plants. Based on thermodynamics, the minimum electrical energy input required for water electrolysis at 800 °C has been estimated to be about 2.32 kWh per Nm^3 of H_2 produced as compared to 3.07 kWh per Nm^3 total energy required leading to potentially 25% savings in electrical energy input due to embedding of solar heat [23, 24].

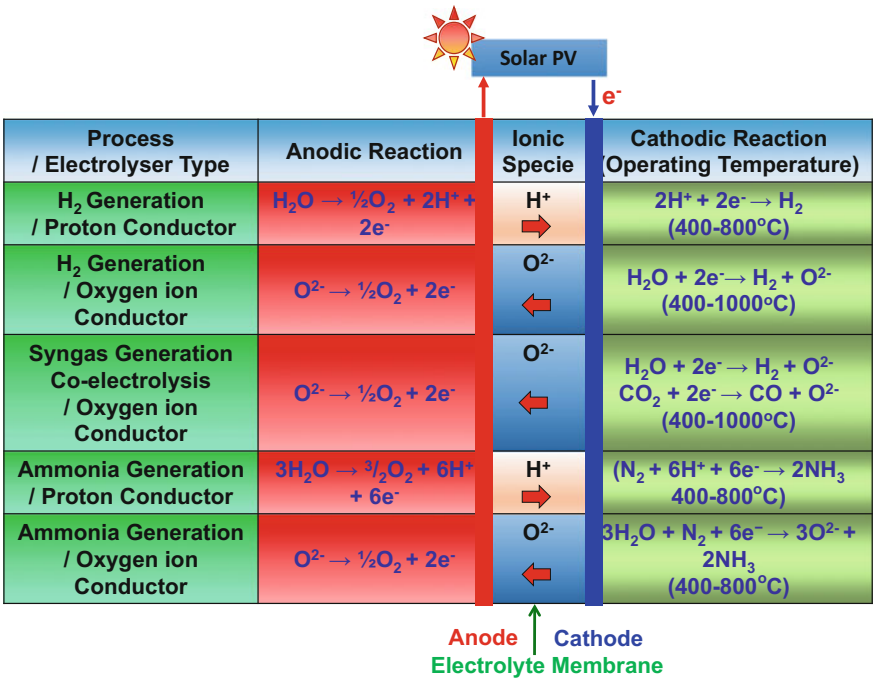

Fig. 6 High temperature electrolytic processes for the production of solar fuels

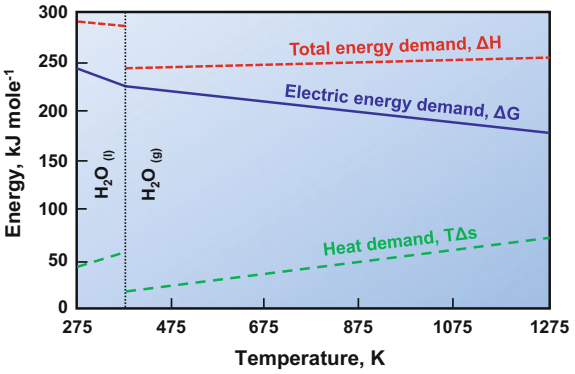

Fig. 7 Thermodynamic energy requirements as a function of temperature for electrolytic water splitting [60]

Typical materials used in HT electrolysis processes are similar to those used in Solid Oxide Fuel Cells (SOFCs). Oxygen ion conducting 8 mol% yttria doped zirconia (8YSZ) electrolyte is by far the most preferred material for HT electrolysis cells. Other variants include scandia doped zirconia and rare earth oxide doped ceria. The electrolyte is almost pure ionic conductor under cell operating conditions with an ionic conductivity of 8YSZ of about 0.045 S cm^{-1} at 800 °C [25].

The anode (oxygen evolution electrode) may be a ceramic perovskite (e.g., $La_xSr_{1-x}MnO_{3-\delta}$ (LSM) or mixed electronic ionic conducting $La_xSr_{1-x}Co_yFe_{1-y}O_{3-\delta}$ (LSCF), $Ba_xSr_{1-x}Co_yFe_{1-y}O_{3-\delta}$ (BSCF) and $La_xS_{1-x}CoO_3$ (LSC). To improve the electrode performance and adhesion to electrolyte, a small amount of electrolyte may be added to the electrode [25].

For cathode (steam side electrode), a metal ceramic composite of Ni and YSZ (Ni-YSZ) is the most widely reported electrode. In this electrode metallic Ni provides path of electronic conduction and YSZ acts as ion conducting phase. NiO is usually used a starting material along with YSZ, and reduced in situ to form metal during cell operation. The metallic Ni is a proven electro-catalyst and excellent electronic conductor and shows minimum phase interaction with YSZ electrolyte. One of the major drawbacks of such an electrode is its poor redox stability in the presence of steam. As reduced Ni metal is prone to oxidation, usually additional H_2 needs to be provided along with steam to keep Ni in reduced state. The H_2 produced in reactor itself can be used to maintain Ni in reduced state by recirculation; however, this not only adds to system complexity but also poses a significant challenge in coupling such reactors with solar energy which is intermittent in nature. To mitigate issues related to redox stability and thermal cycling, significant efforts are being made to develop alterative electrodes such as redox-stable all ceramic electrodes [26].

Besides, oxygen ion conducting electrolytes, proton conducting materials such as trivalent-ion (Nd^{3+}, Y^{3+}, Yb^{3+}, La^{3+}, etc.) doped $BaCeO_3$, $SrCeO_3$, and $BaZrO_3$ have been trialed for application in HT electrolysis cells [4, 23]. The typical oxygen evolution electrodes may be similar to those used for oxygen ion conducting electrolyte cells, while steam electrodes could be a cermet composite of Ni with ceramic materials same as the electrolyte. These cells generally are operated at relatively lower temperatures; 650 °C as opposed to 800–1000 °C typically required for YSZ-based cells, however, lower proton conductivity at operating temperature (in the order of 10^{-3} S cm^{-1}) and poor materials stability compared to YSZ remains key issues.

For technology up-scaling and commercialization, two geometric configurations have been considered: planar cells where the electrolyte is in form of flat plates, and tubular cells where the electrolyte is shaped in the form of dense ceramic tubes. Typical electrolyte fabrication methods used are tape casting, isostatic pressing, and ceramic extrusion. Another configuration, so called anode supported cells where the anode is fabricated first using techniques such as extrusion, tape casting, dry freezing, or isostatic pressing followed by deposition of thin layers of electrolyte and cathode materials [25]. Such geometry offers minimal ohmic resistance due to the use of a thin electrolyte thereby improving current densities, and hydrogen production rates. However, lower mechanical strength of the anode and its lower redox stability limits the application of such a design for HT electrolyzer coupled to intermittent energy sources.

Most of the HT electrolysis cells operate at the temperatures of 800 °C with typical current densities varying from 0.6 to 1 A cm^{-2} at voltages from 1.3 to 1.7 V for YSZ electrolyte supported cells, and up to 1.5–2 A cm^{-2} for anode supported

cells [23, 26]. The Faradaic efficiency of such cells is near 100% as electrolyte is almost pure ionic conductor. The conversion efficiencies depend upon reactors designs, steam flow rate, and other process conditions including operating pressures.

While there are no commercially available HT electrolyzers at present, multi-cell stacks up to 15 kW have been tested [12]. Key issues in the development of HT electrolysis cells are relatively faster materials degradation rates compared to SOFCs, factors such as delamination and phase degradation at cathode/electrolyte interface, and degradation of anode microstructure due to redox cycling. Lowest degradation rate reported for YSZ-based cell with Ni-YSZ cathode under practical operating conditions is ~3.8% (40 mV) per 1000 h of operation at current density of 1 A cm^{-2} over test period of 9000 h at 850 °C, which is still very high for practical systems [26]. Several reports have performed techno-economic analysis of overall system for the production of hydrogen indicating prices in range of \$1.6–5.0 kg^{-1} H_2; however, actual demonstration of such plant at commercial scale is required to validate the costing models [23, 27]. Further, integration of such system with solar energy sources needs to be factored in for accurate cost estimation.

3.2.2 Carbon and Hydrocarbon Assisted Steam Electrolysis

As coal and hydrocarbon-based fuels have an important place in the future energy mix at least over next few decades, technologies are being sought for the use of such fuels in an efficient and clean manner. Integration of hydrocarbons and solid carbon in generation of hydrogen using electrolytic processes is one such approach where the chemical energy of carbon or hydrocarbon is used to reduce the electric energy input required for water electrolysis. The process theoretically requires less than 66% of the electricity (Sect. 3.1.2) as discussed earlier and in combination with HT operation the overall energy input can be significantly reduced using HT carbon/hydrocarbon assisted water electrolysis process. However, there are serious challenges, as mentioned in the previous section, in coupling such reactors with solar energy, being intermittent in nature, providing both heat and electricity components.

Figure 8 shows schematic representation of carbon/hydrocarbon assisted HT electrolysis. The solid carbon fuel or methane is supplied to the anode and steam is supplied to the cathode. The oxygen ions formed by splitting the steam on cathode side travel via electrolyte and reacts with the solid carbon particles or methane in the anode chamber to form CO or CO + H_2. Overall reaction mechanism is complex as further electrochemical reactions of CO and H_2 with O^{2-} can lead to formation of CO_2 and water. The CO_2 formed in situ can also react with solid carbon to form more CO via the Boudouard reaction. Whether solid carbon or CO participates in the electrochemical reactions, the voltage required for electrolysis can significantly reduce from 1.21 V to about 0.2–0.4 V depending on the H_2/H_2O ratio in the cathode chamber and CO/CO_2 ratio in anode chamber, and operating

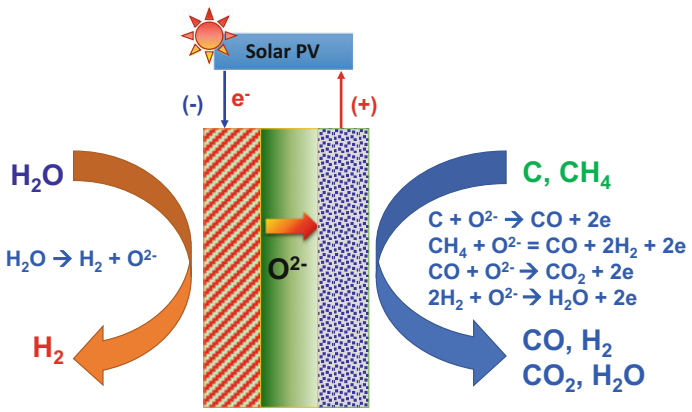

Fig. 8 A schematic representation of carbon/hydrocarbon assisted HT electrolysis

conditions. Reduction in the electrolysis voltage from 1.3 to 0.4 V has been demonstrated practically [28].

The technology is at early stage of development, and is limited to lab scale studies. Materials used are same as those described for HT electrolysis in Sect. 3.2.1. Based on some preliminary lab results combined with modeling studies, it has been proposed that current densities in excess of 700 mA cm^{-2} could be achieved with a carbon fuel utilization rate of over 85% using packed bed of carbon fuel in HT elecrolyzer at voltages well below the thermo-neutral voltage for steam electrolysis alone [29]. However, solid fuel feed for a continuous operation, delivery of solid fuel to the electrode/electrolyte interface, impurities in feed stock and their influence on cell degradation are some of the critical challenges which must be resolved for the technology to be successfully deployed.

3.2.3 Co-electrolysis of Steam and CO_2

Co-electrolysis of water (steam) and CO_2 to generate synthetic fuels using HT electrolyzers is one of the increasingly researched topic over the past few years. Although the concept was proposed and demonstrated in late 1970 s, the recent advances in solar PV and ionic technologies have accelerated research in this area [30]. This process can effectively convert waste CO_2 from industrial processes into an energy carrier and storage media for storing renewable energy. The process is based on simultaneous decomposition of CO_2 and water at high temperatures, embedding thermal energy from concentrated solar or waste heat from industrial processes. The embedding of heat has the potential to further boost the process efficiency considering that the conversion of solar radiations into heat is more efficient than its conversion to electrical energy [31].

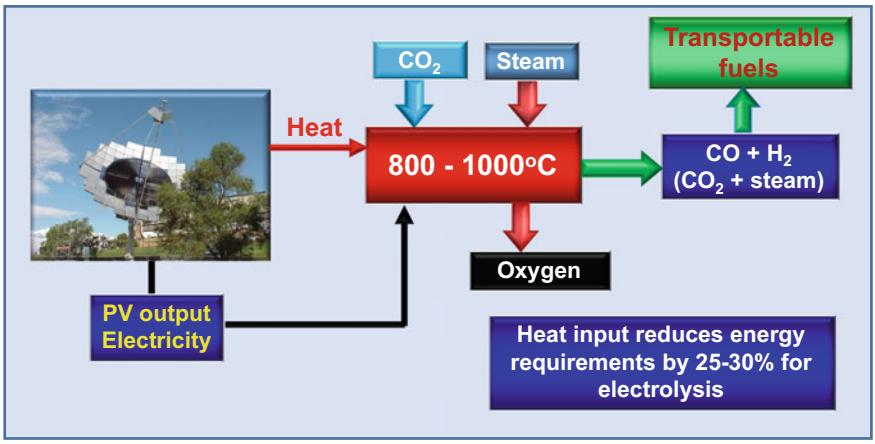

Fig. 9 A schematic representation of steam/CO_2 co-electrolysis system to generate solar fuels with a solar thermal concentrator providing both heat and electricity to reduce electric energy input

The low temperature reactors for such processes are usually limited by the low product yield, sluggish process kinetics, and complex process chemistry while HT systems have faster reaction kinetics and therefore can effectively break down stable molecules such as CO_2 with high conversion rates. The basic operating principle for such reactors is similar to HT water electrolysis with only difference being additional CO_2 is supplied to the cathode chamber along with steam as shown in Fig. 6.

The major product of HT co-electrolysis is syngas with H_2 to CO ratio depending on steam/CO_2 ratio, reaction conditions, and electrode materials. The syngas can be fed to conventional Fischer–Tropsch (F–T) catalytic reactors to form liquid hydrocarbons. A schematic representation of such system is showed in Fig. 9 with a typical solar thermal concentrator providing both heat and electricity (Sect. 3.2.5). Several studies report the electrical efficiency of such a process up to 70%, and the cost of synthetic liquid hydrocarbon fuels (diesel, gasoline, DME) with co-electrolysis and F–T reactors estimated to be around US$0.4–3.0 per liter [23, 32].

The typical anode and cathode materials used for co-electrolysis are similar to HT water electrolysis; however, in recent years more specifically tailored cathodes for CO_2 reductions are being investigated as an alternative to state of the art Ni-YSZ cathode. These includes perovskites such as chromium doped lanthanum strontium manganite (LSCM), and lanthanum-doped strontium titanate (LST) which can be infiltrated with various catalysts selective to CO_2 splitting to improve conversion rates [23, 31].

Key challenges to further the technology are; electrode delamination from the electrolyte at high current densities, phase degradation at oxygen evolution electrode and redox stability of Ni-YSZ cermet cathode. For larger stacks with a number of cells connected, issues related to thermal cycling as well thermal

management during operation needs to be addressed. Compared to SOFCs, such challenges are more severe for these electrochemical reactors due to more frequent thermal cycling and variable electrical loadings expected from intermittent solar energy sources. Nevertheless, a number of commercial outfits (e.g., Sunfire GmBH-Audi consortium in Germany, New CO_2 Fuels Ltd. in Israel, and Dioxide Materials LLC and Ceramtec in USA) are already working in this space to scale up and commercialize the technology.

3.2.4 Ammonia Production by Electrochemical Routes

Ammonia is one of the high energy density fuels with substantial infrastructure and know-how already in place for the transportation, storage, and utilization as discussed earlier in Sect. 3.1.5. The synthesis of ammonia in high temperature solid state membrane reactors can be based either on oxygen ion conductor electrolytes or proton conductors and again heat can be embedded into the process to reduce electrical energy input. In oxygen ion conducting membrane-based reactors, the mixture of nitrogen and steam is fed to cathode side and oxygen evolution takes place on the anode side. The overall reaction taking place is given by:

$$6H_2O + 2N_2 \rightarrow 4NH_3 + 3O_2 \quad (4)$$

The operating temperature of between 400 and 500 °C is desired to maximize ammonia synthesis rates and to avoid decomposition of ammonia formed in the reactor. However, the conductivity of oxygen ion conducing electrolytes is very low (of the order of 0.001 S cm^{-1}) at these temperatures, thus such reactors have been operated at temperatures up to 780 °C [4, 33]. To compensate for the lower ionic conductivity thinner electrolytes may be used, however, fabrication of crack free thin film electrolytes is often not cost effective and maintaining structural stability of thin film electrolyte during thermal cycling of the reactors is challenging. Very few studies on NH_3 synthesis using oxygen ion conducting electrolytes have been reported to date with synthesis rates in the order of 1×10^{-10} to 10^{-11} mol cm^{-2} s^{-1} using YSZ electrolyte and Ru catalyst along with Pd as an electrode and using steam and N_2.

The proton conducting ceramic electrolytes have been more widely investigated for this application. In proton conducting electrolyte-based reactors, steam or hydrogen is supplied to the anode side and nitrogen is supplied to cathode side. Protons migrate to combine with nitrogen on the cathode side to form NH_3 as shown in Fig. 6. It is believed that hydrogen in the form of protons is more reactive than gaseous hydrogen and reaction kinetics substantially faster due to higher operating temperatures in the range of 400–750 °C. A number of proton conducting electrolytes including perovskites (A-site doped $SrZrO_3$ and $SrCeO_3$) and oxides with the fluorite structure (e.g., doped ceria) have been investigated for synthesis of ammonia in HT electrochemical reactors. The electrode materials used in these studies were porous Ag or Ag–Pd composites [4, 33]. The NH_3 synthesis rates in

the range of about 1×10^{-9} to 8×10^{-9} mol cm^{-2} s^{-1} have been reported at an ambient pressure in the temperature range of 400–750 °C. Due to relatively lower synthesis rates, limited systematic studies on the tailoring of electrode materials, and fabrication issues with the electrolyte, the technology is far from commercialization at this stage.

3.2.5 Integration of Heat into High Temperature Electrochemical Reactors

One of the major advantages of high temperature electrochemical processes over the low temperature processes for generation of solar fuels is the ability of the high temperature reactors to incorporate heat to reduce the electrical energy input. The heat energy from solar radiation can be incorporated into these systems either by using a separate solar thermal concentrator in addition to photovoltaic cells or using a spectral beam splitting method. In spectral beam splitting method, the solar radiation is split into two components using an optical filter; first component (shorter wavelengths) is fed to photovoltaic cells to generate electricity and other component (longer wavelengths) is fed to the HT electrolyzer as heat [34, 35]. The heat can be transferred using light guide and temperatures up to 1,100 °C can be achieved. The conversion efficiencies of such combined process can be up to 35% which is significantly higher than current PV systems [34, 35]. Moreover, the fuels generated can be stored in the form of liquid or gaseous fuels and used in fuel cells or other energy conversion technologies as and when required.

4 Solar Thermal Processes

The concentrated solar radiation can be converted into power or chemicals. The main solar thermal processes being explored are concentrated solar power (CSP), thermolysis, thermochemical cycles, and solar assisted fossil fuel reforming. These processes require the collection of solar radiation from a large area on to a smaller area where a heat absorbing fluid/reactor is placed to raise its temperature to required value for carrying out one of the above processes. The reactor temperature required for the process to sustain varies in the range 350–2,000 °C and the main feedstock used are water, CO_2, ammonia, biomass, and/or fossil fuels (NG, coal, oil). The thermal energy of the sun this way is used to generate steam or heat CO_2, air or a fluid for power generation (CSP); thermal splitting of steam, CO_2 or methane to hydrogen/CO (thermolysis); thermochemical cycles for hydrogen generation or fossil fuel reforming/gasification by embedding solar heat to produce syngas and liquid fuels. Here the processes that require water and/or CO_2 as the only feedstock can be considered as fully renewable systems while the processes where fossil fuels are used as feedstock can be considered as hybrid (RE-fossil fuel) systems [8, 9, 36–38]. Hybrid solar thermal processes can also be integrated to CO_2

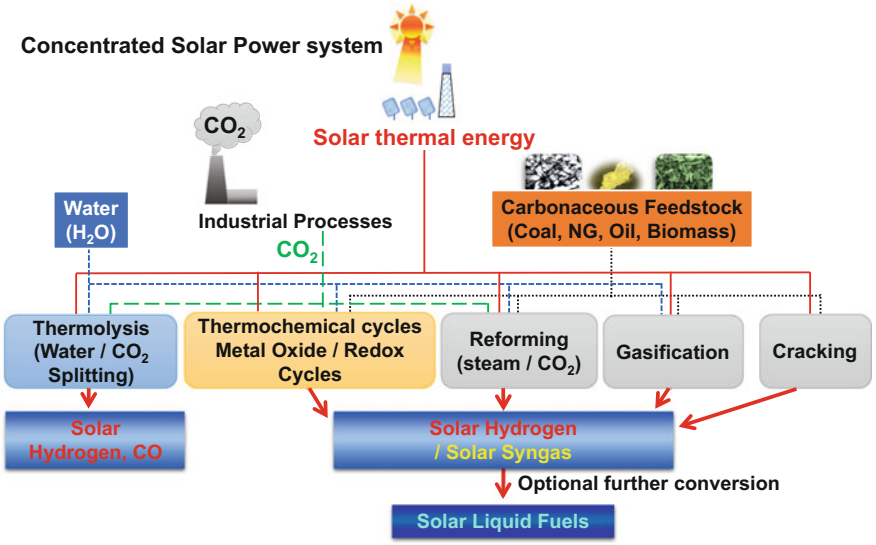

Fig. 10 Classification of solar thermal process via the CSP for producing solar fuels

capture and storage (CCS) for CO_2 free fuels and chemicals [7]. Figure 10 shows a flow chart of various solar thermal driven processes for power and chemicals generation. A detailed description of each of these technologies is given in the following sections.

4.1 Solar Thermal Concentrating Systems

Concentrating solar plants involve mirrors to direct and concentrate solar radiations on to a smaller area (or focal point) to raise temperature of a heat transfer fluid (water, CO_2, oil or molten salt), which is then utilized in a turbine or engine to generate electricity. Solar concentrators are also used for the production of solar fuels by various solar thermal processes briefly mentioned above and discussed in more detail in the sections below. There are four types of concentrating solar technologies: parabolic trough systems, linear Fresnel reflectors (LFR), solar dishes, and solar towers [7, 36].

Parabolic trough system, which is the most deployed system worldwide, consists of parallel rows of parabolic mirrors and tubes. The tubes carrying heat transfer fluid are placed at the focal point of mirrors running along the length of the mirrors. A single axis tracking system allows mirrors to track the sun during the day and continue heating the fluid circulating in the tubes. Steam is generated either directly in the tubes and fed to the power generation turbine or by using the heat transfer fluid in the heat exchanger, and then fed to the power generation turbine. In a linear

Fresnel reflector system, flat or slightly curved mirrors are mounted on trackers to reflect sunlight on to the fluid carrying tubes/receivers fixed in space above the mirrors. In both concentrated solar technologies discussed above, the achievable temperature is typically below 500 °C. Due to the high temperatures required for most solar fuel generation technologies, these systems have limited applications.

In a dish/engine system, a parabolic dish consisting of several mirrors reflect sunlight on to the receiver (10–400 kW_{th}) placed at the focal point of the dish. The dish is supported on a structure that tracks the sun during the day. The thermal energy absorbed by the heat transfer fluid in the receiver is then utilized for power generation typically by a Stirling engine or provide heat for solar fuels generation. The achievable temperature at the focal point of the dish can be up to 2,000 °C. Dish systems are modular in nature with many units placed in a field to achieve the desired thermal output.

In a tower system, a large number of flat mirrors called heliostats track the sun and reflect the sunlight on to a receiver placed on top of a tall tower. The heated fluid in the receiver is then utilized in the power generation turbines or to generate solar fuels. The maximum temperature achievable with solar tower system can be above 1,500 °C. Figure 11 shows an image of 1.2 MW CSP solar power tower research and demonstration facility with 450 heliostats at CSIRO Energy Centre, Newcastle, Australia [39]. The Ivanpah Solar Electric Power System in California's

Fig. 11 1.2 MW Concentrated Solar Power research and demonstration facility at CSIRO Energy Centre, Newcastle, Australia [39]

Fig. 12 An aerial view of the 392 MW Ivanpah concentrated solar power tower facility at sunrise, showing three towers. Picture taken from US DOE website with permission [40]

Mojave Desert is the largest solar power tower system in the world that consists of around 300,000 heliostats and three towers, capable of generating 392 megawatts of power, and serve nearly 100,000 average size homes [40]. Figure 12 shows the aerial view of the plant.

Worldwide the total power generated by CSP has reached over 4 GW, with a number of additional plants under construction. The CSP systems offer solar to electric efficiency in the 15–30% range. The present levelized cost of electricity from CSP systems is around US$0.13 per kWh, and US DOE under the SunShot Initiative has set the cost goal of US$0.06 per kWh by 2020 [40]. The major issues with CSP technologies are related to the materials required to work at high operating temperatures and the excessive cooling water used in the process (i.e., 3 L per kWh compared to 2 and 0.8 L per kWh for coal fired and combined cycle NG plants, respectively.) [41].

CSP technology can be used to store thermal energy (in the form of heated oil or molten salt) produced in excess during the day time when sun is available, and generating the electricity during the night time and during the cloudy days, thus reducing some intermittency issues related to the supply of renewable electricity. CSP can also be integrated with traditional NG power plants to operate as hybrid system for continuous power supply as well as capturing the benefits of both technologies including significant reduction in CO_2 emissions.

4.2 Thermolysis—Thermal Decomposition of H_2O, CO_2, NH_3, CH_4

Thermolysis of water is a process of splitting water molecule into oxygen and hydrogen using only thermal energy. As water molecule is one of the most stable molecules with a high bond dissociation energy of 436 kJ mol^{-1}, [42] thermolysis process requires extremely high temperatures in excess of 2,000 °C. Fundamentally, thermolysis is a simple one step reaction ($2H_2O \leftrightarrow 2H_2 + O_2$). However, in actual practical operating conditions, thermolysis of water is a complicated reaction. It is often referred to as a partial decomposition reaction because the rate of the forward reaction is comparable to the backward reaction, and recombination of reaction products; hydrogen and oxygen is highly facile. To avoid this recombination of products, the temperatures in the excess of 2,200 °C are often required in combination with the membrane reactors to separate the hydrogen from oxygen [43, 44]. Overall efficiencies of these systems are found to be significantly lower than other competing technologies such as electrolysis. Thus thermolysis of water is not considered amongst the economically viable technologies for solar hydrogen production [38, 45].

Besides thermolysis of water, a direct thermal splitting of CO_2 to CO and oxygen ($CO_2 \leftrightarrow CO + ½\ O_2$) has been explored in ceramic reactors operating at temperatures > 1,500 °C. The oxygen produced may be separated using oxygen permeable membranes such as doped zirconia. The process is less energy intensive compared to thermolysis of water. The overall process yield up to 20% has been demonstrated at 1,727 °C [46]. Due to extreme operating conditions and relatively lower yield, the economic prospect of this technology is bleak.

Another thermolysis process of interest is methane splitting into hydrogen and solid carbon ($CH_4 \leftrightarrow 2H_2 + C$) at temperatures in the range of 527–1,227 °C. The process produces pure hydrogen and, in principle, it does not require further separation as carbon is deposited on a catalyst bed in the form of solid carbon. Thus the hydrogen produced can be used directly in low temperature fuel cell systems. Up to 1 MW methane decomposition systems have been demonstrated at about 15% thermal efficiencies, and almost 100% conversion of methane using tubular reactors based on graphite tubes and parabolic solar concentrator. The key issues in furthering this technology are uncontrolled deposition of solid carbon on various parts of reactors resulting in blocking of gas flow during continuous operation, and low thermal efficiency [38, 47].

Thermal energy from solar concentrators can also be used to crack ammonia at high temperatures over a catalyst bed [48].

4.3 Thermochemical Cycles

A thermochemical cycle involves a series of chemical reactions leading to the net decomposition of H_2O and/or CO_2 into H_2 and/or CO and O_2 with heat provided from an external source such as concentrated solar or a nuclear reactor. The chemicals in the overall process are regenerated and recycled. The research into thermochemical cycles started in the 1960s, however, the integration of CSP system is relatively a new area compared to heat energy from nuclear reactors. These cycles are an attractive alternative to overcome the intrinsic problem of large heat requirement of a single step process for thermolysis of water and CO_2. A number of different cycles have been proposed. The most common cycles are sulphur–iodine, calcium–bromine, copper–chlorine, hybrid sulphur, ammonia cracking/synthesis to generate steam for Rankine power cycle, photolytic sulphur–ammonia, and continuously cycling metal oxide redox pairs with efficiencies in the 40–60% range and process temperatures up to 2000 °C [37, 38, 43, 49, 50].

An example of Sulphur–Iodine cycle for hydrogen generation is given below:

$$H_2SO_4 \rightarrow 1/2\,O_2 + SO_2 + H_2O \ (830 - 900\,^{\circ}C) \tag{5}$$

$$SO_2 + I_2 + 2H_2O \rightarrow 2HI + H_2SO_4 + \text{heat} \ (120\,^{\circ}C) \tag{6}$$

$$2HI \rightarrow I_2 + H_2 (300 - 450\,^{\circ}C) \tag{7}$$

$$\text{Net reaction: } H_2O \rightarrow H_2(g) + 1/2\,O_2(g). \tag{8}$$

In this cycle, SO_2 and I_2 react at a lower temperature with water to produce HI and sulfuric acid. HI is converted to H_2 and I_2 at an intermediate temperature and the sulfuric acid is converted to SO_2 at a moderately higher temperature with the overall process being conversion of water to hydrogen and oxygen via embedding of solar energy.

Although, there is a long history of process and technology development, most thermochemical cycles suffer from serious technical issues such as corrosion of reactor containment materials due to use of aggressive chemicals; significant materials degradation; reaction kinetics being too slow for different chemical reactions; conversion efficiency at each step combined with separation of reactants; and overall efficiency and cost of multistep process.

In general, two-step solar thermochemical cycles based on metal oxide redox pair systems shown in Fig. 13 have been more intensively investigated for production of solar thermal fuels (H_2, CO, syngas) due to potential high efficiencies (30–65% with heat recovery) and the use of less or non-corrosive materials. This process is also referred to as chemical looping. The typical reaction steps are:

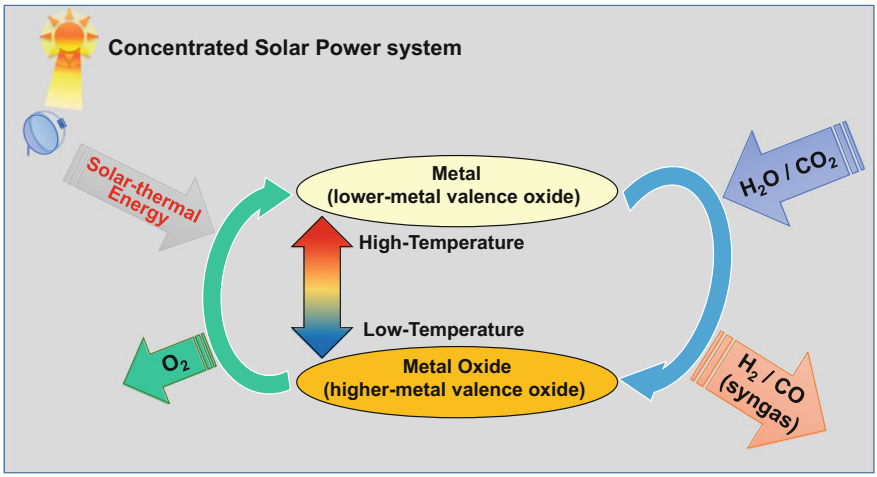

Fig. 13 A schematic of solar thermochemical cycles based on metal/metal oxide redox pairs

$$\mathrm{MeO} \rightarrow \mathrm{Me} + 1/2\,\mathrm{O_2} \quad \text{(reduction, high temperature)} \tag{9}$$

$$\mathrm{Me} + \mathrm{H_2O} \rightarrow \mathrm{MeO} + \mathrm{H_2} \quad \text{(oxidation, low temperature)} \tag{10}$$

$$\mathrm{Me} + \mathrm{CO_2} \rightarrow \mathrm{MeO} + \mathrm{CO} \quad \text{(thermal oxidation/splitting of } \mathrm{CO_2}\text{)} \tag{11}$$

Depending on the aim of thermochemical cycle process, syngas can be flexibly produced via combining reactions (10) and (11). In the regeneration step of reaction (9), the metal oxide can be reduced either to metal again (zero valence) or to a lower-metal valence oxide. A large number of different redox metal/metal oxide materials have been extensively studied. These metal oxide redox pairs can be divided into volatile (e.g., ZnO/Zn, CdO/Cd, SnO_2/SnO, GeO_2/GeO, etc.) and nonvolatile (e.g., Ce_2O_3/CeO_2, ferrites, sodium manganese, sodium manganate, hercynite ($FeAl_2O_4$), preovskites, etc.) cycles [7, 37, 38, 43, 49, 50]. Thermodynamic efficiencies for metal oxide-based thermochemical cycles have been discussed in recent reports and can be above 50–60% with heat recovery [38, 50].

The technology for the production of solar thermal fuels via thermochemical cycle routes has been under development, and projects at scales up to 100 kW or above have been considered and demonstrated and economic analysis performed for fuel production [7, 38, 43, 50]. Some of the challenges for such metal oxide redox cycles include sluggish reaction kinetics, sintering of metal oxides and long term stability, low oxygen retention capability; recombination of the decomposition products, melting/evaporation of metal reactant and phase/composition changes.

4.4 Solar Thermal Reforming/Gasification

Typically, highly endothermic reaction steps are involved in many large-scale industrial fossil fuel processes (steam reforming of methane, pyrolysis of LPG or natural gas and coal gasification) which require the combustion of some of the feedstock to drive the production of more useful chemical forms. However, if the heat component for the endothermic reaction can be supplied by concentrated solar radiation, the energy content of the product gases will be boosted as shown in Fig. 14 for methane as the fuel feed. Embedding of solar energy leads to reduction in the amount of feedstock required to provide heat for the endothermic reaction as well as reduction in CO_2 emissions and another avenue for the storage of solar energy. Indeed carbon-based solar synthetic fuels have been produced by modifying conventional fossil fuel processing for carbonaceous feedstocks (coal, natural gas) by embedding solar thermal energy from concentrated solar plants [7, 36, 38].

Solar thermal reforming of methane was firstly introduced in 1982 by US Naval Research Laboratory and since then it is one of the most widely researched solar thermal process globally. Two different main reactions considered are:

$$CH_4 + H_2O \rightarrow 3H_2 + CO \quad (\Delta H = 206 \text{ kJ mol}^{-1}) \tag{12}$$

$$CH_4 + CO_2 \rightarrow 2H_2 + 2CO \quad (\Delta H = 247 \text{ kJ mol}^{-1}). \tag{13}$$

Depending on the final product desired, the mixtures of CO_2/H_2O can be used in the solar thermal co-reforming process [36, 38]. The process has been widely investigated and up-scaled to several hundred kW size solar thermal plants in various configurations and reactor designs [7, 37, 38]. Residual technical issues

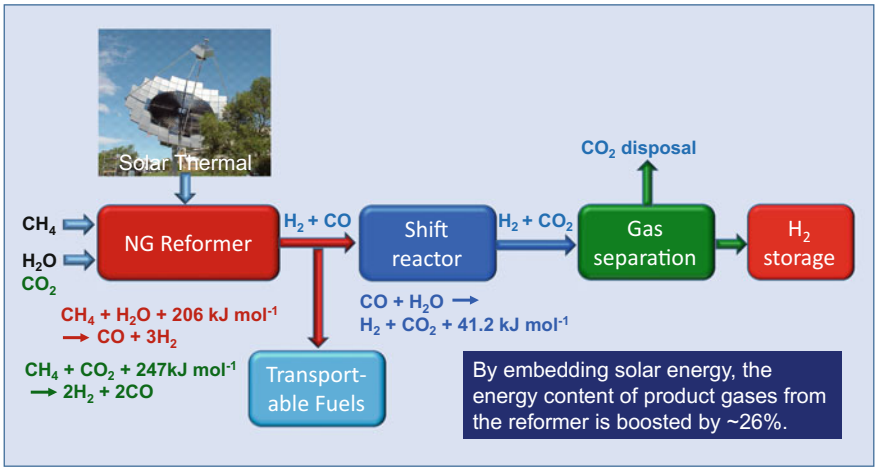

Fig. 14 A schematic of the solar thermal assisted methane reforming process

relate to the life time of the reactor and degradation of the steam/methane reforming catalyst due to daily thermal cycling as well as start-up and shut down issues.

Solid coal and biomass can also be utilized in a solar thermal assisted gasification process in the temperature range of 850–1,610 °C or to heat the feed stock (e.g., coal slurry drying) to increase process efficiency. However, as with most solar thermal processes, the challenge is to get heat of required quality and its transfer to an industrial process where it is needed. A 500 kW solar thermal steam gasification plant with petcoke as the feedstock (50 kg h^{-1}) was constructed with the solar radiation provided by 91 heliostats each of 39.3 m^2 surface area to produce syngas [51].

In addition, methane cracking (decomposition or pyrolysis) is also an endothermic reaction and can be assisted by embedding solar thermal energy to produce hydrogen and solid carbon ($CH_4 \leftrightarrow 2H_2 + C$) at temperatures above 500 °C. In this solar-aided methane decomposition process, small-scale reactors (<10 kW) have been operated with CH_4 conversion efficiency close to 100% (thermal energy efficiency of about 15%) at >1300 °C using pilot-scale 10 and 50 kW multi-tubular solar reactor [47]. However, the solid carbon particles produced in the process deposit on the reactor window and block the reactor exit [38].

5 Photo-Electrochemical and Photo-Biological Processes

5.1 Photo-Electrochemical Processes

As discussed above, hydrogen can be generated by first converting solar energy to electricity with solar cells and then coupling it to water electrolysis unit. In a very simplistic form, the photo-electrochemical process for hydrogen production combines these two separate processes into a single reactor. In this process semiconductor materials (somewhat similar to those used in photovoltaic cells) absorb sunlight to excite electrons from the valance band to the conduction band to electrochemically split water. Obviously for a given semiconductor material, the maximum of the valence band and the minimum of the conduction band determine how much of sunlight can be absorbed, the efficiency of conversion and suitability of a material. Doped or un-doped TiO_2 is one of the most widely studied materials, however, the band gap is too wide leading to low conversion efficiency. A number of other materials with or without doping (e.g., $BiVO_4$, Fe_2O_3, Ta_3N_5, GaN, (SrBa) TiO_3) and with the addition of a catalyst have been explored [52]. There is a significant global effort in developing viable concepts, new strategies, suitable materials and understanding the mechanism of the process to improve sunlight to hydrogen conversion efficiency. Although in small-scale laboratory devices, solar to hydrogen conversion efficiencies over 10% (threshold for practical devices) have been demonstrated in complex device structures, many key challenges remain related to device engineering, up-scaling, photo-electrode materials with high

conversion efficiency and long term stable performance, life time demonstration. Other issues relate to hydrogen collection from rather large area and economic viability of the process [52].

5.2 Bio-Photolysis Processes

The main ingredients of bio-photolysis are water, CO_2, and sunlight, all available in abundance. The process involves splitting of water with green algae and cyanobacteria under certain conditions using the photosynthetic process [53]. The same process can be used for the conversion of water and CO_2 to produce organic molecules or biomass. The main drawback of the process is very low light conversion efficiencies (<1%) and hydrogen production rates leading to the requirement for extremely large photo bio-reactors and high cost. Oxygen is also co-generated with hydrogen thus limiting the technology progression. The process is at a very early stage of development with most research directed at small laboratory scale experiments (using different micro-organisms, hydrogen enzymes, electron carriers, substrates, reactor designs, etc.). A substantial effort is required for these processes to be commercially viable [54].

6 Prospects of Solar Fuels

The solar fuels will play a significant role in the future energy mix as shown schematically in the solar fuel technology road map in Fig. 15. Currently, hydrogen, methanol and ammonia production contribute over US$200 billion to global economic activity and this will increase in the future as these products find penetration in the energy market. As a fuel, hydrogen has the best energy density by weight (about three times the energy density of gasoline at 142 MJ kg^{-1} (HHV) and 120 MJ kg^{-1} (LHV)) but has a very low volumetric energy density (0.0127 MJ L^{-1} (HHV) and LHV value is 0.0107 MJ L^{-1} at atmospheric pressure and ~4.7 MJ L^{-1} at 700 bar) and thus its transportation and storage are major issues in addition to the currently high cost of generation using renewable energy sources.

Hydrogen can be compressed using reciprocating compressors up to 700 bar and can be transported in gaseous form in pipelines or tube trailers (in steel tubes which store up to 280 kg at 250 bar and in composite tubes up to twice the amount per trailer at 700 bar). Hydrogen can also be transported in liquid form in cryogenic tanks at or below −253 °C. However, hydrogen compression to 350 or 700 bar or to convert it to liquid form is cost and energy intensive requiring up to 5–20% and 20–40%, respectively, of the energy content of hydrogen depending on the efficiency of the process used. Alternative technologies under consideration include ionic pumps and electrochemical compressors. Many commercial electrolysers

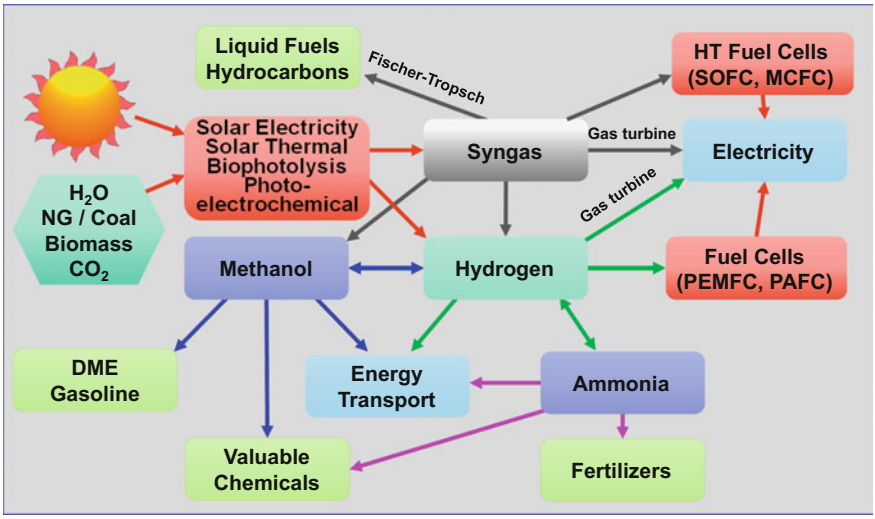

Fig. 15 A schematic of the solar fuels technology road map (adapted) [61]

coupled to solar PV can generate hydrogen easily at 35 bar pressure which is adequate for many stationary applications. Other potential H_2 carriers include metal hydrides, carbon or other nanostructures or high surface area materials (e.g., nanotubes and graphite nanofibers), borohydrides, metal organic frameworks and reversible or rechargeable hydrocarbons (methylcyclohexane (C_7H_{14}) and toluene (C_7H_8)), all requiring further research and development to attain required specifications for safe storage, transportation and recovery of spent or dehydrogenated chemicals [55].

Other major solar fuels, methanol containing 12.5 wt% H_2 (and volumetric energy density about half that of gasoline) and ammonia containing 17.65 wt% H_2, are liquids at room temperature and under low or mild pressures in comparison to hydrogen, are easy to store and transport. Methanol and ammonia offer a means of transporting solar energy from areas of high solar intensity to areas where solar intensity is low. Infrastructure for transportation of methanol and ammonia already exists. Ammonia can be transported in modified LPG tankers requiring pressure below 10 bar to keep it in liquid form. Fuels such as methanol and DME can be produced from CO_2 and water, and ammonia from water and nitrogen separated from air with input from renewable energy sources.

Hydrogen as a fuel can be used in fuel cell vehicles (cars; buses; trucks; locomotives; small transporters at airports, railway stations, shipyards; forklift; scooters; bikes; auto rickshaws; forward strategic defence vehicles, etc.). Fuel cells offer the highest efficiency (power or combined heat and power) amongst various combustion technologies. Hydrogen can also be used in an internal combustion engine (ICE) directly or mixed with compressed natural gas, co-combusted with diesel or burnt in a gas turbine.

Ammonia and methanol can be directly utilized in high temperature fuel cells (SOFC, MCFC) without the need for external cracking or hydrogen separation and methanol in low temperature fuel cells either directly or following external reforming [56, 57]. Both ammonia and methanol can be combusted directly in ICE. Methanol can also be combusted in ICE either neat or blended with gasoline noting that methanol like ammonia is a toxic fuel requiring extreme precautions.

The major potential for solar ammonia as an energy vector or fuel is in the future transport based on fuel cell vehicles. Ammonia can be easily transported and stored at service stations where high purity hydrogen can be generated from ammonia on-site. Various routes for hydrogen production are:

- Cracking over a supported catalyst, followed by absorption of residual ammonia for example in water (solubility is ~900 g per liter of water) or in a mild acidic solution.
- Metal membrane gas separation unit integrated with an ammonia cracking reactor [58].

In all these cases, hydrogen is generated at low pressures (~3 bar) and needs to be compressed to 350 or 700 bar for on-board use in fuel cell cars. This being both cost and energy consumption step, need to be factored in the overall life cycle analysis for comparison with other forms of hydrogen transport.

Prospects for solar fuels in the future energy mix look very promising in view of reducing prices of emerging solar technologies leading to significantly lower renewable fuel production costs. As an example, the water electrolysis with solar PV has the potential to generate hydrogen at less than US$5 per kg [59]. With another US$2–3 added for distribution, compression, dispensing, the price at the pump can be around <US$8 per kg or US$40 per fuel tank containing 5 kg hydrogen which will give >500 km driving distance in a fuel cell car. This is very competitive with current ICE cars with very low or net zero greenhouse or pollutant emissions. Methanol and dimethyl ether are increasingly being used as a replacement fuel or as blends with gasoline or diesel and ICE operating on such fuel are expected to be more efficient with significantly lower GHG and pollutant emissions. Ammonia is now beginning to be considered as another energy and hydrogen carrier. However, a complete life cycle analysis is required to establish the viability of using it as transporting media for renewable energy.

7 Conclusion

Currently fossil fuels are the major source of energy carriers. However, with increasing pollution, depleting carbon-based resources and concern over global warming our dependency on fossil fuels derived energy carriers cannot continue too long into the future. Solar derived fuels such as hydrogen, syngas, methanol and ammonia generated where the solar radiation is used for their production,

have the potential to play an increasing role in the future energy mix. Solar fuels are also means of transporting solar energy as the raw resource, from locations with high solar intensity to locations where the solar energy intensity is low. Solar fuel production in addition to water may involve utilization of CO_2 (from chemical and power plants and refineries) as well, and embedding of solar energy in fossil fuels such as carbon (biomass, coal) or NG to generate hydrogen or syngas which can then be used as energy carriers or used as precursors for the production of liquid fuels. A number of solar processes and technologies are under development globally. The main solar processes include concentrated solar power plants (CSP) for providing heat for solar fuel generation or electricity via solar photovoltaic (PV) or both heat and electricity. Solar fuels may include H_2, CO, syngas, methane, methanol, formic acid, ammonia, dimethyl ether (DME) and diesel. Many processes are in the early research and development phase but showing great promise and also requiring substantial investment of resources. Other technologies such as water electrolysis and solar thermal reforming of natural gas are at an advanced stage of development and reaching commercialization.

Acknowledgements The authors would like to thank Dr. Daniel Roberts for reviewing this manuscript. This article is dedicated to the memories of Late Professor John O'M Bockris whose contribution to Electrochemistry, Solar Fuels, and Hydrogen Economy has been of immense significance for the betterment of this world.

References

1. Olivier JGJ, Janssens-Maenhout G, Muntean M, Peters JAHW (2015) Trends in global CO_2 emissions: 2015 Report, The Hague: PBL Netherlands Environmental Assessment Agency; Ispra: European Commission, Joint Research Centre. 2015 PBL publication number: 1803. http://www.pbl.nl/sites/default/files/cms/publicaties/pbl-2015-trends-in-global-co2-emisions_2015-report_01803.pdf. Accessed 8 Nov 2016
2. Bockris JOM (1975) Energy: the solar-hydrogen alternative. Wiley, New York
3. Bockris JOM (1980) Energy options : real economics and the solar-hydrogen system. Taylor & Francis, London
4. Giddey S, Badwal SPS, Kulkarni A (2013) Review of electrochemical ammonia production technologies and materials. Int J Hydrog Energy 38:14576–14594
5. Bozzano G, Manenti F (2016) Efficient methanol synthesis: Perspectives, technologies and optimization strategies. Prog Energy Combust Sci 56:71–105
6. Armaroli N, Balzani V (2016) Solar electricity and solar fuels: status and perspectives in the context of the energy transition. Chem Eur J 22:32–57
7. Hinkley J, Hayward J, McNaughton R, Edwards J, Lovegrove K (2016) Concentrating solar fuels roadmap: final report. CSIRO, Australia
8. Herron JA, Kim J, Upadhye AA, Huber GW, Maravelias CT (2015) A general framework for the assessment of solar fuel technologies. Energy Environ Sci 8:126–157
9. Philibert C (2014) Technology roadmap: solar thermal electricity—2014 edition. IEA, Paris, France
10. Roy SC, Varghese OK, Paulose M, Grimes CA (2010) Toward solar fuels: photocatalytic conversion of carbon dioxide to hydrocarbons. ACS Nano 4:1259–1278

11. Steinfeld A (2005) Solar thermochemical production of hydrogen–a review. Sol Energy 78:603–615
12. Badwal SPS, Giddey S, Munnings C (2013) Hydrogen production via solid electrolytic routes. WIREs Energy Environ. 2:473–487
13. Decourt B, Lajoie B, Debarre R, Soupa O (2014) Leading the energy transition factbook, hydrogen-based energy conversion—more than storage: system flexibility. SBC Energy Institute. http://www.sbcenergyinstitute.com/Publications/Hydrogen.html. Accessed 2 Nov 2016
14. Teledyne Energy Systems, Inc (2016) Titan EL. http://www.teledynees.com/our-products/hydrogen-oxygen-generation-systems/titan-el. Accessed 6 Feb 2017
15. Siemens (2016) Silyzer systeme. http://www.industry.siemens.com/topics/global/en/pem-electrolyzer/silyzer/discovering-pem-technology/Pages/Discovering-pem-technology.aspx. Accessed 2 Nov 2016
16. Giddey S, Kulkarni A, Badwal SPS (2015) Low emission hydrogen generation through carbon assisted electrolysis. Int J Hydrog Energy 40:70–74
17. Clarke RL, Foller PC, Wasson AR (1988) The electrochemical production of hydrogen using a carbonaceous fuel as an anode depolarizer. J Appl Electrochem 18:546–554
18. Sethu SP, Gangadharan S, Chan SH, Stimming U (2014) Development of a novel cost effective methanol electrolyzer stack with Pt-catalyzed membrane. J Power Sources 254:161–167
19. Delacourt C, Ridgway PL, Kerr JB, Newman J (2008) Design of an electrochemical cell making syngas ($CO + H_2$) from CO_2 and H_2O reduction at room temperature. J Electrochem Soc 155:B42–B49
20. Badwal SPS, Giddey SS, Munnings C, Bhatt AI, Hollenkamp AF (2014) Emerging electrochemical energy conversion and storage technologies. Front Chem 2:1–28
21. Xu G, Liu R, Wang J (2009) Electrochemical synthesis of ammonia using a cell with a Nafion membrane and $SmFe_{0.7}Cu_{0.3-x}Ni_xO_3$ ($x = 0 - 0.3$) cathode at atmospheric pressure and lower temperature. Sci China, Ser B Chem 52:1171–1175
22. Muthuvel M, Botte GG (2009) Trends in ammonia electrolysis. In: White RE (ed) Modern aspects of electrochemistry, vol 45. Springer, New York, pp 207–245
23. Ebbesen SD, Jensen SH, Hauch A, Mogensen MB (2014) High temperature electrolysis in alkaline cells, solid proton conducting cells, and solid oxide cells. Chem Rev 114:10697–11073
24. Dönitz W, Erdle E (1985) High-temperature electrolysis of water vapor–status of development and perspectives for application. Int J Hydrog Energy 10:291–295
25. Badwal SPS, Giddey S, Munnings C, Kulkarni A (2014) Review of progress in high temperature solid oxide fuel cells. J Aust Ceram Soc 50:23–37
26. Moçoteguy P, Brisse A (2013) A review and comprehensive analysis of degradation mechanisms of solid oxide electrolysis cells. Int J Hydrog Energy 38:15887–15902
27. Mathiesen BV, Ridjan I, Connolly D, Nielsen MP, Vang Hendriksen P, Bjerg Mogensen M, Højgaard Jensen S, Dalgaard Ebbesen S (2013) Technology data for high temperature solid oxide electrolyser cells, alkali and PEM electrolysers. Department of Development and Planning, Aalborg University, Denmark. http://vbn.aau.dk/files/80222058/Technology_data_for_SOEC_alkali_and_PEM_electrolysers.pdf. Accessed 8 Nov 2016
28. Ewan BCR, Adeniyi OD (2013) A demonstration of carbon-assisted water electrolysis. Energies 6:1657–1668
29. Alexander BR, Lee A, Mitchell R, Gür T (2010) Carbon-free hydrogen production in a steam-carbon electrochemical cell. ECS Trans 28:67–76
30. Halmann MM, Steinberg M (1998) Greenhouse gas carbon dioxide mitigation: science and technology. CRC press, LLC. https://www.crcpress.com/Greenhouse-Gas-Carbon-Dioxide-Mitigation-Science-and-Technology/Halmann-Steinberg/p/book/9781566702843. Accessed 2 Nov 2016
31. Alioshin Y, Kohn M, Rothschild A, Karni J (2016) High temperature electrolysis of CO_2 for fuel production. J Electrochem Soc 163:F79–F87

32. Jensen S, Larsen P, Mogensen M (2007) Hydrogen and synthetic fuel production from renewable energy sources. Int J Hydrog Energy 32:3253–3257
33. Amar IA, Lan R, Petit CTG, Arrighi V, Tao S (2011) Electrochemical synthesis of ammonia based on a carbonate-oxide composite electrolyte. Solid State Ionics 182:133–138
34. Edwards JH, Badwal SPS, Duffy GJ, Lasich J, Ganakas G (2002) The application of solid state ionic technology for novel methods of energy generation and supply. Solid State Ionics 152–153:843–852
35. Imenes A, Fell C, Stein W (2007) Spectral beam splitter for solar hydrogen production. Proc Sol 7. https://publications.csiro.au/rpr/pub?list=BRO&pid=procite:e8c8de76-709f-4ea4-9d34-83ba09fff05f. Accessed 6 Feb 2017
36. Agrafiotis C, von Storch H, Roeb M, Sattler C (2014) Solar thermal reforming of methane feedstocks for hydrogen and syngas production—a review. Renew Sustain Energy Rev 29:656–682
37. Agrafiotis C, Roeb M, Sattler C (2015) A review on solar thermal syngas production via redox pair-based water/carbon dioxide splitting thermochemical cycles. Renew Sustain Energy Rev 42:254–285
38. Yadav D, Banerjee R (2016) A review of solar thermochemical processes. Renew Sustain Energy Rev 54:497–532
39. CSIRO (2016) http://www.csiro.au/en/Research/EF/Areas/Solar/Solar-thermal/Solar-thermal-hub. Accessed 2 Nov 2016
40. US Department of Energy (2014) Fuel cell technologies office, Hydrogen production. http://energy.gov/eere/fuelcells/hydrogen-production. Accessed 2 Nov 2016
41. Rajavi Y (2013) Concentrating solar power. http://large.stanford.edu/courses/2013/ph240/rajavi1/. Accessed 2 Nov 2016
42. Wiberg E, Wiberg N, Holleman AF (2001) Inorganic chemistry. Academic press, San Diego, USA
43. Stolten D (2016) Hydrogen science and engineering: materials, processes, systems and technology, vol 2. Wiley
44. Yilanci A, Dincer I, Ozturk HK (2009) A review on solar-hydrogen/fuel cell hybrid energy systems for stationary applications. Prog Energy Combust Sci 35:231–244
45. Agrafiotis CC, Pagkoura C, Lorentzou S, Kostoglou M, Konstandopoulos AG (2007) Hydrogen production in solar reactors. Catal Today 127:265–277
46. Itoh N, Sanchez MA, Xu W-C, Haraya K, Hongo M (1993) Application of a membrane reactor system to thermal decomposition of CO2. J Membr Sci 77:245–253
47. Rodat S, Abanades S, Sans J-L, Flamant G (2010) A pilot-scale solar reactor for the production of hydrogen and carbon black from methane splitting. Int J Hydrogen Energy 35:7748–7758
48. Nakamura N (2012) Method for converting solar thermal energy. US patent no: 8,272,216 B2, 25 September 2012
49. Funk JE (2001) Thermochemical hydrogen production: past and present. Int J Hydrogen Energy 26:185–190
50. Perret R (2011) Solar thermochemical hydrogen production research (STCH)—thermochemical cycle selection and investment priority, Sandia National Laboratories SANDIA REPORT: SAND2011-3622. http://energy.gov/sites/prod/files/2014/03/f9/solar_thermo_h2.pdf. Accessed 3 Nov 2016
51. Vidal A, Denk T, Steinfeld L, Zacarías L, Almería T (2010) Upscaling of a 500 kW solar gasification plant. In: Proceedings of 18th world hydrogen energy conference 2010—WHEC 2010, vol 78, pp 177–81. Forschungszentrum Jülich GmbH, Zentralbibliothek, Verlag
52. Giménez S, Bisquert J (2016) Photoelectrochemical solar fuel production: from basic principles to advanced devices. Springer International Publishing, Cham
53. Yu J, Takahashi P (2007) Biophotolysis-based hydrogen production by cyanobacteria and green microalgae, Communicating current research and educational topics and trends in applied microbiology. In: Méndez-Vilas A (ed), pp 79–89. http://www.formatex.org/microbio/pdf/Pages79-89.pdf. Accessed 3 Nov 2016

54. Sen U, Shakdwipee M, Banerjee R (2008) Status of biological hydrogen production. J Sci Ind Res 67:980–993
55. Riis T, Hagen EF, Vie PJS, Ulleberg Ø (2006) Hydrogen production and storage R&D priorities and gaps: OECD/IEA, 2006. IEA, Paris, France
56. Lan R, Tao S (2014) Ammonia as a suitable fuel for fuel cells. Front Energy Res 2(35):4
57. Giddey S, Badwal SPS, Kulkarni A, Munnings C (2012) A comprehensive review of direct carbon fuel cell technology. Prog Energy Combust Sci 38:360–399
58. Rizzuto E, Palange P, Del Prete Z (2014) Characterization of an ammonia decomposition process by means of a multifunctional catalytic membrane reactor. Int J Hydrogen Energy 39:11403–11410
59. Colella WG, James BD, Moton JM, Saur G and Ramsden T (2014) Techno-economic analysis of PEM electrolysis for hydrogen production. In: Electrolytic hydrogen production workshop, NREL, Golden, Colorado, 27 February 2014
60. Laguna-Bercero MA (2012) Recent advances in high temperature electrolysis using solid oxide fuel cells: a review. J Power Sources 203:4–16
61. Harris DJ, Roberts DG (2013) Coal Gasification and Conversion. In: Osborne D (ed) The coal handbook—towards cleaner production, Volume 2: Coal utilisation. Woodhead Publishing, Philadelphia